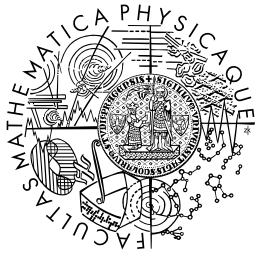

FACULTY
OF MATHEMATICS
AND PHYSICS
Charles University

DOCTORAL THESIS

Matěj Tomeš

Forward and Backward Modelling of Spectroscopic Diagnostics in Fusion Plasmas

Department of Surface and Plasma Science

Supervisor of the doctoral thesis: Mgr. Jakub Seidl, Ph.D.

Study programme: Physics of Plasmas and Ionised Media

Prague 2024

I declare that I carried out this doctoral thesis independently, and only with the cited sources, literature and other professional sources.

I understand that my work relates to the rights and obligations under the Act No. 121/2000 Sb.., the Copyright Act, as amended, in particular the fact that the Charles University in Prague has the right to conclude a license agreement on the use of this work as a school work pursuant to Section 60 subsection 1 of the Copyright Act.

In Prague on 4$^{\text{th}}$ of January 2024

Author's signature

Dedication

As one of my supervisors once told me during my master studies, dedication is the part of a thesis where you can try to make some internal jokes to make yourself look less serious. After the marathon of writing and finishing this thesis, I'm not sure I can squeeze out of myself any good humor. I will however try to give it my best. In any case, and this is important, I would not like these attempts to undermine my gratitude to all the people who helped me during my PhD studies.

In first place I have to, sorry, want to (**wink**), express my deepest gratitude to my wife Eva Tomešová who supported me in my studies. Especially for the last months when I was writing my thesis. Not only did she give me the space and time to finish my work, but she actively helped me with proofreading, editing and suggested many improvements which helped me to get this thesis into a much better shape. I have to thank her for preventing me from adding jokes into the preface, such as comparing the length of this thesis to the book by Ernest Hemingway "The old man and the sea". I have to mention that she did all this while taking care of our son Matěj who by the time I was handing in this thesis was only 7 months old. I would also like to thank to the rest of my family and especially to my mother Irena Tomešová for helping us with our son Matěj during the final months of my studies. I would like to thank my son Matěj for being such a positive and happy child who always charged me with positive energy and who could honestly start sleeping a bit more.

I would like to thank Jakub Seidl for his guidance and the time he invested in helping me. Jakub's help with my transition from the charge exchange spectroscopy diagnostic to forward and backward modelling was invaluable. This was even more important to me since he initially started investing large amounts of time and effort in discussions, suggestions and guidance without being officially connected to my studies. He is one of the most talented, knowledgeable and thorough people I had the chance to collaborate with. No matter how much I tried to resist some of his very demanding suggestions, in the end I always had to admit that he was right. Not always tho! Not everything is suited for GPU acceleration and neural networks! At least not today!

During my work at the COMPASS tokamak I had the privilege to be seated in the best office in the world, the FIST. The F stands for David Fridrich who supported our office with daily rations of jokes and fun facts. I would also like to thank David for the consultations regarding numerical simulations and his support with IT issues. The I stands for Martin Imríšek, the silent force moving mountains. Martin was probably the first person I had to interact with at COMPASS, this is because I had to share a desk with him and he constantly kept occupying the right region of my desk. I would like to thank Martin for always being ready and willing to help with pretty much anything. From proofreading this thesis to going out for a beer in the evening. I also have to express my admiration to him that he finally took the courage and started switching from Matlab to Python. The S stands for Jakub Svoboda, the youngest. I have to thank Jakub for his extremely critical and realistic views of problems. Also I have to admit he can prepare a decent tea. The T stands for me, Matěj Tomeš. I would like to thank myself for being such a joy to work and share an office with. I was a calm and silent officemate, always in a good mood, constructive and positive. I also have to thank

myself for being so humble and modest (**wink**).

Another round of my gratitude goes to Matthew Carr and Alex Meakins who are the founders of Raysect and Cherab framework. Since I discovered it at an EPS conference in Belfast I saw its enormous potential. After certain operational issues with the charge exchange diagnostic on COMPASS, Raysect and Cherab became the main focus of my work. I owe a large part of my PhD thesis to this framework and thus to Matt and Alex who also invested a non-negligible amount of time in training me to become a better programmer and developer. I would also like to thank Jack Lovell and Vladislav Neverov, the co-developers of Cherab, for their help, code maintenance, development and extensive code reviews.

I would also like to thank the members of the COMPASS Thomson scattering team Petra Bílková, Petr Böhm and Miroslav Sos. Their insight and devotion to the development of the forward model of Thomson scattering was invaluable. I would like to thank Miro for his proofreading of the Thomson scattering chapter and his suggestions for improvements. Also, I would like to thank them for being able to sit in the office next to FIST which sometimes meant listening to our discussions, jokes and laughs. All together the members of the two offices were able to create a very nice atmosphere in our corridor. For example by sharing great coffee breaks. I would also like to thank the members of the synchrotron team Eva Tomešová, Ondřej Ficker and Jakub Seidl for a great working experience, support and fun during the development of the model.

I would like to mention my thanks to the members of the COMPASS team for creating such a great work environment and for all the effort put in operation of the COMPASS tokamak. It was a great and motivating experience to spend time in the control room during experiments. Many of the work relations grew into great friendships. For example, I would like to thank Tomáš Markovič for forming our Dungeons and Dragons group and for being our great dungeon master. It is almost impossible for me to name all the people from COMPASS who positively influenced me during my studies. My thanks for example belongs to Stanislav Tokoš, Jakub Urban and Pavel Cahyna for their contributions and maintenance of our IT infrastructure. I would like to say thanks to the director Radomír Pánek and the heads of the department Martin Hron and Michael Komm for being understanding and supportive during certain heavier times.

My gratitude also belongs to many foreign colleagues who I met during my studies. There are so many I could fill a whole page with their names. I hope those who are not mentioned here will not be offended. I would like to mention Carine Giroud for including me in the JET related work I did. I would also like to thank Scott Silburn for his support in the field of JET cameras. Gergo Pokol and Örs Asztalos for the interesting work regarding neutral beams and diagnostics. I also had the chance to become friends with many people from other topis who were just passing by during their studies. For example Filip Janky who worked for COMPASS only for six months before leaving abroad or Pedro Lourenço who worked on on COMPASS during his studies. With both I enjoyed many interesting discussions and fun times and managed to stay in contact until now.

At last I would like to give my gratitude to the Department of Surface and Plasma science. I would like to thank Jana Šafránková, Zdeněk Němeček and Jiří Pavlů for their roles in the study programmes and for organising the Week of doctoral students conference and the winter seminars. Without the winter

seminars I wouldn't have experienced and achieved the best thing which happened to me. It was at my first winter seminar where I met my wife Eva.

At the end, I would like to express my gratitude to Jan Mlynář who was my official supervisor during most of my studies. Sadly, Jan passed away before I was able to finish my thesis and didn't get the chance to see it. I would like to thank him for giving me the chance to become a PhD student and for becoming my supervisor.

Title: Forward and Backward Modelling of Spectroscopic Diagnostics in Fusion Plasmas

Author: Matěj Tomeš

Department: Department of Surface and Plasma Science

Supervisor: Mgr. Jakub Seidl, Ph.D., Institute of Plasma Physics of the Czech Academy of Sciences

Abstract: The thesis primarily focuses on developing forward and backward models for fusion diagnostics. It encompasses the development and application of these models for Thomson scattering, the inference of neon concentrations in JET's divertor and for synchrotron radiation.

In the first chapter, the forward model of Thomson scattering designed for Cherab is detailed. This includes the development of a laser module intended for a wide range of applications, primarily to facilitate Thomson scattering simulations. An application example is provided by a comprehensive model of the Thomson scattering diagnostic used at the COMPASS tokamak. The model of the diagnostic is combined with experimentally obtained electron profiles to assess its performance. The second half of the chapter focuses on the development of a backward model for Bayesian inference of temperature profiles from measured Thomson scattering data. The effectiveness of this model is compared to the conventional approach based on least square error optimization, revealing clear advantages of the Bayesian model.

Chapter two elaborates on the development of a zero transport backward model, based on Bayesian inference of neon spectral line intensity, for deducing neon concentration in JET's divertor during neon seeded discharges. Prior to applying this model to actual data, its performance is rigorously evaluated using data generated by a forward model. A method for comparing statistical inference with forward modeling is introduced. The quality of the inverted experimental concentration profiles is then scrutinized in light of several factors: reflections, concentration measurements at the midplane, and theoretical predictions derived from SOLPS simulations.

Chapter three introduces a novel synchrotron model for Cherab. The model's versatility includes the ability to simulate reflections from the first wall and the effects of toroidally asymmetric runaway electron distributions and 3D magnetic fields. The capabilities of the model are demonstrated on forward modelling of JET's infrared cameras KLDT-E5WC and KL7-E8WB. In the case of KLDT-E5WC, the model successfully replicates image patterns resulting from magnetic islands. For both cameras similarity in measured and forward modelled reflection patterns is observed.

Keywords: forward model backward model Raysect Cherab Thomson scattering synchrotron radiation neon seeding

Contents

Preface

Before the main contents of the thesis, I would like to introduce the reader to the general approach and style I applied to this thesis. I wrote the text in the passive form since it comes more naturally to me and is in my opinion more natural for scientific texts. It also increased my writing efficiency. I acknowledge that this goes slightly against the point of a dissertation thesis, which is to summarise and highlight the work I performed during my Ph.D. studies.

To solve this collision, I have separated the contents according to authorship into three categories. The first is knowledge taken from external sources I assumed to be generally known and available. By this I mean for example Bayesian inference methods. By saying I applied it I certainly didn't want to assert my authorship. The second category is my contribution. The third category is knowledge and findings of others I reused in the thesis and which in my opinion didn't belong to the generally available knowledge. In the case of the first category I reserved myself from adding citations periodically whenever this category came up. The citations in this case are used for the sake of reader to be pointed to a source of additional information. In the case of the third category, proper citations were used every time. Whenever I felt that the content I was writing is in a grey zone between any of these categories, I either added a citation or mentioned whether the work is mine or taken from an external source.

I would also like to give a remark to the structure of the thesis. The thesis includes three separate topics which are loosely connected by forward and backward modelling and statistical data analysis. For this reason I decided not to adapt the standard separation into introduction, body and conclusion for the whole thesis. This structure is kept for the individual chapters. In every chapter, I tried to give an introduction to its topic, then I described what I did and I tried to draw some conclusions and outline future work. At the end, I added a general conclusion in which I tried to summarise what was done altogether.

When I started writing I wanted to aim for handing in a short thesis. I tried to make it shorter by excluding long introductions into general topics. I think that there are already many widely available and great introductory texts into all of the topics included in this thesis. I assumed it is not worth trying to compete with those by trying to reinvent the wheel. Instead, I tried to point the reader in the direction of interesting sources that can provide more information. To give an example, I didn't include any introduction into thermonuclear fusion, why we need it and what are the basic principles of magnetic plasma confinement. If anyone is interested in refreshing their knowledge about these topics, I recommend to start from the book by Freidberg [1] and continuing where your interest takes you from there.

The last thing before I take on my scientists hat is to wish you a good reading experience and that you find the time invested in reading the following text useful.

1. Introduction

This thesis focuses on developing forward and backward models for spectroscopic diagnostics in fusion plasmas and is divided into three main chapters. Each chapter presents a selection of models developed during the Ph.D. studies. As the connection between chapters is mainly through ray tracing and statistical data analysis, each includes its own dedicated introduction and conclusion.

The first chapter details the Thomson scattering module developed for the Cherab package [2], a key part of this thesis. It outlines the core principles and structure of the module. This chapter also demonstrates the module's application in modeling the COMPASS tokamak's Thomson scattering diagnostic. Additionally, it introduces a novel backward model for the statistical inversion of electron temperature and density from Thomson scattering diagnostic data. This model employs Bayesian inference, with its benefits illustrated using data from the COMPASS tokamak's diagnostic.

The second chapter describes how neon impurity concentrations in the JET (Joint European Torus) tokamak's divertor during neon-seeded discharges are inferred. This process uses measured intensities of spectral lines and their ratios. The backward model's performance is initially tested using forward-modelled spectroscopic data. For this, a Cherab model of the divertor spectroscopy diagnostic was developed. Combining this model with SOLPS [3] simulation results, forward models for neon and deuterium line spectra are generated. A new statistical method, accounting for diagnostic and plasma state characteristics, is developed to assess the backward model. This model is then applied to experimental data from the JET tokamak.

The third chapter discusses the development of a synchrotron radiation model for Cherab, a significant aspect of this work. This model's implementation is distinct from other forward modelling codes for synchrotron radiation, as it avoids particle tracking. Instead, it adopts a kinetic approach, relying on a six-dimensional runaway electron distribution function as its input. This methodology not only enhances simulation efficiency but also increases versatility. It accommodates the effects of toroidally asymmetric runaway electron distributions and fully 3D magnetic fields, such as those in magnetic islands. Furthermore, in conjunction with Raysect's [4] general ray tracing capabilities, the model can simulate the effects of reflections from plasma facing components. The chapter also presents practical applications of this model on infrared camera measurements from JET tokamak runaway electron discharges, capturing effects like component reflections and magnetic island influences.

Fusion plasmas, such as those in the Joint European Torus (JET), are complex physical systems. The charged particles within these plasmas interact over relatively long distances, creating collective behaviors. Their charge also enables interaction with and generation of electromagnetic waves, including specific types like Langmuir waves. Magnetically confined plasmas, characterized by large gradients, exhibit diverse phenomena influencing particle transport, such as turbulent transport. These phenomena span various temporal scales, from the slow evolution of tokamak current profiles over seconds to rapid microsecond-scale events related to turbulent transport. The given list of phenomena and scales only scratches the

surface of the complexity faced in hot magnetically confined plasmas.

The experimental chambers in magnetic confinement devices, designed more for testing future reactor concepts than for easy access, pose challenges for measurement and diagnostics. The focus on plasma performance often limits the number and type of diagnostic tools available. Consequently, only a subset of necessary phenomena is measured directly with sufficient resolutions. To overcome these limitations, diagnostic systems at fusion devices must be pushed to their limits. This involves precise instrument design and operation, including accurate calibration and detailed documentation of system properties. Effective data engineering is also crucial, ensuring comprehensive descriptions of each dataset for correct interpretation later. Detailed annotations should include time base, instrument state, calibration, and more. Only meticulous approach to these aspects ensures that the maximum information is extracted from the data, optimizing the use of resources.

The process termed 'information extraction' in plasma diagnostics notably involves the application of backward models. A backward model computes an estimate of a specific plasma quantity from measured data, taking into account the diagnostic state (such as the size of the measured region or frequency band) and the theoretical understanding of the phenomena utilized by the diagnostic tool. For instance, the calculation of electron temperature (T_e) using the Thomson Scattering (TS) diagnostic hinges on the spectral analysis of laser light scattered by electrons, as detected by the diagnostic system. Essential properties of the diagnostic, like the scattering angle determined by its geometry, and the theoretical principles of Thomson scattering, are integrated into a computational model. This model interprets the measured data in reverse to derive the electron temperature. The accuracy of this inverted information depends on several factors: the reliability of the input data (e.g., scattering angle), the precision of the theoretical description, and the quality of the backward model's implementation.

The diagnostic methods in fusion research have significantly evolved throughout its history, transitioning from the analysis of graphical outputs on cathode ray oscilloscopes to contemporary digital data acquisition systems. Initially, the analog nature of data necessitated manual backward modeling, often using mechanical calculators like slide rules. With the advent of digital data and modern computing, numerical analysis of measured data became possible. Contemporary numerical backward models predominantly utilize optimization techniques in a specific metric space. A common example is the least square approach, which minimizes the disparity between measured and modeled data, often under simplifications like assuming normally distributed uncertainties. Recent advancements in computational power, notably from CPUs (Central Processing Units) and GPUs (Graphics Processing Units), have facilitated the use of more computationally intensive solutions in backward models. These include the application of statistical inferences and machine learning techniques for converting measured data into physical quantities.

The advent of enhanced computational power has not only revolutionized backward modeling but has also significantly improved the quality of forward modeling in diagnostic data analysis. As previously described, backward models estimate plasma quantities from measured data, functioning inversely to the diagnostic process. Conversely, forward models emulate the diagnostic process

itself, translating plasma quantities into anticipated diagnostic data. These models encapsulate both the diagnostic's characteristics and the theoretical understanding of the phenomena it measures, outputting an estimate of the diagnostic data for a given plasma state.

The sophistication of a forward model is directly proportional to the desired accuracy of its output. For instance, forward models for electrical probes may range from simple formulae, which calculate a Volt-Ampere characteristic based on electron density and temperature, to more intricate models. These advanced models might employ fluid dynamics to simulate the probe sheath or even use particle-in-cell simulations for greater precision.

The increase in computational power has significantly enhanced forward modeling capabilities for spectroscopic diagnostics across infrared, visible, and ultraviolet wavelengths. Spectroscopic systems benefit from the assumption that plasma is mostly optically thin in these ranges, facilitating measurements across various regions and conditions. However, this also presents a substantial challenge: a spectroscopic diagnostic system captures light from its entire field of view (FOV), making both the backward calculation of plasma properties and forward modeling equally demanding. In some cases, forward modeling can be simplified by integrating over a reduced FOV, using basic geometric shapes like cylinders or cones. However, in scenarios where the FOV is too complex for such elementary approximations, particularly in chambers with reflective surfaces such as metals, ray tracing becomes the most viable method for integration.

Traditionally, the high computational demands of ray tracing limited its frequent application. However, recent improvements in ray tracing algorithms, along with the surge in computational capabilities, have rendered its use viable for forward modeling within reasonable timeframes. This advancement enables the creation of more intricate models for spectroscopic diagnostics, which can now include detailed descriptions of detectors, optical systems, and extensive plasma state characterizations.

The integration of forward and backward models can substantially enhance both the efficacy of diagnostic systems and the accuracy of the inferred plasma properties. Forward models offer crucial insights during the design phase of diagnostics, aiding in the identification and mitigation of potential performance issues and facilitating optimization. Furthermore, forward modeling plays a pivotal role in the development and refinement of backward models. By generating diagnostic data from a predefined plasma state, forward models enable a comprehensive evaluation of the backward model's performance, ensuring more reliable and accurate plasma diagnostics.

To conclude, forward and backward modeling are indispensable components of experimental design and operation. In essence, every experimentalist engages in this modeling process, often unconsciously, while planning and conducting experiments. This process involves deciding what and how to observe and how to interpret observations, a practice as old as experimental science itself. The recent advancements in fusion research have not introduced novel concepts in this realm but have significantly enhanced the depth and efficiency of these models. This evolution mirrors the transformative impact of digital data processing in experimental physics.

The contemporary trends in modeling, particularly the use of Bayesian analysis

for constructing complex, integrated backward models, are opening new horizons. These models, which assimilate data from various diagnostics and incorporate comprehensive theoretical knowledge, are unlocking insights into plasma properties that were previously unattainable. It's important to view forward and backward modeling as tools for scientific advancement, developed with specific goals in mind. Their development should be need-driven, tailored to the requirements of the experiments, and done in close collaboration with experimentalists and diagnosticians. This ensures that the evolution of these models is not just a pursuit in itself, but a means to enhance experimental physics.

1.1 Forward and Backward Modelling

Diagnosing fusion plasma can essentially be viewed as a process of loosely sampling the plasma state, followed by attempts to reconstruct the complete plasma state from these samples:

$$\begin{aligned} O_M(\boldsymbol{r}_i, t_i) &= \sum_{i=(\boldsymbol{r},t)} \delta(\boldsymbol{r} - \boldsymbol{r}_i, t - t_i) \cdot \mathcal{D}_M \left(\mathcal{F}_M \left(\mathcal{P}(\boldsymbol{r}, t) \right) \right), \\ \tilde{P}(\boldsymbol{p}, \boldsymbol{r}_i, t_i) &= B(O_M(\boldsymbol{r}_i, t_i), D_M). \end{aligned} \tag{1.1}$$

In the equation, the first row describes how the plasma observations O_M at a specific time t_i and position $\boldsymbol{r}_i$ result from sampling the plasma with a diagnostic set, denoted as M. The function $\mathcal{D}_M$ indicates the operation of this diagnostic set M in extracting plasma properties. $\mathcal{F}_M$ refers to the physical principles the diagnostic system uses for its measurements, and $\mathcal{P}(\boldsymbol{r}, t)$ represents the state of the plasma at a given time and place.

The term referred to as forward model is a model describing the whole process expressed in the first line of (1.1):

$$\tilde{O}_M(\boldsymbol{r}_i, t_i) = \sum_{i=(\boldsymbol{r},t)} \delta(\boldsymbol{r} - \boldsymbol{r}_i, t - t_i) \cdot D_M \left(F_M \left(P(\boldsymbol{p}, \boldsymbol{r}, t) \right) \right) \tag{1.2}$$

where the main difference is that the physical and diagnostic processes and the plasma state $\mathcal{D}_M$,, $\mathcal{F}_M$ and $\mathcal{P}(\boldsymbol{r}, t)$ are replace by their respective models D_M, F_M and $P(\boldsymbol{p}, \boldsymbol{r}, t)$. The vector $\boldsymbol{p}$ stands for a set of plasma parameters and $\tilde{O}_M$ expresses the estimates of forward models of diagnostic data.

The second row of equation (1.1) represents the estimated plasma state $\tilde{P}(\boldsymbol{p}, \boldsymbol{r}_i, t_i)$, derived from the observations O_M using the backward model B.

Equation (1.1) not only expresses the process of plasma diagnosis but also illustrates its connection to the Nyquist-Shannon theorem. In the realm of plasma diagnostics, fortunately, enhancing the quality of sampling is not limited to increasing the sampling rate in space and time. It also encompasses improvements in the diagnostics and diagnostic set D_M, as well as enhancements to the backward model B. High-quality forward models are crucial in facilitating both these improvements.

When designing diagnostic sets and individual diagnostic systems, forward models are invaluable for evaluating the utility of each diagnostic. Combined with backward models, they enable optimization of the diagnostic set M and effective

resource allocation. For instance, diagnostics can be prioritized in terms of port space based on their contribution to improving the quality of the estimated plasma state $\tilde{P}$. Thus, a tight connection between forward and backward models and their quality is instrumental in these optimization processes.

While the investment in advanced forward and backward modeling might seem like an unnecessary overhead, given that previous methodologies were functional, this perspective is akin to preferring analog oscilloscopes over digital data acquisition systems. It's true that for certain systems, the application of advanced modeling techniques may yield only marginal improvements. However, in other cases, the enhancements can be substantial, and forecasting these effects in advance is often challenging.

1.2 Ray Tracing, Raysect and Cherab

The Raysect and Cherab platform comprises two interconnected packages. Raysect is essentially a general-purpose 3D ray tracing engine, while Cherab functions as a repository of materials and tools within Raysect, specifically tailored for fusion applications. To provide a foundational understanding of the framework, an overview of the ray tracing methods employed is presented first, followed by a detailed description of Raysect and Cherab. For more comprehensive information about the framework, interested readers can refer to the projects' GitHub pages [4, 2] or consult the online documentation [5, 6]. An extensive book about physical based rendering is recommended for further reading [7].

In Fig. 1.1, the first two images on the left illustrate the fundamental methods of ray tracing. Forward ray tracing, as shown in the first image, involves tracing rays from the light source through the scene in the direction of light propagation. The process continues until specific termination criteria are met, such as a maximum number of interactions with scene objects or encountering an absorbing material. Data collection by an observer, like a camera chip, is achieved by replicating this process multiple times, launching rays from light sources at varying angles. A limitation of this method is the low probability of a ray originating from the light source directly striking the observer, leading to many trajectories that do not contribute useful information. This inefficiency is exponentially worsened when reflections are taken into account.

The middle image in Fig. 1.1 presents the reverse approach to ray tracing. Here, rays originate from the observer and are traced in the opposite direction of light propagation until they meet termination criteria. This method is repeated to ensure adequate sampling of the observer's surface and solid angle. Generally, this reverse approach is more efficient, as it increases the likelihood of the rays gathering relevant light information along their paths.

The final panel on the right in Fig. 1.1 depicts the recursive method of backward ray tracing. In this approach, a ray is launched from the observer, and Raysect's algorithms determine the closest object intersecting the ray. The interaction at this intersection point, whether reflection, transmission, or termination, depends on the material properties of the object. If reflection or transmission occurs, the angle is dictated by these properties, and a subsequent ray is launched from the point of intersection to continue the process until termination is reached.

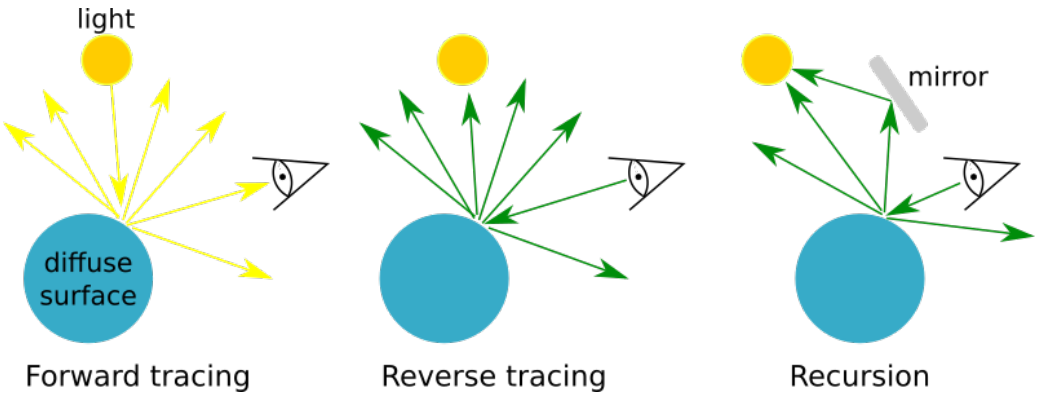

Figure 1.1: Pictures show general approaches to ray tracing which is the forward and reverse direction. Raysect approach to ray tracing is recursive depicted in the right most picture. Reprinted from [8].

Upon determining the complete path of a ray, that is, when a termination event for the ray is reached, the spectral contributions from all materials and objects encountered along the ray's path are integrated. This integration, conducted in the direction of light propagation, accurately accounts for phenomena such as the attenuation of light during reflection or the accumulation of volumetric radiation. Such a method ensures a precise representation of the light's interaction with various materials and its behavior in different environments.

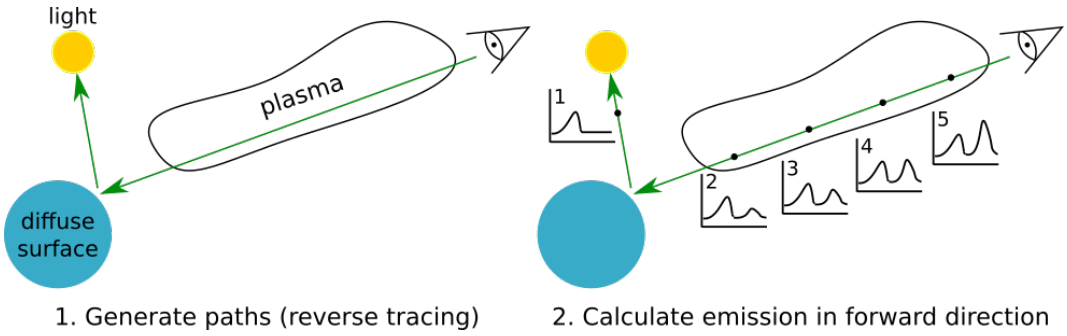

Figure 1.2: Schema showing the integration of the contributions to the ray's spectrum. In the left image, the ray is traced in the reversed direction. In the right picture, the contributions to the ray's spectrum and the interaction of the ray spectrum with the ambience is calculated in the forward direction. Reprinted from [9].

In Raysect, scene construction is facilitated by assembling *Node*s into a directed acyclic graph structure. Each *Node* represents a frame of reference, and the nodes are interconnected through affine transformations. These transformations define the rotation and translation of a node relative to its parent node. Within this framework, *Primitive*s are *Node* that define ray-intersectable volumes or surfaces. Raysect offers a range of *Primitive*s, from simple geometric shapes like spheres to more complex structures formed by triangle meshes. Additionally, primitives can be created using constructive solid geometry (CSG), which involves applying boolean operations such as addition, subtraction, and intersection to combine two primitives.

In Raysect, each *Primitive* must be associated with a material. The material determines how the surface and volume of the *Primitive* interact with a ray. Examples of such interactions include surface radiation or reflection, and volumetric radiation captured as the ray passes through a primitive's volume. Particularly for volumetric radiation, numerical integration is often employed to calculate the contributions to the ray's spectrum. This process involves segmenting the ray's path, and at each segment evaluating material's local contribution to the spectrum. As illustrated in the right panel of Fig. 1.2, this is represented by black dots along the ray's path. Such a method enables the material to account for local effects, like spectral line broadening due to force fields or variations in local temperature and density.

Cherab's integration becomes particularly crucial when dealing with inhomogeneous volume emission, as previously introduced in this section. Cherab essentially functions as a repository of Raysect's materials and a suite of tools specifically designed for fusion applications. Its primary objective is to offer radiation models suitable for simulating spectroscopic diagnostics in fusion settings. These models are capable of considering local plasma properties and force fields as 3D scalar and vector functions, thereby encompassing a wide spectrum of radiation phenomena.

The range of models available in Cherab includes Bremsstrahlung radiation and spectral line radiation, with considerations for temperature and pressure broadening, Zeeman splitting, among others. Additionally, Cherab models radiation resulting from interactions between neutral beams and plasma, alongside various other scenarios. Where necessary, these models can draw on atomic data for properties like excitation rates. While Cherab is flexible in terms of atomic data sources, allowing for custom databases, its default atomic data currently comes from OpenADAS [10].

Cherab enhances its modeling capabilities by implementing a general representation of the particle velocity distribution function in six-dimensional space. This broadens its applicability across various phenomena. However, recognizing that a full kinetic approach can be excessively detailed and time-consuming for some applications, Cherab also includes models that assume particles follow a Maxwell-Boltzmann distribution. These models simplify the process by utilizing only the moments of the distribution function, such as bulk velocity, temperature, and density, thus optimizing computation times.

Cherab's *Plasma* is a helpful tool designed to assist in building detailed plasma models. It enables users to construct plasmas that consist of various species populations differentiated by their charge, element and distribution function. Additionally, this class includes the functionality to describe magnetic fields within the plasma model.

To conclude, the combination of Raysect's robust ray tracing framework and Cherab's specialized radiation models forms an effective tool for forward modeling in spectroscopic diagnostics within thermonuclear fusion research. These models are capable of simulating a wide array of diagnostic signals, addressing various radiation phenomena. Raysect's compatibility with triangular mesh-based primitives enables the creation of detailed simulation scenes, incorporating complex geometries like full reactor models, complete with vacuum vessels and internal components such as plasma-facing tiles.

2. Forward & Backward Modelling of Thomson Scattering

Sec. This chapter describes the forward [11] and backward models of Thomson scattering (TS) diagnostic developed in the frame of this work. The newly contributed TS module for Cherab [12] allows to deliver forward models of diagnostic systems with high fidelity and accuracy while offering the effectivity, flexibility and adaptability of the Rasect & Cherab framework [12, 13]. The developed backward statistical model for inversion of electron temperature profiles from measurements of Thomson scattering diagnostic is also presented in this chapter. It shows the advantages of Bayesian approach to data analysis by improving quality of the inverted profiles and in general providing more information about the measurements. This is used to point towards instrumental problems and their solutions. The application of both models is shown on the example of the COMPASS tokamak Thomson scattering diagnostic [14]. It shows that thorough application of new trends in data science and computer simulations can improve and aid fusion diagnostics.

A brief introduction to the physics of TS is provided in Sec. 2.1.1 and Sec. 2.1.2 to justify the chosen implementation. The developed forward model of Thomson scattering for Cherab is described in Sec. 2.4. Subsequently, the architecture of the added module and its components are detailed in Sec. 2.4.1. Examples of applications include modelling of the COMPASS tokamak High Resolution Thomson Scattering [14], and support for the design of TS diagnostics for the COMPASS Upgrade [15]. It should be noted at the outset that the term "Thomson Scattering" refers to incoherent Thomson scattering; coherent Thomson scattering is a separate phenomenon and is not discussed in this text.

The motivation for adding the model of Thomson scattering to Cherab arose from the extensive level of optimisation required in Thomson scattering diagnostic designs [16, 17] to meet spatial characteristics and electron profile accuracy requirements. Forward modelling of TS spectra can undoubtedly be done to a high level of accuracy with simple models [17]. This is because the scattering volume is typically small (on the order of cubic centimetres) and is well described by the cross-section of the laser beam intersecting with the field of view (FOV). Even a rudimentary approach that assumes constant plasma properties and approximates the scattering volume as a line of a certain length can yield sufficiently accurate estimates for successful diagnostic design and operation. The numerous successful Thomson scattering diagnostics in operation around the world serve as definitive proof [14, 18, 19]. The advantage of the TS module for Cherab, developed in this work, lies in the capability to combine the model of TS with other features of Raysect and Cherab [12]. This facilitates the construction of comprehensive models of collecting optics, which not only enhances the accuracy of simulating the collected scattered spectra but also significantly improves the simulation of background intensity. The complexity arises because the FOV of a sight line can have intricate shapes and may intersect the majority of the plasma, which

contains various sources of radiation. If reflections from the first wall are to be considered, the complexity of the problem necessitates the use of ray tracing for accurate background prediction. Another advantage is the model's adaptability; once created with Cherab, it can be utilised for various applications with minimal overhead, such as the development and testing of backward models.

2.1 Thomson Scattering in Fusion Plasmas

Light scattering is a powerful diagnostic tool employed across various scientific and engineering disciplines, including but not limited to physics, chemistry, biology, materials science, and even civil engineering. Scattering techniques can leverage either passive radiation, which is automatically generated by the environment, or an active approach where the source of scattered radiation is controlled by the experimenter. A comprehensive overview of light scattering as a plasma diagnostic is provided in A. W. DeSilva's article "The Evolution of Light Scattering as a Plasma Diagnostic" [20]. From the initial demonstrations of scattering of electromagnetic waves in neutral gas under laboratory conditions by R. J. Strutt in 1918 [20], it took nearly half a century to demonstrate Thomson scattering (TS) of light in the optical range by electron beams [21]. The Thomson scattering diagnostic gained prominence as a tool for measuring profiles of electron temperature and density in magnetically confined plasmas through measurements performed by a group of scientists from the Culham Centre for Fusion Energy, led by N. J. Peacock [22]. This group utilised the diagnostic technique to confirm the effectiveness of TOKAMAK as the leading approach to hot plasma confinement. Since then, it has become an essential diagnostic tool for any fusion experiment of significance.

2.1.1 Physics of Thomson Scattering

In the classical framework, Thomson scattering can be conceptualised as the radiation emitted by an electron accelerated by a passing electromagnetic wave. A comprehensive summary of the physics underlying Thomson scattering is presented in the article "A primer on the theory of Thomson scattering for high-temperature fusion plasmas" by S. Prunty [23]. For a refresher on relativistic physics and the radiation of accelerated charges, the book "Classical Electrodynamics" [24] is recommended.

The typical setup in which TS systems operate is known as standard geometry and is illustrated in Fig. 2.1. The directions of propagation of the incident wave, $\hat{\boldsymbol{i}} = \boldsymbol{k}_i/|\boldsymbol{k}_i|$, and the scattered wave, $\hat{\boldsymbol{s}} = \boldsymbol{k}_s/|\boldsymbol{k}_s|$, define the scattering plane. The direction of the electric field of the incident wave, $\hat{\boldsymbol{e}} = \boldsymbol{E}_i/|\boldsymbol{E}_i|$, is perpendicular to this scattering plane. The angle between the incident and scattered waves is given by $\theta = \arccos\left(\hat{\boldsymbol{i}} \cdot \hat{\boldsymbol{s}}\right)$.

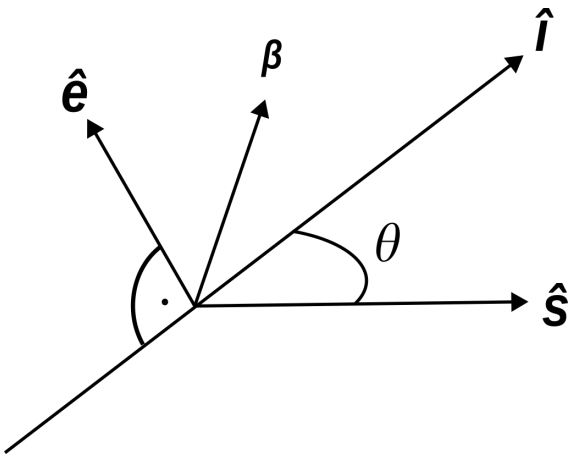

Figure 2.1: The standard geometry of Thomson Scattering is as follows: The incident wave propagates in the direction of the unit vector $\hat{\boldsymbol{i}}$. The light is scattered in the direction of the unit vector $\hat{\boldsymbol{s}}$. The angle θ represents the scattering angle. The scattering plane is defined by the vectors $\hat{\boldsymbol{i}}$ and $\hat{\boldsymbol{s}}$. The direction of the electric field, $\hat{\boldsymbol{e}}$, of the incident wave is perpendicular to the scattering plane. The vector $\boldsymbol{\beta}$ is the electron velocity divided by the speed of light.

A comprehensive formula illustrating the general properties of scattered light in standard geometry is provided in [25, 26]:

$$\begin{aligned}&\frac{\mathrm{d}^2 P}{\mathrm{d}\Omega_\mathrm{s}\mathrm{d}\omega_\mathrm{s}}\\&= {r_\mathrm{e}}^2 \int \langle \boldsymbol{S}_\mathrm{i}\rangle \mathrm{d}^3\boldsymbol{r} \int \left\{1 - \frac{(1-\cos\theta)\beta_\mathrm{e}^2}{(1-\beta\cos\theta_1)\,(1-\beta\cos\theta_2)}\right\}^2\\&\times \left\{\frac{1-\beta\cos\theta_1}{1-\beta\cos\theta_2}\right\}^2 \left(1-\beta^2\right) f(\beta)\delta(\boldsymbol{k}\cdot\boldsymbol{v}-\omega)\mathrm{d}^3\boldsymbol{v}.\end{aligned} \tag{2.1}$$

The above equation describes the scattered power P from a single electron into a unit solid angle Ω_s per unit frequency ω_s. The other variables include classical electron radius r_e, the mean of the Poynting vector of the incident wave $\langle \boldsymbol{S}_\mathrm{i}\rangle$, and the electron velocity as a ratio of the speed of light $\boldsymbol{\beta} = \boldsymbol{v}/c$. The component of the electron velocity parallel to the electric field of the incident wave is denoted by $\beta_\mathrm{e} = \boldsymbol{\beta}\cdot\hat{\boldsymbol{e}}$. The angle of scattering is θ, while θ_1 and θ_2 are the angles between the electron velocity and the incident and scattered waves, respectively. $f(\boldsymbol{\beta})$ represents the electron velocity distribution function. The wave vector $\boldsymbol{k}$ and angular frequency ω are defined by $\boldsymbol{k} = \boldsymbol{k}_\mathrm{s} - \boldsymbol{k}_\mathrm{i}$ and $\omega = \omega_\mathrm{s} - \omega_\mathrm{i}$. The term in the first curly bracket accounts for the depolarisation effect. The term in the second curly bracket describes the blue shift of the spectra caused by the motion of the electron relative to the passing wave and the observer. Finally, the term $(1-\beta^2)$ quantifies the decrease in scattered light intensity due to the relativistic increase in the electron mass.

Upon performing the velocity integration in Equation (2.1) over a Maxwell-Boltzmann distribution, it has been shown [25, 26] that the equation can be

rewritten in a factorized form as follows:

$$\begin{aligned} \frac{\mathrm{d}^2 P}{\mathrm{d}\Omega_s \mathrm{d}\epsilon} &= {r_\mathrm{e}}^2 \int \langle\, \boldsymbol{S}_\mathrm{i} \rangle \, \mathrm{d}^3 \boldsymbol{r} S(\epsilon, \theta, 2\alpha) q(\epsilon, \theta, 2\alpha), \\ \epsilon &= \frac{\lambda_s - \lambda_i}{\lambda_i}, \quad 2\alpha = \frac{m_\mathrm{e} c^2}{T_\mathrm{e}} \end{aligned} \tag{2.2}$$

Here, λ_i and λ_s denote the wavelengths of the incident and scattered waves, respectively. T_e represents the electron temperature, and m_e is the electron mass. The factor S is the spectral density function, while q is the depolarization factor.

Depolarization becomes increasingly important at temperatures exceeding approximately 10 keV. As shown in Fig. 7 by [23], the effect of depolarization is subtle on the shape of the spectra but reduces the overall intensity of scattered radiation.

The factorization reveals the useful capability to separate influences from variables such as laser intensity $\langle\, \boldsymbol{S}_\mathrm{i} \rangle$, geometry, and the depolarization effect. Also, the depolarization effect can be ignored in calculations for which the T_e is sufficiently low.

A simplified analytic formula describing the spectral density function S was introduced by Selden [27, 28] as

$$S(\epsilon, \theta, \alpha) = c(\alpha) A^{-1}(\epsilon, \theta) \exp[-2\alpha B(\epsilon, \theta)], \tag{2.3}$$

where

$$\begin{aligned} A(\epsilon, \theta) =& (1+\epsilon)^3 \left[2(1-\cos\theta)(1+\epsilon) + \epsilon^2 \right]^{1/2}, \\ B(\epsilon, \theta) =& \left\{ 1 + \epsilon^2 / [2(1-\cos\theta)(1+\epsilon)] \right\}^{1/2} - 1, \\ c(\alpha) =& (\alpha/\pi)^{1/2} \left(1 - \frac{15}{16}\alpha^{-1} + \frac{345}{512}\alpha^{-2} + \ldots \right) \text{ when } \alpha \gg 1 \end{aligned} \tag{2.4}$$

and ε and α are the same as in (2.2).

Examples of the scattered spectra from a laser with 1064 nm wavelength are plotted in Fig. 2.25. In general, the width of the scattered spectra broadens with increasing temperature and scattering angle. For fusion relevant conditions the spectra stretch over hundreds of nm.

2.1.2 Basic Properties of Thomson Scattering Diagnostics

Thomson scattering serves as a pivotal diagnostic tool in fusion plasmas, and is a standard feature in major fusion devices. Typically, TS diagnostics employ near-infrared lasers, with Nd:YAG lasers at a wavelength of 1064 nm being particularly popular. At these wavelengths, current scales of fusion devices and particle densities, the interaction of laser photons with the plasma is minimal.

The total Thomson scattering cross-section, denoted by σ_{TS}, is given by Equation 7.2.6 in [29]:

$$\sigma_\mathrm{TS} = \frac{8\pi}{3} {r_\mathrm{e}}^2 \approx 6.65 \times 10^{-29}\,\mathrm{m}^2. \tag{2.5}$$

For a typical fusion plasma density $n_e = 10^{20}$ and a plasma column height $H = 10\,\mathrm{m}$, the scattering probability is low: $\sigma_{TS} n_e H = 6.6 \times 10^{-8}$. This low interaction rate allows TS to operate as a non-invasive diagnostic. The laser attenuation by the plasma is negligible, facilitating measurements of electron temperature and density profiles across the entire plasma cross-section.

To obtain high-quality profile data, TS diagnostic systems aim for spatial resolutions better than 1 cm [14, 30]. Such resolution is adequate for capturing spatial dynamics in both the core and edge regions of magnetically confined plasmas [31, 32].

Due to the low scattering probability and small observed scattering lengths L, TS diagnostic systems must be highly efficient. For instance, in a plasma with density $n_e = 10^{20}\,\mathrm{m}^{-3}$, scattering region length $L = 1\,\mathrm{cm}$, and optics distance $d = 1\,\mathrm{m}$ and optics radius $o_r = 5\,\mathrm{cm}$, the probability of capturing a scattered photon is approximately:

$$P(\text{detection}) = \sigma_{TS} n_e L \frac{\pi o_r^2}{4\pi d^2} \approx 4.16 \times 10^{-14}. \tag{2.6}$$

This example provides only an approximate estimate of the likelihood of photon detection due to the assumption of isotropic scattering.

To counteract this low probability, lasers used for TS diagnostics deliver high-power pulses, typically in the lower units of Joules within a narrow temporal window of a few nanoseconds [33]. A 1064 nm laser with pulse energy of 1 J includes $\approx 5 \times 10^{18}$ photons. This necessitates fast data acquisition systems, which also helps in reducing the influence of plasma background radiation. The short pulse length enables treating the temporal evolution of plasma radiation as a constant background, thereby improving the accuracy in back-calculating electron properties. Additionally, the pulse duration is much shorter than macroscopic time scales in the plasma, such as the Alfvén time for ITER-like parameters, which is around 0.3 μs[34].

2.2 Thomson Scattering at COMPASS

As it will be reasoned in section Sec. 2.5.1, the Thomson scattering diagnostic system which was operated on COMPASS tokamak in Prague was used to give application examples of the developed forward and backward models. This section provides a brief overview of the diagnostic system and the experimental data selected for the examples, benchmark and tests.

2.2.1 Thomson Scattering Diagnostic System

To increase the insight into the next chapters about forward and backward models of TS, a description of the system [14] which was in operation at the COMPASS tokamak is given in this section. Although the concrete COMPASS realisation is used to give example, it uses the same solution as all the major Thomson scattering diagnostics which are in use [35, 36] or planned [16]. A block schema of a diagnostic is plotted in Fig. 2.2. It is composed of five main components:

- Laser systems are usually based on industrial grade lasers with temporal pulse width up to 10 ns in which they deliver several units of Jof energy.

The pulse frequency of such lasers is usually up to a 100 Hz.

- Collection optics focus laser light scattered by plasma electrons onto an array of fibre bundles. Because of the low scattered light intensity, the optics are required to be high throughput and due to the spectral features of the scattered light, it also has to be optimised for wide wavelength band.

- Fibre bundles are usually arranged to measure a plasma profile along the cross section of the plasma with the laser beam line. The number and formation of the individual optical fibres in the bundles are determined by the required spatial resolution which is defined by the local gradients of electron kinetic profiles. The fiber bundles then guide the collected light outside of the experimental halls into polychromators.

- Polychromators are used to spectrally separate the light brought by the fibre bundles. They are typically composed of a few band pass filters of variable widths and central wavelengths. The spectral properties of the filters are optimised to suit the spectral characteristics of the scattered light, which is determined by the electron temperature. The detection elements are usually avalanche photodiodes and can also include some signal processing electronics as frequency filters and amplifiers. On the output, each polychromator channel provides an analog signal with temporal evolution of the intensity in the respective wavelength band.

- Data acquisition digitises the analog polychromator into discrete levels and stores them for futher processing. To use the data provided by the acquisition for inference of electron properties, the data has to be combined with the system calibrations.

The diagnostic system employs multiple Nd:YAG lasers, each with a wavelength of 1064 nm and an approximate pulse energy of 1.5 J. The lasers enter the vacuum vessel from the top, traversing vertically at the radial position $R = 0.56\,\mathrm{m}$. The plasma profile measurements occur in the upper half of the plasma, covering a vertical range from $Z = -15\,\mathrm{mm}$ to $Z = 320\,\mathrm{mm}$. The scattered light is focused onto optical fibre bundles via two lenses. The first objective is specialized for edge plasma measurements and its field of view represented in blue in Fig. 2.3. The second objective's FOV, aimed towards core plasma measurements, is illustrated in green in the same figure.

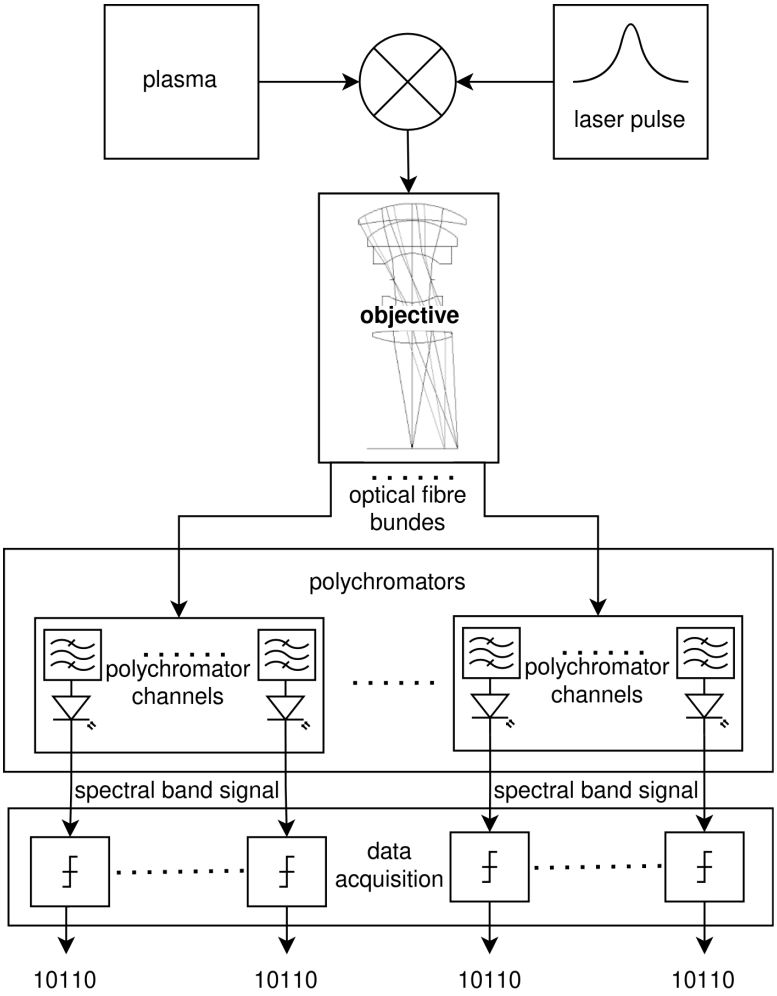

Figure 2.2: A block schema of the TS diagnostic system which was in operation on COMPASS. The main components were the laser systems, collection optics, fibre bundles, polychromators and data acquisition system.

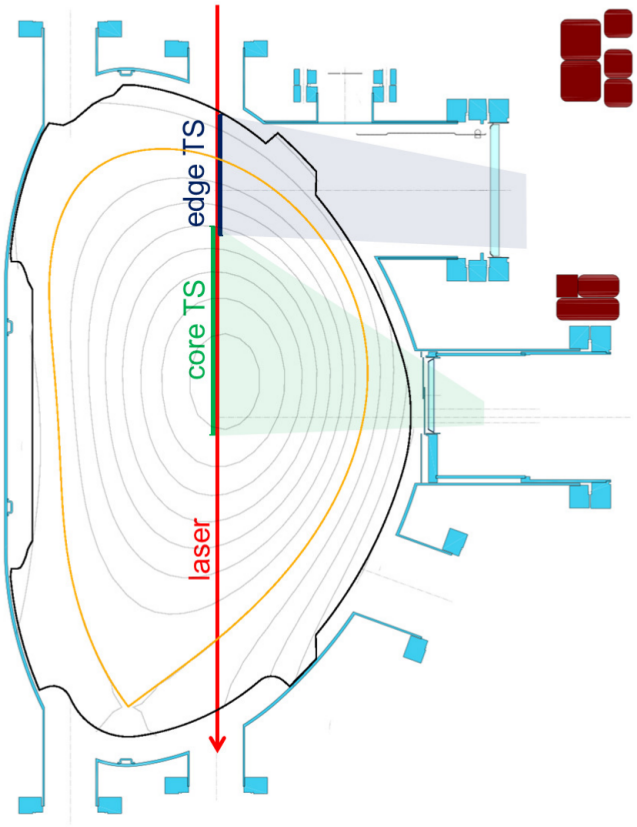

Figure 2.3: COMPASS Thomson scattering diagnostic. The laser beams, depicted with the red arrow, enter the vacuum vessel at the top and traverse it vertically at the position $R = 0.56\,\mathrm{m}$. The plasma profile measurements were performed over the upper section of the plasma, covering the vertical range from $Z = -15\,\mathrm{mm}$ to $z = 320\,\mathrm{mm}$. The light was focused onto a set of fibre bundles by two objectives: Core (green) and Edge (blue). Figure reprinted from [14].

The TS system provided information on 54 spatial points in total. Each spatial point was defined by a fibre bundle onto which the objectives focused the scattered light. The edge objective accommodated 30 fibre bundles, and the core objective 24. The schema of the bundles is depicted in Fig. 2.4. The core and edge bundles were composed of different numbers of optical fibres and also had different orientations. These variations were made to meet the requirements for spatial resolution of the measurements and to optimise light collection based on the laser beam width. The core bundles were composed of 66 optical fibres positioned on a staggered grid with 11 rows and 6 columns. The edge bundles were composed of 60 optical fibres positioned on a staggered grid with 6 rows and 10 columns; see Fig. 2.4. The used optical fibres had a $210\,\mu\mathrm{m}$ core diameter.

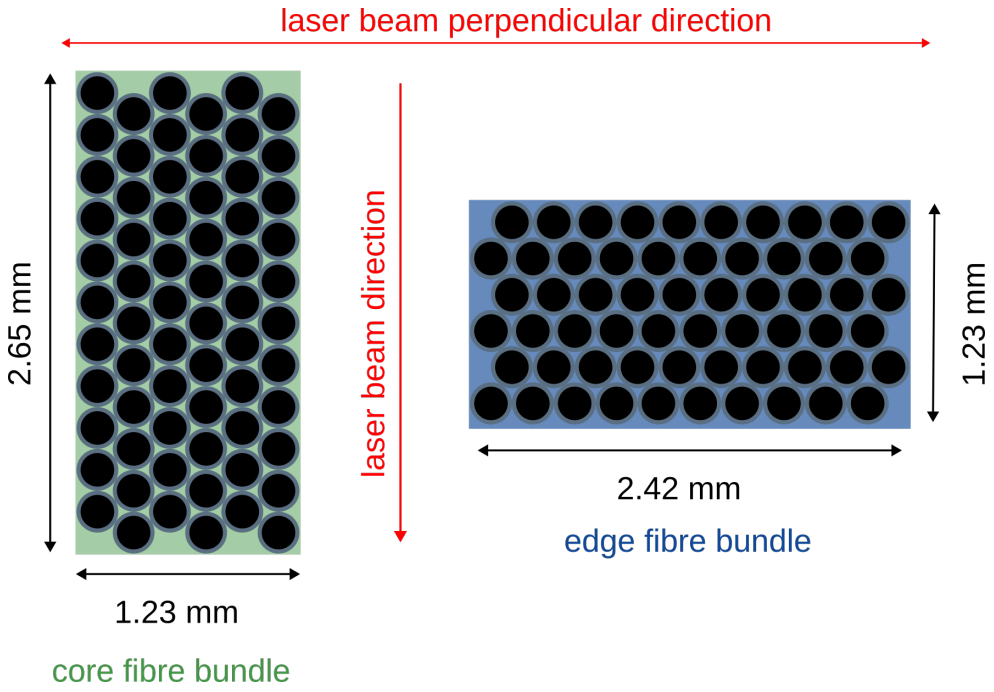

Figure 2.4: The schema of the fibre bundles used in the COMPASS TS. Each bundle is composed of a number of fibres positioned on a staggered grid. The black circles depict the fibre cores, and the grey circles represent the fibre claddings. Laser light propagates from top to bottom. The horizontal direction shows the radial direction of the laser, perpendicular to the laser's wave vector. The core fibre bundle is composed of 66 fibres (11 rows, 6 columns), and the edge is composed of 60 optical fibres (6 rows, 10 columns) [37].

Polychromators of the TS system on COMPASS were equipped with five spectral channels. An illustrative example of the experimentally acquired spectral characteristics for polychromator 505 channels (more information in Tab. 2.1) can be seen in Fig. 2.5. The figure shows the five wavelength bands with their width inversely proportional to the central band. This is because the low temperature electrons cause only small broadening of the laser light so the spectral resolution has to be higher.

Out of the five spectral channels in each polychromator, only four were connected to the data acquisition. The channel transmitting the shortest wavelengths was disconnected for the diagnostic channels observing the edge part of plasma. The temperature in this region of plasma was expected to be low which makes the data from the shortest wavelengths less important (with low probability of the scattered spectrum reaching to the filter band). Contrary to the edge channels, the core channels weren't equipped with the channel transmitting the longest wavelength because of the lower importance of the spectral band for the expected electron temperatures.

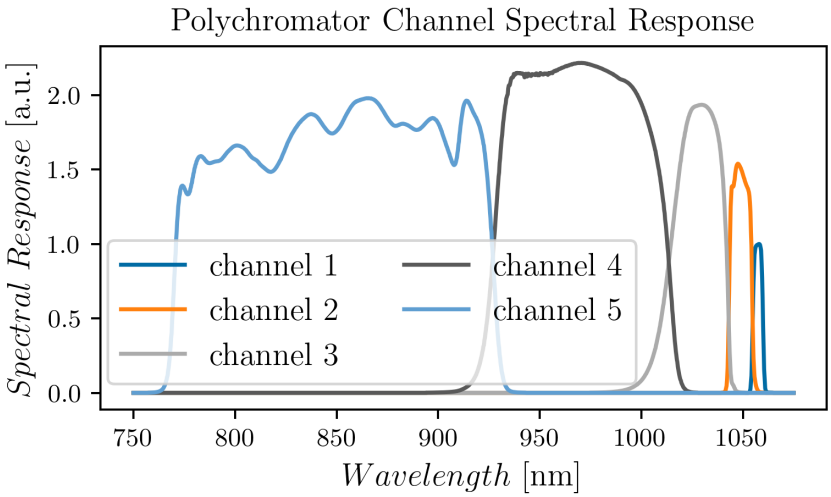

Figure 2.5: Transmission functions of polychromator 505 channels acquired through experimental calibration.

Figure 2.6 provides an example of raw signal data from the COMPASS TS diagnostic. This data is from polychromator 505, channel 1, with spectral band focusing on lower temperature ranges closest to the laser wavelength. The discrete steps of the ADC are clearly visible and provide insight into the low intensities and signal-to-noise ratios that ADC systems must contend with.

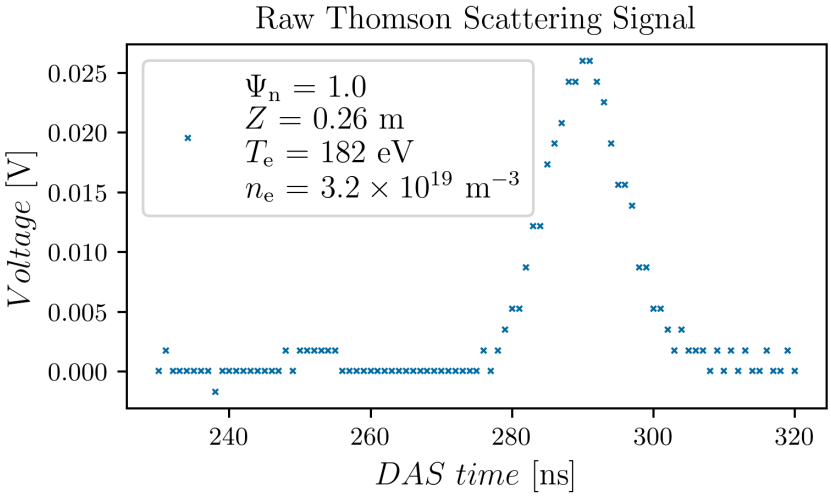

Figure 2.6: Example of a signal recorded during a single laser pulse on the COMPASS tokamak's edge Thomson scattering diagnostic system. The data is from polychromator 505, channel 1, taken during the H-mode phase in shot 20385 at pulse time 1168 ms. The symbol Ψ_n is the normalised poloidal flux, and Z is the vertical coordinate.

To lower the number of required polychromators and data acquisition channels, the diagnostic used time duplexing. Each of the polychromators had two fibre bundles on its input and thanks to their different lengths the pulses from the two bundles were separated in time. Examples of signals measured by a single polychromator for a single laser pulse are shown in Fig. 2.7. The first set of peaks was delivered by the shorter bundle which measured the scattered light

at $Z \approx 0.16\,\mathrm{m}$ and the second set of peaks was delivered by the longer bundle which measured the scattered light at $Z \approx 0.18\,\mathrm{m}$. The first channel of the polychromator was not connected to the data acquisition system.

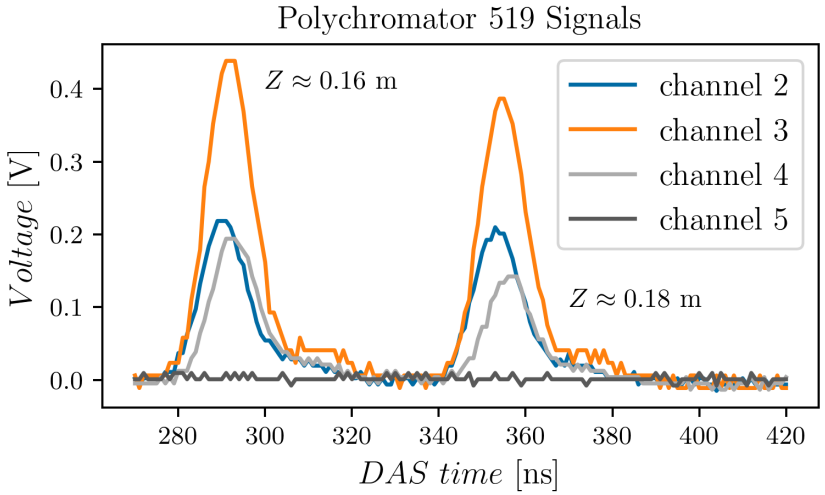

Figure 2.7: Signals from polychromator 519 captured in shot 20385 at the time 1169 ms. The COMPASS TS system utilised time duplexing, facilitated by different fibre bundle lengths, to measure signals from two sight lines with a single polychromator. The first pulse collects light at $Z \approx 0.16\,\mathrm{m}$ and the second at $Z \approx 0.18\,\mathrm{m}$. The channel 1 for the core lines was not connected to the data acquisition system.

To improve orientation between the polychromator numbers and measured spatial coordinates, the Tab. 2.1 is presented. The scattering angles θ are also included. The polychromators including NaN values are those connected to split fibre bundles. The split fibre bundles measure the same spatial point and their assessment is used to align objectives with the laser beams.

ID	Z_1 [m]	Z_2 [m]	θ_1 [°]	θ_2 [°]	ID	Z_1 [m]	Z_2 [m]	θ_1 [°]	θ_2 [°]
501	0.296	0.300	83.24	82.66	516	0.311	0.314	80.91	80.33
502	0.289	0.292	84.41	83.83	517	0.303	0.307	82.07	81.49
503	0.281	0.285	85.59	85.00	518	0.200	0.213	53.66	51.76
504	0.270	0.274	87.36	86.77	519	0.164	0.176	59.32	57.44
505	0.263	0.267	88.54	87.95	520	0.140	0.152	63.07	61.20
506	0.256	0.259	89.73	89.14	521	0.278	NaN	87.77	NaN
507	0.248	0.252	90.93	90.33	522	0.118	0.129	66.79	64.93
508	0.241	0.244	92.12	91.52	523	0.097	0.108	70.49	68.65
509	0.023	0.031	85.07	83.26	524	0.077	0.087	74.17	72.33
510	0.007	0.015	88.65	86.86	525	0.058	0.067	77.83	76.00
511	-0.007	0.000	92.21	90.43	526	0.040	0.049	81.46	79.64
512	-0.014	NaN	93.98	NaN	527	0.233	0.237	93.32	92.72
513	0.188	NaN	55.55	NaN	528	0.226	0.230	94.53	93.92
514	0.215	NaN	96.34	NaN	529	0.218	0.222	95.74	95.13
515	0.318	0.322	79.75	79.17					

Table 2.1: The table relates polychromator numbers (the ID column) to the measured vertical coordinates Z and scattering angles θ. The indexes 1 and 2 denote the two fibres connected to a single polychromator. The rows with NaN values represent the polychromators connected to split fibres.

2.2.2 Experimental Data

In Sec. 2.3.2 and Sec. 2.5 experimental data measured by the TS diagnostic at COMPASS were needed to test the newly developed statistical inference of electron temperature profiles and forward model of Thomson scattering. The COMPASS pulse number 20385 was selected, featuring a plasma current of 200 kA and a line-averaged electron density of $5 \times 10^{19}\,\mathrm{m}^{-3}$. The main characteristics of the discharge are displayed in Fig. 2.8, where the vertical line indicates the temporal position of the laser pulse for which the experimental electron profiles were used. As the plot of the D-alpha emission time trace in Fig. 2.8 reveals, the plasma was in H-mode at the time of the laser pulse and was transitioning from an ELMy (Edge Localised Mode) to an ELM-free phase. An example of raw polychromator data for this particular laser pulse is shown in Fig. 2.6.

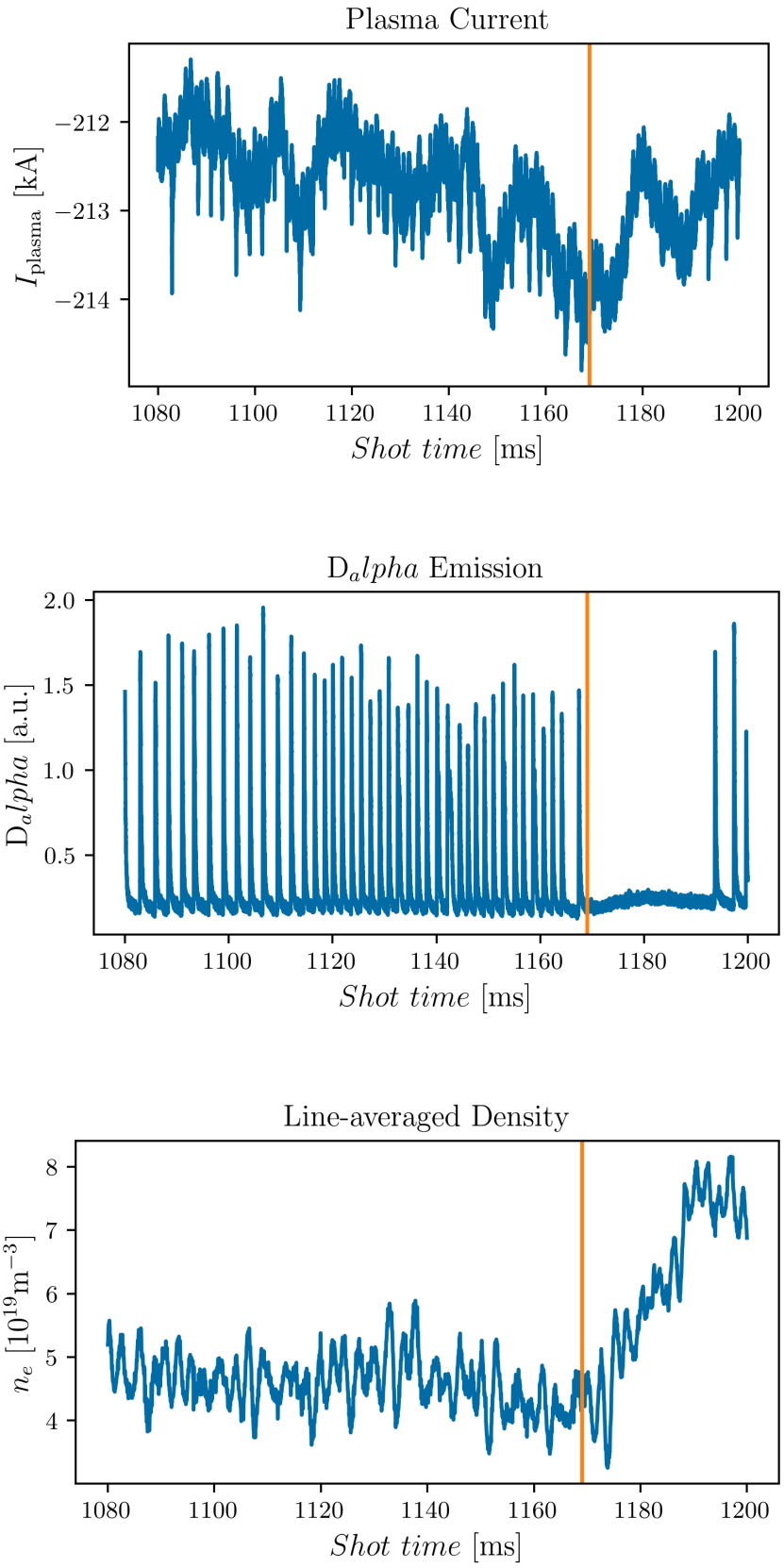

Figure 2.8: Characteristics of the pulse 20385 selected for testing. The vertical line indicates the time of the laser pulse. The D-alpha signal reveals that the plasma was entering an ELM-free H-mode at a line-averaged density of $5 \times 10^{19}\,\mathrm{m}^{-3}$ and a plasma current of $\approx 200\,\mathrm{kA}$.

The profiles of electron temperature and density measured by the TS are depicted in Fig. 2.9. Both profiles exhibit strong spatial gradients (in the pedestal region) between Z=0.25 m and Z=0.30 m, and a flat top in the core region. The temperature scale in the profile ranges from tens of eV to 1.2 keV, and the density reaches up to $6 \times 10^{19}\,\mathrm{m}^{-3}$. The experimental data were fitted using the modified hyperbolic tangent function [38], which is routinely employed for pedestal studies at COMPASS[1]. These fitted profiles were later used in the forward modelling of the scattered spectra. Both profiles should offer sufficient magnitudes of T_e and n_e as well as magnitudes of their spatial gradients to properly test both the forward and backward models of TS.

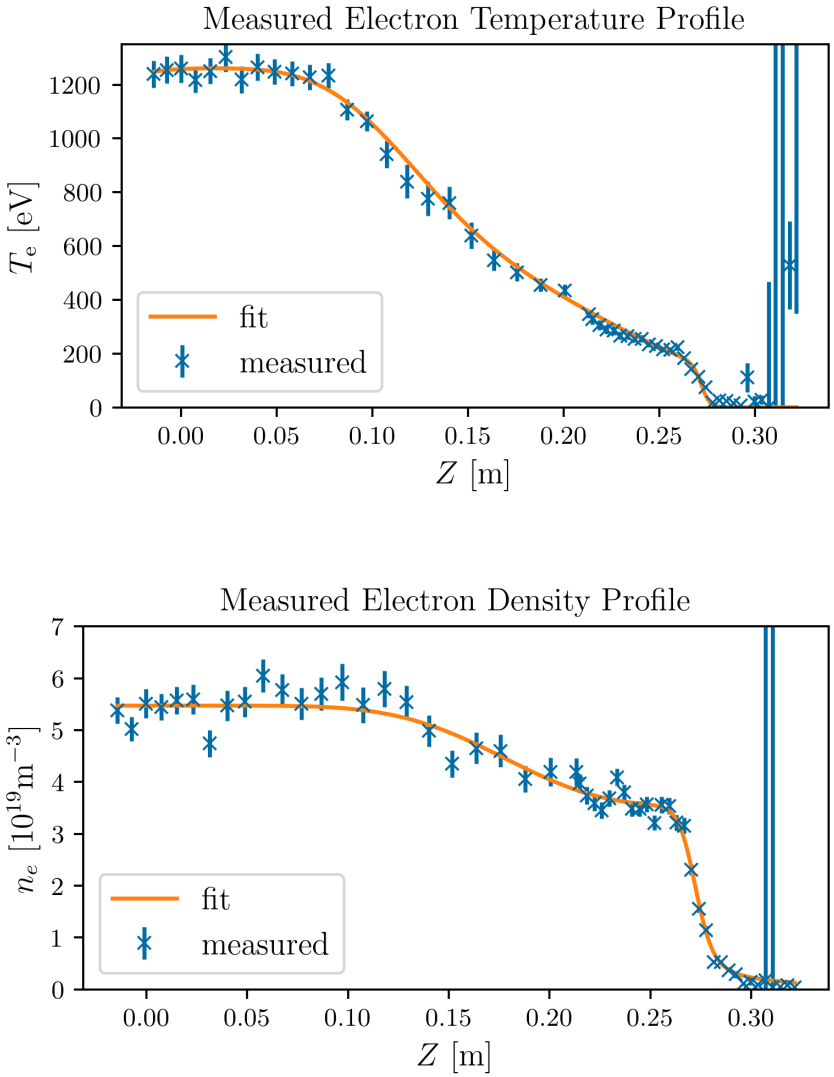

Figure 2.9: Electron kinetic profiles measured by the Thomson scattering diagnostic in shot 20835 and shot time 1169 ms. Orange lines represent fits of the data using the modified hyperbolic tangent function.

The forward model simulation in Sec. 2.5 necessitates 3D profiles of electron properties as input. These were acquired by iso-mapping 1D profiles from Fig. 2.9 onto the 2D profile of the normalised poloidal flux obtained by EFIT code [39].

[1]Fits were provided by Miroslav Šos, to whom I would like to express my thanks.

An illustrative plot of the outcome is displayed in Fig. 2.10. While the assumption that electron temperatures and densities are functions of flux surfaces may not hold outside the confined region, the mapping was nonetheless applied in the SOL region. The error incurred by this mapping in the SOL is negligible, owing to the laser width being approximately $1 - 3\,\mathrm{mm}$ and the evolution of electron density and temperature over this length along a field line is negligible. The 3D profiles for the simulation were then generated by assuming toroidal symmetry and applying axi-symmetric mapping in the toroidal direction.

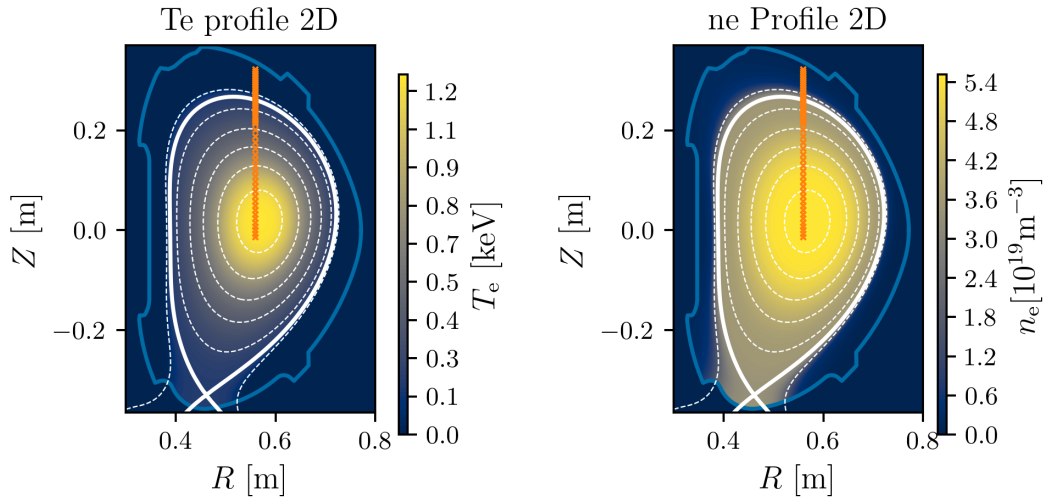

Figure 2.10: Two-dimensional profiles of electron density and temperature obtained from 1D profiles in Fig. 2.9 by applying iso-mapping onto the normalised poloidal flux.

2.3 Backward Model for Thomson Scattering

Backward modelling is a process in which a sought plasma quantity is inferred from diagnostic data. In the case of Thomson scattering the sought quantities are electron temperature and density profiles. The following section describes the standard algorithm which was used at COMPASS to calculate the electron profiles. Then, a statistical method for inference of the profiles, developed as a part of this thesis, is described and its performance is compared to the standard algorithm.

2.3.1 Standard TS Backward Model at COMPASS

In general, to infer electron properties from the measured signals, three main steps have to be made:

- The spectrum measured by a polychromator has to be obtained by getting intensities of the pulses.

- The electron temperature can be infered from the polychromator spectrum.

- The electron density can be obtained if the measured spectra are combined with calibration constants.

The standard backward model used at COMPASS for the reconstruction of electron temperature and density profiles from the measured data, developed by J. Seidl, O. Grover and M. Sos was based on the lmfit [40] python package which uses optimisation of least square errors. It inferred the electron properties in two main separate steps.

First step was the estimation of the pulse intensities. This was done by fitting each pulse with a scaled Gaussian function and taking its integral as the pulse intensity. It should be stressed here that every pulse fit was performed as a separate least-squares optimisation. The model was optimising the sum of residuals of the model waveform where the fit parameters were the position, width and height of the pulses. Because the experimental pulse waveform was suffering from a "long tail" feature following the main pulse (an example of this feature can be seen in Fig. 2.7 for the channel 3), only the raising part of a pulse was taken into account during the optimisation. The "long tail" feature of pulses comes from the electronic circuits of the polychromator. Example of the pulse fits is given in Fig. 2.11 and examples of the pulse intensities for $Z \approx 0.16\,\mathrm{m}$ and $Z \approx 0.18\,\mathrm{m}$ are plotted in Fig. 2.12. The pulse intensities inform about the spectral shape of the scattered light.

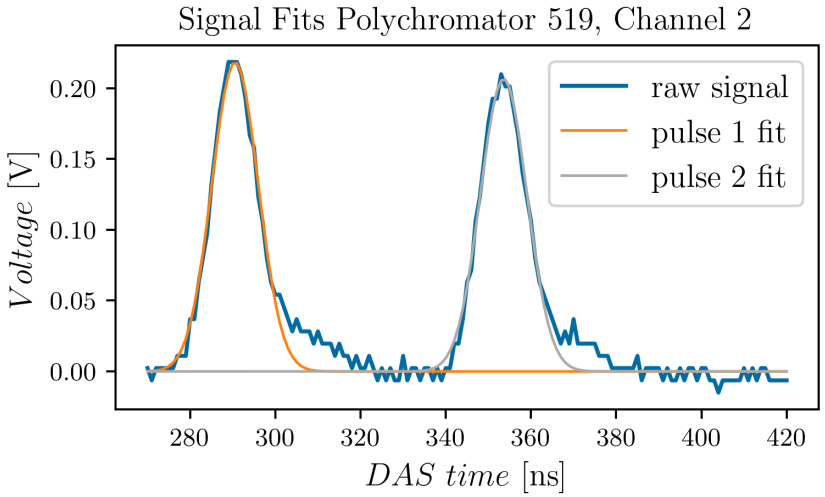

Figure 2.11: Pulse fits conducted by the standard inter-shot analysis codes form the spectrum measured by the polychromator. The raw data were captured by the second channel of polychromator 519 in shot 20285 at time 1169 ms. The same data are displayed in Fig. 2.7.

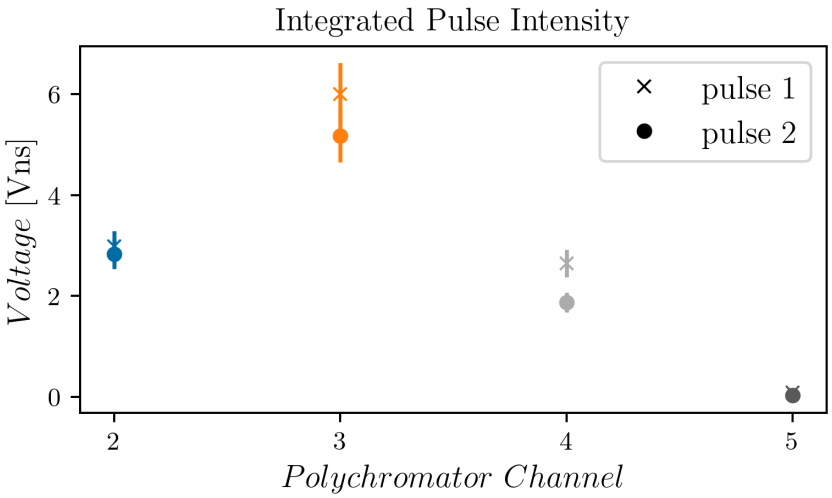

Figure 2.12: Signal intensities obtained through waveform fitting, from polychromator 519, captured in shot 20385 at 1169 ms.

The second step was the inference of electron temperature and density from the obtained polychromator spectra. This was again done with use of the least-squares optimisation. As the algorithm flowchart in Fig. 2.13 shows, the estimate of T_e was optimised by minimising the sum of squared errors of the polychromator spectra obtained in the first step and theoretical spectra calculated from the T_e estimate. The shape of the ideal spectrum was calculated with the Selden formula [27, 28] written in (2.3). The ideal polychromator spectra were then obtained by filtering the Selden spectrum with experimentally obtained polychromator filter characteristics. Once the optimum was found, the system absolute calibration constants were used to calculate the estimate of the observed n_e. The described procedure was done separately for every measured spatial point.

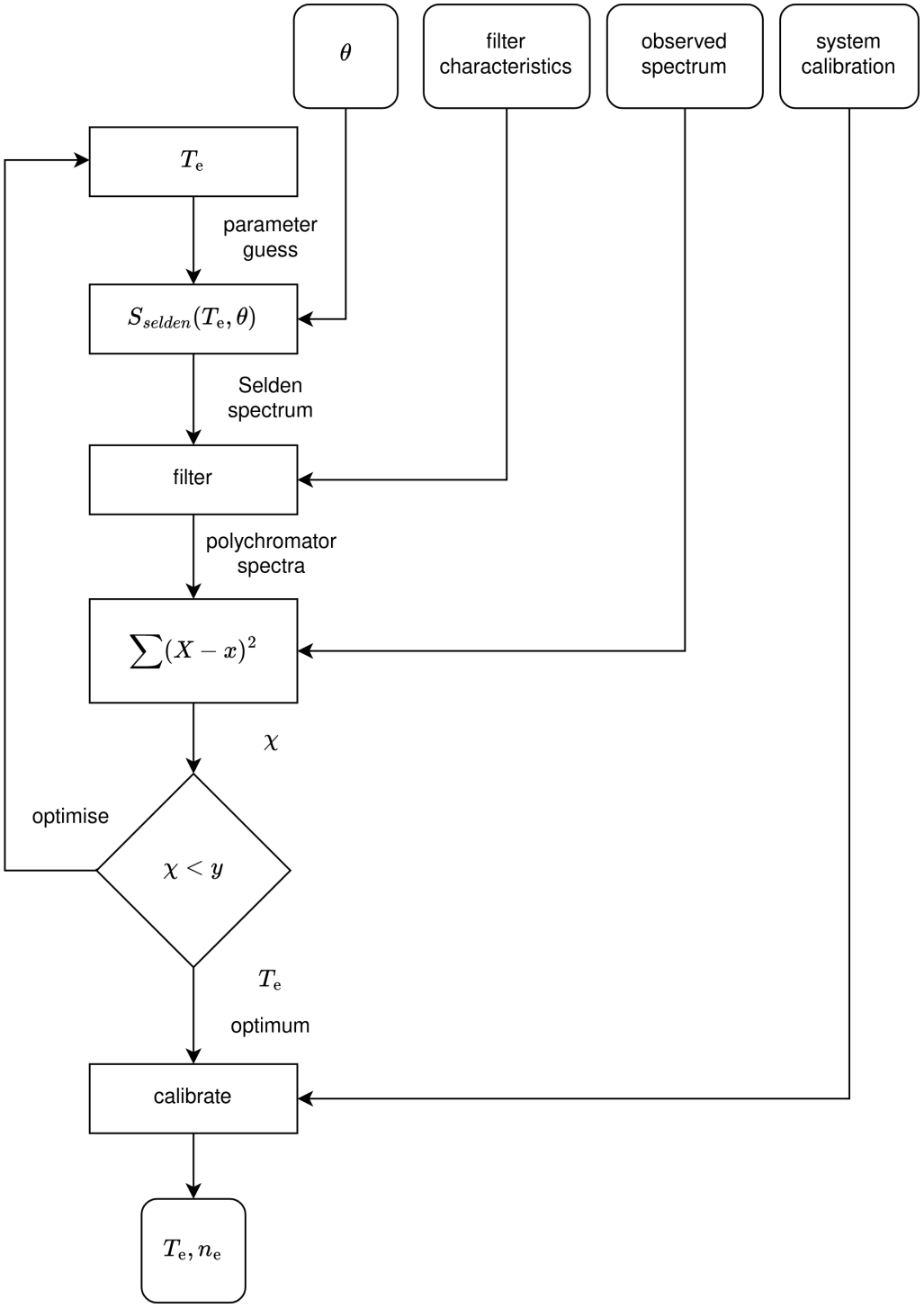

Figure 2.13: Flowchart with the algorithm used to infer electron temperature and density from the measured spectra based on least-squares optimisation.

An example of reconstruction of electron temperature from measured data is shown in Fig. 2.9. The mean values of the reconstructed temperatures are plotted with crosses, and the corresponding vertical lines indicate the estimated standard deviations of the uncertainties.

Least squares optimisation in case of such non-linear model has some important limitations. It starts from an initial guess and an iterative optimisation algorithm, searching for the optimum, is applied. A point estimate is returned when the

optimisation algorithm reaches its criteria (e.g. stability of estimates, small gradient) or number of maximum steps. This has important implications on the provided results:

- Local optimum is provided as a single point estimate. There is no further information about the parameter space.
- Uncertainties are computed from the covariance matrix of the parameters which is also influenced by the weights of the observations (in case of the weighted least squares). Usually, the weights are set to be equal to the inverse of the variance of the observations which are assumed to be normally distributed. This can lead to bias and underestimation of the uncertainties.
- It is difficult (or even impossible) to introduce prior knowledge into the model (other than parameter bounds). For example, probability of the electron temperature in the far SOL is much higher to be below 10 eV than 40 eV.
- Models can have multiple minima. In combination with the single point estimate, this can lead to the algorithm being prone to converge to a local minimum without any warning. Which minimum is found by the algorithm is highly influenced by the initial guess.
- The models have limited complexity. For example it is difficult to introduce a model which would infer both pulse intensity and temperature for multiple spatial points at once.
- Limited possibilities of model comparison makes it more difficult to select the optimal one from multiple options.
- Although the weighted least squares optimisation helps with treatment of heteroscedastic data, the metric is not suitable for combining data with too different orders of magnitude. For example from different diagnostic systems.

For example, the point at $Z = 0.15\,\mathrm{m}$ in Fig. 2.9 is clearly below the fitted curve, but its error bar suggests that its uncertainty is small. Without a more thorough analysis, any of the following reasons could be responsible: wrongly estimated uncertainty; a physics phenomenon; or a systematic error (e.g. caused by the discrepancy in calibration data and instrument state). The outlier temperature close to $Z = 0.3\,\mathrm{m}$ may be merely a local optimum found by the optimisation algorithm.

Most troubling, however, is the large scatter of the temperature at $Z > 0.3\,\mathrm{m}$ with relatively low uncertainties which is quite common phenomenon in the profiles. It is reasonable to expect that such values are not physical, since in the edge the temperature should converge to low values (units of eV and smaller). This happens when the signal to noise ratio in every channel of a polychromator gets too low and the polychromator spectrum shape is not governed by the electron properties. In this case of low evidence, the least squares optimisation can converge to physically incorrect results. A more proper behavior would be introducing a prior knowledge which would make the optimisation converge to low values. The current behavior

can pose problems to automatic fitting of the profile, which could be skewed by these unreasonable results. Introducing a prior knowledge which would cause convergence to realistic values is proposed in the following part as a superior method for profile inference.

2.3.2 Statistical Inference of Electron Temperature Profile

Because of the limits of the standard processing algorithms, it was decided by the author to develop a statistical inference of the electron temperature profile of the Thomson scattering module. A probabilistic model using a Bayesian approach was implemented in Numpyro [41, 42], a Probabilistic Programming Language (PPL) based on JAX, an automatic differentiation library for Python. A useful introduction to statistical data analysis can be found in the series of lectures available online by Richard McElreath, and the corresponding book [43] or online material [44].

Probably the biggest advantage of Bayesian approach is its fully probabilistic nature. The model parameters are defined in form of prior distributions and the output posterior is also a distribution. This has some far reaching consequences which offer some advantages over the standard least squares optimisation:

- The model parameters are defined as prior distributions. This allows to introduce prior knowledge into the model, to regularize the model and to avoid overfitting. For example, introducing the prior knowledge that electron temperature in the far SOL is more likely to be below 10 eV than 40 eV.
- The results of an inference is a posterior distribution which provided information about the parameter space. This allows to cover problems of multiple minima and gives more robust information about the uncertainties of the parameters.
- It allows to build more complex models. For example, developing a model which would infer the whole profile at once, starting at the measured data, is feasible.
- The probabilistic approach removes problems of least square optimisation with heteroscedasticy. This means data of various magnitudes and properties are easy to be combined and covered.
- Bayesian models are generative, they can be used not only for interpretation of measured data in backward models but also as predictive models, for example in combination with forward models.

The developed model performs inversion of an electron temperature profile directly from the measured data at once, but the individual temperature values are assumed to be independent. To briefly describe the model and its generative nature, for every polychromator a value of electron temperature is selected (among other model priors) from a respective prior distribution of T_e. The values are then used to calculate theoretical shapes of spectra with the Selden formula [27, 28]. The spectra are then filtered by the spectral properties of polychormator

channels and integrated to get the polychromator spectrum. The intensities in the individual channels are then used to generate model time traces for the polychromator channels. The likelihood of the model time traces is calculated for the given observed polychromator channels. During the inference the values of model parameters are optimised to reach maximum likelihood.

To give a more thorough description of the model and its implementation, it has to be noted that the Bayesian inversions are in general much more computationally intensive than the least square optimisation. In order to reduce computational time, it is necessary to build the model in form of tensors. In the developed model, the following physics dimensions were used to form the tensor:

- **Laser shot** dimension defines a single shot of a laser which gives one electron kinetic profile for a given shot time. The laser shot dimension is considered as independent which means that the individual profiles are also independent. The model can invert multiple shots at once, depending on the RAM memory of the graphics card used.
- **Polychromator** dimension separates the individual polychromators.
- **Channel** separates channels of the polychromators. Every channel of every polychromator has its own spectral calibration specified.
- **Pulse** dimension separates the two temporal pulses measured by each polychromator channel. The pulses are caused by a single laser pulse but separated in time by the different lengths of the fibre bundles. Each pulse has its own set of calibration constants (i.e. absolute calibration, spatial calibration).

The above dimensions were used to form tensors generated from the priors and acted upon by the inference. For a single laser shot inversion run on a GPU (Graphical Processing Unit) (GeForce RTX 2080 Ti) with two chains and 800 samples took ≈ 2.5 minutes.

As it was mentioned previously, the posterior values of electron properties are obtained by optimising the likelihood of the modelled and observed signal waveforms in polychromator channels (example of measured data is in Fig. 2.7). Before the model is described in more detail, it should be pointed out that Fig. 2.14 and Fig. 2.15 serve as graphical aid for the model explanation. To calculate the likelihood, the modelled waveforms have to be expressed as a probability distributions. This is achieved by expressing every sample within the waveform as an independent probability distribution:

$$O(t) = \mathcal{N}(W(t), U(t)) \tag{2.7}$$

Where the $O(t)$ is the probability distribution for time t. The $\mathcal{N}$ is the chosen normal distribution with mean $W(t)$ and standard deviation $U(t)$. Although the intuition tells that the actual uncertainty has an asymetric distribution (due to the nature of the analog-digital conversion and electronic circuits), the assumption of the normal distribution was selected as a zero order step. In future, other distributions will be tested to improve the agreement with observations. The $W(t)$ is a function describing the expected shape of the waveform and $U(t)$ is a

function describing the uncertainty of the measurement. During the development of the backward model a number of functions describing the pulses were tested in an attempt to reach optimal agreement with the measured data. At the end the following conclusion was reached:

- To deal with the "long tail" feature of the pulses, second half of each pulse should have lower effect on the inference. This was achieved by introducing a time warying uncertainty function $U(t)$.
- Although the anticipated ideal form of a pulse was expected to be a scaled Gaussian, it was discovered during the model development, that the actual shape of the pulses deviates and is better described by a scaled generalised Gaussian function.

The $W(t)$ and $U(t)$ were defined as follows:

$$\begin{aligned} W_{p,ch}(t) =& B_{p,ch} + \sum_n I_{p,ch,n} \exp\left(-\left|\frac{t-\mu_{p,ch,n}}{\alpha_{p,ch,n}}\right|^{\beta_{p,n}}\right), \\ U_{p,ch}(t) =& U_{p,ch,c} + 0.1 W_{p,ch}(t) + \sum_n U_{p,ch,n} \exp\left(-\left|\frac{t-\mu_{p,ch,n}-\Delta_U}{A}\right|^{B}\right). \end{aligned} \tag{2.8}$$

The subscripts p and ch denote the affiliation to the polychromator and channel, respectively. The subscript n denotes the order of the pulses within a polychromator time trace and takes values of 1 or 2. The term B is the constant baseline of the signal. The term μ is the location parameter and the terms α and A are the scale parameters of the Gaussian functions. The term β is the generalisation parameter which equals to 2 in case of the Gaussian function. As β parameter goes to 1, the function approaches the shape of the Laplace distribution. As it goes to infinity, it approaches a rectangular function. The I terms are the intensity parameters and are the height (or integral) of the pulse. The uncertainty of the observations was expressed with a constant level $U_{p,ch,t}$, scaled intensity of the pulses and two additional waveforms (also described by scaled generalised Gaussian) shifted by a margin $\Delta_U = A$ after the pulse waveforms. The scale parameter $A = 0.2T_{duplex}$ (T_{duplex} is defined below). This way a lower influence of the second halves fo the pulses and the tails on the inference was achieved.

The pulse parameters were further described by the following parameters and hyper parameters:

$$\begin{aligned} \mu_{p,ch,1} =& M_1 + \delta_{\mu,p,ch,1}, \\ \mu_{p,ch,2} =& M_1 + T_{duplex} + \delta_{\mu,p,ch,2}, \\ \alpha_{p,ch,1} =& A + \delta_{\alpha,p,ch,1}, \\ \alpha_{p,ch,2} =& A + \delta_{\alpha,p,ch,2}, \end{aligned} \tag{2.9}$$

where the M_1 is the average location of the first pulse, T_{duplex} is the average delay between the pulses and A is the average scale of the pulses.

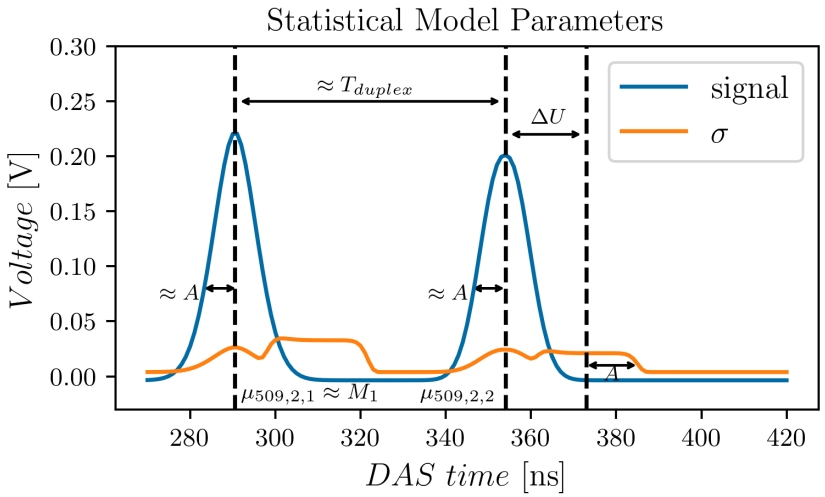

Figure 2.14: Sample of polychromator data model with the standard deviation of uncertainty marked as σ. The text labels show the basic parameters of the model also used in (2.8) and (2.9).

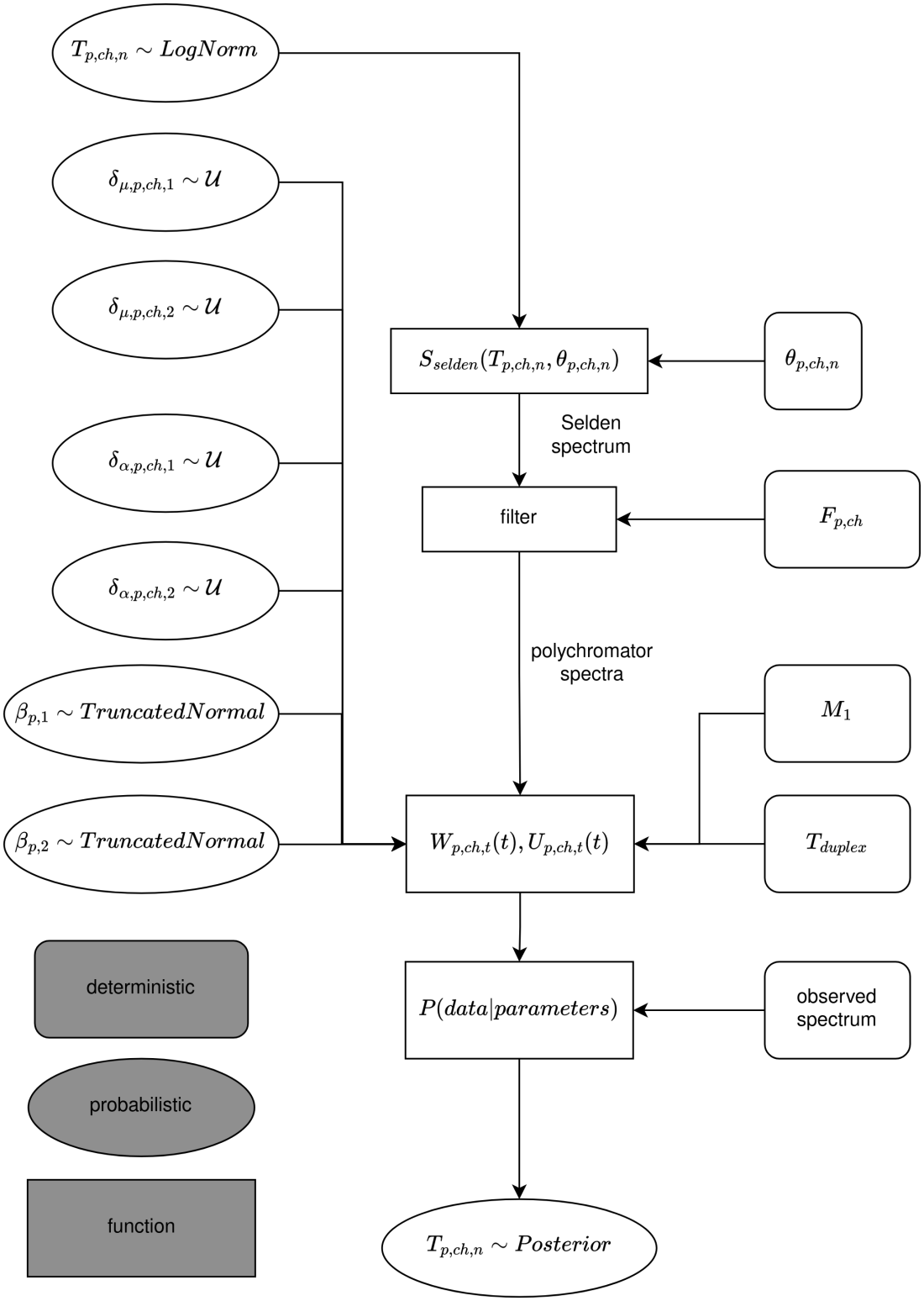

Figure 2.15: Flowchart graphically describing the Bayesian model for inference of electron temperature profile. The $\mathcal{U}$ denotes the uniform distribution.

The expected properties of the diagnostic were projected into the design of model parameters. The data acquisition systems were synchronised up to 1 nswhich means that the location of the first pulse $\mu_{p,ch,1}$ over all polychromator channels can be expected to vary only by a small margin $\delta_{\mu,p,ch,1}$ from the location

M_1[2]. The time duplexing was achieved by the constant difference of 13m in length of the optical fibres [37]. This allowed to specify the time delay of the second pulse over all polychromator channels with a general parameter $T_{duplex} = 64\,\text{ns}$ and a small variation $\delta_{\mu,p,ch,2}$.

The third assumption was that all pulses within a single laser shot have very similar variance $A = 8\,\text{ns}$ with a small allowed variance δ_α. The prior distributions of the parameters were defined as uniform distributions $\mathcal{U}(a,b)$, having constant nonzero probability in the interval (a,b), or a truncated normal distribution $TruncatedNormal(a,b,l,u)$ where a is the localisation parameter, b is the scale parameter, l is the lower bound and u is the upper bound:

$$\begin{aligned}
\delta_{\mu,p,ch,1} =& \mathcal{U}(-4,4),\\
\delta_{\mu p,ch,2} =& \mathcal{U}(-4,4),\\
\delta_{\alpha p,ch,1} =& \mathcal{U}(-2,6),\\
\delta_{\alpha p,ch,2} =& \mathcal{U}(-2,6),\\
\beta_{p,n} =& TruncatedNormal(2,1,1.5,\infty).
\end{aligned} \tag{2.10}$$

Basing the hyper parameters on the expected behavior of the parameters improves the model performance with respect to least square optimisation. The propagation of the mutual information between individual time traces makes the inference much more robust against uncertainty caused for example by the signal noise. This is especially important for the edge channels where the signal to noise ratio is low.

The last part to introduce in the model is the connection of (2.8) to the electron temperature which is achieved through the factors $I_{p,ch,1}$ and $I_{p,ch,2}$. As it was already mentioned previously, the intensity of the pulses in polychromator channels form the spectrum of the scattered light which is determined by the electron temperature. The intensity of the pulses can be described with

$$I_{p,ch,n} = C_{p,ch,n} \int S(T_{p,ch,n}, \theta_{p,ch,n}, \lambda) * F_{p,ch}(\lambda) d\lambda \tag{2.11}$$

The constant $C_{p,ch,n}$ encompasses the constants obtained via absolute calibrations (e.g. system throughput, spot size), the term $F_{p,ch}$ is the spectral characteristic of the polychromator channel, the term $S(T_{p,ch,n}, \theta_{p,ch,n}, \lambda)$ is the Selden formula [27, 28] which describes the shape of the spectrum and $\theta p, ch, n$ is the scattering angle. It should be noted here that the label p, ch, n determines which of the sight lines the pulse belongs to and thus determines the scattering angle, spot position and other constants. $T_{p,ch,n}$ is then the electron temperature parameter for the given sight line.

The prior distribution for temperature $T_{p,ch,n}$ was chosen to use the lognormal distribution which is natural for temperature since its values are only positive. The temperature parameter $T_{p,ch,n}$ was defined as

$$T_{p,ch,n} = exp\left(Lognormal(\mu_{T_p(z)}, \sigma_{T_p(z)})\right) \tag{2.12}$$

where $\mu_{T_p(z)}$ is the location parameter and $\sigma_{T_p(z)}$ is the scale parameter of the lognormal prior distribution[3]. The parameters of the temperature distributions

[2]The parameter M_1 was found as maximum of averaged intensities of the first pulse

[3]Here the notation p, ch, n was switched to z which also denotes the pulses uniquely.

were defined to assign higher probabilities to lower temperatures in the edge and higher in the core sight lines:

$$\mu_{T_p(z)} = \begin{cases} log\left(f(z)\right) = log\left(-\frac{z}{z_{\mathrm{far}}} \cdot T_{\mathrm{core}} + T_{\mathrm{core}}\right) & \text{for } f(z) > 0, \\ 0. & \text{otherwise.} \end{cases} \tag{2.13}$$

The z_{far} parameter is the vertical position above which only low values of electron temperature are expected. The T_{core} parameter defines the T_e which is expectable in the plasma core. The scale parameter was set to be $\sigma_{T_p(z)} = 0.1\mu_{T_p(z)}$.

Prior predictive distributions of a model are obtained by sampling the prior distributions. This is also to what the inference will converge to, if there is no or weak evidence in the data. Prior predictive distributions of the T_e for two channels of the COMPASS TS diagnostic are plotted in Fig. 2.16. The channel observing the plasma core ($Z = 0\,\mathrm{m}$) has its location set to ≈ 1.2 meanwhile the channel observing the plasma edge ($Z = 0.3\,\mathrm{m}$) has its location set to ≈ 1.5. This reflects the prior expectation of the electron temperature in the far SOL to be relatively low. The whole profile of the prior predictive distribution is plotted in Fig. 2.17.

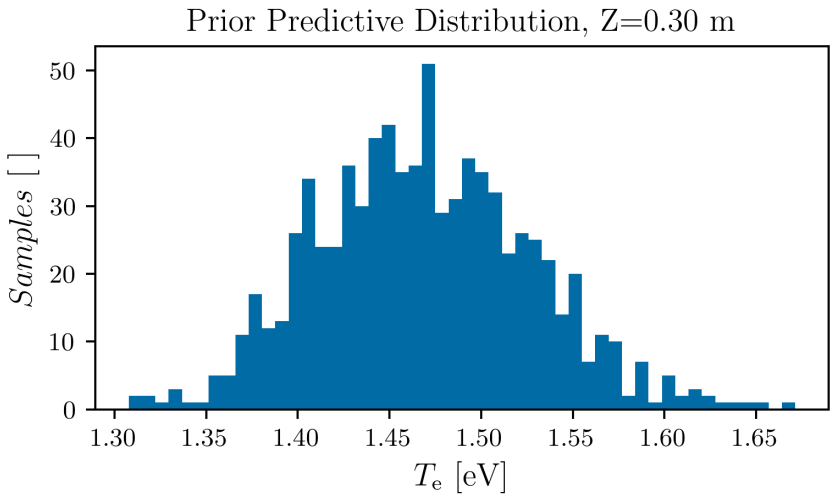

(a)

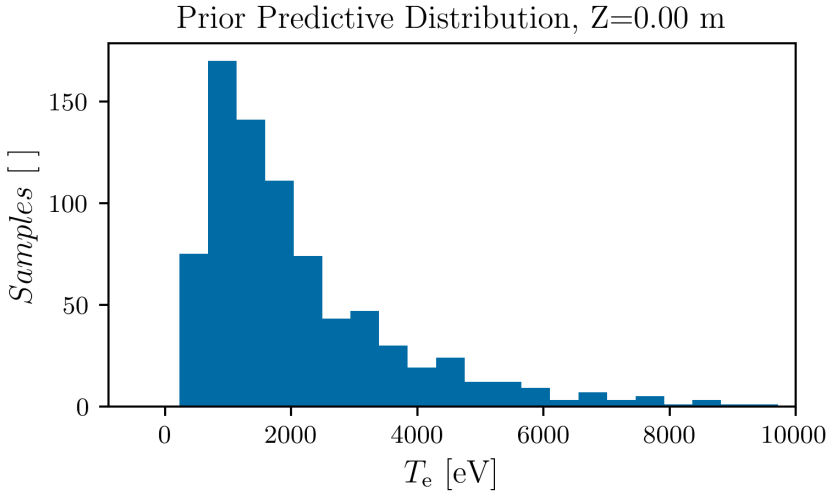

(b)

Figure 2.16: The figures show prior predictive distributions of T_e for two TS sight lines observing $Z = 0\,\text{m}$ and $Z = 0.3\,\text{m}$. Both distributions are lognormal. The location of the prior distribution in the top figure is set to ≈ 1.4 eV because the fibre is observing edge plasma where T_e is expected to be low. In the bottom figure the location of the distribution is ≈ 1.2 keV which reflects the experience with core T_e measured at COMPASS. Both histograms are composed of 800 samples.

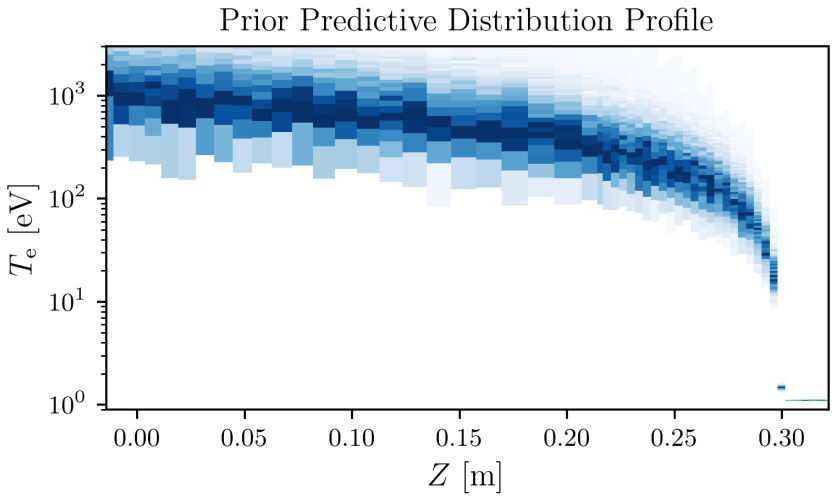

Figure 2.17: The figure shows the prior predictive distributions for the whole electron temperature profile. Every spatial point has its own lognormal distribution. The distribution is composed of 800 samples.

An example of application of the new statistical backward model was performed on the data from shot 20835 at time 1169 ms described in Sec. 2.2.2. An example of histograms of the posterior samples of T_e for $Z = 0.0\,\mathrm{m}$ and $Z = 0.3\,\mathrm{m}$ are displayed in Fig. 2.18. The height of the bars is proportional to the probability of T_e having the respective value. The prior predictive histograms for the same channels is plotted in Fig. 2.16. Comparing the prior predictive and posterior distribution for the edge sight line shows that bot distributions are practically identical. This suggests that the observations don't provide any evidence to determine the electron temperature. The comparison of the core channels on the other hand shows that both distributions are very different. The posterior distribution is close to a normal distribution, the location suggests T_e to be ≈ 1.2 keV. In this case the observations provide evidence about the electron temperature which is projected into the posterior distribution. This is visually confirmed in Fig. 2.19 where the pulses in the polychromator signals for the edge sight line are hidden in the background except for the channel 1. This only provides evidence, that the T_e has to be low enough not to generate any signal in the second channel. Even a worse case scenario happens when there is no detectable pulse in any of the polychromator channels. In this case the Bayesian inversion converges to the prior distribution of electron temperature, which predicts low values of T_e, but the least squares optimisation can converge to relatively hight values because of the missing prior information. This results in the unwanted oscillations in the edge.

The same information as in Fig. 2.18, but in two dimensions and for the entire profile, is presented in Fig. 2.20. The horizontal axis represents the vertical coordinate of the tokamak, the vertical axis represents the temperature, and the shading is proportional to the posterior probability. The darker the colour, the higher the probability. The orange colour for the seven core-most sight lines indicates a set of challenging points for reconstruction, belonging to four polychromators: 509, 510, 511, and 512. It was the statistical analysis which showed that the scatter of the points is larger than the uncertainty of the measurements. The random pattern of the scatter suggests that the cause is most likely of an instrumental origin. One hypothesis is a distortion of the pulse shapes

caused by electronics of the polychromator or data acquisition.

A comparison of the profile reconstructed with least-squares optimisation and the statistical one is shown in Fig. 2.21. Both profiles, on average, exhibit relatively good agreement when uncertainty is taken into account. A significant improvement was achieved in the edge region $Z > 0.28\,\mathrm{m}$. Least-squares optimisation results in a scattered profile, largely due to the low signal-to-noise ratio in all polychromator channels. Consequently, this type of optimisation can, and often does, converge to a wide variety of unphysical high temperatures. In contrast, the Bayesian approach mitigates this issue by imposing priors that favour lower temperatures, thus including our knowledge on realistic SOL conditions. When weak evidence is present in the data, the posterior distribution starts to mirror the prior. When evidence is available, the posterior is governed by the data. As a result, the temperature in the edge-most channels $Z > 0.3\,\mathrm{m}$ converges to the prior $T_\mathrm{e} = 1\,\mathrm{eV}$, because the intensities of the signal peaks in all channels are comparable to, or lower than, the noise level.

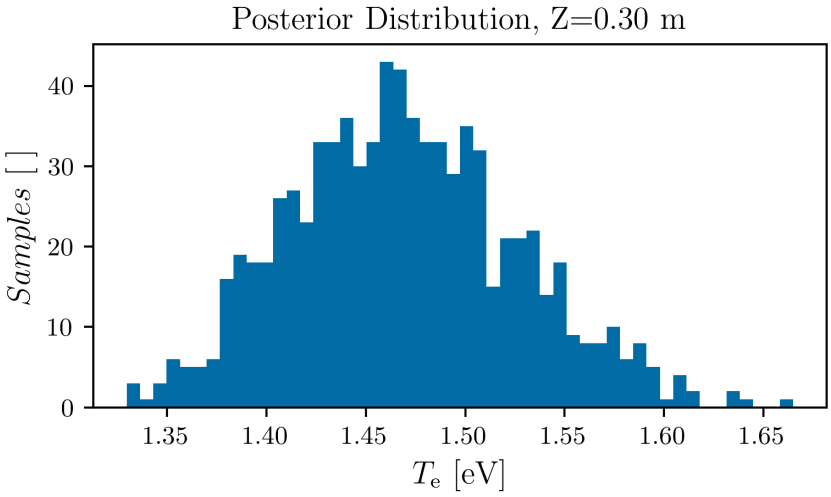

(a)

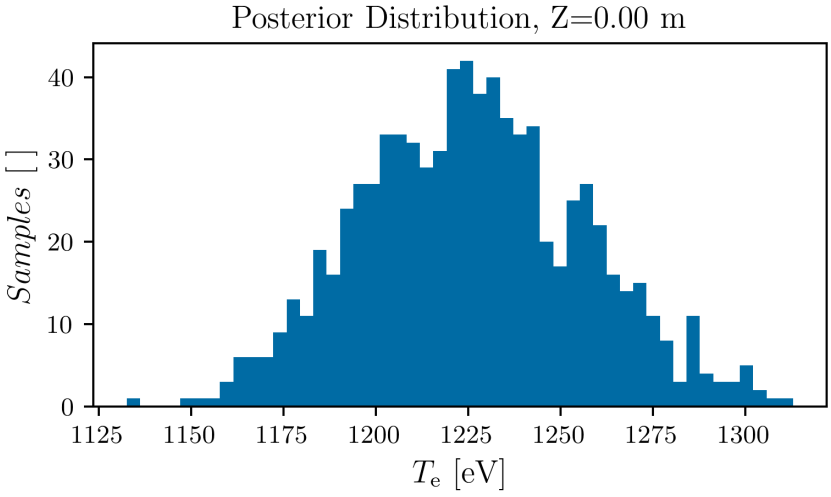

(b)

Figure 2.18: Histogram of posterior samples of T_e for two sight lines. The height of the bars is proportional to the posterior probability of T_e. The two plots show the same sight lines as the prior predictive histograms from Fig. 2.16. The inference composed of 800 samples distributed into two computational chains.

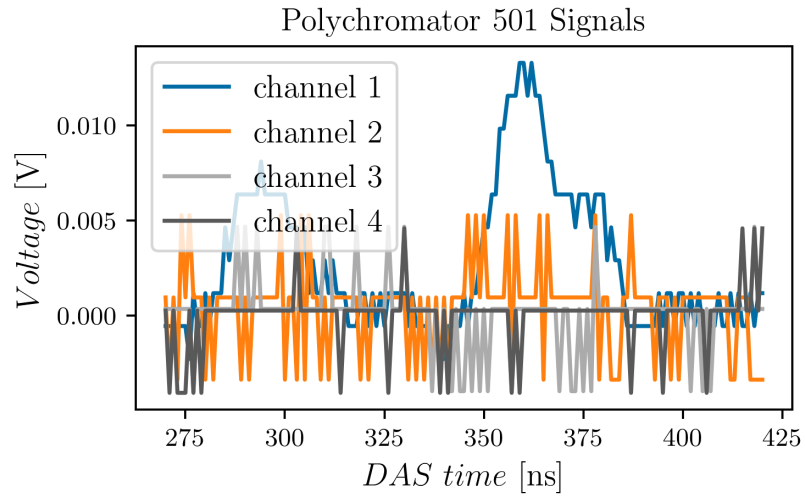

(a)

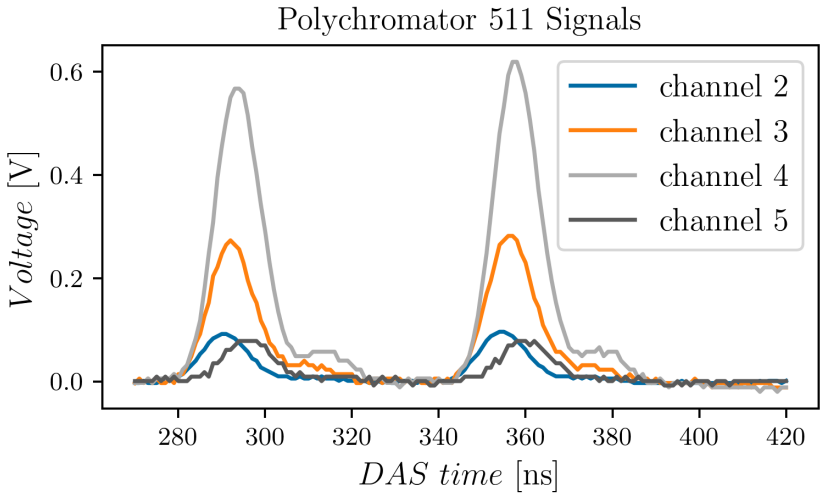

(b)

Figure 2.19: The plots show time traces measured by the polychromators 501 and 511. The second pulse in the polychromator 501 belongs to the sight line observing the plasma edge at $Z = 0.3\,\mathrm{m}$. The second pulse in the polychromator 511 belongs to the spatial point with $Z = 0.0\,\mathrm{m}$.

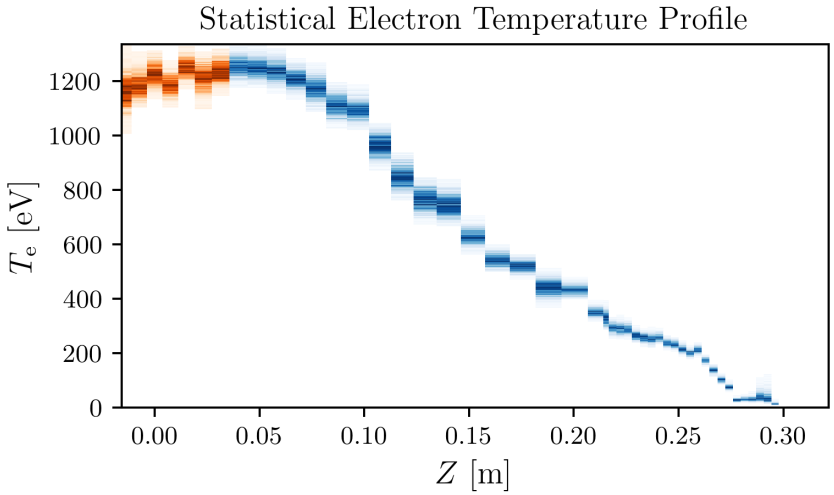

Figure 2.20: Statistical reconstruction of an electron temperature profile from experimental data. The shading of the colour is proportional to the posterior probability of T_e. The darker the colour, the higher the probability. The orange colour map in the core part of the profile marks the sight lines which are more problematic for inference due to stronger signal waveform distortion. The values for $Z > 0.3$ m are not visible due to too small scale of the distribution but their location is ≈ 1 eV.

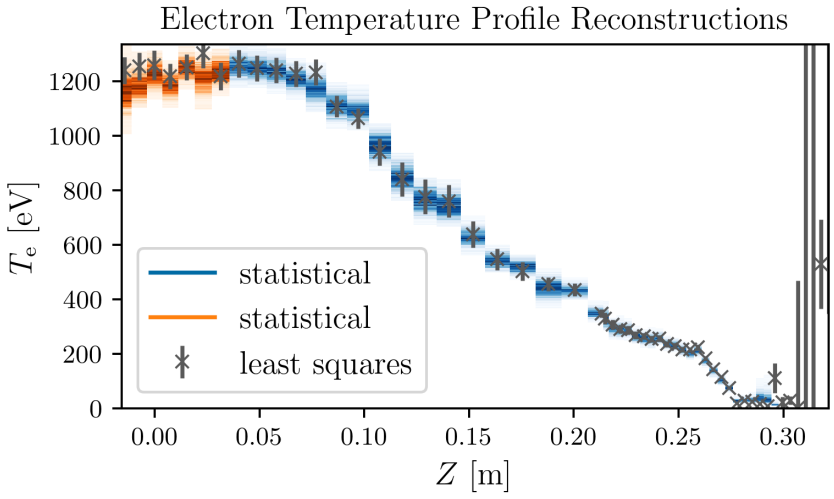

Figure 2.21: Comparison of the T_e profiles reconstructed using standard least-squares optimisation and the Bayesian approach.

During the development of the probabilistic model, various pulse waveforms W from (2.8) were tested in an attempt to reach an acceptable agreement between the posterior shape and the measured data. As it was already mentioned, the selected solution was to introduce a time-varying uncertainty function $U(t)$ to compensate for the deviation from the ideal shape. Although this step helped in tackling the most problematic channels with the strongest deviation and helped to lower the systematic errors, it increased the variance of the posterior samples above the apriory expected levels.

A plot depicting the posterior signal waveforms alongside the uncertainty waveforms can be found in Fig. 2.22. The orange curve represents the observed signal, and the blue lines depict the posterior signal waveforms. The grey lines are waveforms of the standard deviation of the signal uncertainty, which was assumed to have a normal distribution. The consequence of this solution is that the increased standard deviation reduces the significance of the data points, altering the properties of the posterior space. As already mentioned, this results in the posterior distributions to produce data with reduced systematic errors. The trade-off for this solution is an increase in the variance of the T_e posterior samples.

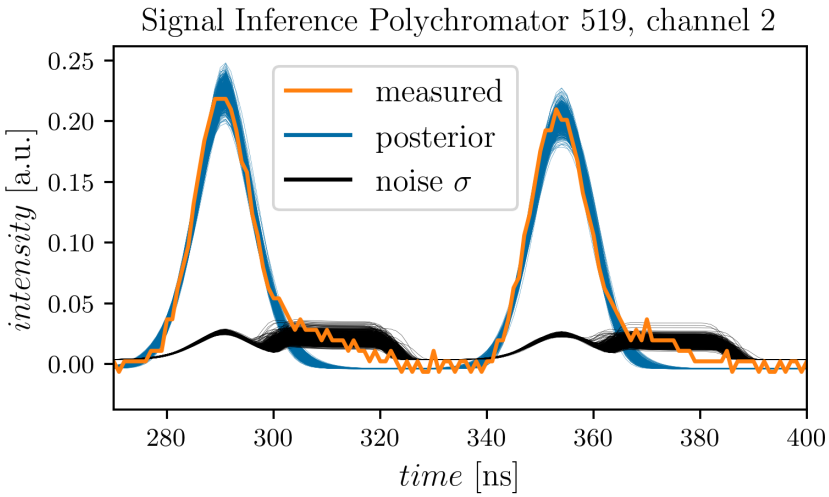

Figure 2.22: The figure displays the posterior signal waveforms in blue and the observed data in orange. The grey lines indicate the standard deviation of the signal noise, assumed to be normally distributed. The increases in the region of the pulse peak and the right tail serve to compensate for unknown characteristics of the circuit responses.

The profiles provided by the least squares optimisation and Bayesian inversion seem to be in good agreement. The statistical approach appears to eliminate issues with scattered and unreasonable values of T_e in the edge region. In the outlook this improvement should open the possibilities to improved automatic post processing of the electron kinetic profiles, as for example profile fitting. The Bayesian inversion also pointed out the problems caused by pulse waveform distortions and suggested that the reason is differences in electronics of the separate polychromator channels. One way of reducing this effect is better description of behavior of the electronics and its inclusion into the backward model. The inversions of the electron density profiles were not included in this work because they showed up to be more demanding. The resulting profiles were suffering from low accuracy and precision. One hypothesis for this behaviour is the problem with the deformation of the temporal shape of the pulses. The developed statistical inference used results of absolute calibration calculated by the standard backward model which uses different description of the pulse shapes. The use of different descriptions probably results in the suboptimal performance in case of the density profiles. Because the standard least squares optimisation uses the same approach for post processing of the calibration and experimental measurements, the flaws are likely to cancel out. This also support the hypothesis.

2.4 Forward Model of Thomson Scattering

This section provides an overview of the Thomson scattering module contributed to Cherab, highlighting the newly incorporated functionalities and the rationale behind the chosen implementation. Details on the module and its application have been published in [11].

Before the contributed module is described one important guiding principle behind Cherab's design, which influenced the implementation, has to be mentioned. It is to provide users with the flexibility to implement their models at varying levels of complexity. Generally, the more intricate the model, the more computational time it requires. In scenarios with less stringent accuracy requirements, deploying highly detailed models may not be required. Moreover, in some cases focus on computational speed makes detailed modelling impractical. Therefore, Cherab allows users to decide the level of model complexity, based on their specific requirements. The incorporated model of TS tries to follow this ideology by allowing multiple levels of complexity of its components.

As was roughly calculated in Sec. 2.1.2, the scattering probability is extremely low and to incorporate this in the model would be extremely computationally inefficient. For this reason, the implemented model of TS ignores the scattering in the sense of changing of the propagation direction of photons. As is shown in Fig. 2.23 it uses the reverse ray tracing nature of Raysect. The rays launched from observers are assumed to transits the laser unperturbed. The contributions of scattered laser light is added to the rays as an integral over the intersection of the ray with the laser beam (marked with the blue line segment). This approach is more efficient since every ray that intersects the laser collects the scattered light. The absolute calibration is secured by implementing the correct scattering cross sections and by including the energy density of the laser pulse and particle density of the electrons in the plasma.

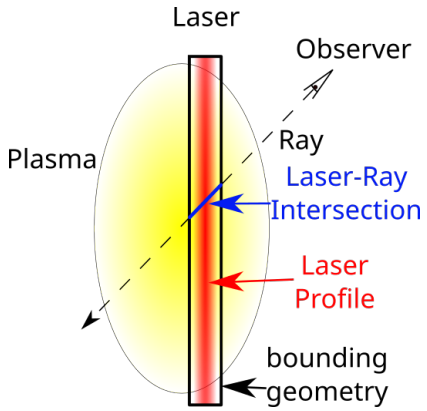

Figure 2.23: A crude and exaggerated schema of the principles of the implemented TS model. The yellow color depicts the plasma volume. The red color shows the profile of energy density of laser light surrounded by its envelope defined by a *primitive* shape. The dashed arrow is the ray trajectory and the blue segment is the intersection of the ray path with the laser over which the contribution of the scattered light is integrated.

In ray tracing simulations, Raysect calculates the intersections of rays with *primitive*s in a scene and adds their contributions to the ray's spectrum, depending

on the *primitive*'s material properties. For the TS laser, the relevant material type is the *InhomogeneousVolumeEmitter*, designed for volumes exhibiting inhomogeneous volumetric radiation, such as the scattering of an incident laser pulse. The newly added material class *LaserMaterial* acts as an interface between the newly added TS code and Raysect.

An emission method *emission_function* such as (2.2) must be implemented in order to add contributions of the scattered laser light to the rays. This method returns point contribution to ray spectrum in units of spectral radiance per metre [W/sr/nm/m^3], which is subsequently integrated by the *InhomogeneousVolumeEmitter* integrator along the intersection of a ray with a geometrical shape defined by a *primitive*.

2.4.1 Module Architecture

To incorporate the Thomson scattering module into Cherab, a laser framework was introduced. Although the main reason for this framework was primarily the Thomson scattering implementation, the framework is designed to be adaptable for any laser-plasma interactions such as collective Thomson scattering and laser induced fluorescence. It was anticipated that such interactions would necessitate information on two key entities: the laser (e.g., energy density, direction of propagation) and the plasma (e.g., species distribution function, force fields). Cherab's class *Plasma* serves as the source of information for the latter. Information about laser properties has been divided into two new classes, namely *LaserProfile* and *LaserSpectrum*, for the sake of simplicity. In an ideal scenario, laser properties would be encapsulated by a four-dimensional function $f(\boldsymbol{r}, \lambda)$. The choice to segregate this information into two classes (i.e. $f(\boldsymbol{r}, \lambda) = g(\boldsymbol{r})h(\lambda)$) was motivated by three main reasons. Firstly, laser light dispersion is generally inconsequential in fusion applications. Secondly, separating the models simplifies their definition. Lastly, if dispersion is relevant, it can be addressed by employing multiple overlapping lasers with differing wavelengths and spatial distributions. An additional class, *LaserModel*, has been introduced to encapsulate the physics model describing radiation due to laser interactions, such as Thomson scattering. It is the *LaserModel* class that has the mentioned *emission_function* as its method. One of the significant advantages of this tripartite class structure is the flexibility it provides for implementing models with varying levels of complexity and for diverse purposes. For instance, it permits the implementation of a computationally intensive TS model for an arbitrary electron distribution function based on Equation (2.1), or a more streamlined one assuming a specific type of distribution function (e.g., Maxwell-Boltzmann), as in Equation (2.2). A simplified schema of the model architecture is depicted in Fig. 2.24. Solid lines indicate object references, while dashed lines represent the flow of information provided by class methods. A detailed description of each component follows below.

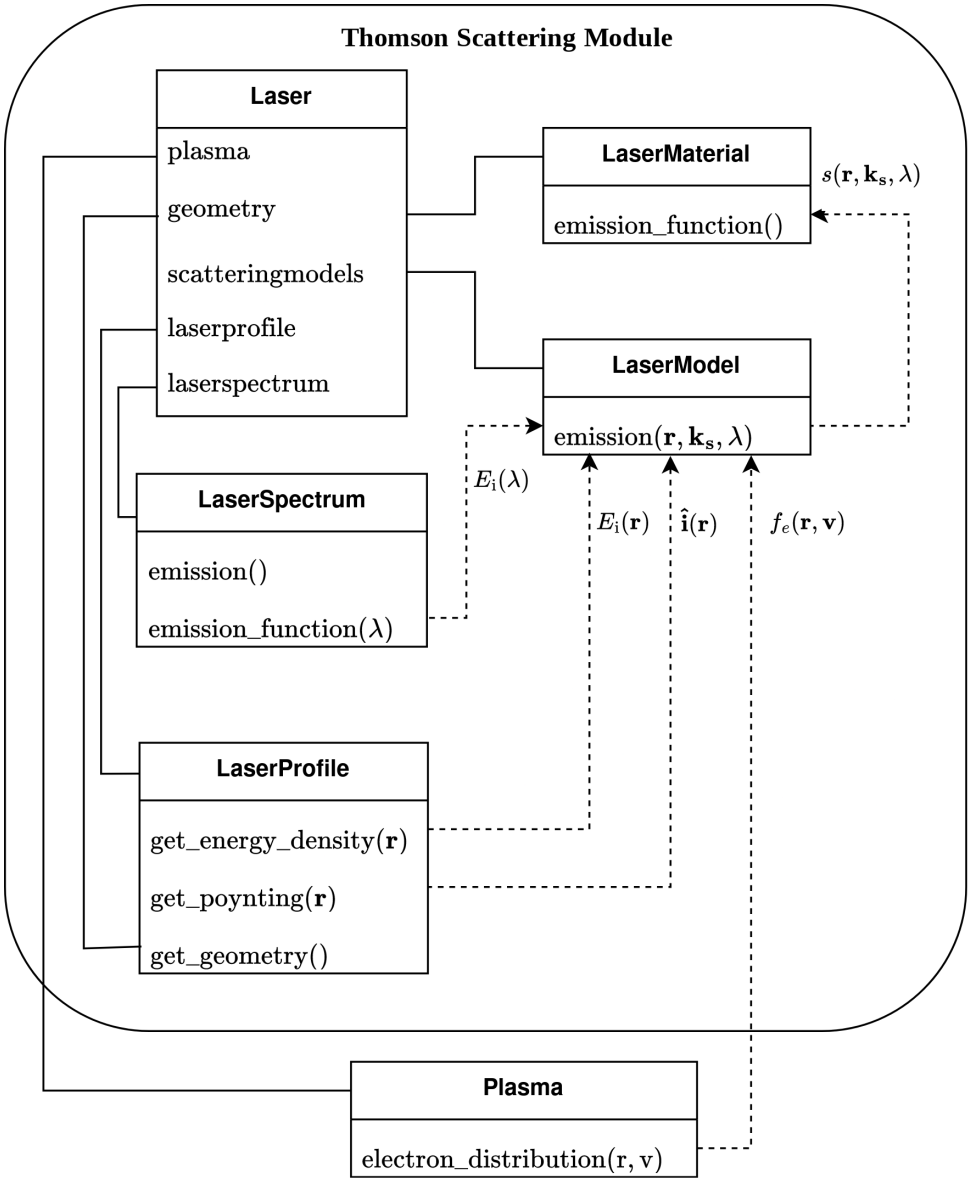

Figure 2.24: A simplified schema of the Thomson scattering model architecture is presented. Solid lines indicate references between objects and functions. For example, *Laser* object has a reference to *LaserProfile* object and its *get_geometry* method. The dashed lines illustrate the flow of information provided by class methods. For example, *LaserProfile* provides the emission function with the value of energy density $E_i(\boldsymbol{r})$. The variable s represents the point contribution of the laser to the ray's spectrum, $\boldsymbol{r}$ denotes the position, $\boldsymbol{k}_\mathrm{s}$ signifies the wave vector of the scattered wave (i.e., the direction of the scattered photon), λ is the wavelength, and E_i is the laser energy density.

Laser Class

The *Laser* class serves primarily as a container that furnishes references for the remainder of the model. It specifies the position and orientation of the laser within the scene and maintains the laser's geometry. The geometry can be thought of as a bounding envelope within which laser interactions are assessed and added to rays. To accommodate arbitrary laser geometries, it was decided that the bounding

geometry would be supplied by the *LaserProfile* as a list of Raysect's *primitive*s. Additionally, the *Laser* class holds a list of *LaserModel*s, each potentially governing different laser interactions. The *Laser* class subsequently assigns a *LaserMaterial* to the *primitive*s, thereby linking it, among other things, to the *LaserModel*s.

Laser Spectrum Class

The *LaserSpectrum* class houses information concerning the laser's spectrum, i.e. the angular frequency ω_i from (2.1). Its design parallels native Raysect *Spectrum*, featuring a defined wavelength range (*min_wavelength*, *max_wavelength*) partitioned into a number of spectral bins. The units employed for the spectrum are those of power spectral density, [$\mathrm{W\,nm^{-1}}$]. The class is versatile, accommodating lasers with negligible spectral width by employing a single spectral bin, for instance. Moreover, the *LaserSpectrum* class allows prescription by a general 1D function, such as Gaussian, if the application requires a more detailed representation.

Laser Profile Class

The primary aim of this class is to furnish a spatial description of laser light via arbitrary three-dimensional scalar and vector functions within the bounding geometry. In Fig. 2.23 this is depicted as the distribution of red color. The vector functions delineate the laser light's direction of propagation and polarisation, indicated by the electric field vector's direction. The scalar functions specify the laser light's intensity in units of [$\mathrm{J\,m^{-3}}$], notwithstanding that the more natural units for Raysect and Cherab would be [$\mathrm{W\,m^{-3}}$]. This decision was made with the preference of short-pulse lasers in fusion research in mind, rendering it more intuitive to consider the intensity's spatial distribution as a 'frozen' laser pulse in time. The class is structured to accept Raysect's *VectorFunction3D* and *ScalarFunction3D* for defining laser properties, thereby facilitating straightforward implementation of diverse laser profiles even pure Python functions only. For example to implement energy distribution specified by the Gaussian beam model with a focus point. A final pivotal function of the *LaserProfile* class is to prescribe the bounding geometry. This definition was transferred to this class to enable geometry design in harmony with laser profile properties, thereby providing flexibility and scope for optimisation. For example, partitioning the laser beam into segments can, under specific conditions, improve the efficiency of ray tracing. Or for example prescribing conic bounding geometry to an expanding laser pulse. In Fig. 2.23 the bounding geometry is the black envelope around the laser light. The intersection of a ray with the bouding geometry defines the intersection along which the laser radiaton is integrated.

Laser Model Class

The *LaserModel* class is designed to encapsulate the physics models describing laser-plasma interactions, such as Thomson scattering. Utilising information provided by the *Plasma*, *LaserProfile*, and *LaserSpectrum*, this class calculates the point contribution to the ray's spectrum in units of spectral radiance per metre [$\mathrm{W/sr/nm/m^3}$]. The class accommodates the implementation of physics models with varying degrees of generality, either at the kinetic level (based on

(2.1)) or at the fluid level (based on (2.2)). While the primary motivation for the introduction of this laser module was Thomson scattering, the *LaserModel* class is also engineered to address other phenomena, such as collective Thomson scattering, for example.

2.4.2 Thomson Scattering Implementation

The laser module described above was utilised to implement a Thomson scattering model. As part of this work, subclasses of *LaserProfile* and *LaserSpectra* were added to Cherab, thus providing a basic set of ready-to-use laser descriptions. The physical model selected for the Thomson scattering implementation is based on the formulae published by Selden [27, 28]. This model is centred around a simple analytic formula that yields the spectral density function S as per equation (2.2). It assumes a standard scattering geometry and employs a Maxwell-Boltzmann distribution for the velocity distribution of electrons. The depolarisation effect q is assumed to be 1, which leads to decreased accuracy for temperatures above approximately 10 keV. The model's advantage lies in its simplicity and speed, making it also suitable for inverse models that infer electron distribution properties from measured data. The formula internally evaluated by the model is similar to equation (2.2):

$$\begin{aligned} &\frac{d^6P}{d^3\boldsymbol{r}d\Omega d\lambda_s d\lambda_i} = \frac{n_e(\boldsymbol{r})r_e^2 c}{\lambda_i} E_r(\boldsymbol{r})E_\lambda(\lambda_i)S(\epsilon,\theta,2\alpha), \\ &\epsilon = \frac{\lambda_s-\lambda_i}{\lambda_i}, \quad 2\alpha = \frac{m_\mathrm{e}c^2}{T_\mathrm{e}}. \end{aligned} \tag{2.14}$$

Here, $E_r(\boldsymbol{r})$ is the volumetric energy density, $E_\lambda(\lambda_i)$ is the power spectral density of the laser for the given incident laser wavelength λ_i, and n_e is the electron density. The spectral density function S is as defined in [27]. Due to the distribution of intensity being returned by the laser profile in units of $[\,\mathrm{W}\times\mathrm{m}^{-3}]$, it is necessary to multiply by the speed of light to obtain the correct units. As mentioned previously, both factors E_r and E_λ must be carefully combined to achieve the correct laser intensity.

Examples of scattered spectra over varying scattering angles and plasma temperatures are presented in Fig. 2.25. These curves were obtained by tracing a single ray through a plasma with a uniform electron temperature and density of $10^{19}\,\mathrm{m}^{-3}$. The laser wavelength was set at 1064 nm and the laser featured a cylindrical shape with a 3 mm radius and uniform energy density of $1\,\mathrm{J\,m}^{-3}$. The spectra were derived by tracing a single ray through the laser at different scattering angles and for different electron temperatures. Both Fig. 2.25a and Fig. 2.25b show the impact of plasma temperature and scattering angle on the differential cross-section S from equation (2.14), and thus on the shape of the scattered spectrum.

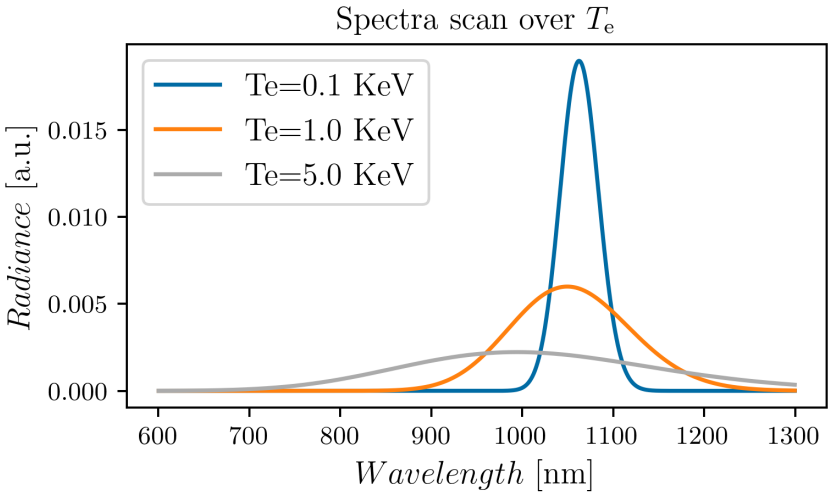

(a) Scan over electron temperature at a scattering angle of $\theta = 90°$.

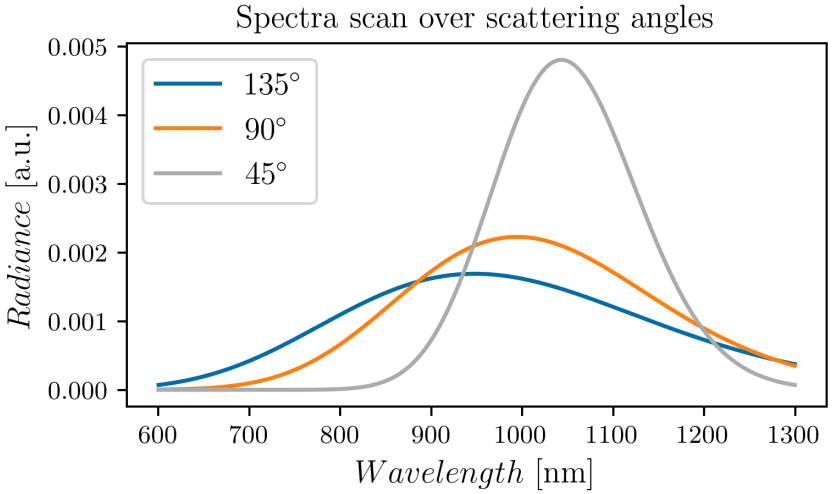

(b) Scan over scattering angle at an electron temperature of $T_e = 5\,\mathrm{keV}$.

Figure 2.25: Orthogonal scans of scattered spectra over electron temperature and scattering angles. The plotted spectra are normalised and were obtained by tracing a single ray under varying directions and plasma conditions. The constant parameters included the laser wavelength of 1064 nm, a plasma density of $10^{19}\,\mathrm{m}^{-3}$, and a laser energy density of $1\,\mathrm{J\,m}^{-3}$. The laser had a cylindrical shape with a 3 mm radius and uniform energy density.

2.5 Benchmarking of the Thomson Scattering Module

The essential steps in introducing a new computational model are sanity checks and benchmarking. These are critical for ensuring that the code produces accurate results and is free of significant errors. For the TS model, sanity checks were conducted similarly to the example of scattered spectra displayed in Fig. 2.25. Alongside the model, a series of tests was implemented to assess the agreement between semi empirical solutions and the spectra obtained by tracing single rays for straightforward scattering cases. The cases included three geometrically simple

scenarios. The laser is assumed to be cylindrical with uniform energy density and the profile of the electron density and temperature is also set to be constant. The scattered spectra are calculated with the Selden formula for three scattering angles (45°, 90° and 135°) and for three temperatures (0.1 keV, 1.0 keV and 5). The spectral shapes are plotted in Fig. 2.25. The spectral shapes are then multiplied by analytically calculated constants encapsulating the influence of the scattering length and electron density to obtain proper units. The agreement of the semi empirical results and ray traced spectra is then tested.

Benchmarking is a more complex task. It was decided that validation could be accomplished by comparing T_e profiles reconstructed from forward-modelled diagnostic signals to profiles reconstructed from experimental data. A reliable model should achieve errors lower than uncertainties in experimentally obtained profiles. Assessing this error is complicated; it is influenced by the level of detail captured in the diagnostic system model and by unknown factors such as discrepancies between tabulated and real instrumental parameters. Because the latter is not readily quantifiable and would be time-consuming to characterize[4], the main effort was focused on level of detail with which the model was created. This entails approximating the FOV of the diagnostic with high precision. A detailed model of the TS diagnostic's collection optics, laser beam line, and data acquisition system is essential for this purpose. The key steps in the chosen benchmarking procedure are:

- Creating a detailed Raysect model of the collection optics for the TS diagnostic system.
- Benchmarking the Raysect model against Zemax software by comparing ray tracing outcomes.
- Properly positioning the optics model and fibres within the COMPASS frame of reference.
- Selecting appropriate profiles of electron densities and temperatures as measured by TS.
- Fitting these profiles with an analytic function and using mapping techniques to project the 1D profiles into 3D space.
- Constructing a plasma model using the acquired profiles.
- Incorporating a model of the COMPASS TS laser.
- Assembling a scene that includes the COMPASS first wall, vessel, plasma model, laser, and collection optics.
- Executing a forward simulation to produce scattered spectra.
- Applying relative calibrations to polychromator channels to generate forward models of signal intensities.
- Utilizing the same inter-shot analysis codes that were employed to calculate the experimental profiles.

[4]One approach would be to obtain manufacturing and positioning tolerances and conduct a probabilistic study of the effects of deviations

2.5.1 Model of COMPASS Thomson Scattering Diagnostic System

The Thomson scattering diagnostic system previously in operation at the COMPASS tokamak [45, 14] was chosen for benchmarking primarily due to the ease of access to design specifications, experimental data, and consultation with the COMPASS Thomson scattering team—namely Petra Bílková, Petr Böhm, and Miroslav Šos. This accessibility to information was crucial, because as described in the previous paragraph, the diagnostic model required high accuracy. A satisfactory level of accuracy was targeted through the integration of a detailed model of the tokamak-side of the diagnostic system into the Cherab & Raysect frameworks, supplemented by relative calibrations for the remainder of the system. Specifically, the model comprises:

- A model of the laser beam.
- A model of the collecting optics.
- A model of the optical fibre bundles.
- Positioning of the system relative to the tokamak.
- Application of relative spectral calibrations to the polychromator channels.

The first step in modelling the diagnostic was the composition of the fibre bundles. It was decided that the first model of the bundles would include all 3420 optical fibres. Although this increases the computational time needed to obtain spectra simulation for a single spatial point, the time requirements were not an issue for benchmarking purposes, as only a single plasma profile had to be simulated. If further analyses require more spectra to be calculated, a model approximating the bundles with a square detector with the correct acceptance angle would have to be added and used.

The second step was to add a model of the collection optics of the Thomson scattering system. Models of the objectives, created in Raysect, are displayed in Fig. 2.26. The picture shows that the models include all the optical elements present during experimental measurements. The top objective, dedicated to edge measurements, comprises six lenses and also includes the vacuum window and the polariser. The bottom objective, dedicated to core measurements, consists of five lenses and also incorporates the vacuum window. The objectives in Fig. 2.26 are positioned as they were during experiments. The axes indicate the coordinates of the tokamak's Cartesian frame of reference. Although not visible in the image, fibre bundles would be situated to the right of the last optical element of each objective. The model was based on the Zemax descriptions of the objectives[5]. The only modification made was the introduction of a small gap of 1 μm between touching optical elements. This was done because Raysect and Zemax define scenes differently, and touching surfaces can lead to numerical issues during Raysect ray tracing.

[5]Zemax models, Zemax ray tracing, and general support were provided by Miroslav Kral and Petr Böhm, to whom I would like to express my thanks.

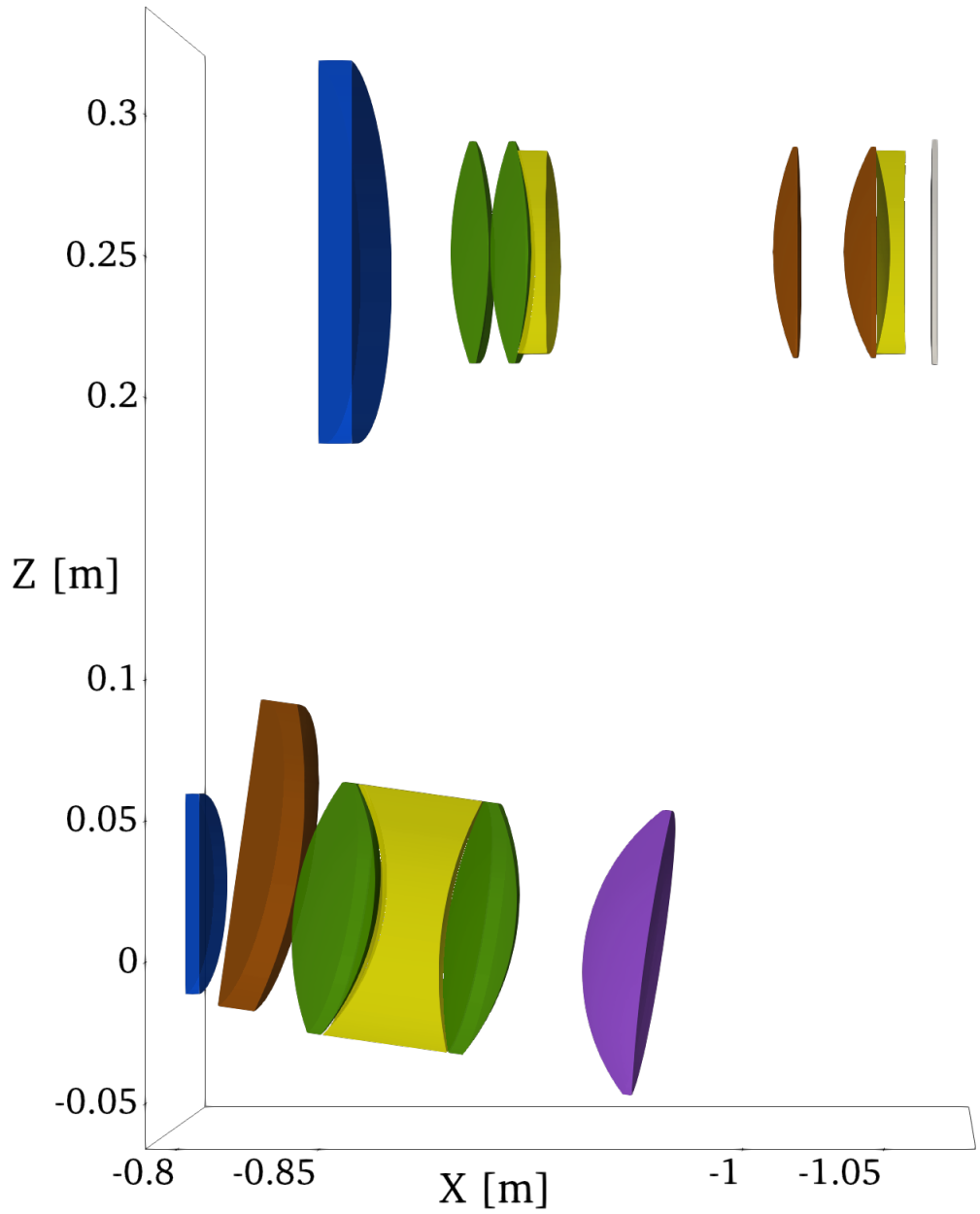

Figure 2.26: Models of COMPASS Thomson Scattering objectives. The top objective is dedicated to edge measurements; the bottom objective is for core measurements. Both are positioned as they were during tokamak operation. The colour code of the optical elements distinguishes their types: vacuum windows in blue, biconvex lenses in green, biconcave lenses in yellow, planoconvex lenses in brown, meniscus lenses in purple, polarisers in grey.

To assess the accuracy of the Raysect objective models, a set of rays was traced using Zemax and compared to ray traces generated by Raysect. Zemax ray path data were imported and transformed from the Zemax reference frame to the tokamak frame of reference. The initial points and directions of the Zemax rays were noted, and the traces were replicated using Raysect's *LoggingRay*, which provides information about ray-scene interactions (e.g., the ray path). Both paths were then compared to identify any non-negligible differences. The ray paths obtained from Zemax are plotted in Fig. 2.27 as red lines. The left ends of the

lines indicate the orientation of the laser axis, while the right ends show the expected positions of the surfaces on which the fibre bundles are located.

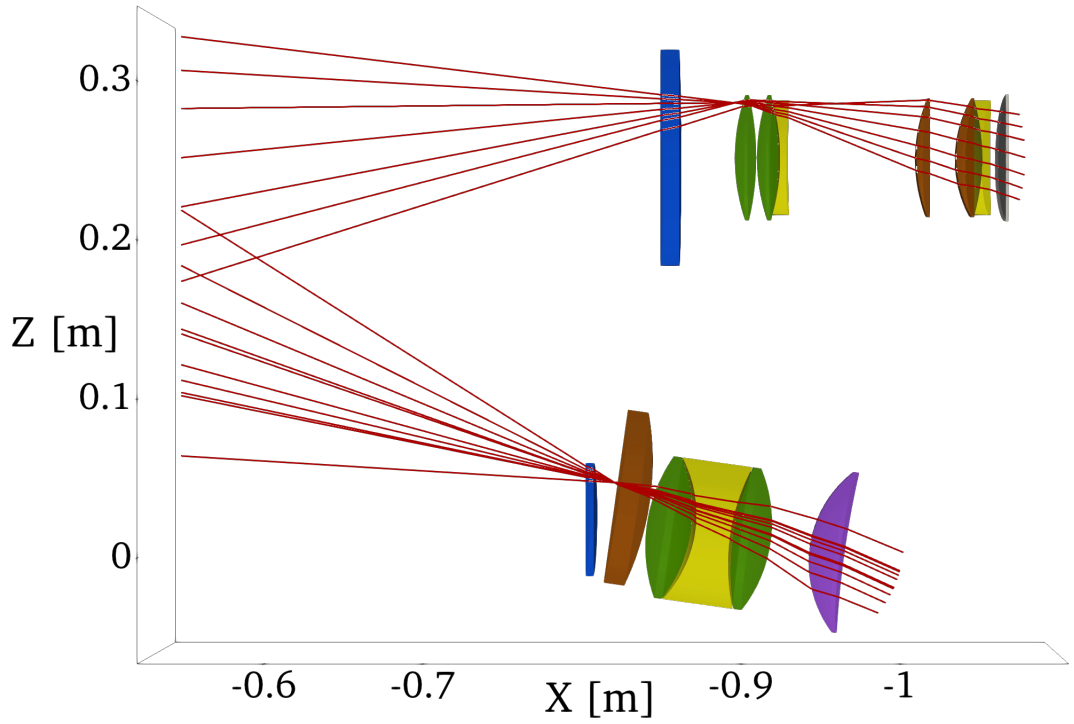

Figure 2.27: Models of COMPASS Thomson Scattering objectives with red lines showing ray paths calculated by Zemax.

To assess the similarity between the ray paths generated by Zemax and Raysect, the differences in intersection points of rays with optical elements were calculated. The Euclidean distances between ray-surface intersections of corresponding rays in Zemax and Raysect are plotted in Fig. 2.28. The horizontal axis indicates the affiliation of the intersection to a specific optical element. Each ray produces two intersections for every optical element: one upon entry and another upon exiting the element's volume. The maximum error observed is below 0.6 μm, which is less than 0.3% of the fibre core diameter and well below the error margins for fibre position accuracy. Given these results, it can be confidently stated that the ray tracing capabilities and performance of Raysect are exceptionally reliable, especially considering that Zemax is the most widely recognized, used, and respected optical design software. Utilising these objectives for calculating the TS spectra should not introduce any significant errors into the benchmarking process for the Thomson scattering module added to Cherab.

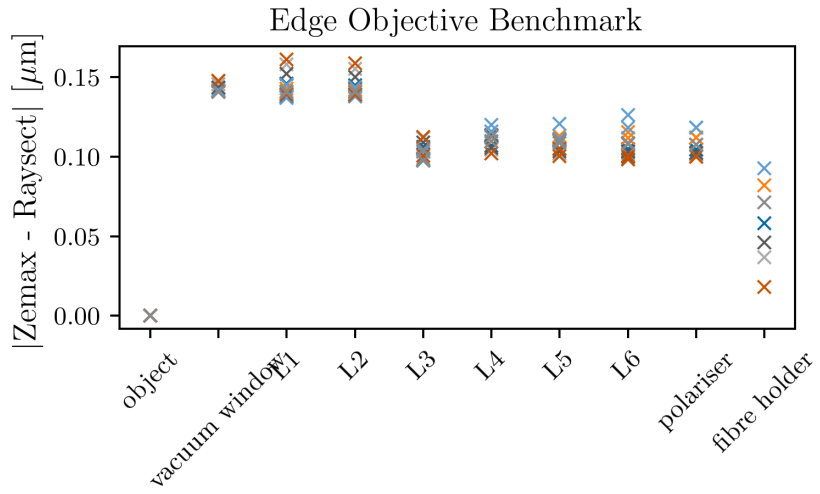

(a)

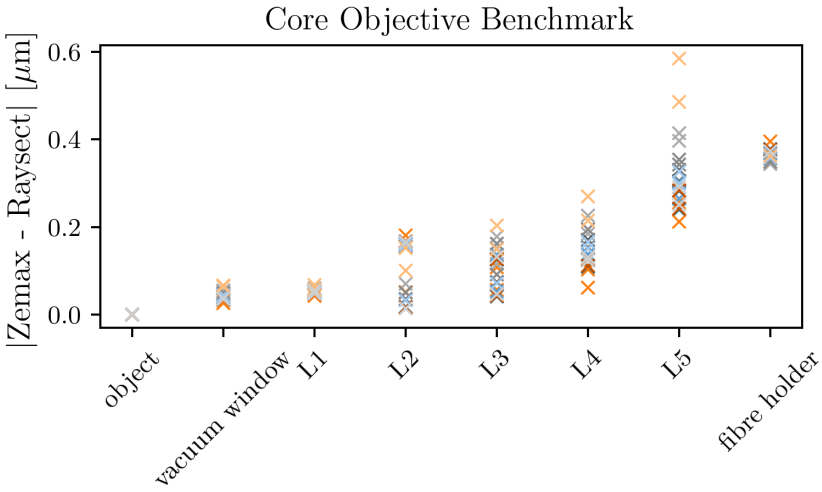

(b)

Figure 2.28: Euclidean distances of ray-surface intersections calculated by Zemax and Raysect for the TS objective models. The rays were initiated with identical starting positions and directions. The horizontal axis indicates the affiliation of the intersected surface to the optical element. Each ray generates two intersections per element: one upon entry and another upon exit. The vertical axis displays the Euclidean distance between intersections calculated by Zemax and Raysect.

An essential part of preparing the diagnostic model involved accurately positioning it within the tokamak's reference frame. While the objective models could be positioned based on their expected locations in the tokamak hall, placing the fibre bundle models presented a challenge due to the uncertainty in their precise positioning relative to the objectives. Given the small size of the fibre bundles and the inherent difficulty in measuring their exact positions, spatial calibration data were employed instead. This calibration data includes information about each sight line's position on the laser axis and scattering angles. An automated minimization function was created to optimize the minimum distance between the calibrated and ray-traced positions of a sight line at the laser axis, by adjusting the vertical position of the fibre bundles on the image plane. The results are depicted in Fig. 2.29, which demonstrates that the optimization achieves negligible differences in

sight line positions at the laser axis. The outliers in the top panel are caused by the convergence criteria of the optimization algorithm and it converting to a slightly worse optimum. The difference is nevertheless negligible. Furthermore, the relative positioning of the fibre bundles and the objectives was found to be reasonable, indicating the accuracy of the objective models. The bottom graph in Fig. 2.29 presents the discrepancies between calculated and measured scattering angles θ. For the edge objective, errors are below 2° and centered around zero, likely attributable to measurement uncertainties. For the core objective, however, there is a notable negative offset, with errors reaching up to −7°. This may be due to discrepancies between the assumed and actual positions of the core objective, which could potentially influence the reconstructed T_e values by orders of tens of eV. As a result, the scattering angles used for inferring T_e from the forward-modeled data were taken to be those obtained via ray tracing.

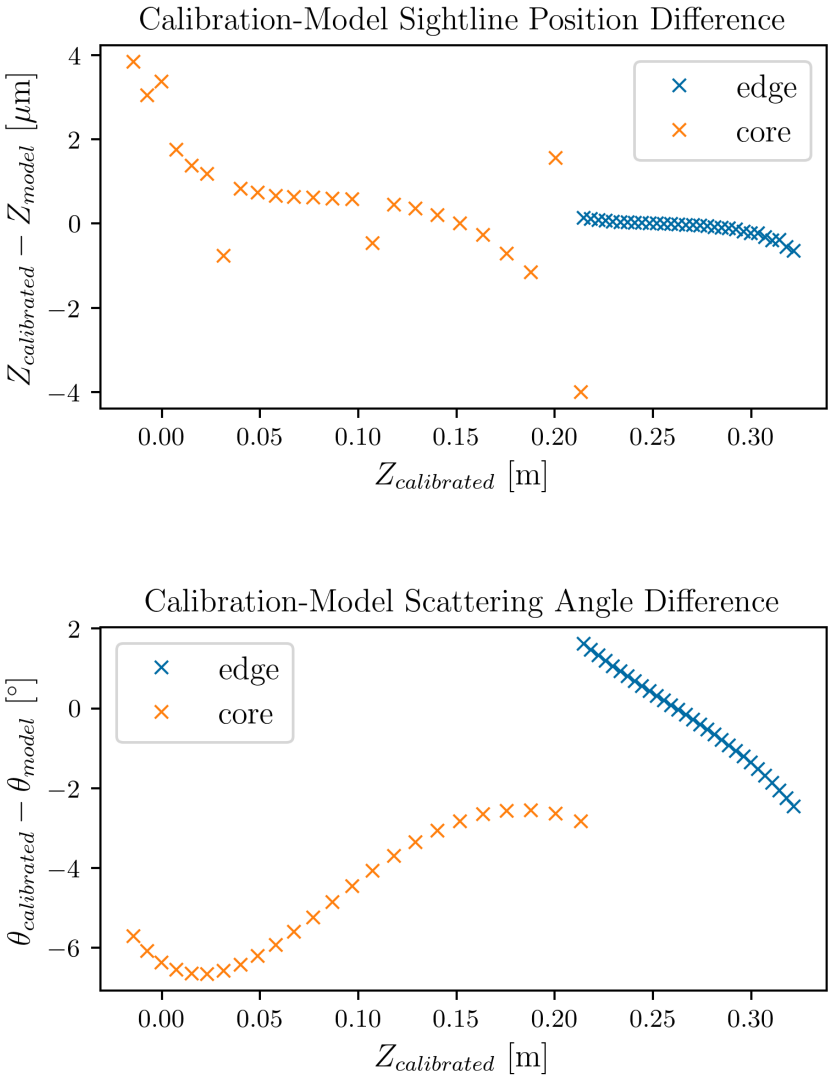

Figure 2.29: The differences between calibrated and model sight line properties are shown here, including position and scattering angles. The outliers in the top panel are caused by the convergence criteria of the optimisation algorithm and are negligible.

2.5.2 Profile Comparison

The benchmarking procedure of the contributed TS module was based on the similarity between profiles obtained from the experiment and forward models of the TS data. The requisite steps for this task were as follows:

- Creating the entire scene, including all optical elements, plasma-facing components, and the vacuum vessel
- Running a ray-tracing simulation for all optical fibres
- Applying the transmission curves of the polychromators
- Reconstructing the electron temperature profiles using the inter-shot codes

The forward models of the scattered spectra were generated using Raysect's ray tracing of the scene, which incorporated models of the Thomson scattering viewing optics, plasma-facing components, vacuum vessel, and the plasma model[6]. A visual representation of the scene is displayed in Fig. 2.30.

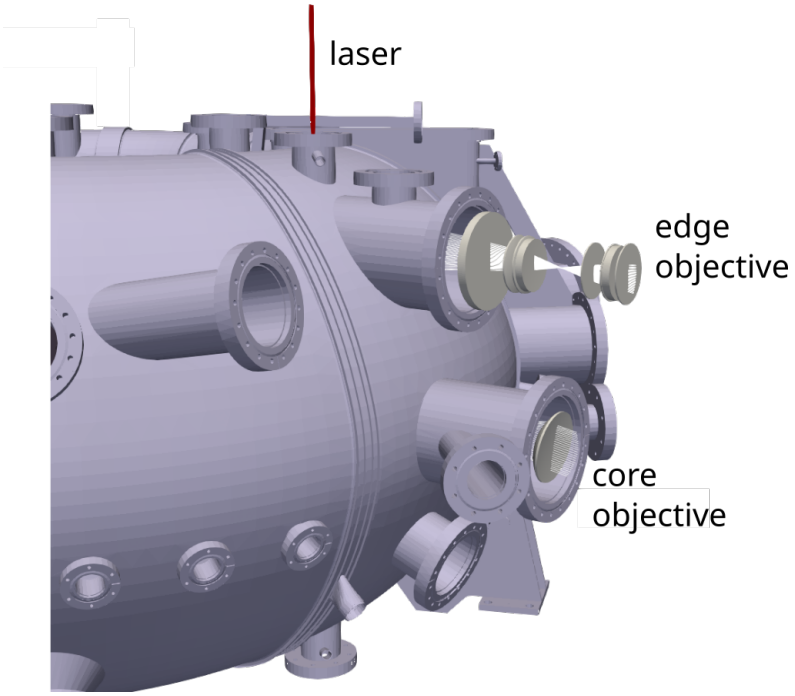

Figure 2.30: The complete scene used for the forward modelling of the COMPASS Thomson scattering diagnostic includes both viewing optics of the diagnostic, the vacuum vessel, plasma-facing components, and the laser.

The materials for the vacuum vessel and plasma-facing components were set to be absolutely absorbing (*AbsorbingSurface*) to simulate conditions without reflections. Owing to the short temporal nature of the laser pulse and rapid data acquisition, the contributions to the signal from direct and reflected light are temporally separated. This separation is dependent on the distance of the

[6]Models of the plasma-facing components and vacuum vessel were provided by the COMPASS engineering team.

reflecting surface. Because Raysect does not account for the temporal dimension, and given that the dimensions of the COMPASS vacuum vessel would cause the reflected and direct contributions to overlap, it was decided to omit reflections from the benchmark. The laser was modelled using a *UniformEnergyDensity* laser profile with a cylindrical shape, having a radius of 6 mm and an infinitely narrow laser spectrum at 1064 nm. The plasma model was constructed using the electron profiles previously described in Sec. 2.2.2.

Ray-tracing simulations were conducted for all optical fibres across all fibre bundles in the models. The sight-line spectra were obtained as the sum of all spectra observed by individual fibres in each fibre bundle. Signals in the polychromator channels were derived by filtering the fibre bundle spectra through their respective transmission curves. The calculated intensities for the polychromator channels were then provided to Miroslav Šoš, who applied the standard least-squares inter-shot codes to reconstruct the electron temperature profiles. Because Raysect simulations directly yield scattered spectral power densities for an entire laser pulse, the initial step undertaken for experimental data—analysing time traces from polychromator channels to obtain scattered light intensities—could be skipped. Only the second step of determining the temperature corresponding to the simulated intensities in the polychromator spectra was necessary. Results of the profile reconstruction are presented in Fig. 2.31. The plot depicts the input plasma profile as a blue line and the reconstructed temperatures with orange 'x' markers. Visually, the reconstructed profile aligns well with the input profile. Grey dots indicate the relative errors of the reconstructed values. The magnitude of the errors in the edge region can be disregarded. The extremely low values of T_e exagerate any small discrepancy between the input and inverted profiles (because $error = (|T_{inverted} - T_{plasma}|/T_{plasma})$). The discontinuity in the errors at $Z \approx 0.22\,\mathrm{m}$ marks the transition from edge to core objectives. Fig. 2.31 also shows, that the magnitude of relative errors is influenced by the magnitude of the profile derivative, if the edge region with extremely low temperatures is neglected. This is expected since each sight-line collects light from a finite volume, which is subsequently characterised by a single number. Excluding the edge region, where the temperature values drop below 10 eV, the errors remain below 10% and are often units of percentage and lower. The magnitude of errors for temperatures reconstructed from forward-modelled data is modest in comparison to the uncertainty in the experimental profiles. The relative uncertainties of the values reconstructed from experimental data and the relative errors of the profiles reconstructed from forward models of the polychromator spectra are compared in Fig. 2.32. The figure illustrates that, except for the problematic edge region, errors in the forward-modelled profile remain below the experimental uncertainty, suggesting that the Thomson scattering module provides data with acceptably high accuracy.

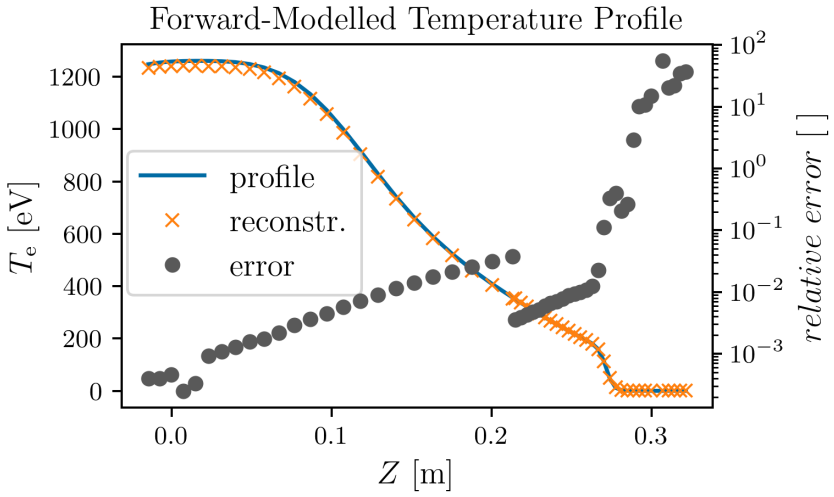

Figure 2.31: The profile of T_e reconstructed from forward models of polychromator signals is indicated by orange crosses. The input profile of plasma electron temperature is represented by the blue line. Visually, the reconstructed profile closely follows the input profile. Grey dots indicate the relative errors of the reconstructed values.

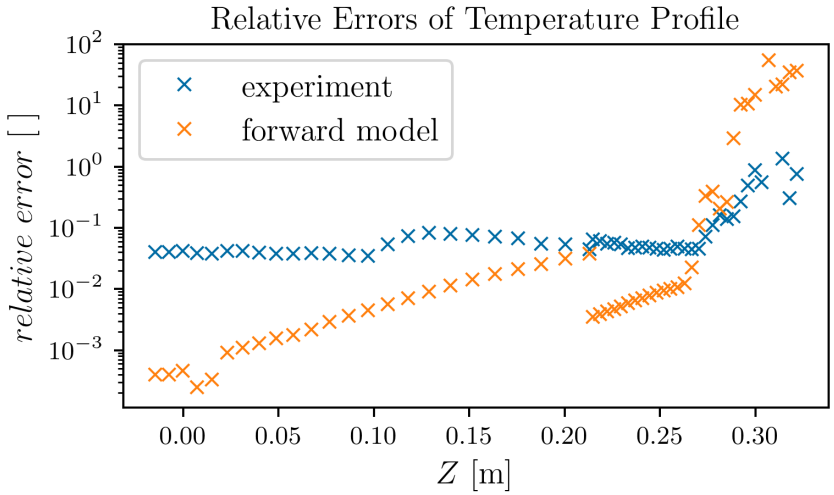

Figure 2.32: The orange crosses indicate the relative uncertainty of electron temperature profiles reconstructed from experimental measurements. The blue markers represent the relative uncertainty of profiles reconstructed from forward-modelled data. Relative errors in forward-modelled data are generally smaller than those in experimental data, except in the edge region where the signal-to-noise ratio is low.

2.6 Conclusion

Laser module and Thomson scattering system was added to Cherab. The aim of the laser module is to suit any diagnostic systems based on laser beams. The Thomson scattering radiation model contributed to Cherab is based on the Selden approximation of scattered spectrum. The benchmarking of the

model with experimental data shows that the error of the values of electron temperature inverted from forward modelled data is smaller than the uncertainty of experimentally obtained values of T_e. The errors of the forward modelled profiles can be explained to a large degree by the instrumental function of the diagnostic. Namely the gradients in the profile generate systematic errors in the reconstructed values. This also points to the benefits of creating detailed forward models of diagnostic systems. Because it delivers forward modelled data with high accuracy, it can be used to design the backward models to meet experimental requirements. For example, the analysis of synthetic data in Fig. 2.31 clearly showed that the inferred electron profiles suffer largest errors in the pedestal region and gave estimate of their approximate magnitude. If the experimental needs require the errors to be lowered, the diagnostic model can be used to design a more advanced backward model which would for example take into account the gradients and measured volumes. Such diagnostic modelling also allows to estimate the possibilities given by the diagnostic instrumentation and help to mitigate too ambitions requirements, unnecessarily over engineered backward models and most importantly save time of people.

One of the examples of application of the TS model as a support of diagnostic design is given in [11]. It shows the possibility to start with simple diagnostic models which help to set margins for possible performance and can help to locate the biggest problems. The article for example shows the effect of the thermal radiation of the first wall on the recorded signals estimated for the COMPASS Upgrade tokamak [15]. It also estimates the worst case scenario for reflections by assuming no temporal shift between reflected and direct contributions of laser scattered light. The application of the model for the design of the COMPASS Upgrade TS diagnostic is currently ongoing. Work is also ongoing on creating forward models of ITER's Thomson scattering diagnostics under the implementing agreement $LGA - 2015 - M - 08$. Currently the model of the core system is being prepared [16]. The future work will also include modelling of the edge and divertor systems and application of the developed statistical backwad model to invert electron profiles from forward modelled data.

The future work on the laser module should include adding Raman scattering radiation model [46] which would aid calibration procedures of TS. A Thomson scattering model taking into account correction for the depolarisation effect [25, 26] should also be added to make modelling of scattering from high temperature plasma more accurate.

The Bayesian inversion of electron temperature profiles from experimental data was developed. It clearly showed that the statistical approach can remove some unwanted properties of the profiles reconstructed by the least square error optimisation. For example the unphysical oscillations in the edge region where the appriory expectation of the temperature being low helps to mitigate unwanted oscillations caused by unfavorable signal to noise ratio. Another immediate outcome was determination of the problematic core sight lines. The difficulty of describing the polychromator channel signal waveforms, and their discovered distrortions, seems to be causing the oscillations of the reconstructed T_e profiles in the core region. Although the oscillations can be detected also in the profiles calculated by the least-squares optimisation, when a larger dataset of profiles is analysed, it was the statistical analysis and the information provided by its

posterior distributions which pointed out the possible sources of the problem. The most likely reason is a systematic error caused by the incapability of the model's signal waveform to cover the shape of the experimental signal. As a consequence the optimisation slides to a local minimum which doesn't describe the data well. The reason for the core channels having distorted pulse shapes can be differences in the properties of the electric circuits and APDs, reflections of scattered light in the vacuum vessel or combination of both. One possibility how to tackle this problem would be to experimentally obtain circuit responses of all of the polychromator channels. It would then be possible to separate the influence of the electronics and reflections. Because the temporal evolution of the laser pulse is identical for all the channels, it can be introduced as a single hyper parameter for all the polychromator channels and the signal waveforms without reflections can be then obtained by convolution of the laser waveform and the circuit responses. This would introduce a more realistic dependence of the signal waveforms and would leave only the contributions from the reflections as variable independent for each channel. To test this improvement the diagnostic model can be also used. For example the influence of reflections on the polychromator signals can be estimated with ray tracing. These can be then compared to effects caused by theoretical circuit responses.

To conclude the chapter, the detailed forward modelling of diagnostic systems can be a useful tool for diagnostic design and operation. This statement doesn't imply that it is impossible to operate or design a complicated diagnostic without such tools as Cherab. It is possible that their creation doesn't bring improvement worth the invested effort. In many occasions this is difficult to estimate before the model is created and applied. In this case it seems to be better to rather invest some time rather than risk unwanted artefacts in diagnostic outputs or lower performance of the system in general. One additional advantage of the Raysect and Cherab framework is its high standard of architecture and coding which makes its application simple. Once a diagnostic model is added it can be used for various applications without need of investing any overhead time. The application of the statistical approach to backward modelling showed that it can point out possible problems with instrumentation and mitigate some unwanted phenomena. The combination of the forward and backward modelling is a powerful tool for both diagnostic design and operation. Utilisation of combination of both can lead to improvement of the diagnostic performance, data quality and realiability and also can lead to increased effectivity of human work.

3. Neon concentration inference in the JET divertor

In this chapter, the method of inference of neon concentration in the JET divertor, developed in the frame of this thesis, is described. A Bayesian inversion of the concentration is based on the spectroscopic measurements of neon spectral lines originating from the divertor. Before the method is applied to experimental data, its performance is tested on forward modelled spectroscopic data based on results of SOLPS [3] simulations. For this reason a model of KT3 diagnostic was contributed to Cherab in the frame of this work. The chapter is concluded with the application of the method to experimental data and a discussion of the results.

The material limits for long term operation of tungsten plasma facing components set the limit of power flux to $10\mathrm{MWm}^{-2}$ [47]. Because the divertor power fluxes for large machines [47, 48, 49, 50] are predicted to be above this threshold, active methods of mitigating the power load on divertor targets [51, 52] will have to be used. One of the mitigating techniques is impurity gas seeding [52, 53] which helps to decrease the power flux on the surface of the divertor targets by increasing the radiative losses [.] The effect of the impurity gas seeding on machine performance is not yet fully understood. The rate at which the seeding gas is seeded into the vacuum vessel and its type [54, 55] is an important parameter. At too low rates the dissipation of energy is too low and the plasma facing components are not protected sufficiently. At too high rates, the plasma performance is degraded due to the penetration of the impurity elements into the confined region. These two limits are not constant and are influenced by various aspects as for example divertor shape and plasma parameters. For the mentioned reasons, knowing the approximate value of seeded impurity in the divertor region is an extremely important aspect in the operation of the machine and ongoing physics studies.

The neon seeded JET discharges are part of an ongoing effort inside Eurofusion's WPTE (Work Package Tokamak Exploitation) which goal is to provided physics basis for the operation of ITER [56]. Although seeding of nitrogen gas is relatively well described, ITER opts for avoiding nitrogen seeding due to engineering constraints [47]. For this reason neon seems to be a good candidate for ITER. Neon selection also makes JET a good machine for ITER relevant seeding studies due to its divertor configuration, size and high plasma heating.

3.1 Models of Plasma Radiation Processes

This section provides a concise overview of the models employed for plasma line radiation, plasma radiated power, and spectral line shapes, thereby elucidating the methods used to validate SOLPS simulations and determine impurity concentrations from spectroscopic measurements. Presently, Cherab exclusively utilizes the Open-ADAS atomic database [10] as its source of atomic data. In accordance with the procedures outlined in [10, 57], Cherab calculates line emissivity and ionization balance. For further information, references [57, 29, 58] are recommended.

The spectral lines emitted by plasma result from radiative decay, transitioning

from a higher energy state to a lower one. The emitted photon's wavelength corresponds to the energy gap between these states, giving the line radiation its characteristic narrow spectral profile. The ADAS framework [59] provides a detailed description of spectral line emissivity ε, as documented in [57], specifically in Equation 3.8.16 of ADAS208.

$$\begin{aligned}\varepsilon_{j\to k} =& A_{j\to k}\left(\sum_{\sigma=1}^{M_z} F_{j\sigma}^{(\mathrm{exc})} N_\mathrm{e} N_\sigma + \sum_{\nu'=1}^{M_{z+1}} F_{j\nu'}^{(\mathrm{rec})} N_\mathrm{e} N_{\nu'}^{+} + \right.\\ & \left.\sum_{\nu'=1}^{M_{z+1}} F_{j\nu'}^{(\mathrm{CX})} N_\mathrm{H} N_{\nu'}^{+} + \sum_{\mu'=1}^{M_{z-1}} F_{j\mu'}^{(\mathrm{ion})} N_\mathrm{e} N_{\mu'}^{-}\right)\\ =& \sum_{\sigma=1}^{M_z} PEC_{\sigma,j\to k}^{(\mathrm{exc})} N_\mathrm{e} N_\sigma + \sum_{\nu'=1}^{M_{z+1}} PEC_{\nu',j\to k}^{(\mathrm{rec})} N_\mathrm{e} N_{\nu'}^{+} + \\ & \sum_{\nu'=1}^{M_{z+1}} PEC_{\nu',j\to k}^{(\mathrm{CX})} N_\mathrm{H} N_{\nu'}^{+} + \sum_{\mu'=1}^{M_{z-1}} PEC_{\mu',j\to k}^{(\mathrm{ion})} N_\mathrm{e} N_{\mu'}^{-}\end{aligned} \tag{3.1}$$

where the model variable definitions are:

N_e - Density of electrons..

N_H - Density of neutral hydrogen.

N_σ - Population density of the selected ion metastable state σ.

$N_{\nu'}^{+}$ - Population density of the adjacent higher ionisation metastable state ν'.

$N_{\mu'}^{-}$ - Population density of the adjacent lower ionisation metastable state μ'.

$F_{j\sigma}^{(\mathrm{exc})}$ - Effective contribution to the population of the upper state j from excitation from the metastables.

$\mathrm{F}_{j\nu'}^{(\mathrm{rec})}$ - Effective contribution to the population of the upper state j from free electron capture.

$\mathrm{F}_{j\nu'}^{(\mathrm{CX})}$ - Effective contribution to the population of the upper state j from charge exchange collision with neutral hydrogen.

$\mathrm{F}_{j\mu'}^{(\mathrm{ion})}$ - Effective contribution to the population of the upper state j from ionisation.

$A_{j\to k}$ - Einstein coefficient for the transition from the orbital j to k.

$PEC_{X,j\to k}^{Y}$ - Respective photon emissivity coefficients, calculated using $A_{j\to k}F_X^Y$.

To summarize, (3.1) states that the total emissivity is a cumulative result of various processes, namely ionisation, recombination, excitation, and charge exchange collisions, all contributing to populating the upper state j. PECs represent reaction rates, quantifying the extent to which each collisional process contributes to the emissivity. These rates are highly dependent on T_e and n_e, with CX additionally being influenced by the kinetic properties of ions. Equation (3.1) details the metastable-resolved scenario, accounting for contributions from

metastable states. ADAS also furnishes a model and data for situations where metastable states are not distinctly resolved. In such cases, contributions from ionic states are bundled, achieved by resolving the summations in (3.1), thereby simplifying the equation.

$$\begin{aligned}\varepsilon_{j\to k} =& PEC^{(\mathrm{exc})}_{j\to k} N_\mathrm{e} N + PEC^{(\mathrm{rec})}_{j\to k} N_\mathrm{e} N^+ + \\ & PEC^{(\mathrm{CX})}_{j\to k} N_\mathrm{H} N^+ + PEC^{(\mathrm{ion})}_{j\to k} N_\mathrm{e} N^-.\end{aligned} \tag{3.2}$$

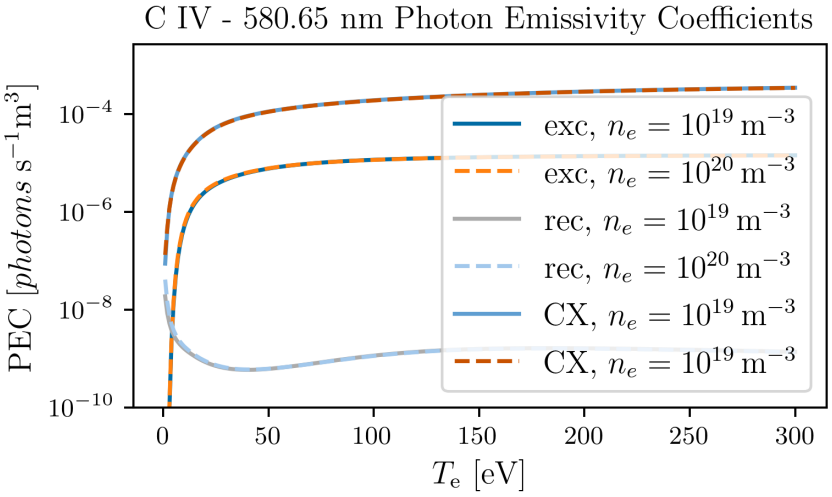

Figure 3.1: The figure displays PEC values for the Carbon IV transition $1S2\ 3P1\ 4DJ$ — $1S2\ 3S1\ 2SJ$. This specific transition emits light at a wavelength of 580.65 nm. The lines shows that the influence of T_e on PEC is much more pronounced than the influence of electron density.

Figure Fig. 3.1 illustrates an example of PEC coefficients for the Carbon 3+ ion. This particular line was selected as the dataset includes the $PEC^{(\mathrm{CX})}$ values. The plot delineates the dependency of PEC on electron temperature (T_e) and density (n_e). Notably, the curve's shape indicates that the variations in PEC values due to different processes and changes in T_e are significantly larger, spanning several orders of magnitude, compared to the relatively minor changes resulting from a tenfold difference in n_e. The dataset does not include PEC^{ion} values, most likely due to the negligible PEC values.

Both (3.2) and (3.1) highlight that the emissivity of a spectral line is also determined by the population density N of the states involved in the collisional processes. In fusion plasmas, the state distribution is primarily determined by collisional-radiative processes and particle transport. ADAS employs a set of equations (referenced as Eq. 5.5.2 in ADAS405 in [57]) to model the metastable unresolved population distribution of plasma elements.

$$\begin{aligned}\frac{d}{dt}N^{(z)} =& N_\mathrm{e} S^{(z-1\to z)}_{\mathrm{CD}} N^{(z-1)} \\ & - \left(N_\mathrm{e} S^{(z\to z+1)}_{\mathrm{CD}} + N_\mathrm{e}\alpha^{(z\to z-1)}_{\mathrm{CD}} + N_\mathrm{H} C^{(z\to z-1)}_{\mathrm{CD},\rho\to\rho'}\right) N^{(z)} \\ & + N_\mathrm{e}\alpha^{(z+1\to z)}_{\mathrm{CD}} N^{(z+1)} + N_\mathrm{H} C^{(z+1\to z)}_{\mathrm{CD}} N^{(z+1)}\end{aligned} \tag{3.3}$$

The model variables are as follows:

$N^{(z)}$ - Density of the ionization stage of the element with charge z.

N_e - Electron density.

N_H - Density of neutral hydrogen.

$S_{\mathrm{CD}}^{(z\to z+1)}$ - Collisional-dielectronic ionisation coefficient, representing the reaction rate.

$\alpha_{\mathrm{CD}}^{(z\to z-1)}$ - Collisional-dielectronic recombination coefficient, indicative of the reaction rate.

$C_{\mathrm{CD}}^{(z\to z-1)}$ - Collisional-radiative charge exchange recombination coefficient, also a measure of the reaction rate.

The total density of the plasma element, N_{tot}, is defined as:

$$N_{tot} = \sum_{z=1}^{z_0} N^{(z)} \tag{3.4}$$

Here, z_0 denotes the nuclear charge. The fractional abundances of the ionisation stages, denoted as F, are calculated using the ratio $N^{(z)}/N_{tot}$.

The coefficients S_{CD}, α_{CD}, and C_{CD} are supplied by ADAS in the ADF11 file format, covering a range of elements and isotopes. Equation (3.3) portrays a transient state, illustrating the evolution of fractional abundances $N^{(z)}$ over time in response to changing plasma conditions. In scenarios where plasma conditions remain stable, an equilibrium balance can be applied by setting the time derivatives in (3.3) to zero.

Figure Fig. 3.2 exemplifies the equilibrium ionisation balance for neon. It depicts the evolution of fractional abundances of neon ionization stages as a function of temperature. In this illustration, solid lines represent calculations for $n_\mathrm{e} = 1 \times 10^{19}\,\mathrm{m}^{-3}$ and the dashed lines for $n_\mathrm{e} = 1 \times 10^{20}\,\mathrm{m}^{-3}$. Comparison of these lines clearly demonstrates that temperature variations have a more pronounced impact on the fractional abundances than changes in electron density.

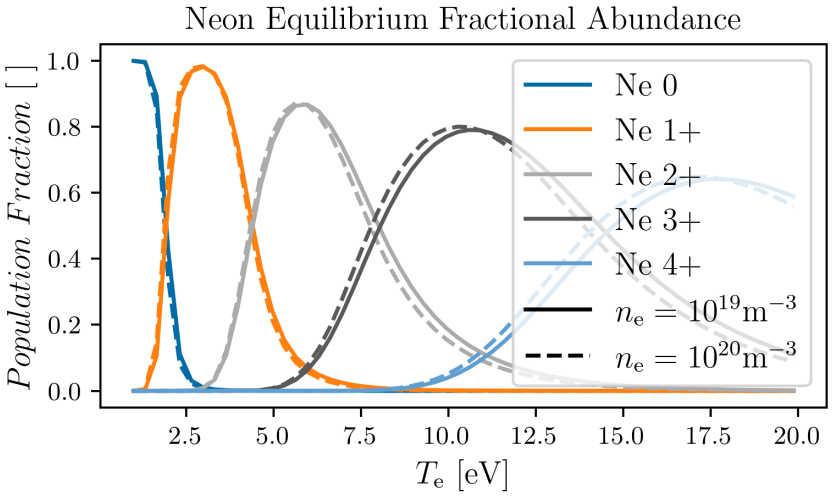

Figure 3.2: The figure illustrates the development of the equilibrium ionisation balance for the first five ionisation stages of neon as a function of electron temperature. Full lines in the graph represent the balance at an electron density of $n_e = 1 \times 10^{19}\,\mathrm{m}^{-3}$, while the dashed lines correspond to an electron density of $n_e = 1 \times 10^{20}\,\mathrm{m}^{-3}$. This visualization clearly indicates that the variations in the ionisation balance profile are predominantly influenced by temperature changes rather than by electron density. To improve graphical clarity, the impact of charge exchange with neutral hydrogen is not included in this plot.

The evolution of emissivity, denoted as $\varepsilon_{j\to k}$, from (3.1) is influenced by both the PEC coefficients and the ionization stage densities $N^{(z)}$. In an equilibrium state, a spectral line is emitted within the electron temperature range where the ionization stage z is prevalent.

In practical scenarios, observed spectral lines are not perfectly narrow. They experience broadening due to various physical phenomena, which are contingent on plasma conditions, electromagnetic fields, and other factors, such as viewing geometry. Within the framework of Cherab, the spectrum of a local contribution to the overall observed radiation can be approximated as:

$$S(\boldsymbol{r}, \boldsymbol{d}, \lambda) = \varepsilon_{j\to k}(\boldsymbol{r}) L(\lambda, \boldsymbol{r}, \boldsymbol{d}, P, \boldsymbol{E}, \boldsymbol{B}) \tag{3.5}$$

In this equation, $S(\boldsymbol{r}, \boldsymbol{d}, \lambda)$ represents the spectral radiance in units of $\mathrm{W}nm^{-1}sr^{-1}$ for a specific position $\boldsymbol{r}$, direction $\boldsymbol{d}$, and wavelength λ. The local photon emissivity, $\varepsilon_{j\to k}$, is quantified in W. Here, P symbolizes plasma properties such as electron temperature and density distributions, while $\boldsymbol{E}$ and $\boldsymbol{B}$ denote the three-dimensional electric and magnetic fields, respectively. The function L characterizes the local spectral shape and accounts for any anisotropies in radiation.

In this study, two primary spectral line shapes are considered: temperature broadening and Stark broadening. Temperature broadening imparts a Gaussian shape to spectral lines, with the width dependent on ion temperature and the shift on the mean ion velocity. Stark broadening arises from the interaction between the radiating atom and surrounding electrons, as detailed in [60]. Currently, Cherab does not support the combination of multiple line shapes, necessitating the specification of the predominant one.

The ADF11 format provides several types of datasets, notably the radiated power coefficients, which are instrumental for forward modeling in diagnostic ap-

plications spanning wide wavelength ranges, such as bolometry. These coefficients include:

PLT - Radiated power due to excitation.

PRB - Continuum and line power from recombination and Bremsstrahlung.

PLS - Line power for specific transitions.

PRC - Line power driven by charge exchange with thermal neutral hydrogen.

Figure Fig. 3.3 illustrates the radiated power coefficients for the first five ionisation stages of neon. It is evident from the figure that line radiation is the predominant contributor to the total radiated power within the plotted electron temperature (T_e) range. The significance of each ionisation stage's contribution to the radiated power changes as the electron temperature increases. This variation is influenced by the rate of excitation of the stages and the escalation in photon energy accompanying an increase in charge.

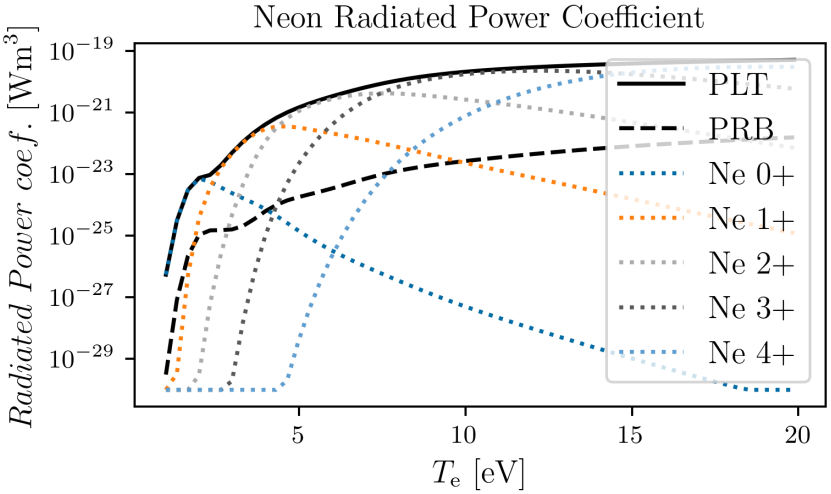

Figure 3.3: The figure depicts the variation of neon's radiated power coefficients as a function of temperature. In this visual representation, the solid black line illustrates the line radiated power coefficient, denoted as PLT, while the dashed black line represents the recombination and Bremsstrahlung coefficient, PRB. Additionally, the dotted lines trace the evolution of the total radiated power contributed by the first five ionization stages of neon.

3.2 SOLPS Simulation Data

The results of SOLPS simulation used in this thesis were provided to the author in the frame of WPTE. More information about the SOLPS simulations of JET seeded discharges is given in [61]. The simulation grid plotted in Fig. 3.4 shows the domain covered by the fluid simulation performed within SOLPS. The fluid simulation doesn't extend to the plasma facing components except in the region of the vertical divertor plates and divertor baffle as displayed in Fig. 3.5.

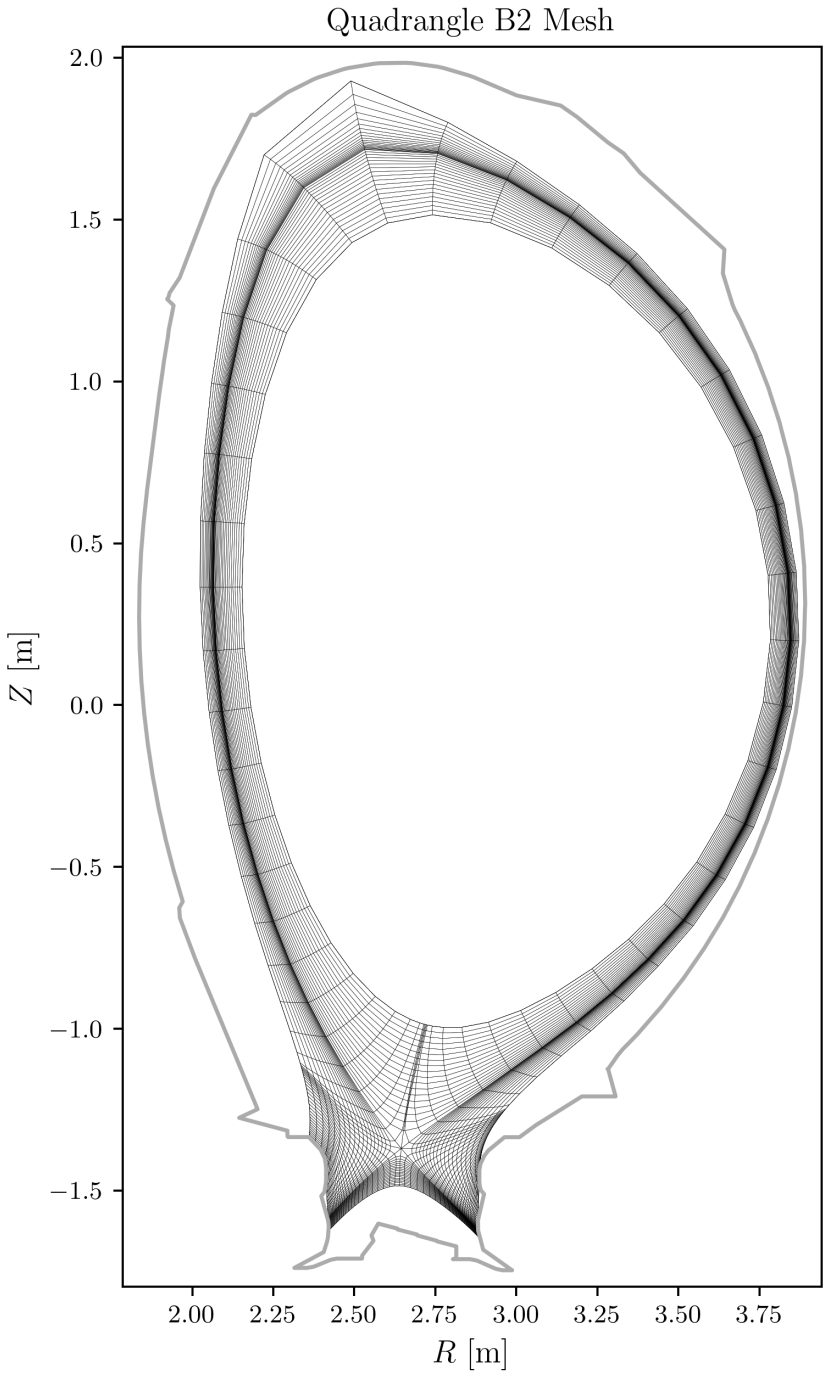

Figure 3.4: Simulation mesh of the B2 code with contour of JET's first wall contour. B2 code performs fluid simulations and is integral part of SOLPS.

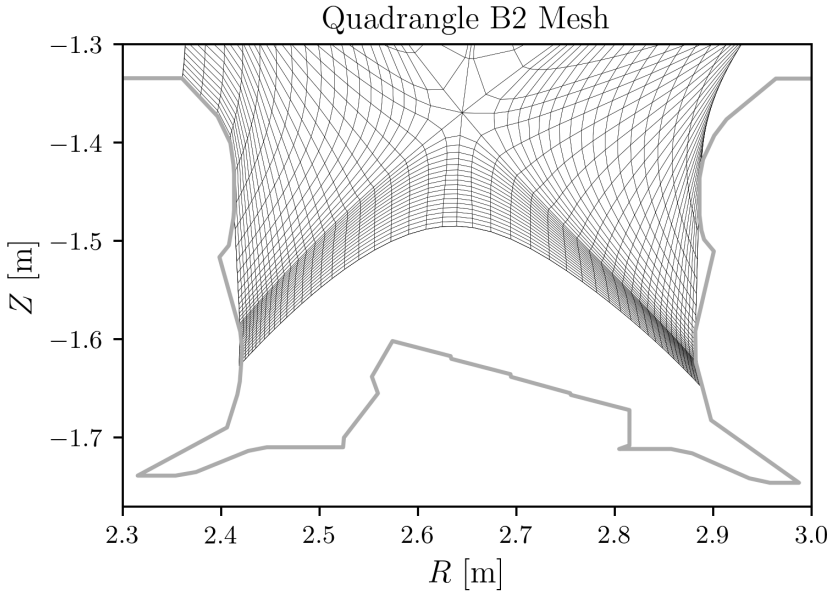

Figure 3.5: Divertor detail of B2 simulation mesh with contour of JET's first wall.

3.3 Cherab Model of Mirror-link Divertor Spectroscopy (KT3)

This chapter details the modeling of the KT3 diagnostic which was implemented in Cherab. The primary motivation for developing this model was to establish forward algorithms capable of deducing the concentration of seeded neon impurities from KT3 experimental spectra, thereby assisting in the validation of SOLPS simulation results which were provided to the author in the frame of WPTE (Work Package Tokamak Exploitation) collaboration. The model's description encompasses the implications of various input parameters, such as sightline definitions, on the realization of KT3 in Cherab. The section also addresses the simplifications made in the KT3 model and the fidelity of the generated output spectra. The radiation models employed to simulate the forward models of KT3 spectra are also discussed. Subsequently, synthetic spectra based on SOLPS simulations are compared with experimental data.

Mirror-link Divertor Spectroscopy, a system originally designed for CXRS measurements [62], offers vertical observation of the JET divertor. Despite its initial design, its vertical sight lines also cover the divertor region and intersect the magnetic legs at angles close to 90 degrees. This coverage provides valuable insights into local plasma processes, aiding in the derivation of critical plasma quantities. Consequently, the collecting optics of KT3 were upgraded to enhance divertor coverage [63]. The diagnostic data are now routinely utilized to investigate divertor plasma properties, such as electron temperature and density [60]. The diagnostic includes multiple spectroscopic instruments that cover different spectral bands. Specifically, for the purpose of this thesis, KT3A and KT3B spectrometers were employed, covering spectral bands approximately between 360 nm and 420 nm. This range encompasses some Balmer series spectral lines (refer to [60]) and multiplets of low ionization stages of neon and nitrogen. Forward models of these spectral lines are used to validate SOLPS simulation results [3] and to infer the

concentrations of neon and nitrogen [64].

3.3.1 Diagnostic

The light emanating from the divertor region is captured by a lens located in the upper vertical port (*Oct8-uvimp-b*) and is then directed onto the spectrometers in the diagnostic room using a series of mirrors and lenses. The total length of this optical path, extending from the divertor to the spectrometers, is approximately 30 meters. This optical link enables the system to conduct spectral measurements spanning a wide range, from near-ultraviolet ($300 - 450\,\mathrm{nm}$) to the NIR (near-infrared) region ($750 - 1200\,\mathrm{nm}$) [63]. The FOV (field of view) of this setup encompasses a radial span of 360 mm on the divertor plates. Notably, the FOV undergoes radial shifts during a discharge due to the movement of a mirror, which is influenced by the magnetic force generated by one of JET's power coils. Of all the spectroscopic instruments that utilize the KT3's optical path, only the KT3A and KT3B spectrometers have been modeled and employed in this study because of their favorable spectral band covering neon and nitrogen line radiation from divertor.

3.3.2 KT3A and KT3B Diagnostic Models

Developing a diagnostic model using Raysect involves accurately replicating the characteristics of the optics and detectors within the system. The attainable level of precision in this modeling is constrained by the availability and the quality of the diagnostic's descriptive data. The requirements for the model and the information available dictate the necessary simplifications and dictate how the model can be constructed utilizing Raysect's features. This section describes the available information and the subsequent procedures, solutions and simplifications applied in the frame of this work in order to deliver the diagnostic model. Specifically for KT3A and KT3B, the information routinely accessible from JPF (JET Pulse File) and PPF (Post Processed File) files includes the default radial positions of the sight lines ($\mathbf{r}_{\mathrm{ch}}$) on *tile*5 (tile type in the divertor of JET, see Fig. 3.7), the common origin of the sight lines $\boldsymbol{r}_o$ (cross in Fig. 3.6), and the time-dependent shift R_{corr} in the spot's radial position during each JET pulse.

In the model, the first key simplification is the approximation of each spectrometer channel's FOV as a cone. This approach enables an accurate enough representation and facilitates the use of Raysect's *FibreOptic Observer*, which is well-suited for sampling over a conical FOV. Another crucial aspect is the precise alignment of the *Observer*s, ensuring the FOV of these observers matches the volumes from which the KT3A and KT3B channels collect radiation.

Since the available data in the JPF files are provided in cylindrical coordinates, the alignment process initially takes place within this coordinate system. It is then transformed into JET's three-dimensional Cartesian coordinate system. This transformation involves rotating the poloidal plane to correctly position the observers above the diagnostic port. The position $\boldsymbol{r}_o$ (sourced from JPF) is assumed to be a common origin for all FOVs, this meaning that the apexes of the conical FOVs are located at $\boldsymbol{r}_o$. In Fig. 3.6 the point $\boldsymbol{r}_o$ is plotted with the cross and dashed lines mark the axes of the FOVs.

The orientation of each *Observer* is determined by the point $\boldsymbol{r}_o$ and the respective spot positions $\boldsymbol{r}_{ch}$. These spot positions represent the intersections of the KT3 sight lines with the *tile*5 plane, as illustrated in Fig. 3.7. The positions $\boldsymbol{r}_{ch}$ can be calculated as follows:

$$\boldsymbol{r}_{ch} = (R_{ref} + R_{corr}, A_{t5} + \Delta_{t5}(R_{ref} + R_{corr})). \tag{3.6}$$

To determine the (R, Z) coordinates of $\boldsymbol{r}_{ch}$, the reference spot position (R_{ref}, Z_{ref}), available from JPFs, and a radial correction R_{corr} (as provided in A Meigs' JPFs) are utilized. The R_{corr} accounts for the spot displacement relative to the reference position, a consequence of the mirror's movement induced by the current in one of the JET's power coils. The Z component of $\boldsymbol{r}_{ch}$ is computed using the R component and a straight line equation, where the vertical offset A_{t5} and slope Δ_{t5} of *tile*5 are derived from the reference spot positions (R_{ref}, Z_{ref}).

As previously mentioned, knowing the coordinates of $\boldsymbol{r}_o$ and $\boldsymbol{r}_{ch}$ is crucial not only for orienting the *Observer*s correctly but also for calculating their vertex angle α_{ch}. This calculation is based on the assumption that the conical FOVs of adjacent channels are tangent. The vertex angle is determined using the following equations:

$$w_{ch} = \frac{|\boldsymbol{r}_{ch-1} - \boldsymbol{r}_{ch+1}|}{4}, \alpha_{ch} = \frac{|\boldsymbol{r}_{ch} - \boldsymbol{r}_o|}{w_{ch}}. \tag{3.7}$$

Here, w_{ch} represents half the distance between the adjacent spots, and α_{ch} is the tangent inverse of the ratio of the distance from the *Observer*s to the channel and w_{ch}.

Furthermore, the fibre radius rad_{ch} for the *FibreOptic Observer*s has to be greater than zero. To achieve this, the *Observer*s are shifted along their observation direction to a new position, $\widetilde{\mathbf{v}}_o$. This shift and the radius are defined as:

$$\widetilde{\mathbf{v}}_o = \boldsymbol{r}_o + \Delta(\boldsymbol{r}_{ch} - \boldsymbol{r}_o), rad_{ch} = \Delta(\boldsymbol{r}_{ch} - \boldsymbol{r}_o)\tan(\alpha_{ch}). \tag{3.8}$$

In this equation, Δ is a small number (1 mm) that adjusts the position and radius of the fibre based on the calculated vertex angles and distances.

To correctly position the *FibreOptic Observer*s in the toroidal direction, aligning them above the *Oct8-uvimp-b* port, the poloidal plane was rotated by $-56.25°$ along the Z-axis. This rotation ensures that the *Observer*s are placed within the correct Cartesian coordinates.

During the testing phase of the diagnostic model, an issue was identified: when the radial position of the spots, calculated as $R_{ref} + R_{corr}$ exceeded 2.512 m, part of the inboard channel became obstructed by the vessel structure. Interestingly, this obstruction was not observed during the experimental operation of KT3. The discrepancy in the KT3 model may arise from the fact that the displacement of the spots, was achieved by shifting the spot position only. In practice, however, the movement of the mirror could also cause a displacement of the common origin point (mirror rotation), $\boldsymbol{r}_o$, in the outward direction which would also move the FOVs outwards and remove the blocking. To prevent any blockage of the inboard channel in the model, the position $\boldsymbol{r}_{ch}$ is adjusted outwards. This adjustment ensures that the inboard edge of the innermost FOV just clears the edge of the obstructing structure, which is estimated to be located at the position $(R, Z) = (3.051, 2.008)$ m.

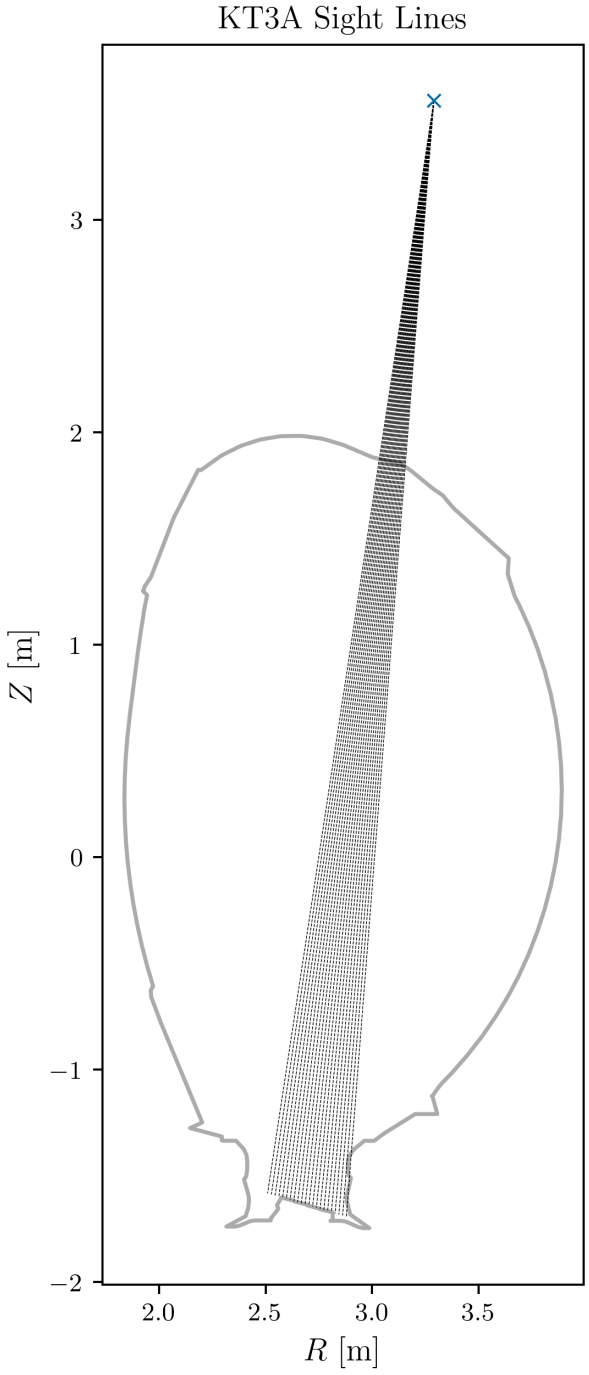

Figure 3.6: The visualization showcases all 22 KT3A sight lines during JET pulse number 97482 at the timestamp of 50.0 seconds. These sight lines are depicted as black dashed lines against the backdrop of JET's inner wall contour, which is highlighted in grey. All sight lines originate from a common point, denoted as $\boldsymbol{r}_o$, represented in the figure by a cross. These sight lines serve as the axes for the conical FOVs that are modelled using *FibreOptic* observers.

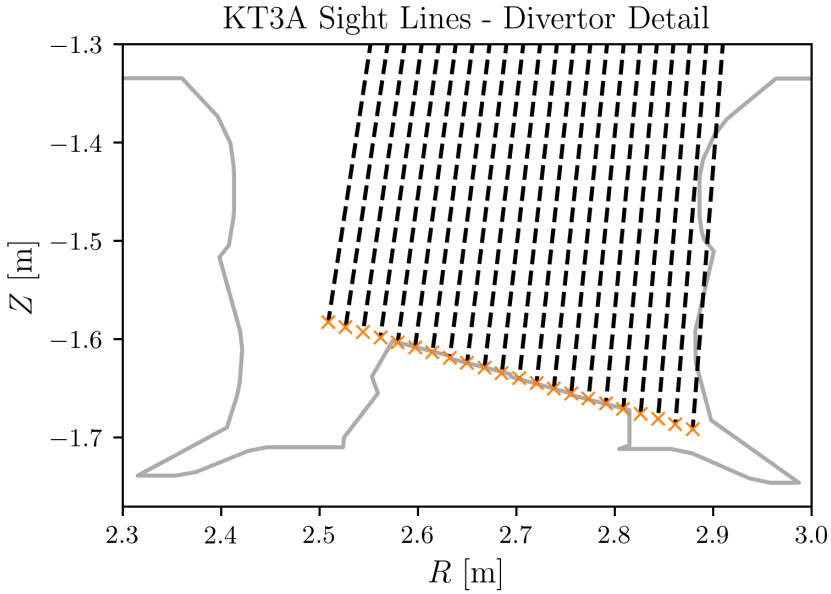

Figure 3.7: The KT3A sight lines for JET pulse number 97482 at 50.0 seconds are shown as black dashed lines, with JET's inner wall contour highlighted in grey. Crosses indicate the corrected spot center positions $\boldsymbol{r}_{ch}$ on the *tile*5 plane.

The list of relevant neon seeded pulses and their respective time ranges is detailed in Tab. 3.1. While ideally all KT3A sight line shifts would be incorporated in the validation of SOLPS simulations and the development of backward models, this approach is computationally demanding and complex. To reduce both computational load and complexity, the average sight line shift for each JPN and the specified time ranges was used instead. The maximum deviation between these average positions and the actual experimental positions was less than 4mm, remaining within 30% of the radial resolution, thus deemed acceptable for the study's purposes. In the Tab. 3.2 the applied positions of the sight lines $\boldsymbol{r}_{ch}$ on *tile*5 with the channel numbers are listed for later convenience.

JPN (Jet Pulse Number)	**Pulse Time Range (s)**	**Average Neon Seeding Rate [particle/s]**
97492	[52.5317, 55.1740]	7.0×10^{20}
96133	[53.3651, 55.2221]	8.7×10^{20}
97482	[51.4471, 53.0281]	1.6×10^{21}
96915	[54.2666, 55.7237]	1.9×10^{21}
97484	[51.9426, 54.4940]	2.2×10^{21}
97490	[52.4776, 55.1921]	2.7×10^{21}

Table 3.1: The table provides a list of neon-seeded discharges along with their corresponding time ranges of interest and average neon seeding rates.

Channel	R [m]	Z [m]	Channel	R [m]	Z [m]
1	2.509	-1.582	12	2.702	-1.639
2	2.526	-1.588	13	2.720	-1.645
3	2.544	-1.593	14	2.738	-1.650
4	2.561	-1.598	15	2.755	-1.655
5	2.579	-1.603	16	2.773	-1.660
6	2.597	-1.608	17	2.790	-1.665
7	2.614	-1.613	18	2.808	-1.671
8	2.632	-1.619	19	2.826	-1.676
9	2.650	-1.624	20	2.843	-1.681
10	2.667	-1.629	21	2.861	-1.686
11	2.685	-1.634	22	2.879	-1.691

Table 3.2: The table shows average KT3A sight line center positions at *tile*5 in cylindrical coordinates, based on data from Tab. 3.1.

3.3.3 KT3A Neon Seeding Emission Models

A crucial aspect of forward modeling the KT3A spectra with Cherab is the implementation of emission plasma models. In the context of neon-seeded experiments and KT3A, two primary categories of radiation models were employed.

The first model is the Bremsstrahlung model, which simulates free-free radiation. It considers the ion species populations in the plasma and the electron distribution function.

The second model category involves spectral line radiation, resulting from the radiative decay of electrons excited in atomic orbitals. This model requires specifying several parameters: ion species, ion charge, transition (which defines the rest wavelength), and line shape. Typically, information about the ion species, charge, and transition is obtained from the atomic database OPEN-ADAS.

The line shape parameter, essential for spectral line broadening, must accurately reflect the key physical phenomena influencing the anticipated experimental shape. In simulations involving KT3A and neon-seeded discharges, both deuterium and neon lines were modeled. The deuterium lines, part of the Balmer series, utilized Stark pressure broadening to define their line shape. In contrast, the neon line simulations focused on two spectral multiplets, with temperature broadening determining their line shape.

Stuart Henderson provided the atomic data for these neon lines in the form of ADAS PEC files. He also derived the ratios of the multiplet lines based on experimental observations. For a comprehensive overview of the models used, refer to the accompanying table Tab. 3.3.

3.3.4 Forward Models of KT3A Spectra

The model for the KT3 diagnostic, developed using Cherab, was employed to generate forward models of spectra. These were based on plasma profiles from SOLPS simulations and the emission models previously described. An example of the modelled spectrum can be seen in Fig. 3.8. These spectra provide detailed information, capturing local intensity and line shape data, which are essential for

Species	**Transition**	**Label**	**Line Shape**	**Wavelength (nm)**	**Line Ratio**
Ne–II	2s2 2p4 3p1 4p5.5 – 2s2 2p4 3s1 4p5.5	Ne_{369}	thermal	366.41, 369.42, 370.96, 373.49, 375.12, 376.63, 377.71	0.43, 1.0, 0.29, 0.12, 0.04, 0.26, 0.24
Ne–II	2s2 2p4 3p1 2d4.5 – 2s2 2p4 3s1 2p2.5	Ne_{371}	thermal	364.39, 371.31, 372.71	0.12, 1.0, 0.419
D–I	7 – 2	D_{ε}	Stark	396.9	
D–I	8 – 2	D_{ζ}	Stark	388.8	
D–I	9 – 2	D_{η}	Stark	383.4	

Table 3.3: The KT3A radiation models table details spectral lines and multiplets and their assigned line shapes. Line ratios indicate each line's relative intensity in the multiplet. Thermal line shapes are Gaussian, while Stark line shapes are Lorentzian. The labels column introduces symbols used in the text to refer to the lines.

validating the plasma simulations and for developing backward models, such as those used to estimate impurity concentrations.

Utilising forward models in the construction of backward models offers significant advantages, because the plasma state sought by the backward model is known. This methodology significantly enhances the precision, accuracy, and validation of the results. Moreover, forward modelling facilitates the segregation of different phenomena impacting the data into individual simulations. Specifically, in the case of KT3A, this means simulating the emission models separately, as shown in Fig. 3.8. The complete spectrum is then compiled from these discrete simulations. This isolation of models simplifies some post-processing analyses, like the determination of spectral line intensity, which can be efficiently achieved through the direct integration of a spectrum.

It's important to note that Raysect outputs spectra as radiation incident on the observer, excluding instrumental effects. However, Fig. 3.9 displays the complete spectrum with instrument-broadened spectral lines. This was accomplished by convolving the forward model of spectra with the instrumental function of KT3A, derived from fitting a Gaussian line to an experimentally measured neon line.

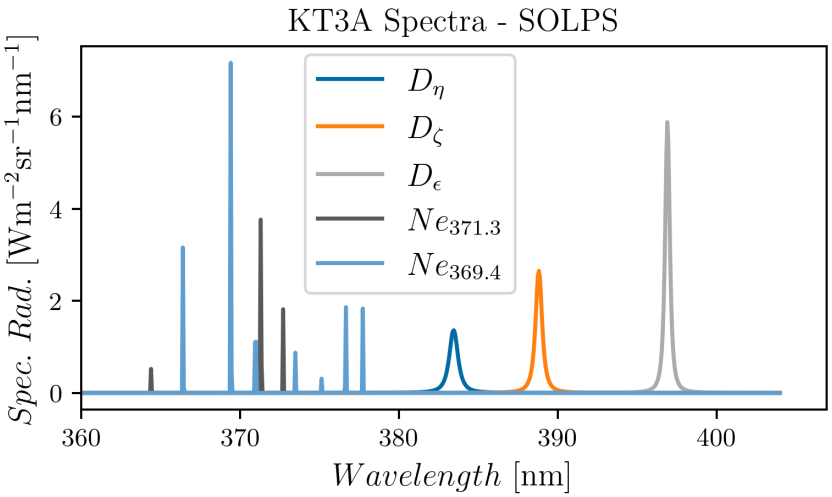

Figure 3.8: The figure contains a forward model of the KT3A spectrum, which was obtained using the KT3A model together with SOLPS simulations. The broadening of the deuterium Balmer line series is due to pressure (Stark) broadening, while the narrow appearance of the neon lines results from the low ion temperature, causing reduced thermal broadening.

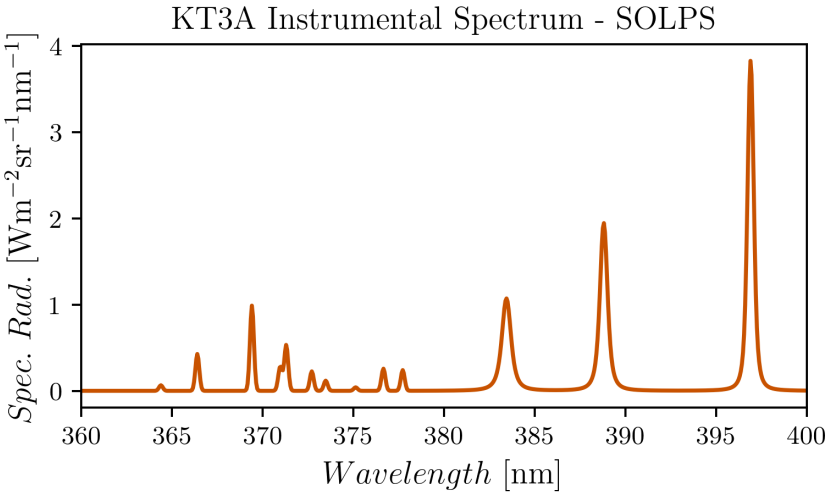

Figure 3.9: Spectra generated through Raysect and Cherab simulations were convolved with the instrumental function of KT3A. This instrumental function was determined by fitting a Gaussian profile to a neon spectral line, which was obtained experimentally.

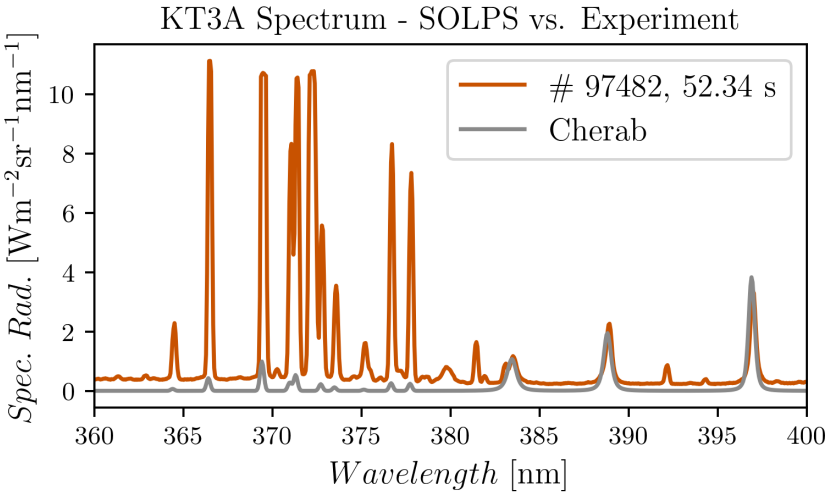

Figure 3.10: The comparison involves the KT3A spectrum observed during a JET pulse 97482 at 52.34 s, and the spectrum forward modelled using Cherab.

The visual comparison between the experimental and Cherab forward modelled spectra in Fig. 3.10 reveals a relatively good match in the line shape and intensity of the Balmer lines, contrasted with notable discrepancies in the intensities of the neon impurity multiplets. This indicates that certain aspects of the SOLPS simulation results may closely resemble the actual plasma state during the experiment. The agreement in the broadening of the Balmer lines appears to be a reliable method for validation, as will be discussed subsequently. However, direct comparison of line intensities should be approached with caution.

The observed intensity discrepancies can be attributed, in part, to differences in sight line FOV. For instance, a smaller FOV volume in the simulation could result in lower intensity, despite accurate plasma profiles. Additionally, reflections from first wall surfaces, which are typically challenging to simulate, can enhance line intensity in experimentally obtained spectra. A large part of the discrepancy can be also carried by the quality of agreement of the SOLPS simulation and the state of the plasma in the experiment. A more robust approach for validation could be the comparison of line intensity ratios. As outlined in Sec. 3.1, these ratios convey information about T_e and n_e, offering a more reliable insight into plasma characteristics.

3.4 Backward Model Validation Methodology

Accurately constructed forward models are instrumental for the development of backward models. Unlike experimentally acquired data where the actual plasma state is unknown, forward models produce data from a well-defined input plasma state. In the context of this work, the plasma state was derived from SOLPS simulations, which characterize plasma within a two-dimensional domain that includes SOL (Scrape Off Layer), PFR (Private Flux region), and extends into part of the confined region's edge. An example of the SOLPS grid is shown in Fig. 3.4. In spectroscopic diagnostic models such as KT3, it is common for the data from forward models to be influenced by several cells.

When assessing the accuracy of a backward model, it's essential to compare

the inferred values of physics quantities with those in the contributing cells, while also factoring in the contribution weight of each cell. This section details the methodology established to address this specific validation challenge. To aid in this explanation, an example will be provided, focusing on electron density as the plasma quantity and the Balmer lines simulated by KT3A as the diagnostic data. This is a step akin to the validation of the method presented in [60].

Contribution weight $W_{i,ch}$ of cell i to a diagnostic channel ch can be expressed as:

$$W_{i,ch} = \frac{C_{i,ch} P_i}{\sum_i C_{i,ch} P_i}. \tag{3.9}$$

The term $C_{i,ch}$ is the cell contribution factor (see Sec. 3.4.1), also known as the sensitivity factor, for cell i in relation to channel ch. This factor determines how much the cell contributes to the diagnostic channel. The P_i denotes the radiation factor (see Sec. 3.4.2), which is essentially the radiated power intensity of the phenomenon utilized in the backward model. The denominator, $\sum_i C_{i,ch} P_i$, is the summation of the product of the cell contribution factor and the radiation factor for all cells contributing to the diagnostic channel. This summation ensures that the contribution weight $W_{i,ch}$ is normalized, allowing for an accurate representation of each cell's relative contribution to the channel.

3.4.1 Contribution Factor $C_{i,ch}$

The contribution factor $C_{i,ch}$[1], crucial for calculating the contribution weight of each cell in a diagnostic model, is influenced by the properties of the cell as size and shape and its position with respect to the FOV of the diagnostic channel. It can be conceptualized as the volume of a cell that is observed by a diagnostic channel, adjusted for the distance to the observer. Consequently, each diagnostic channel ch has a unique $C_{i,ch}$ value for a given cell i.

Cherab provides a method to compute these contribution factors for cells within the SOLPS mesh. This is achieved using Cherab's *ToroidalVoxelGrid* class and its associated functionalities, which were available in Cherab prior to this work. An example of these contribution factors is depicted in Fig. 3.11, highlighting $C_{i,ch}$ for channels 10 and 18. Through ray tracing, Cherab is able to approximate the values of $C_{i,ch}$ in a fully three-dimensional geometry. The figure illustrates that despite the complexity of the SOLPS mesh, ray tracing can accurately estimate the contribution factors $C_{i,ch}$.

It should be noted, however, that the results do not account for reflections from the first wall, which could further complicate the distribution of $C_{i,ch}$. These reflections, if included, would likely affect the intensity and distribution of radiation observed, thus altering the contribution factors.

[1] In tomographic reconstructions, C is sometimes referred to as the contribution or sensitivity matrix.

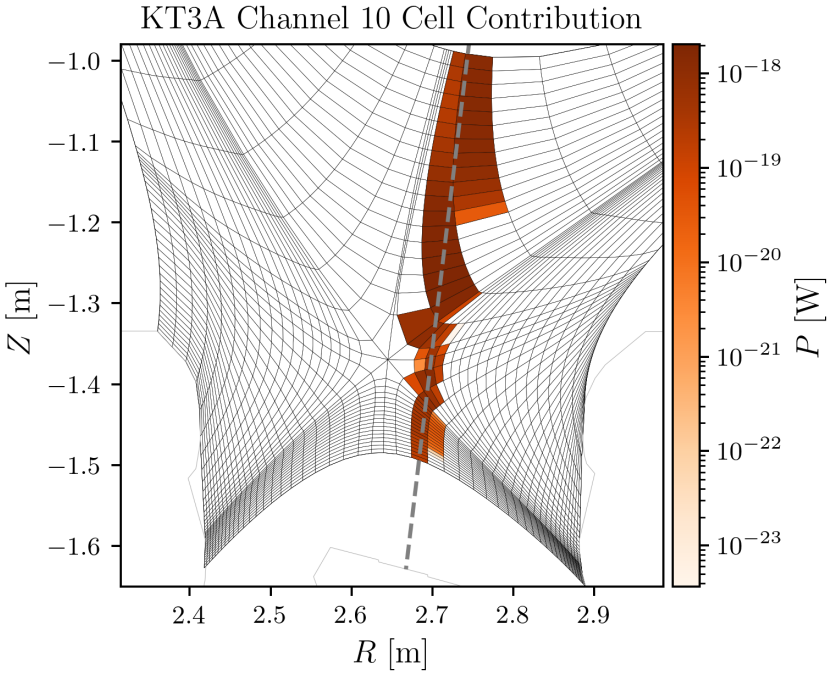

(a)

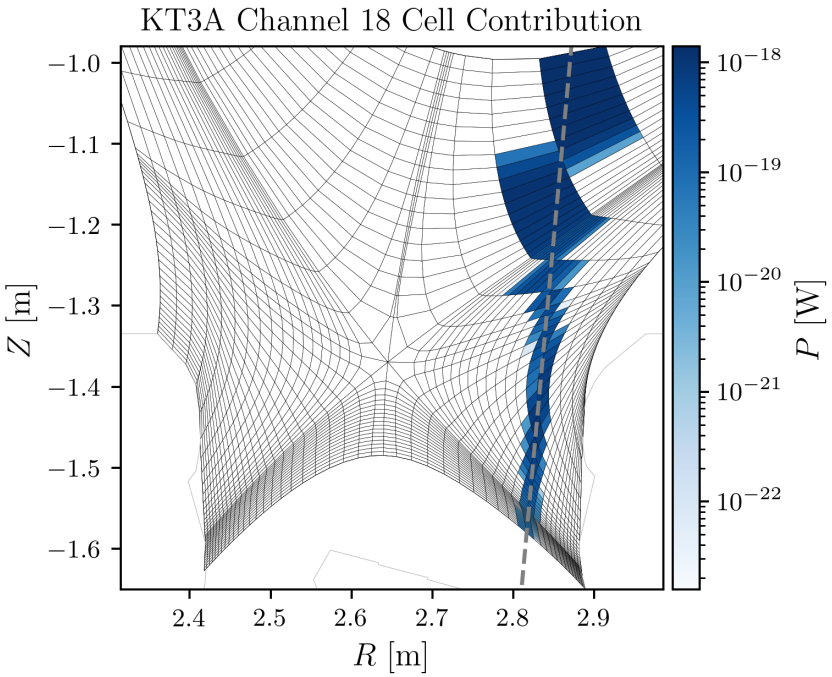

(b)

Figure 3.11: The figures display the contribution factors $C_{i,ch}$ of SOLPS mesh cells to the KT3A channels 10 (top panel) and 18 (bottom panel), with dashed grey lines indicating the center of the diagnostic channel field of views.

3.4.2 Radiation Factor P_i

In employing a forward model to ascertain a plasma quantity Q (as for example n_e) from a spectral feature, such as a spectral line, the influence of a SOLPS cell on Q should be proportional to the radiated power of that spectral feature. This

radiated power can generally be computed for various spectral phenomena using the methodologies described in Sec. 3.1.

The radiation factor P_i (the radiated power) for SOLPS cells for the D_ε, D_ζ, and D_η deuterium spectral lines is depicted in Fig. 3.12. These values were calculated utilizing Cherab and OPEN-ADAS, with inputs of plasma electron density, electron temperature, and ion density sourced from the SOLPS simulations. The resulting distribution highlights that the radiation predominantly emanates from areas proximate to strike points, vertical divertor plates, magnetic legs, and the PFR.

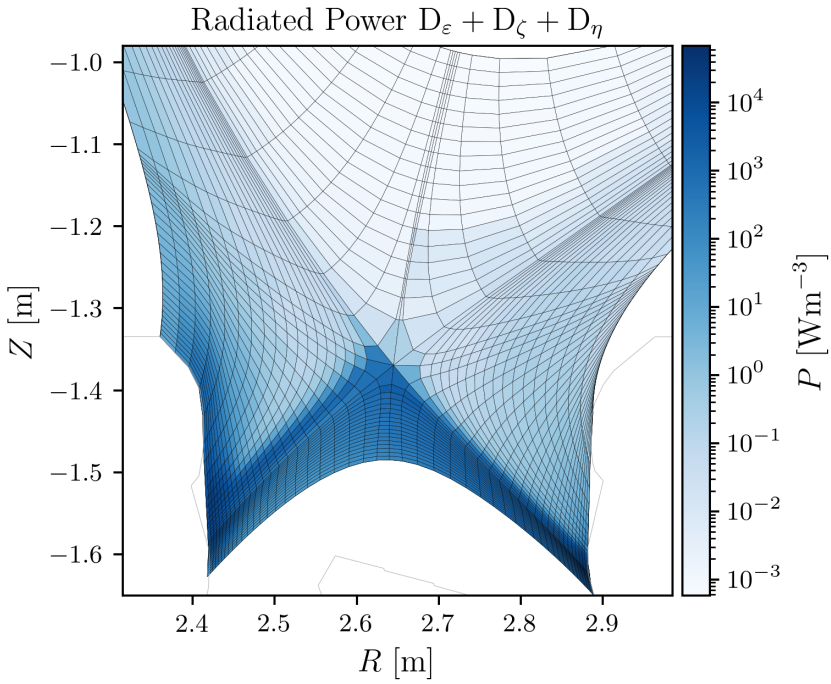

Figure 3.12: The cell shading in the figure illustrates the radiated power from the D_ε, D_ζ, and D_η deuterium spectral lines, as calculated using OPEN-ADAS data derived from SOLPS results. This visualization indicates that the majority of the radiation originates from areas near the strike points, vertical divertor tiles, and the PFR.

3.4.3 Cell Contribution Weights and Weighted Quantity Distributions

The value of $C_{i,ch}P_i$ for each cell i and channel ch reflects the sensitivity to cell radiation as well as the radiated power itself. An example demonstrating the power radiated by D_ε, D_ζ, and D_η, and its relation to KT3A channels 10 and 18 is provided in Fig. 3.13. These examples clearly indicate that any backward model utilizing the spectral lines should account for plasma properties near the magnetic legs, where the contribution weights from the cells are highest.

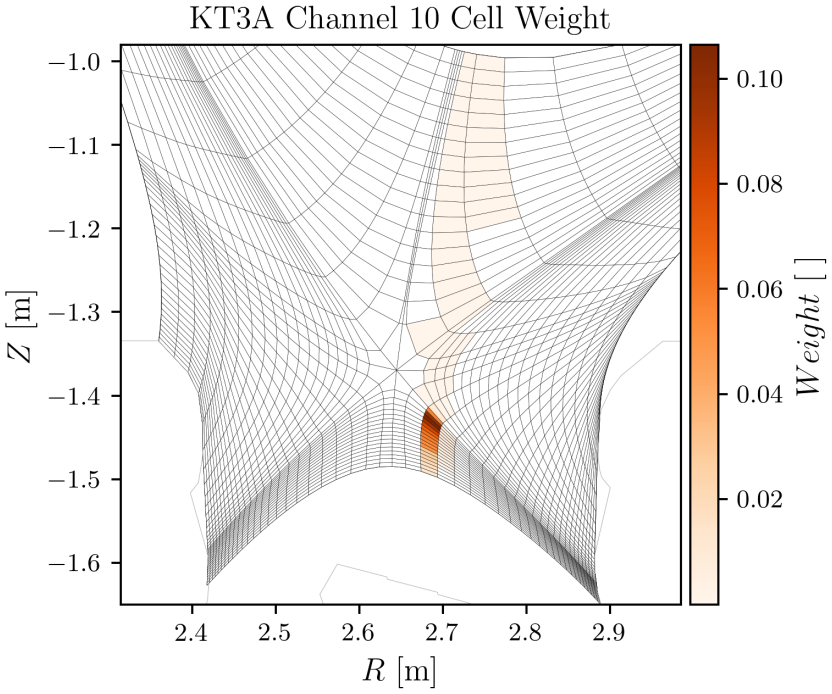

(a)

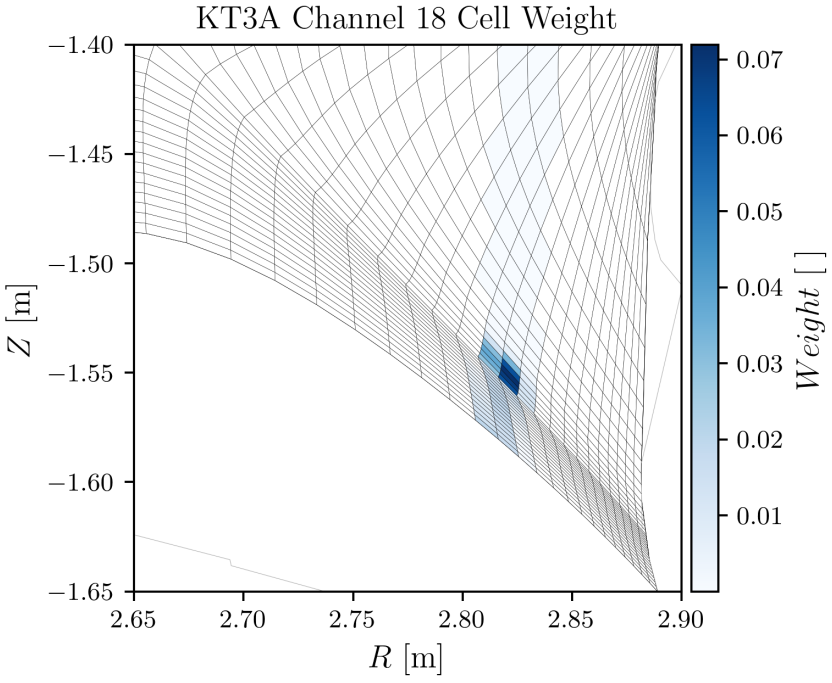

(b)

Figure 3.13: The plots display the cell contribution weights $C_{i,ch}P_i$ for the D_ε, D_ζ, and D_η spectral lines in relation to KT3A channels 10 and 18.

To demonstrate the use of cell contribution weights, an example is provided focusing on the validation of electron density (n_e) inference from Balmer spectral line shapes. The spatial distribution of n_e taken from the SOLPS results is displayed in Fig. 3.14 and the results of the inference are shown in Fig. 3.15. The blue distributions plotted in Fig. 3.15 are derived using the contribution weights $W_{i,ch}$, with the power radiated by the Balmer series lines as P_i, and n_e as the

weighted plasma quantity. Conversely, the distributions in orange represent the results from a backward model of n_e, which is based on the inference from the broadening of the Balmer spectral lines.

In Fig. 3.15a and Fig. 3.15b, these distributions are depicted as 1D histograms for channels 10 and 18, respectively. Fig. 3.15c illustrates the distributions for all channels. The presented distributions provide valuable insights into the accuracy of the backward model, highlighting its strengths and weaknesses, as well as indicating areas for potential improvement.

This approach encourages a deeper engagement with the data and results, allowing for a more comprehensive understanding of the model's performance.

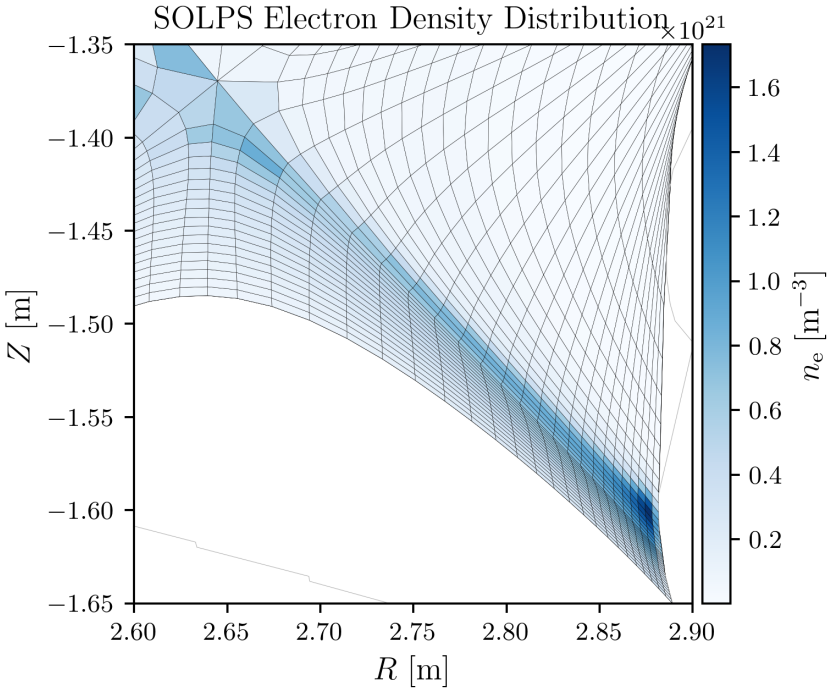

Figure 3.14: Spatial distribution of electron density taken from SOLPS simulations.

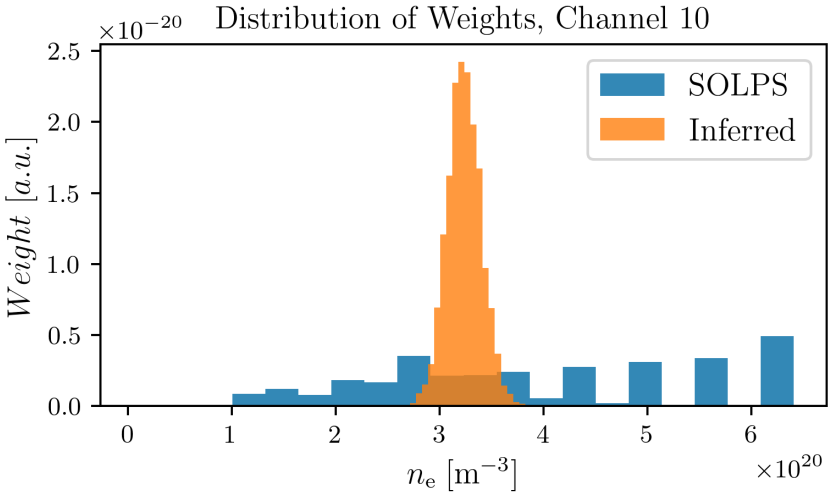

(a)

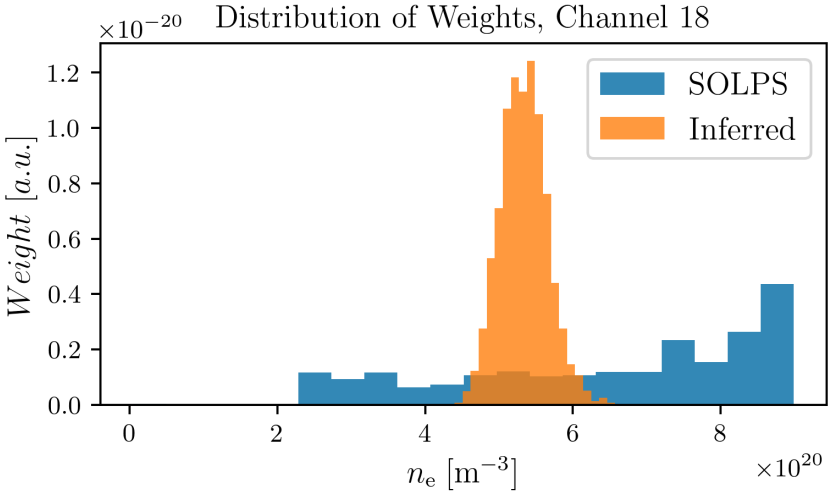

(b)

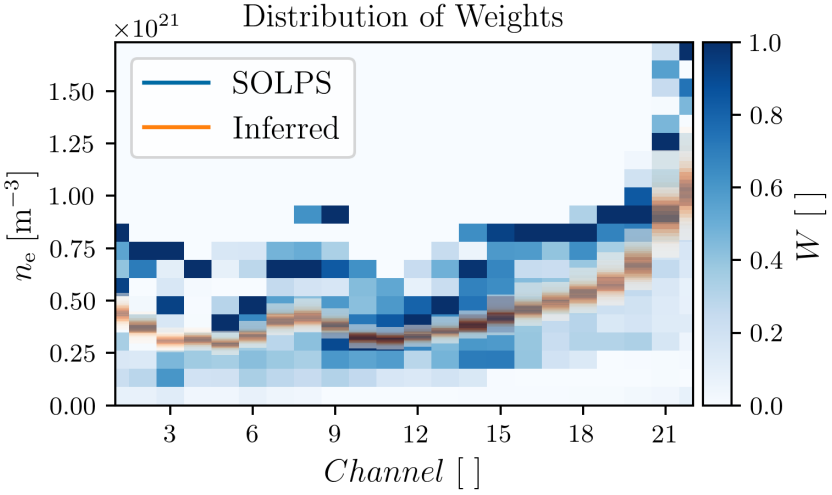

(c)

Figure 3.15: The figures present the weighted distribution $W_{i,ch}$ for determining n_e from SOLPS, with Balmer line radiation as P_i, shown in blue. The posterior distributions of inferred n_e derived from the broadening of Balmer lines are depicted in orange. Figure *a*) and figure *b*) display the 1D distributions for channels 10 and 18, respectively. Figure *c*) illustrates the 2D distribution for all channels.

The methodology described provides an effective tool for evaluating the quality of a backward model by adopting a statistical approach. The contribution weight $W_{i,ch}$ allows the plasma quantity to be viewed as a statistical distribution, which in turn facilitates the assessment of both the precision and accuracy of the backward model.

Furthermore, numerical values for the mean and MAD (Mean Absolute Deviation around the mean) are provided in Tab. 3.4. These values offer a quantitative measure of the central tendency and the variability around the mean, respectively, thereby providing a more detailed and accurate analysis of the model's performance.

Channel	**Mean** $[10^{20}\,\mathrm{m}^{-3}]$	**MAD** $[10^{20}\,\mathrm{m}^{-3}]$
10	3.9	1.4
18	6.4	1.7

Table 3.4: Values of mean and MAD for the channels 10 and 18 for the case of n_e weighted distributions for the case of Balmer lines.

3.5 Neon Divertor Concentration

In order to ascertain the concentration of plasma impurities, a viable approach involves utilising the measured intensity of a specific spectral line, integrated with predictions of the transition's effective emissivity derived from atomic data. This technique has been effectively employed in [64, 55], which focused on ascertaining impurity concentrations within the Asdex Upgrade tokamak. For this concentration analysis, measurements from two distinct neon spectral line multiplets from Tab. 3.3 were utilized. The formula for calculating the impurity concentration is derived from (3.1):

$$\begin{aligned} C_\mathrm{Ne} = \frac{n_\mathrm{Ne}}{n_\mathrm{e}} &= \frac{1}{G}\frac{\varepsilon^\mathrm{exp}_{i\to j}}{{n_\mathrm{e}}^2 PEC^{(\mathrm{eff})}_{i\to j}} \\ &= \frac{1}{G}\frac{\varepsilon^\mathrm{exp}_{i\to j}}{{n_\mathrm{e}}^2\left(f_{Ne1+}PEC^{(\mathrm{exc})}_{i\to j}(n_\mathrm{e},T_\mathrm{e}) + f_{\mathrm{Ne2+}}PEC^{(\mathrm{rec})}_{i\to j}(n_\mathrm{e},T_\mathrm{e})\right)}. \end{aligned} \tag{3.10}$$

The neon concentration, C_Ne, is defined by the ratio of neon density to the electron density n_e. The term $\varepsilon^{(\mathrm{exp})}_{i\to j}$ represents the experimentally measured emissivity for the transition $i \to j$. $PEC^{(\mathrm{eff})}_{i\to j}$, extracted from (3.2), is the effective photon emissivity coefficient for the transition $i \to j$, where ionisation and charge exchange mechanisms are considered negligible. The fractional abundances of singly and doubly ionised neon are represented by $f_{\mathrm{Ne1+}}$ and $f_{\mathrm{Ne2+}}$, respectively, and are not necessarily in equilibrium. The factor G describes the geometrical factor determining the radiation volume, influenced by diagnostic and plasma properties. Analysis of spectral line ratios can also provide viable information:

$$R = \frac{\varepsilon^{(\mathrm{eff})}_{369}}{\varepsilon^{(\mathrm{eff})}_{371}} = \frac{f_{\mathrm{Ne1+}}PEC^{(\mathrm{exc})}_{369}(n_\mathrm{e},T_\mathrm{e}) + f_{\mathrm{Ne2+}}PEC^{(\mathrm{rec})}_{369}(n_\mathrm{e},T_\mathrm{e})}{f_{\mathrm{Ne1+}}PEC^{(\mathrm{exc})}_{371}(n_\mathrm{e},T_\mathrm{e}) + f_{\mathrm{Ne2+}}PEC^{(\mathrm{rec})}_{371}(n_\mathrm{e},T_\mathrm{e})}. \tag{3.11}$$

The ratio R is a function of three key variables: the electron density n_e, the electron temperature T_e, and the ratio of fractional abundances f_{Ne1+} to f_{Ne2+}.

The precision and accuracy of this method, which characterises the observed plasma volume through a single value, are inherently limited by the properties of the plasma volume observed by the diagnostic. Specifically, the accuracy diminishes as the distribution of plasma properties from which the spectral line emanates becomes broader.

Any detailed information about the distribution of plasma parameters in the divertor is unknown. The best available comparison comes from the plasma state predicted by the SOLPS simulation. To exemplify and evaluate the feasibility of the method, the distribution of SOLPS plasma parameters as observed by the KT3A channels was analyzed. The statistical procedure described in Sec. 3.4 was used with radiation factor P_i given by the Ne_{369} line radiated power. The electron density distribution, shown in Fig. 3.16, reveals that channels from 10 up to 16 predominantly exhibit a unimodal distribution, whereas the rest of the channels display a bimodal distribution. For higher channels, the weaker mode's mean value increases to approximately $1.25 \times 10^{21}\,\mathrm{m}^{-3}$, while the stronger mode's mean decreases to about $10^{20}\,\mathrm{m}^{-3}$. The electron temperature distribution, presented in Fig. 3.17, demonstrates a similar bimodal pattern in majority of the diagnostic channels. To examine the effect on the forward models of neon spectral line intensities, the intensity ratios of forward models for Ne_{369} and Ne_{371} lines, calculated using Cherab, was plotted with orange crosses against the weighted distribution in Fig. 3.19. The distribution for channel 18 shown in Fig. 3.18 displays a clear bimodal structure. The difference in location of the modes is ≈ 0.05 which is approximately one third of the observed line ratio value range $(0.25, 0.4)$. In Fig. 3.19 such a bimodal pattern starts to appear in the channel 8 and continues to he HFS channels. Because SOLPS assumes Maxwellian distribution of temperature in its cells, the bimodality seen by the diagnostic channels is caused by each of the modes originating in different location. The intensity ratios of forward models of spectral lines simulated by Cherab (orange crosses) follow the upper mode. The final plot, Fig. 3.20, used to estimate the method's feasibility, displays the weighted concentration distribution. Unlike the previous quantities, this distribution shows a small variation and a bimodal structure for channels up to 5. The figure Fig. 3.20 further shows that the concentration values in a channel vary by up to 0.5%. If the plasma state predicted by SOLPS characterises well the experimental plasma state, then expressing the divertor concentration with a single value per diagnostic channel should be sufficiently accurate. This analysis also showed the advantages of the statistical approach developed in Sec. 3.4 and the amount of information it can provide.

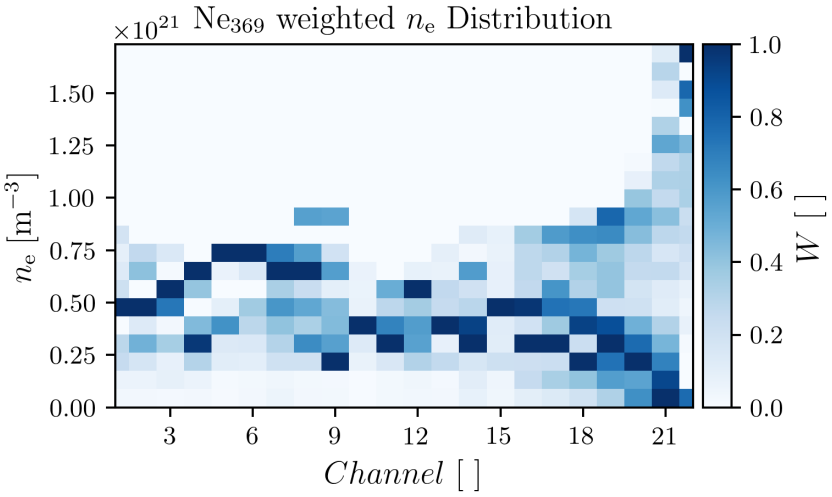

Figure 3.16: The plot shows the Ne_{369} weighted distribution of electron density as seen by the KT3A channels.

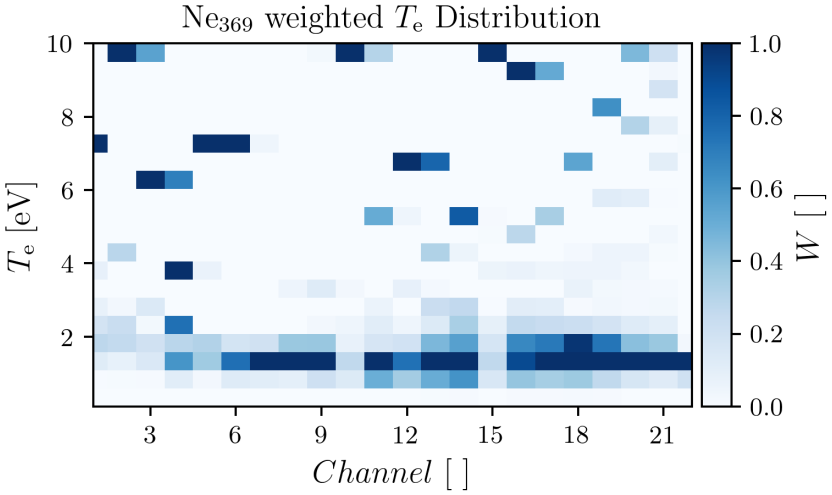

Figure 3.17: The plot shows the Ne_{369} weighted distribution of electron temperature as seen by the KT3A channels.

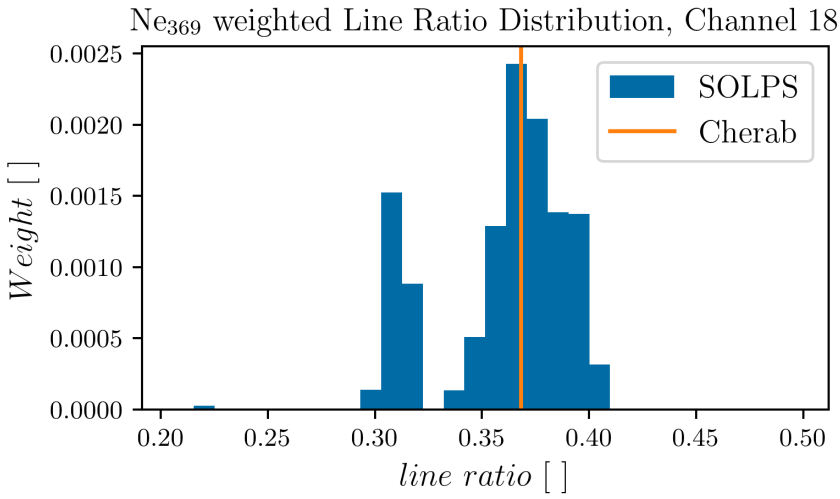

Figure 3.18: The plot shows the Ne_{369} weighted distribution of neon line ratio as seen by the KT3A channel 18. The observed distribution is bimodal with the two modes corresponding to the two different plasma regions.

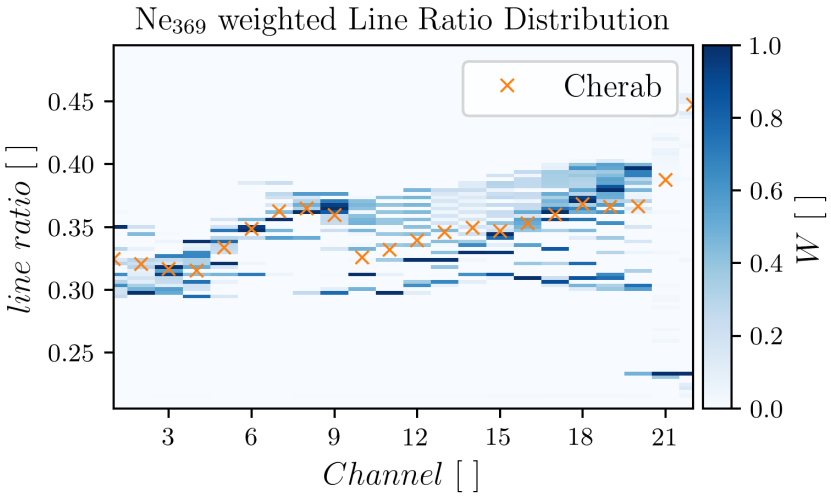

Figure 3.19: The plot shows the Ne_{369} weighted distribution of neon line ratio as seen by the KT3A channels.

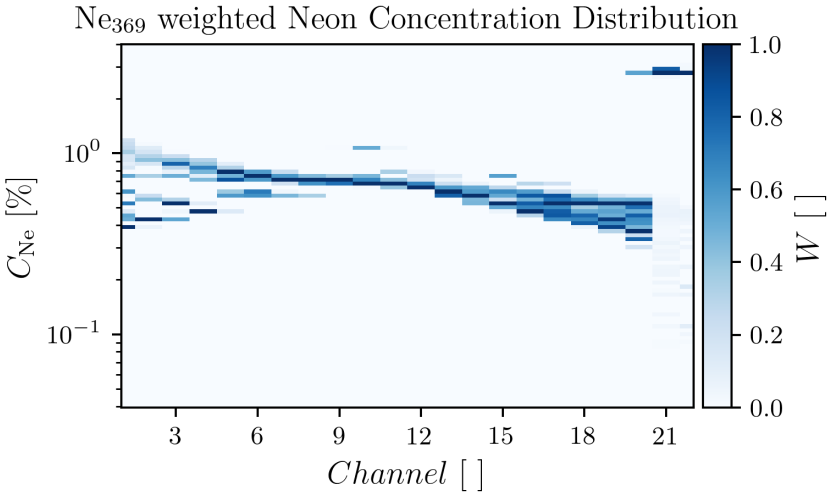

Figure 3.20: The plot shows the Ne_{369} weighted distribution of neon concentration as seen by the KT3A channels.

3.5.1 Zero Transport Model

In the absence of additional data, relying solely on measurements from two spectral lines is insufficient for solving (3.10), which involves four unknown variables: $f_{\mathrm{Ne1+}}$, $f_{\mathrm{Ne2+}}$, n_{e}, and T_{e}. To address this, various levels of simplification can be employed to regularize the solution. The approach used in [64, 55] incorporates an assumption of zero transport. This assumption effectively reduces the number of unknowns to two, as it links the fractional abundances $f_{\mathrm{Ne1+}}$ and $f_{\mathrm{Ne2+}}$ directly to n_{e} and T_{e}.

Fig. 3.21 presents the temperature development of zero transport (or equilibrium) fractional abundance (defined in (3.3)) for the four lowest ionization stages of neon. Notably, the Ne_{1+} and Ne_{2+} stages are the exclusive contributors to the Ne_{369} and Ne_{371} radiation, with their dominance evident in the temperature range of approximately 2 eV to 8 eV. Additionally, Fig. 3.21 reveals the impact of electron density on the fractional abundance. Dashed lines represent calculations for an electron density of $n_{\mathrm{e}} = 1 \times 10^{20} m^{-3}$, while dotted lines correspond to $n_{\mathrm{e}} = 5 \times 10^{21} m^{-3}$. The PEC (defined in (3.2)) for the Ne_{369} spectral line is illustrated in Fig. 3.22. Here, it is observed that the recombination PEC dominates at lower temperatures, being up to eight orders of magnitude stronger. Conversely, the excitation PEC becomes dominant when the electron temperature exceeds approximately 3 eV, increasing in strength by about two orders of magnitude. This suggests that a small quantity of Ne_{2+} ions at low temperatures can have a significant impact on the line intensity due to the prompt recombination of cold electrons. However, under the assumption of zero transport, the ion abundance is determined by the equilibrium balance, which predicts low fractions of such ions at low temperatures. The effective photon emission coefficient, denoted as $\mathrm{PEC}^{\mathrm{eff}}$ (see (3.10)), is the result of combining the abundance profiles from Fig. 3.21 with the PECs from Fig. 3.22. The variation of $\mathrm{PEC}^{\mathrm{eff}}_{369}$ is depicted in Fig. 3.23. In this graph, it is shown that the maximum $\mathrm{PEC}^{\mathrm{eff}}_{369}$ is dependent on electron density, with the values in the presented range peaking between 3 and 4 eV. Notably, the decrease in radiated power from this maximum is primarily a consequence of the

trends in the abundance profiles.

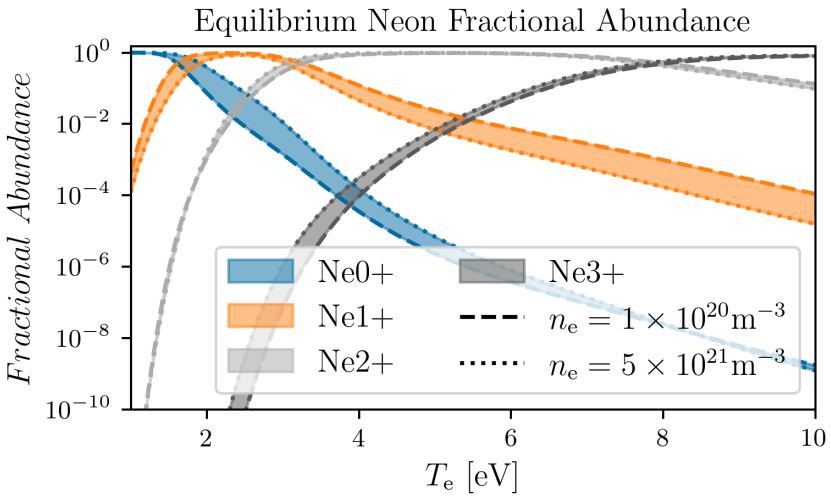

Figure 3.21: The equilibrium fractional abundance for neon is represented in the graph, with the dashed line illustrating the abundances at an electron density of $n_e = 1 \times 10^{20}$ and the dotted line for $n_e = 5 \times 10^{21}$. The filled regions in the graph highlight the variations in abundance attributable to changes in the electron density.

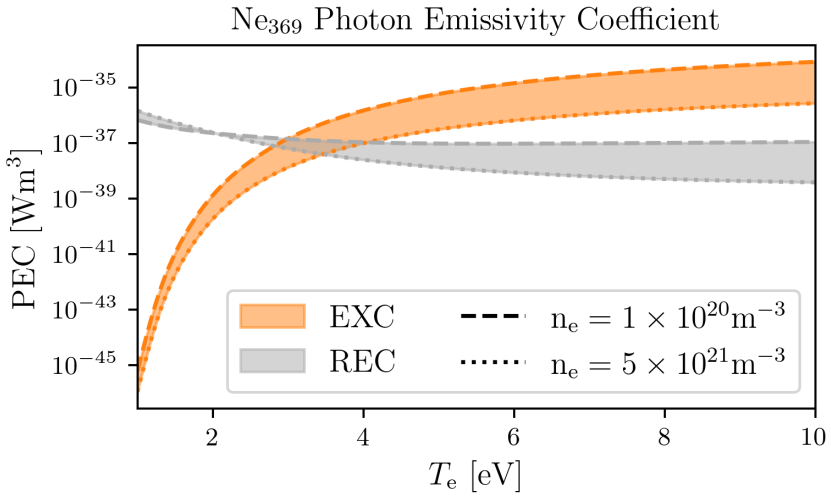

Figure 3.22: The PEC profiles for the Ne_{369} spectral line are delineated in the graph. Here, the dashed line represents the coefficients at an electron density of $n_e = 1 \times 10^{20}$, while the dotted line corresponds to those at $n_e = 5 \times 10^{21}$.

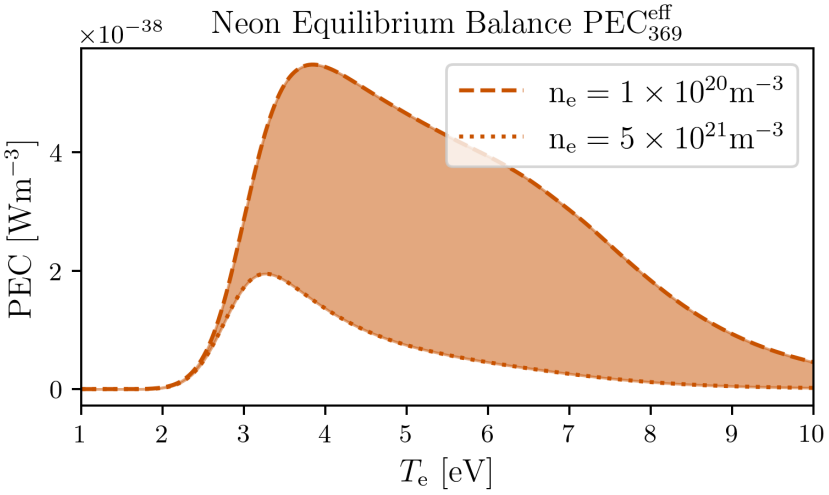

Figure 3.23: The PEC^{eff}_{369} profile for the Ne_{369} is shown for the equilibrium ionisation balance. The dashed line represents the coefficients at an electron density of $n_e = 1 \times 10^{20}$, while the dotted line corresponds to those at $n_e = 5 \times 10^{21}$.

The data from Fig. 3.21 and Fig. 3.22 clearly indicate that the electron temperature (T_e) has a more significant impact on radiation than electron density (n_e), emphasizing its crucial role in accurately determining impurity concentration. The assumption of zero transport further implies that the spectral line ratio, as defined in (3.11), becomes a function of both n_e and T_e. Consequently, the values of the spectral line ratios, denoted as R, create isolines within the n_e, T_e space. An illustrative isoline, with a value of $R = 0.3$, is shown in Fig. 3.24. This representation aids in refining the solution space for n_e and T_e. If an estimate of the electron temperature is available, the ratio space can be utilized to deduce the electron density. However, it's noteworthy that the radiation and abundance curves suggest the electron temperature may vary across several electron volts (eV).

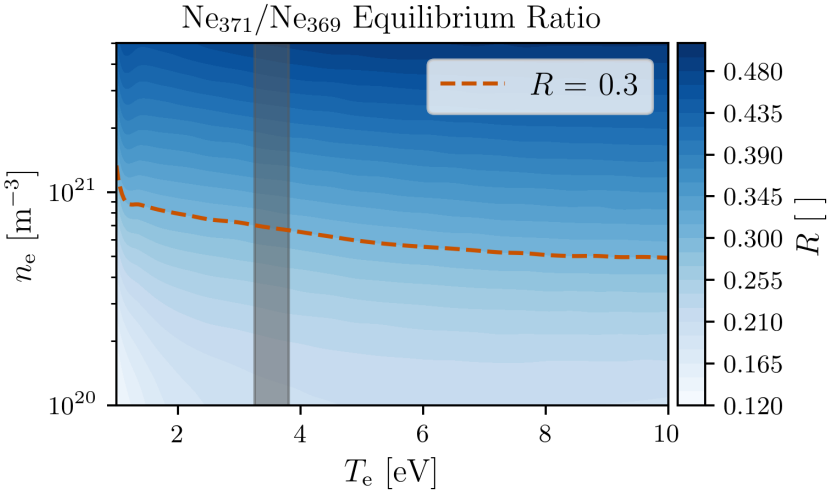

Figure 3.24: The plot shows values of the neon spectral line ratio with zero transport as a function of n_e and T_e. The contours of R uniquely assign n_e, T_e pairs. The vertical grey region higlihts the temperature range where the Ne_{369} line is most effectively radiated, see Fig. 3.25.

In [64, 55], a further simplification is made, constraining the range of T_e based on the premise that radiation detected by a diagnostic is more likely sourced from regions where it is most efficiently radiated. This assumption essentially involves selecting the temperature value at which the line radiates most effectively. While this assumption is logical, it is important to acknowledge that its application introduces an element of uncertainty into the results. The consequence of this assumption is that it transforms the two-dimensional space of possible (T_e, n_e) pairs into a condensed one-dimensional function which can be expressed as $T_e = \varepsilon_{Ne}^{\max}(n_e)$.

To assess the impact of these simplifications, electron temperature values corresponding to maximum radiation were computed across a range of relevant electron densities. This relationship between temperature and density is displayed in Fig. 3.25. This figure indicates that, within the considered n_e range, the T_e value shifts from 3.25 to 3.8 eV. The same range is marked in Fig. 3.24 with the vertical grey region. More crucial, however, is the observed change in radiated power, as depicted in Fig. 3.26. This graph demonstrates that the radiated power in the depicted n_e range increases by approximately 6.7 times. Given the assumption that T_e is determined by the point of maximum radiated power, this factor of 6.7 will has to be transferred by the inference into the uncertainty of the derived neon concentration. It's important to clarify that 6.7 is not a standard deviation, as the prior temperature distribution is uniform between 3.25 and 3.8 eV, based on the available information. These prior assumptions and established relations between the line intensity and neon concentration (3.10), maximum radiated power (Fig. 3.25, Fig. 3.26) and effective photon emissivity ($PEC_{i\to j}^{\text{eff}}$ from (3.10)) were used to build a probabilistic model in Numpyro [41]. The relation $G = l/4\pi$ for the geometrical factor from (3.11) was assumed in the inferences. The $l = 7$ cm was used as the length of the intersection of the KT3A sightline with the region where the line is expected to radiate (taken from [55]).

Furthermore, the grey box in Fig. 3.24 highlights the relevant temperature range determined in Fig. 3.25, showing a significant reduction in the uncertainty of n_e for a given line ratio. When this is combined with the maximum radiated power curve from Fig. 3.26, it suggests that the propagated uncertainty might actually be much smaller.

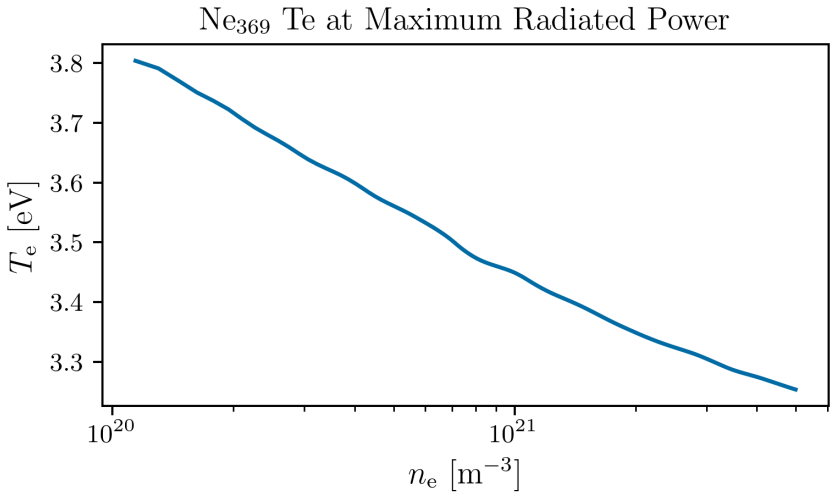

Figure 3.25: The figure depicts the electron temperature at which the Ne_{369} spectral line is most effectively radiated, as a function of electron density. Within the specified range of electron densities, the maximum electron temperature increases from 3.25 to 3.8 eV.

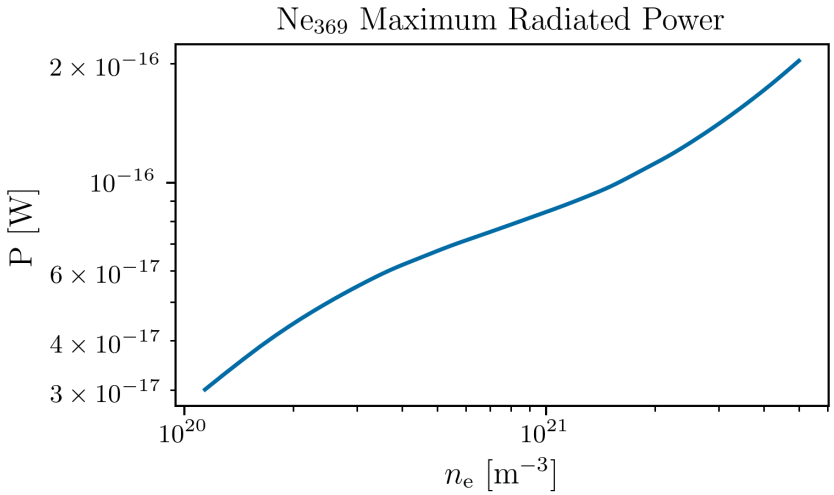

Figure 3.26: The graph shows the variation in the maximum radiated power per neon atom for the Ne_{369} spectral line. The radiated power escalates from 3×10^{-17} W to 2×10^{-16} W.

The validity of the method was first tested on the neon spectral line intensity simulated by Cherab, with the plasma state predicted by the SOLPS simulation. Results are shown in Fig. 3.27. The blue colors represent the concentration distribution inferred by the zero transport model from the spectral lines simulated by Cherab, while the orange distributions display the actual concentration distribution in the SOLPS simulation as observed by the KT3A channels (as in Fig. 3.20). The comparison suggests that the model, with its zero transport and maximum radiation assumptions, converges to lower concentration values. This may be attributed to the electron temperature and densities diverging from the maximum radiation assumption, as well as transport affecting the fractional abundance of neon states.

To gauge the zero transport assumption's validity, the abundance statistics across all SOLPS mesh cells observed by KT3A channels were plotted in Fig. 3.28, alongside the equilibrium ionization balance. In the temperature range important for the maximum radiation assumption, the equilibrium abundance predicts the Ne_{1+} and Ne_{2+} ions, responsible for the spectral lines, to have a combined abundance close to one. However, the SOLPS distribution indicates that these ionization stages contribute only about 60% to the overall neon density in the temperature range from 3 to 4 eV. The main reason is the high abundance of neutral neon predicted by SOLPS simulations which can be a consequence of transport and presence of neutral deuterim which contributes to lower neon stage abundance with charge exchange collisions. This factor explains part of the discrepancy seen in Fig. 3.27, with the remainder likely due to T_e and n_e deviating from the maximum radiation conditions.

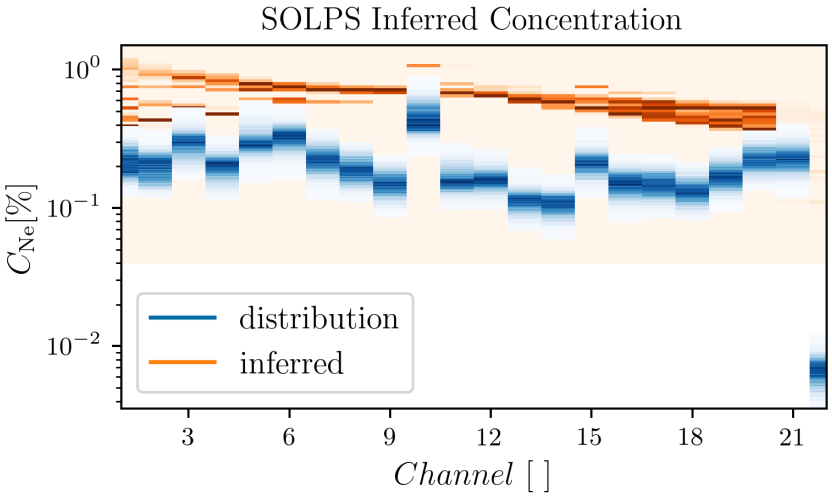

Figure 3.27: The figure displays in blue the posterior distribution of concentration inferred by the zero transport model from the spectral lines simulated by Cherab. The orange distributions depict the actual concentration distribution in the SOLPS simulation as observed by the KT3A channels (as in Fig. 3.20).

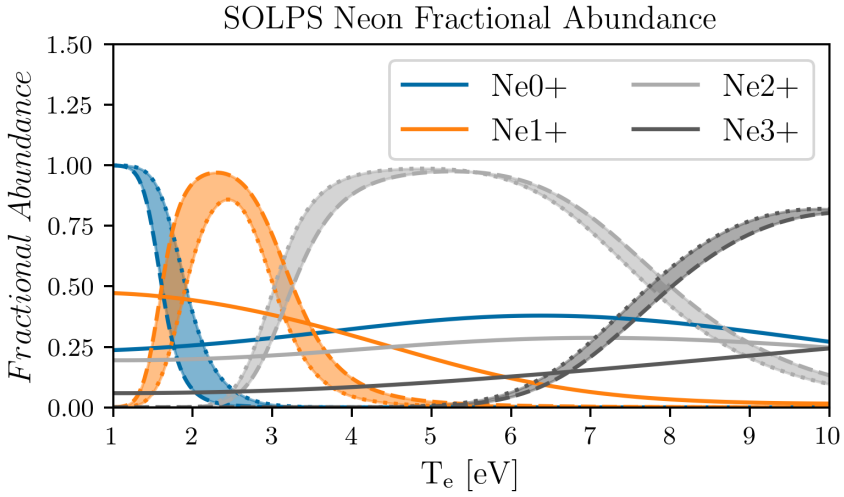

Figure 3.28: The figure utilizes fractional abundances from the SOLPS mesh cells observed by KT3A channels to construct Kernel Density Estimations (KDE) of the neon ionization state balances. The solid lines in the figure represent these KDE profiles of abundance. Additionally, the equilibrium ionization balance, as depicted in Fig. 3.21, is shown with dashed and dash-dot lines for comparison.

The zero transport method, incorporating the assumption of maximum radiated power, was applied to a series of JET pulses, as detailed in Tab. 3.1. To infer neon concentration, the line ratio was calculated using Ne_{369} and Ne_{371} spectral line intensities provided by S. Henderson. This process involved developing a Bayesian model specifically for neon concentration inference. A key advantage of this approach is the ability to incorporate accurate distributions, such as a uniform prior for electron temperature, into the model.

In Fig. 3.29, the intensity values for all analyzed shots are presented. Horizontal dashed lines within this figure indicate the inboard and outboard edges of *tile*5. To enhance the understanding of the spatial shape of the profile, mean intensity values averaged over pulse time are depicted in Fig. 3.30. These intensity profiles exhibit a substantial and stationary gradient near the outboard edge of the tile (at $R = 2.8\,\mathrm{m}$). This gradient remains consistent both during the evolution of a single shot and across different pulses with varying gas puff rates. Such behavior contrasts with observations from other machines, where the spatial distribution of radiation in the divertor changes with gas puff rates, as noted in [65]. This inconsistency suggests that the observed gradients might be influenced by factors other than plasma physics.

Two primary hypotheses are considered to explain the observed phenomena: the variation in radiation region lengths for sight lines closer to the X-point, and reflections from the plasma facing components. As the SOL (Scrape-Off Layer) poloidal flux surfaces extend from the divertor plate towards the X-point, they gradually curve upwards, mirroring the plasma shape. This curvature results in these surfaces becoming more tangent to the KT3A sight lines. If there is an increase in radiation within this region, potentially due to an accumulation of neon, the sight lines would intersect this radiating region over a longer distance. Consequently, these sight lines would integrate more light, indicating the extended interaction with the radiating region.

The second factor contributing to increased intensity values is reflections, which

present significant challenges. Reflections are notoriously difficult to account for accurately, largely due to critical unknowns such as the surface state, including its reflectivity and roughness. A comprehensive discussion on ray-surface interaction can be found in [7]. Reflectivity of surfaces is altered by plasma-surface interactions during device operation, as detailed in [66]. Since fusion devices lack effective means to measure surface properties in situ, completely mitigating the influence of reflections is practically unfeasible.

Another problematic aspect of reflections is their dependency on the distribution of radiation in the plasma. For instance, even a surface with low reflectivity can produce significant reflections if it is reflecting light from a high-intensity radiation region. Surface roughness mainly affects the distribution of light reflected from the surface, as explained in [7]. In the case of KT3A, observing *tile*5 could under some circumstances lead to reflections from high radiation intensity regions, such as the X-point. For shot number 97490, which had the highest neon gas puff flow rate, there was an observed increase in intensity near $R = 2.8\,\mathrm{m}$ of approximately 50%. This magnitude of increase is consistent with the reflectivity of tungsten which can be as high as 0.5 around the 400 nm spectral range.

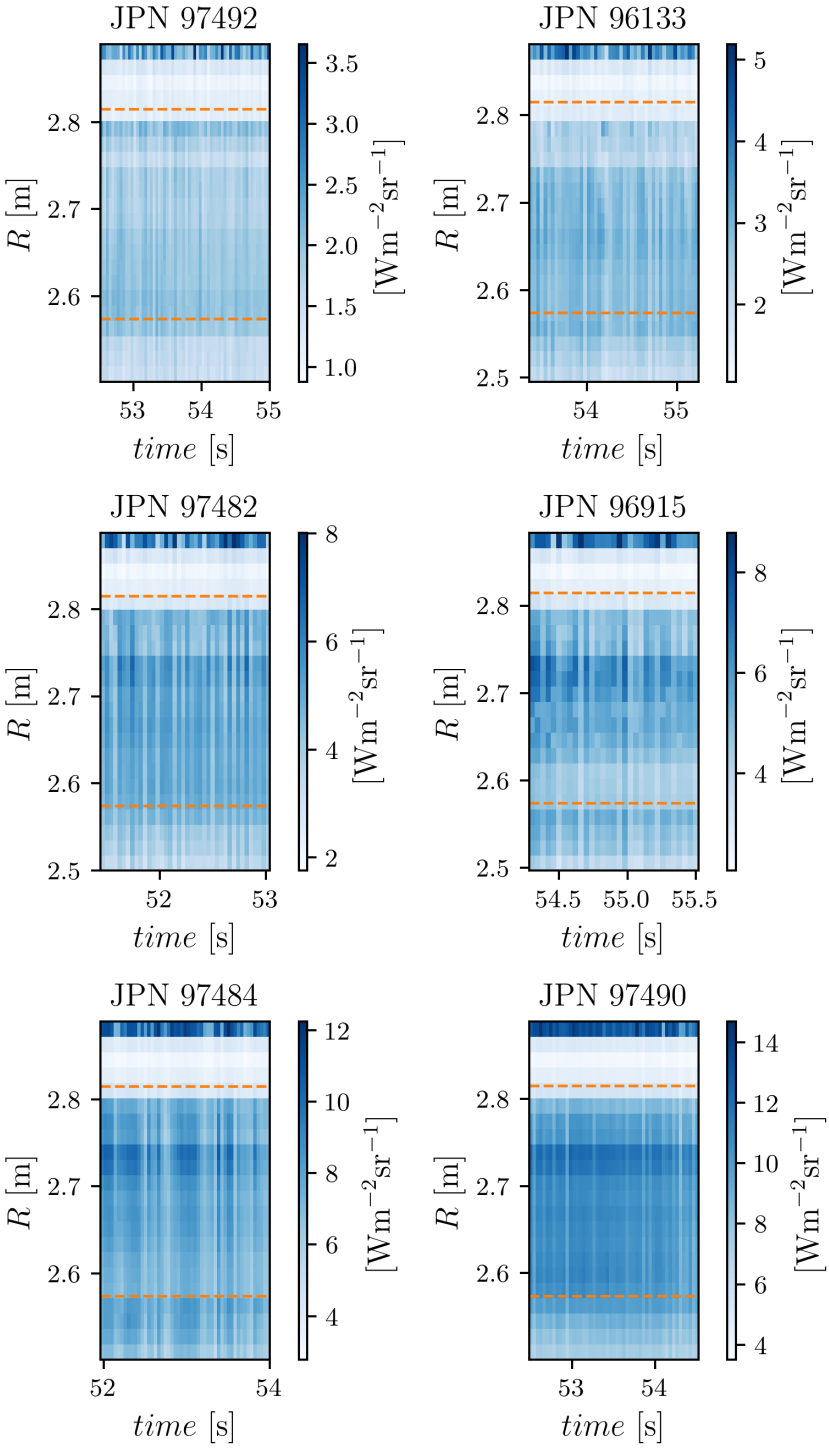

Figure 3.29: The graph displays the measured intensities of the Ne_{371} spectral line for the analyzed shots, with data provided by S. Henderson. Horizontal dashed lines in the graph indicate the radial edges of *tile*5. The shots are arranged in the increasing order of the neon gas puff rate.

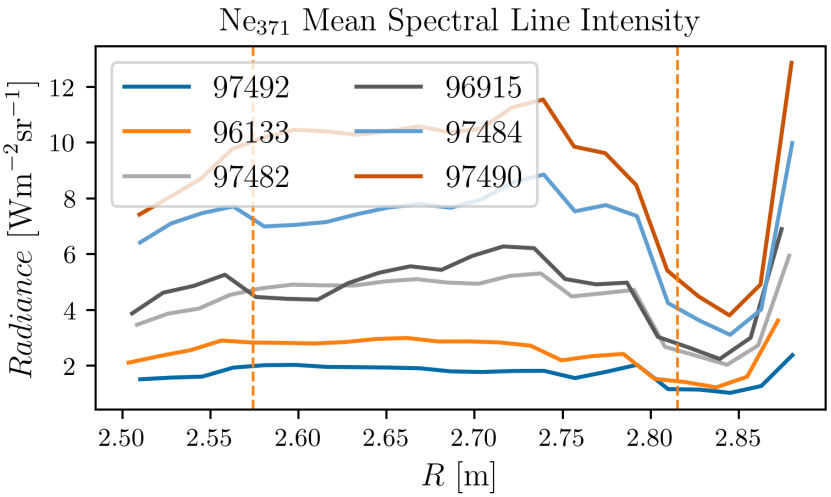

Figure 3.30: The figure presents mean values of the Ne_{371} spectral line intensity, averaged over the duration of each pulse. Vertical lines in the figure mark the edges of *tile*5. Across these profiles, there is a consistently large gradient observed near the High-Field Side (HFS) edge of *tile*5, specifically at $R = 2.8\,\mathrm{m}$.

The time evolution of inferred neon concentration in KT3A channels and for the set of analysed JPNs is depicted in Fig. 3.31, Fig. 3.32, Fig. 3.33, Fig. 3.34, Fig. 3.35, and Fig. 3.36, sequenced by increasing neon gas puff rates. Horizontal orange dashed lines in these figures mark the High-Field Side (HFS) and Low-Field Side (LFS) edges of *tile*5. The grey curves within these plots represent the neon gas puff rates, which, while not completely stable in the chosen time windows, vary by less than 15%.

The effect of the diminishing gas puff rate is visually evident. The decrease in the neon concentration can be observed in the diagnostic channels with the pulse time. Also the shape of the concentration shape evolves in time which is particularly visible in the pulses with the highest gas puff rates. The gradient pattern identified in the intensity profiles in Fig. 3.29 is mirrored in these concentration profiles, observable as reductions in concentration near the edges of *tile*5.

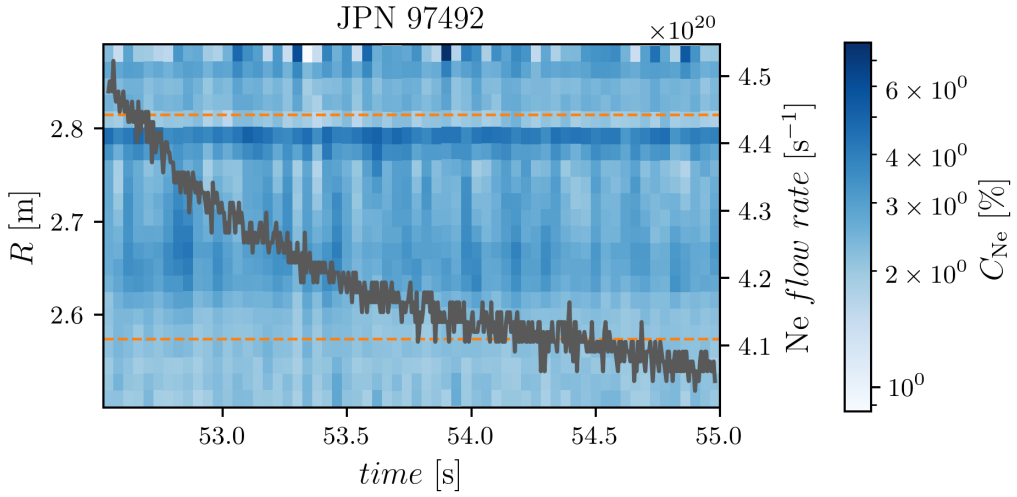

Figure 3.31: The plot illustrates the time evolution of the mean neon concentration derived from KT3A measurements for JPN 97492. Horizontal dashed orange lines in the plot indicate the radial edges of *tile*5, and the grey line represents the neon seeding rate.

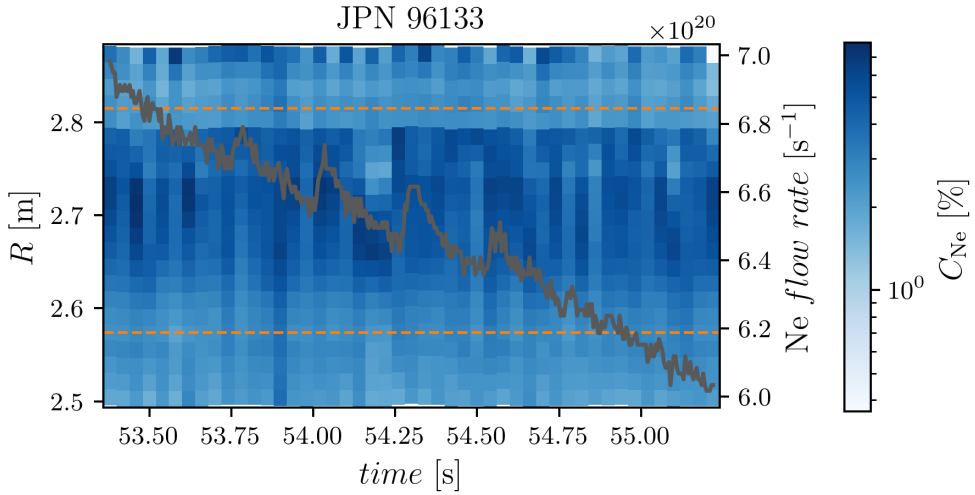

Figure 3.32: The plot illustrates the time evolution of the mean neon concentration derived from KT3A measurements for JPN 96133. Horizontal dashed orange lines in the plot indicate the radial edges of *tile*5, and the grey line represents the neon seeding rate.

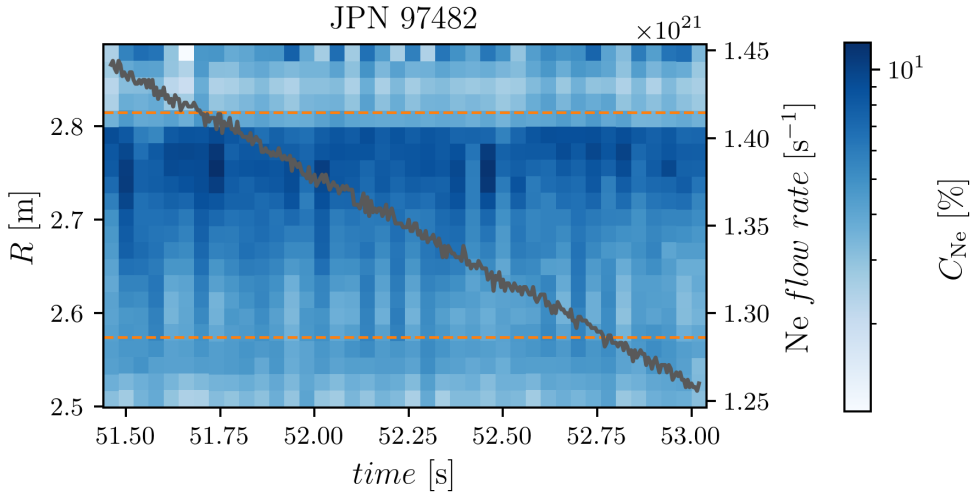

Figure 3.33: The plot illustrates the time evolution of the mean neon concentration derived from KT3A measurements for JPN 97482. Horizontal dashed orange lines in the plot indicate the radial edges of *tile*5, and the grey line represents the neon seeding rate.

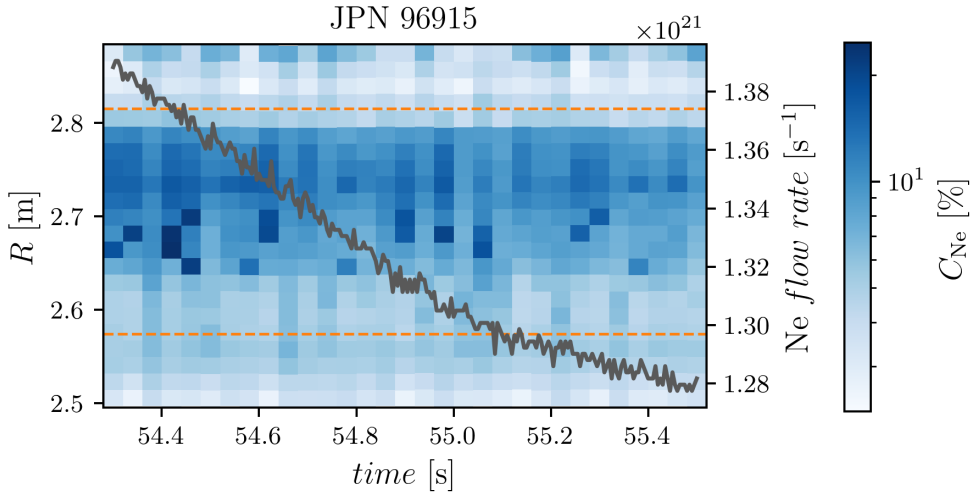

Figure 3.34: The plot illustrates the time evolution of the mean neon concentration derived from KT3A measurements for JPN 96915. Horizontal dashed orange lines in the plot indicate the radial edges of *tile*5, and the grey line represents the neon seeding rate.

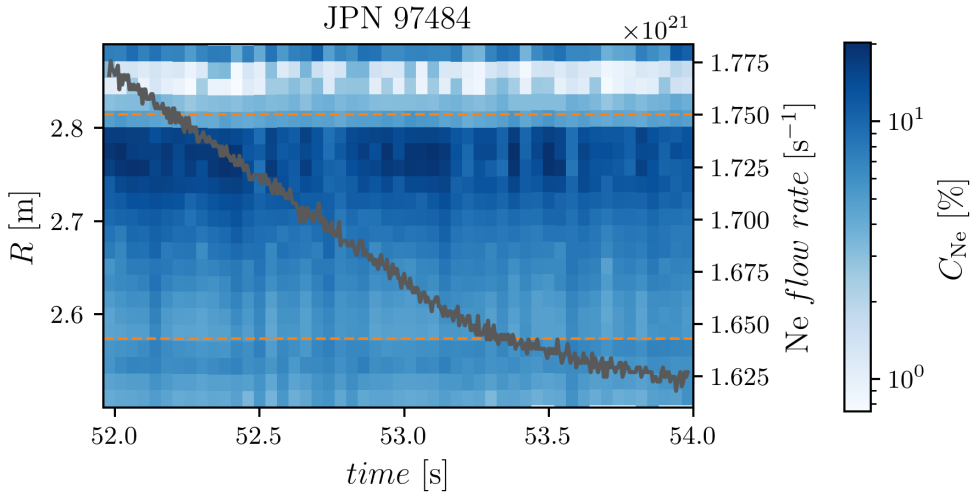

Figure 3.35: The plot illustrates the time evolution of the mean neon concentration derived from KT3A measurements for JPN 97484. Horizontal dashed orange lines in the plot indicate the radial edges of *tile*5, and the grey line represents the neon seeding rate.

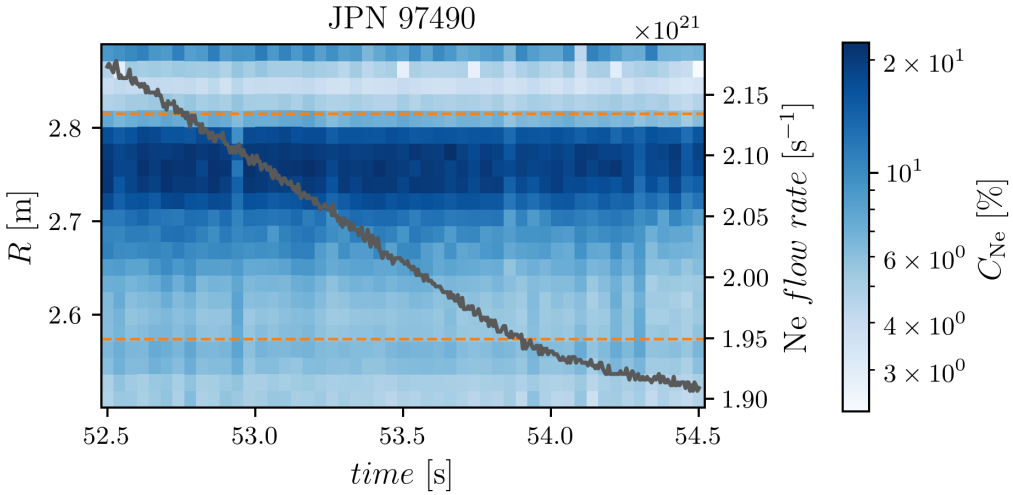

Figure 3.36: The plot illustrates the time evolution of the mean neon concentration derived from KT3A measurements for JPN 97490. Horizontal dashed orange lines in the plot indicate the radial edges of *tile*5, and the grey line represents the neon seeding rate.

Fig. 3.37 provides a detailed illustration of the spatial profiles of neon concentration. The profiles were obtained by marginalising over the time domain and plotting all posterior samples for separate channels in a single plot. In this figure, vertical lines mark the High-Field Side (HFS) and Low-Field Side (LFS) edges of *tile*5. It is observed that as the neon seeding rate increases, so does the average concentration within the discharge. For the lower seeding rates, as seen in JPN 97492 with the average seeding rate $7.0 \times 10^{20}\, particles/s$, the neon concentration is estimated to range from 2% to 4%. In contrast, for the highest seeding rates in JPN 97490 with the average seeding rate $2.7 \times 10^{21}\, particles/s$, the concentration lies approximately between 5% and 25%. A notable discontinuity near the HFS

edge of *tile*5 becomes more pronounced with increasing neon seeding flow rates. This phenomenon is likely due to the combined effects of reflections and the evolution of plasma profiles, as previously discussed. With an increasing seeding rate, it is reasonable to expect that the ionization front will move away from the divertor tiles. This shift can also affect the contribution of reflections, as they are dependent on the spatial distribution of plasma radiation.

In Fig. 3.38, the concentration of neon approximately at the pedestal top (calculated from spectroscopic measurements for radial position $R = 3.72\,\mathrm{m}$ on midplane), obtained from JPF, is shown for comparison with the inferred divertor concentration. The neon concentration at the pedestal top approximately triples, increasing from around 0.5% to 1.5%.

This increase is paralleled in the divertor region, as seen in Fig. 3.37, particularly in the side channels. In the middle channels, the concentration escalates more significantly, about fivefold, from approximately 4% in pulse 97492 to around 20% in 97490. The observed ratio of neon concentration between the pedestal top and the divertor contrasts with SOLPS simulations [61], which predict a higher concentration of neon at the separatrix.

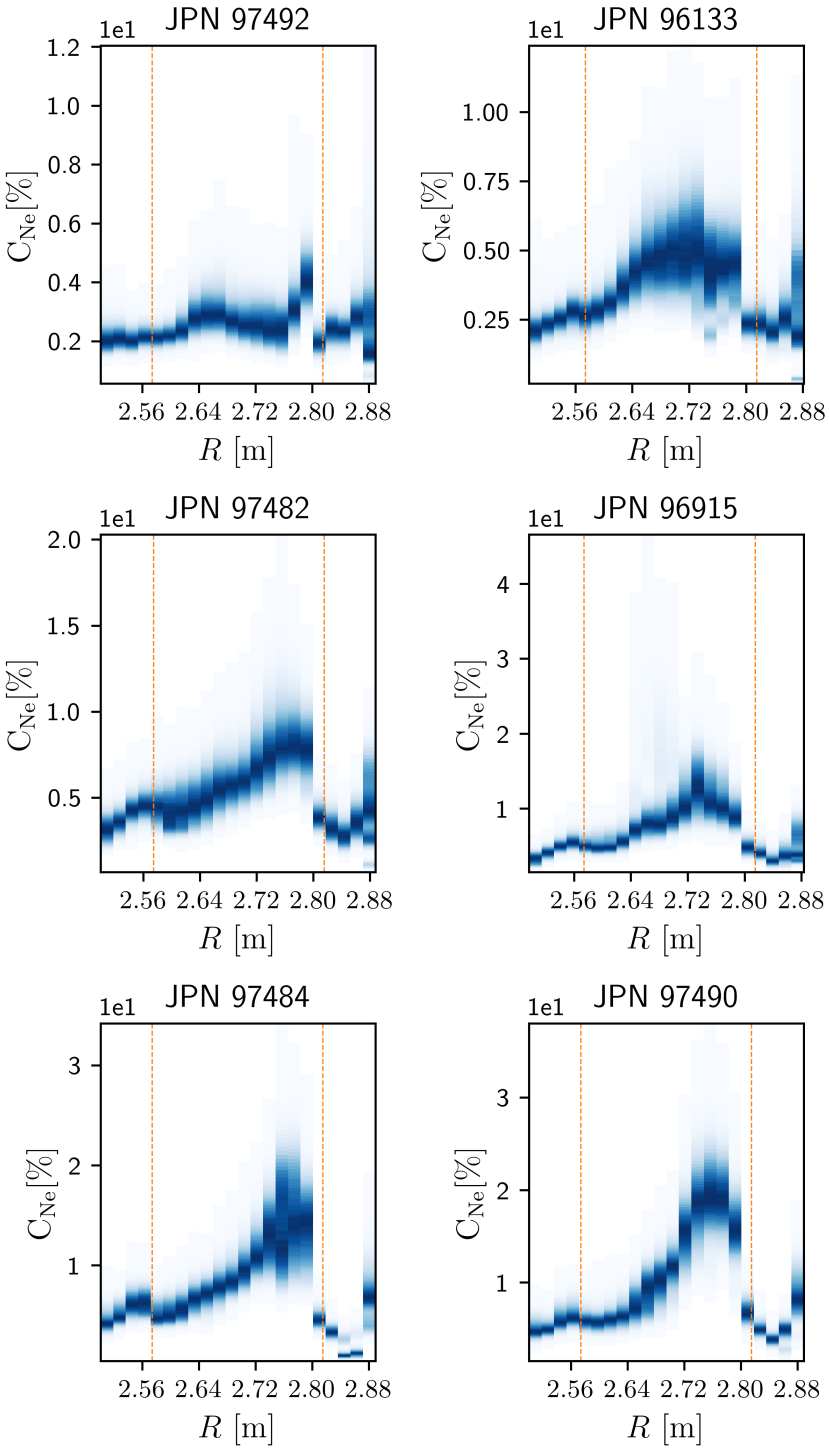

Figure 3.37: The graph depicts spatial profiles of neon concentration posterior distributions for the zero transport model and the analyzed shots. The results were marginalised over the time domain. Vertical dashed lines within the graph mark the radial edges of *tile*5. The arrangement of the data shows an increase in the neon seeding rate from left to right and from top to bottom.

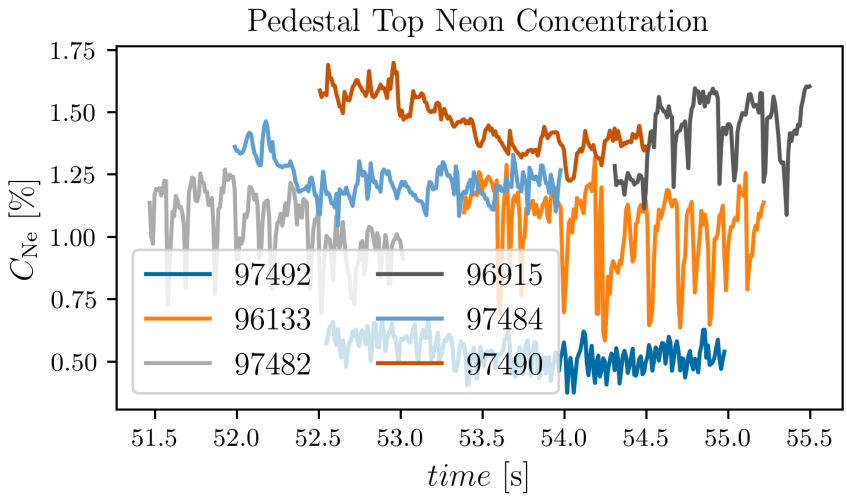

Figure 3.38: The concentration of neon approximately at the pedestal top, as obtained from JPF, is presented.

The final two figures, Fig. 3.39 and Fig. 3.40, present the inferred profiles of electron density and temperature, respectively, derived from the neon line ratios. These values exhibit qualitative characteristics consistent with the phenomenon of detachment. A hallmark of detachment is the reduction of electron temperature near the divertor plates, coupled with an increase in electron density. As the gas puff rates rise, the edge parts of the profiles in Fig. 3.39 show an increase towards the divertor plates, while the electron temperature values in Fig. 3.40 exhibit a decrease.

Although caution is advised in interpreting these quantitative results due to the underlying assumptions of maximum radiation and zero transport, the observed qualitative behavior aligns with the typical patterns of detachment.

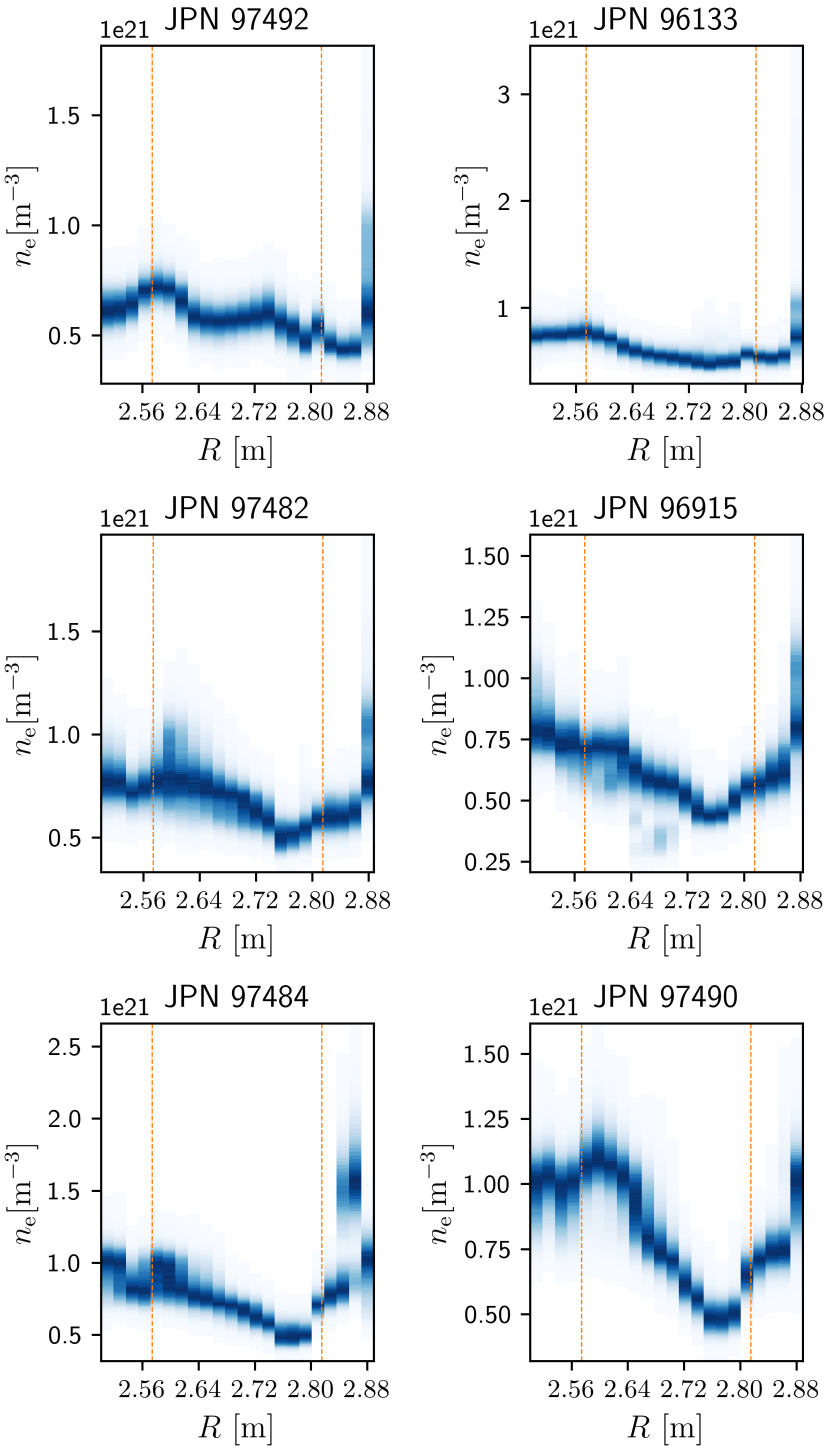

Figure 3.39: The electron density profiles, inferred using the zero transport model from the line ratio values, are illustrated. Dashed vertical lines in the figure indicate the radial edges of *tile*5.

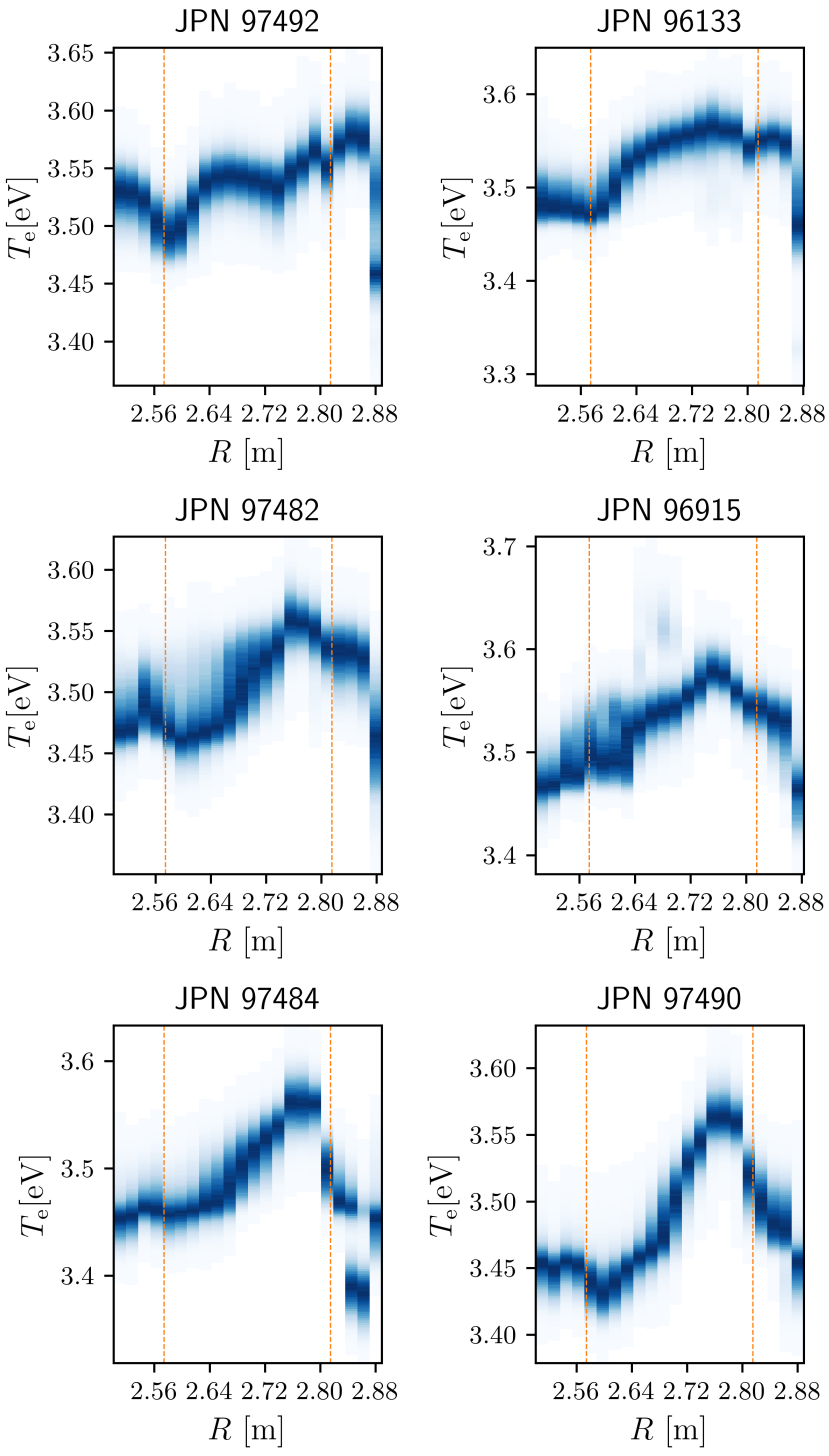

Figure 3.40: The electron temperature profiles, inferred using the zero transport model from the line ratio values, are illustrated. Dashed vertical lines in the figure indicate the radial edges of *tile*5.

3.6 Conclusions and outlook

In this chapter a combination of forward and backward models was used to infer the neon impurity concentration in seeded discharges at JET. The description

of the forward model of the KT3 diagnostic system developed in frame of this work and based on Raysect and Chearb is discribed in Sec. 3.3. The properties of FOV of the individual diagnostic channels are based on the data available in JPFs. The FOVs are approximated with conical shape. The positioning of the diagnostic channels takes into account the changes caused by the movement of the first mirror due to force being excerted on it by JET's force coils. Also a preventive measure was taken to prevent obscuring of the inboard channels.

The model was then used in combination with radiation models for neon and deuterium spectral lines in the wavelength band $(360, 400)$ nm of the KT3A spectrometer (see Sec. 3.3.4). The radiation models were based on ADAS atomic data and employed thermal and pressure broadening to cover main aspects of the observed line shapes. The forward models of spectra provided by ray tracing simulations were then convolved with the instrumental function of the spectrometer to obtain a realistic representation of the observed spectra. The comparison of the forward modelled and the measured spectra shogood agreement in the intensities and line shapes of the deuterium spectral lines. The intensity of the neon lines showed however a strong discrepancy. The hypothesis is that this discrepancy can be caused by the effects of reflection, differences between the diagnostic and its model and also by the fact that the results of SOLPS simulation are not fully consistent with the state of the plasma in the experiment.

The determination of the neon concentration from the measured neon spectral lines was inspired by [64]. The assumption from the article, which narrows the acceptable values of T_e into a region where the neon spectral lines are assumed to be radiated the most effectively, was also adopted and developed further in Sec. 3.5.1. A function $T_\mathrm{e} = \varepsilon_{Ne}^{max}(n_\mathrm{e})$ was determined from the ADAS atomic data to determine the (T_e, n_e) pairs for which the lines are radiated most effectively. These prior assumptions and relations between spectral line intensity, ratio and atomic data were used build a probabilistic model in Numpyro [41].

The performance of the zero transport concentration model with maximum radiated power assumption was assessed with use of the forward modelled KT3A neon spectra. The assessment is not straightforward for plasma quantities inferred from volumetric radiation, such as spectral lines from divertor. For this purpose a method was developed which provides a weighted distribution of the plasma quantity of interest (see Sec. 3.4). It takes into account the topology of the diagnostic and plasma simulation through contribution matrices. The spatial distribution of the radiated intensity of the spectral feature used in the backward model is also taken into account. Because this approach returns a distribution, it allows a good assessment of the backward model quality. For example, in case when the spectral feature is radiated from two plasma regions with distinct properties, the validation method return a bimodal distribution. The accuracy of the backward model then can weighted properly and informatively.

The validation method was used to assess the performance of the zero transport backward model on the case of the SOLPS plasma simulation. The comparison of the distributions in Fig. 3.27 suggest that the backward model returns values of neon concentration underestimated by approximately three to four times. The further analysis suggests that the zero transport assumption doesn't hold and that the transport and charge exchange collisions with neutral deuterium may cause approximately 40% underestimation of the neon concentration. Part of the

discrepancy can be attributed to the deviation of the electron temperature and density from the maximum radiated power assumption. The errors in estimation of the radiation region length l can also conribute.

Concentration of neon in the seeded discharges at JET were inferred with the zero transport model. The concentration profiles in Fig. 3.37 show a steep gradient at $R \approx 2.8$ m which correlates with the HFS edge of the $tile5$. The diagnostic channels observing the $tile5$ close to its outboard edge increase the concentration from approximately 5% to 25% from the lowest to the highest seeding rates. The HFS diagnostic channels which are not observing the $tile5$ see the increase in the concentration only from 2% to 4%. The underestimation estimated from the zero transport model validation would suggest that the highest inferred concentrations are probably not correct. If it holds for the experiment. One hypothesis for the observed gradient is the impact of reflections which increase the observed spectral line intensity. In any case, if the outboard diagnostic channels, showing the low concentration values, can be assumed to give approximately correct values, the neon concentration in the divertor in Fig. 3.37 is predicted to be higher than the concentration at the pedestal top in Fig. 3.38. This is in contrast with findings from SOLPS published in [61].

Although not published in this thesis, a work is ongoing on developing a more sophisticated backward model which would take into account effects of transport on the neon concentration. In future, the performance of the model will be assessed with the SOLPS results. The possibility of incorporating the electron temperature and density estimated from deuterium radiation observed by KT3 spectrometers will be also looked into. Another planned improvement is to try to incorporate data measured by other diagnostics, such as bolometry. This could help to constrain the model and further improve the accuracy of the inferred neon concentration. The future work will also include broadening of the application of the developed methods to validation of SOLPS simulation with the experiment. This should include not only data from KT3 diagnostic, but also for example from bolometry.

4. Towards Forward Modelling of Synchrotron Radiation

This chapter describes the SR (synchrotron radiation) model incorporated into Cherab in the frame of this work. The model distinguishes itself from other already available main SR forward modelling codes by working directly with 6D kinetic distribution function and 3D vector magnetic field. This allows the model to separate the ray tracing simulations from the computationally intensive simulations of particle trajectories and RE dynamics. The separation makes it possible to introduce analytically defined distribution functions and magnetic fields which can be especially useful for direct inversion of RE properties from measured data. Because of Raysect's reverse ray tracing algorithms, the model can also simulate reflections from first wall. This makes the developed model to be unique in terms of its versatility, suitability for simulations of wide range of RE physics phenomena and low computational intensity. Its capabilities are demonstrated through applications to JET's infrared camera measurements of SR, which display visible asymmetries caused by presence of magnetic islands and reflections.

Synchrotron radiation (SR) [67, 68], produced in tokamaks by runaway electrons (REs) [69, 70], is a notable consequence of plasma disruptions [71, 72]. These disruptions, characterized by sudden loss of plasma confinement due to various mechanisms [73, 74, 75], lead to the generation of a toroidal electric field. This field accelerates free electrons to relativistic energies, potentially resulting in the formation of a runaway electron beam that carries a significant portion of the pre-disruption plasma current [76, 77, 78, 79]. RE beams present substantial risks to larger devices, particularly their first walls [74, 80]. The high energy of runaway electrons makes it challenging to measure their properties, this challenge is even more extreme in the case of direct measurements. Various diagnostic methods exist for indirect measurements of REs [81, 70], such as detecting ionising radiation produced by electron interactions with plasma particles and first wall materials [82, 83, 84, 85]. However, synchrotron radiation stands out as one of the few direct methods for measuring of properties of REs. Theoretically it is possible to invert even their distribution function from the SR measurements.

The most renowned codes for modelling SR are SOFT (Synchrotron-detecting Orbit Following Toolkit) [86] and KORC (Kinetic Orbit Runaway-electron Code) [87, 88]. SOFT employs gyro-center particle tracking, toroidal averaging of particle trajectories, and forward ray tracing to construct contribution matrices for generating SR images. This modelling approach, however, does not accommodate toroidal asymmetries, and its forward ray tracing method makes it difficult to cover reflections. Conversely, the KORC code [87, 88], which also relies on particle following and forward ray tracing, offers both gyro-center and full orbit particle tracking. The application of toroidal averaging of trajectories is optional which enables KORC to address toroidal asymmetries. Nonetheless, it remains limited by its forward ray tracing foundation and does not incorporate reflections. As it was already mention in the beginning of this chapter, the model developed for Cherab distinguishes itself from SOFT and KORC by working directly with

6D kinetic distribution and it expects the distribution function to cover all the important aspects of RE dynamics.

In the subsequent chapter, the capabilities of this new model are demonstrated through applications to JET's infrared camera measurements of SR, which display visible asymmetries and reflections. It is important to note that the initial phase of this work aimed to develop a simplified model quickly to garner feedback from the runaway electron community. Therefore, the applied formulae describing synchrotron radiation were also simplified, yielding the benefits of reduced initial time and computational costs, which facilitated faster development and testing.

4.1 Synchrotron Radiation

In tokamaks, synchrotron radiation, a relativistic limit of cyclotron radiation, is emitted by runaway electrons. This phenomenon is thoroughly documented in [67, 68, 89, 70]. The high energy of these particles imparts a relativistic character to the observed radiation. A distinctive attribute of this radiation is its highly directional nature, predominantly emitted along the particle's velocity vector, as detailed in [89]. Additionally, its spectral distribution is notably narrow, peaking at a frequency given by the following equation taken from [89]:

$$\nu \approx \gamma^2 \nu_g = \gamma^2 \frac{eB}{2\pi m_e} \tag{4.1}$$

Here, ν represents the synchrotron radiation frequency, γ is the relativistic factor, ν_g the electron cyclotron frequency, e the electron charge, B the magnetic field's magnitude, and m_e the electron's rest mass. The power radiated by an individual electron, as outlined in eq. 8.80 of [89], is expressed as follows:

$$P(E,B) = \frac{4}{3}\sigma_T c \frac{B^2}{2\mu_0}\left(\frac{E}{m_e c^2}\right)^2 \tag{4.2}$$

In this equation, σ_T denotes the Thomson cross section, c the speed of light, E the electron energy, m_e the rest mass of the electron, and μ_0 the vacuum permeability.

The specific directionality of the radiation and its frequency, tightly correlated with the electron energy and magnetic field strength, render synchrotron radiation as one of the few direct, non-invasive methods for measuring runaway electrons. The observed spectrum can be directly related (with minimum loss of accuracy) to the electron distribution function without the need for complex inversions. As depicted in Fig. 4.1, the synchrotron radiation wavelengths for common toroidal magnetic fields and electron energies intersect the mid infrared (MIR), near infrared (NIR), and visible (VIS) spectral regions, indicated by blue, grey, and orange horizontal bands, respectively. These spectral areas are effectively diagnosed using infrared and visible cameras, which provide high-resolution 2D images, and spectrometry, which offers the necessary spectral resolution. A notable challenge in the visible and infrared regions is the high reflectivity of the first wall materials, the thermal radiation from surfaces and other sources of plasma radiation. Reflections significantly impact the imagery and are notoriously challenging to subtract, underscoring the value of any modelling that can shed light on SR reflections.

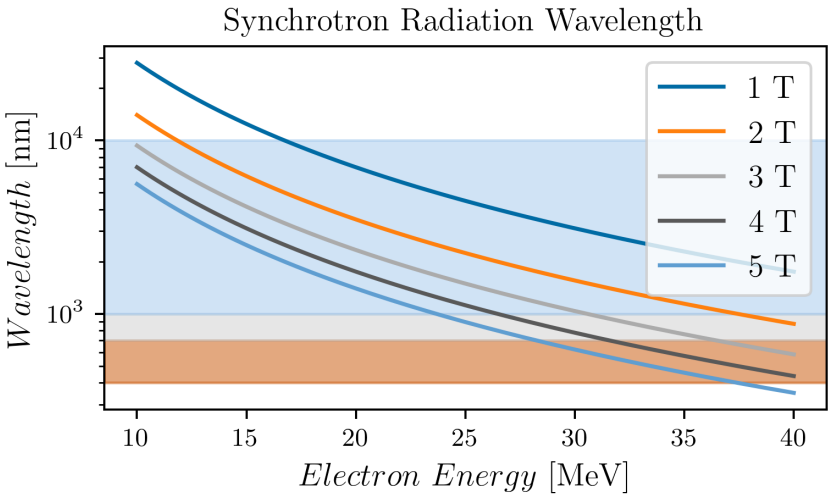

Figure 4.1: Wavelengths of synchrotron radiation for different electron energies and magnetic field magnitudes. The horizontal regions show the mid infrared (blue), near infrared (grey), and visible (orange) spectral regions.

An example of experimentally obtained image of SR radiation is presented in Fig. 4.2. Captured during JET discharge 95135 (same discharge as in [90]), the image was taken by the KLDT-E5WC mid-infrared camera ($3 - 3.5\,\mu$m) [91]. A dashed line in the image indicates the split field of view effect caused by the camera optics. Additionally, the image showcases a typical synchrotron light pattern, reminiscent of a croissant. This pattern results from the interplay between the directionality of the radiation, the magnetic field's magnitude, and the properties of runaway electron distribution function. The most intense radiation is observed at the HFS, where the toroidal magnetic field is strongest. The spectral peak of the synchrotron radiation aligns closely with the camera's sensitivity band. As the camera's view shifts towards the LFS, the intensity diminishes in response to the decreasing magnitude of the toroidal field. An increase in the energy of the REs would shift the intensity from the inboard to the outboard side. The concentration of radiation in the image's bottom-right is attributed to the helicity of the magnetic field lines and the directionality of the SR. In regions of highest intensity, the lines point directly into the camera.

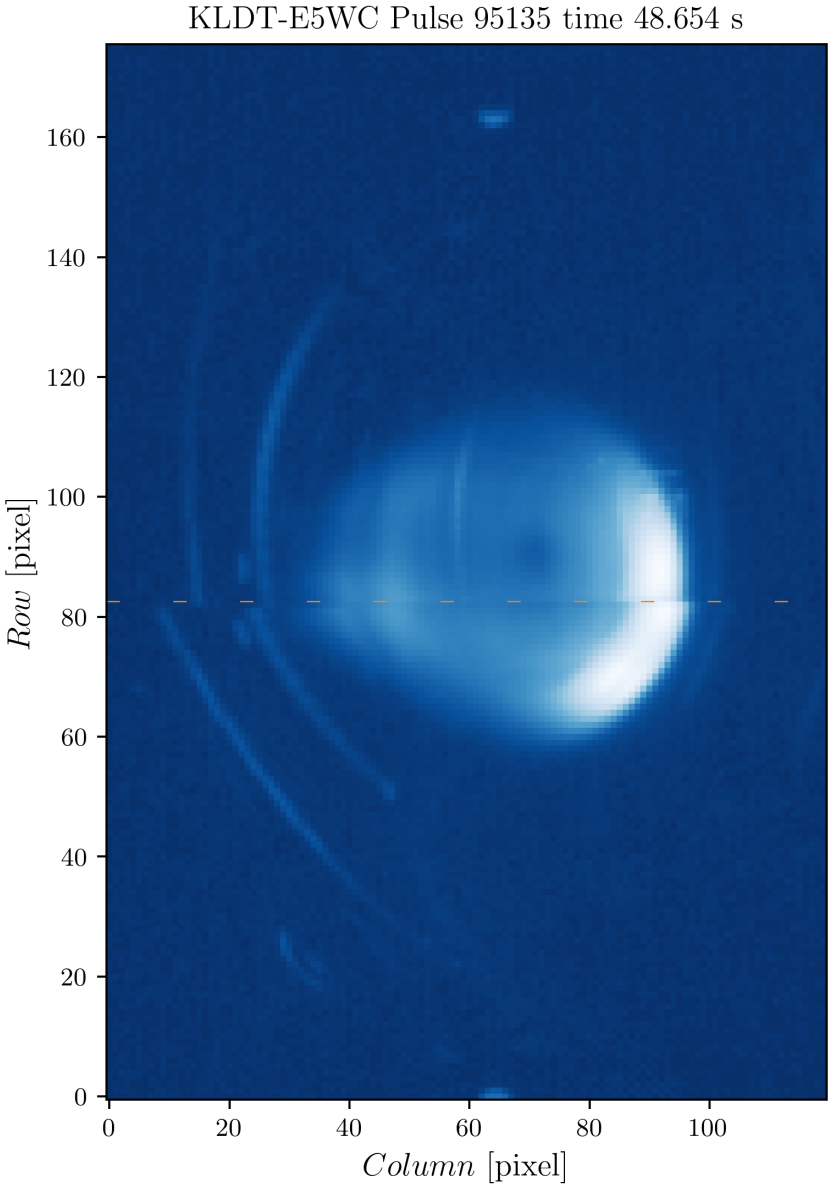

Figure 4.2: Image from JET's KLDT-E5WC infrared camera, capturing pulse 95135 at time 48.654 s. The dashed line delineates the split field of view effect of the camera optics. The displayed light pattern exemplifies typical synchrotron radiation shapes.

4.2 Synchrotron Radiation Forward Model for Cherab

A pivotal assumption underpinning the design of the synchrotron radiation model for Cherab is the notion that radiation is a function of local properties. Consequently, the spectral model can be written in a factorised form as follows:

$$R_S(\boldsymbol{r}, \boldsymbol{d}, \lambda) = r_S(\boldsymbol{r}, \boldsymbol{d}, \lambda) f(\boldsymbol{r}, \boldsymbol{v}(\boldsymbol{d}, \lambda)). \tag{4.3}$$

In this equation $f(\boldsymbol{r}, \boldsymbol{v})$ represents a six-dimensional electron distribution function in velocity and space, delineating the number density of electrons at

a specified position $\boldsymbol{r}$ and with velocity $\boldsymbol{v}$. Meanwhile, $R_S(\boldsymbol{r}, \boldsymbol{d}, \lambda)$ is the total spectral radiance of synchrotron emission radiated at the position $\boldsymbol{r}$ in the direction $\boldsymbol{d}$ with wavelength λ. The function r_S expresses the synchrotron radiation radiated per single electron of given properties. This model presupposes that the spectral radiance of synchrotron radiation generated at position $\boldsymbol{r}$ by electrons moving at velocity $\boldsymbol{v}$ in direction $\boldsymbol{d}$ is essentially a cumulative effect of radiation produced by individual particles. It should be also noted that $\boldsymbol{d}$ and λ replaces the usage of the wave vector $\boldsymbol{k}$ essentialy containing the same information. This was done in order to align the derivation of the formulae with the notation used in Cherab.

Diverging from the particle-following approach, this model bifurcates the problem into two distinct challenges. The first challenge is the simulation of the synchrotron radiation collected by an observer. The calculation of the local contributions of synchrotron radiation r_S and the interaction with the electron distribution function was developed in the frame of this work. The ray tracing simulations utilizing the radiation model are performed with the Raysect & Cherab framework. The second challenge, markedly different from conducting ray tracing simulations, involves defining the distribution function f. Because the developed SR model expects the distribution function to reflect the important effects of RE dynamics (at least those important for the particular SR simulation), the formulation of the distribution function is moved outside the simulation by expecting it as input. This separates the problem by the nature of the tasks and gives it a unique advantage to combine various realisations of distribution functions and radiation models. For example, the definition of the distribution function can be based on an output of a computationally intensive and detailed simulation of RE dynamics. It can also be based on an analytical description which allows for parameter scans and direct inversions from observed data. The radiation models can implement multiple variants of the synchrotron radiation description with varying level of complexity while still being compatible with the distribution functions.

The SR model is designed to interface with a fully six-dimensional distribution function, maximizing versatility and aligning with the model's foundational design around such functions. This setup is equipped with base classes for defining and manipulating these distribution functions, enabling the model to capture a wide range of phenomena describable by the kinetic approach. Additionally, the flexibility to work with simplified versions of the distribution function f is a significant advantage. For instance, a distribution function defined in normalized poloidal flux Ψ_n and pitch angle α can be isomapped into a 2D space over a poloidal flux map and extended to 3D by assuming toroidal symmetry. The incorporation of the magnetic vector field $\boldsymbol{B}$ to convert the pitch angle into Cartesian coordinates completes the transition to a full 6D distribution function. Tools within Raysect and Cherab for mapping, interpolation (ranging from 1D to 3D), and a basic function framework allow for the implementation of distributions from a variety of sources, including numerical outputs of RE simulations, theoretical descriptions, or a combination of both.

The crucial aspect of the model is the computation of the synchrotron radiation r_S emitted by a single particle. This involves translating the theoretical description of radiation into Cherab's radiation model. During initial discussions with the development team (E. Tomešová, O. Ficker, and J. Seidl), a consensus was

reached to start with a simplified implementation. This was primarily to gauge the response from the runaway electron community and to check if any of the underlying assumptions might invalidate the model. Depending on the feedback, a more sophisticated radiation model could be developed. The initial implementation was based on the following assumptions: the radiation lobe of a single relativistic particle is relatively narrow, leading to the simplification that particles emit all their radiation solely in the direction of their velocity. Furthermore, given the narrowness of the synchrotron spectrum emitted by an electron, it was posited that the spectrum could be approximated as a Dirac delta function, with the wavelength determined by the particle's energy

$$R_S(\boldsymbol{r}, \boldsymbol{d}, \lambda) \approx \delta \left(\frac{\boldsymbol{v}}{|\boldsymbol{v}|} - \frac{\boldsymbol{d}}{|\boldsymbol{d}|} \right) R_S(\boldsymbol{r}, \boldsymbol{v}), \tag{4.4}$$

where the notation of the dependance of $\boldsymbol{v}(\boldsymbol{d}, \lambda)$ on $\boldsymbol{d}$ and λ is inherently assumed but the notation dropped for the sake of visual reduction of the equations. The aforementioned simplifications in the SR model are not expected to introduce significant errors in forward models of observed radiation. Crucially, these simplifications eliminate the need for integration in velocity space, thereby reducing computational intensity. This makes the model more suitable for initial tests and evaluations.

In a ray tracing simulation, Raysect invokes radiation models to determine the local contribution to the ray's spectrum. During this process, it supplies the models with essential information: the position $\boldsymbol{r}$, the direction $\boldsymbol{d}$ of radiation, and the wavelengths λ of the ray's spectrum. This information is adequate for calculating the local synchrotron radiation contribution.

To establish a solid physics basis for the model, O. Ficker recommended a set of equations from [89]. In the frame of this work equations provided in [89] were used to derive the formulae needed for synchrotron radiation model in Cherab. Chapter 8 of this reference details formulas that are well-suited for integration into the SR model. It also illustrates a method for calculating SR spectra that aligns closely with the approach selected for implementation in Cherab. The power radiated in a specific wavelength range can be expressed as

$$\begin{aligned} P(\boldsymbol{r}, \boldsymbol{d}, \lambda) d\lambda =& P(E, B) f(\boldsymbol{r}, \boldsymbol{v}) d\boldsymbol{v} = \\ =& \frac{4}{3} \sigma_T c \frac{B^2}{2\mu_0} \left(\frac{E}{m_e c^2} \right)^2 \delta \left(\frac{\boldsymbol{v}}{|\boldsymbol{v}|} - \frac{\boldsymbol{d}}{|\boldsymbol{d}|} \right) f(\boldsymbol{r}, \boldsymbol{v}) d\boldsymbol{v}. \end{aligned} \tag{4.5}$$

The left side of the equation represents the volumetric spectral power density radiated at wavelength λ for a given position $\boldsymbol{r}$ and radiation direction $\boldsymbol{d}$. The right-hand side of the equation redefines the radiated power $P(E, B)$ as elaborated in (4.2). The term $f(\boldsymbol{r}, \boldsymbol{v}) d\boldsymbol{v}$ signifies the volumetric particle density. The Dirac-delta function $\delta \left(\frac{\boldsymbol{v}}{|\boldsymbol{v}|} - \frac{\boldsymbol{d}}{|\boldsymbol{d}|} \right)$ is an expression of the simplification that particles radiate solely in their velocity direction. To integrate (4.5) into Cherab, the velocity vector $\boldsymbol{v}$ must be articulated in terms of the radiation direction $\boldsymbol{d}$ and the observed wavelength λ. This conversion utilizes a set of equations from [89]:

$$\gamma = \frac{1}{\sqrt{1-\frac{v^2}{c^2}}} \approx \sqrt{\frac{\nu}{\nu_g}}, \tag{4.6}$$

$$E = \gamma m_e c^2 = \sqrt{\frac{\nu}{\nu_g}} m_e c^2 = \sqrt{\frac{c}{\lambda \nu_g}} m_e c^2. \tag{4.7}$$

Here, E denotes the kinetic energy of the electron, γ is the relativistic factor, ν represents the frequency of the radiation, and ν_g is the electron cyclotron frequency. The next step involves expressing the particle's energy E in (4.5) using (4.7):

$$P(\boldsymbol{r}, \boldsymbol{d}, \lambda) d\lambda = \frac{4}{3} \sigma_T \frac{B^2}{2\mu_0} \frac{c^2}{\lambda \nu_g} \delta \left(\frac{\boldsymbol{v}}{|\boldsymbol{v}|} - \frac{\boldsymbol{d}}{|\boldsymbol{d}|} \right) f(\boldsymbol{r}, \boldsymbol{v}) d\boldsymbol{v}. \tag{4.8}$$

The second step involves using (4.6) to represent the velocity vector $\boldsymbol{v}$ in terms of λ and $\boldsymbol{d}$, which can be articulated as:

$$\boldsymbol{v} = c\sqrt{1-\frac{1}{\gamma^2}} \frac{\boldsymbol{v}}{|\boldsymbol{v}|} = c\sqrt{1-\frac{\lambda \nu_g}{c}} \frac{\boldsymbol{v}}{|\boldsymbol{v}|} \tag{4.9}$$

Subsequently, the differential $\frac{d\boldsymbol{v}}{d\lambda}$ derived from $d\boldsymbol{v}$ is given by:

$$\frac{d\boldsymbol{v}}{d\lambda} = \frac{\nu_g}{2\sqrt{1-\frac{\lambda \nu_g}{c}}} \frac{\boldsymbol{v}}{|\boldsymbol{v}|}. \tag{4.10}$$

Incorporating (4.9) and (4.10) into (4.8) yields the equation for radiated power density as a function of λ:

$$P(\boldsymbol{r}, \boldsymbol{d}, \lambda) d\lambda = \frac{4}{3} \sigma_T \frac{B^2}{2\mu_0} \frac{c^2}{\lambda \nu_g} \delta \left(\frac{\boldsymbol{v}}{|\boldsymbol{v}|} - \frac{\boldsymbol{d}}{|\boldsymbol{d}|} \right) f \left(\boldsymbol{r}, c\sqrt{1-\frac{\lambda \nu_g}{c}} \frac{\boldsymbol{v}}{|\boldsymbol{v}|} \right) \frac{\nu_g}{2\sqrt{1-\frac{\lambda \nu_g}{c}}} \frac{\boldsymbol{v}}{|\boldsymbol{v}|} d\lambda. \tag{4.11}$$

In the equation above, the $d\lambda$ terms cancel out, resulting in units of W. To align with Cherab's definition of a radiation model that returns spectral radiance in units of $\mathrm{W\,nm^{-1}\,sr^{-}1}$, equation (4.11) needs to be multiplied by $\frac{1}{4\pi d\lambda}$:

$$R(\boldsymbol{r}, \boldsymbol{d}, \lambda) = \frac{1}{12\pi d\lambda} \sigma_T \frac{B^2}{\mu_0} \frac{c^2}{\lambda \nu_g} \delta \left(\frac{\boldsymbol{v}}{|\boldsymbol{v}|} - \frac{\boldsymbol{d}}{|\boldsymbol{d}|} \right) f \left(\boldsymbol{r}, c\sqrt{1-\frac{\lambda \nu_g}{c}} \frac{\boldsymbol{v}}{|\boldsymbol{v}|} \right) \frac{\nu_g}{\sqrt{1-\frac{\lambda \nu_g}{c}}} \frac{\boldsymbol{v}}{|\boldsymbol{v}|}. \tag{4.12}$$

4.3 First Results

The development of the new SR model was primarily driven by the necessity to interpret the diverse features observed in infrared camera images, particularly those highlighted in [90]. A notable example is a frame captured during JET's pulse 95135 by the KLDT-E5WC mid-infrared camera [91], as depicted in Fig. 4.3. The dashed line in the image indicates the split field of view effect due to the camera's optics. Several distinct light structures are visible in the image. In

addition to the conventional synchrotron light pattern, which resembles a croissant, there are three poloidally periodic drops in intensity, evocative of magnetic islands (periodic structures: Fig. 4.3-b). The central area of the image exhibits a notable dip in radiation intensity (hollow profile: Fig. 4.3-c). Furthermore, sharp-shaped light structures, akin to the contours of JET's first wall components (reflections: Fig. 4.3-a), suggest the possibility of synchrotron radiation reflections.

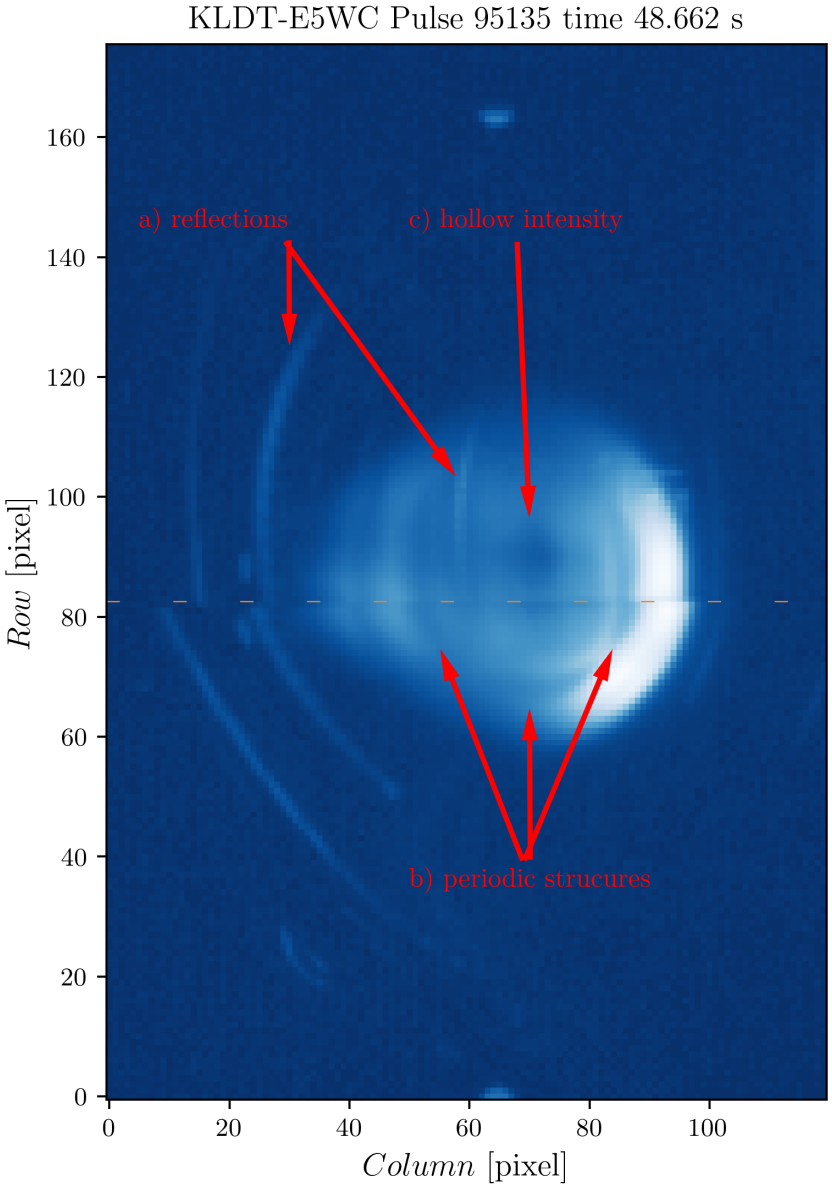

Figure 4.3: Image from JET's KLDT-E5WC infrared camera during pulse 95135, captured at 48.662 ms. The dashed line indicates the split field of view effect. The image reveals typical synchrotron radiation patterns, a hollow intensity profile, three poloidally periodic intensity drops, and sharp-shaped light structures resembling JET's first wall components.

The spectral calibration for the KLDT-E5WC camera, provided by S. Silburn, is illustrated in Fig. 4.4. The camera operates within a spectral band of approximately 3 - 3.5 μm. For simulation purposes, a flat sensitivity of 1 was assumed within this range, but the number of spectral bins was reduced to 10 to expedite

computation. The spectral sensitivity, when compared with the curves in Fig. 4.1, indicates that the camera is responsive to synchrotron radiation from electrons with energies ranging from approximately 15 MeVto 30 MeV, within a magnetic field magnitude of $1 - 5\,\mathrm{T}$. Notably, the toroidal field magnitude for pulse 95135 was around 3.5 T.

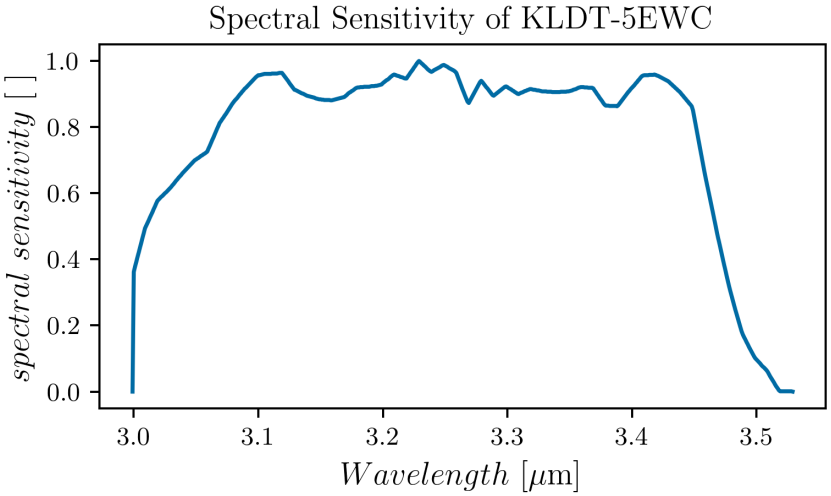

Figure 4.4: Normalized sensitivity curve of the KLDT-E5WC camera. Data kindly provided by S. Silburn.

To facilitate the simulation of synchrotron radiation, a simplified description of the distribution function was developed in collaboration with O. Ficker, E. Tomešová, and J. Seidl. This approach aimed to balance computational efficiency with sufficient variability to encapsulate the primary characteristics of REs that influence synchrotron radiation properties. The distribution function was represented in the following factorised form:

$$f(\boldsymbol{r}, \boldsymbol{v}) = Cn(\boldsymbol{r}) f_\alpha(\alpha) f_v(\boldsymbol{v}). \tag{4.13}$$

Each component of this function addresses a crucial aspect of the distribution:

- $n(\boldsymbol{r})$: This term represents the spatial distribution of runaway electron (RE) density.
- $f_\alpha(\alpha)$: This factor accounts for the dependence of electron density on the pitch angle α.
- $f_v(\boldsymbol{v})$: This component describes the distribution of electrons in velocity space.
- C: A normalization constant to ensure the proper scaling of the distribution.

The form of f_α was chosen to reflect an exponential decay of electron density with an increasing pitch angle α. The function f_v was designed to have a Gaussian shape. This configuration enables the coverage of both an exponential decay with

increasing particle energy and a bump on the tail of a Maxwellian distribution:

$$\begin{aligned} f_v(\boldsymbol{v}) &\propto \exp\left(-\frac{(\gamma-\mu)^2}{2\sigma^2}\right) \\ f_\alpha(\alpha) &\propto \exp\left(-\frac{B_{LFS}}{|\boldsymbol{B}(\boldsymbol{r})|}c\alpha\right) \end{aligned} \tag{4.14}$$

To accurately simulate the synchrotron radiation, the model accounts for the behavior of trapped particles that cannot propagate to the high field side by taking into account the magnitudes of magnetic field. The term B_{LFS} denotes the magnitude of the magnetic field at the outboard intersection of the midplane with the magnetic surface corresponding to $\Psi(\boldsymbol{r})$. The term $\boldsymbol{B}(\boldsymbol{r})$ is the local magnetic field at the position of the particle. The terms μ and σ are respectively the location and scale parameters of the Gaussian distribution expressed in the γ space.

To encompass the effects of magnetic islands, the spatial distribution of runaway electron density $n(\boldsymbol{r})$ and the magnetic field $\mathbf{B}(\boldsymbol{r})$ were informed by the results of JOREK simulations [92, 93], with specific data kindly provided by V. Bandaru [94, 90]. O. Ficker played a pivotal role in interpreting the JOREK data and formulating them for convenient application. The data were adapted for integration into Raysect's function framework, leading to the following expressions:

$$\begin{aligned} \mathbf{B}(\boldsymbol{r}) =& \mathbf{B}_0(\boldsymbol{r}) + \sum_N \mathbf{B}_N(\boldsymbol{r}) = \mathbf{B}_0(\boldsymbol{r}) + \sum_N \left(\mathbf{B}_N^{\sin}(\boldsymbol{r})\sin(N\varphi) + \mathbf{B}_N^{\cos}(\boldsymbol{r})\cos(N\varphi)\right) \\ n(\boldsymbol{r}) =& n_0(\boldsymbol{r}) + \sum_N n_N(\boldsymbol{r}) = n_0(\boldsymbol{r}) + \sum_N \left(n_N^{\sin}(\boldsymbol{r})\sin(N\varphi) + n_N^{\cos}(\boldsymbol{r})\cos(N\varphi)\right). \end{aligned} \tag{4.15}$$

In the implementation, the magnetic field is decomposed into components: the equilibrium field $\mathbf{B}_0(\boldsymbol{r})$ and the perturbative harmonics $\mathbf{B}_N$ with sine $\mathbf{B}_N^{\sin}(\boldsymbol{r})$ and cosine $\mathbf{B}_N^{\cos}(\boldsymbol{r})$ components. The angle φ is the toroidal angle and N indexes the harmonic components. This separation is evident in Fig. 4.5 and Fig. 4.6, which display the radial components of the equilibrium magnetic field $B_{r,0}$ and of the perturbative component $B_{r,1}$, respectively. The perturbation's magnitude is notably smaller ($\approx$ two orders of magnitude) than that of the equilibrium field, rendering it almost invisible in the superposition shown in Fig. 4.7.

This approach of separation was similarly applied to the runaway electron volumetric density $n(\boldsymbol{r})$. The toroidally symmetric and asymmetric spatial distributions of runaway electron densities are shown in Fig. 4.8 and Fig. 4.9, respectively. The superposition of these components, as seen in Fig. 4.10, highlights the more pronounced effect of the perturbative part.

To facilitate the integration of this data into the model, a set of Raysect's 3D vector and scalar functions was utilized, allowing the model to load the data in the format described by equation (4.15). The implementation is versatile, enabling the loading of any component to independently simulate their contribution to the synchrotron radiation.

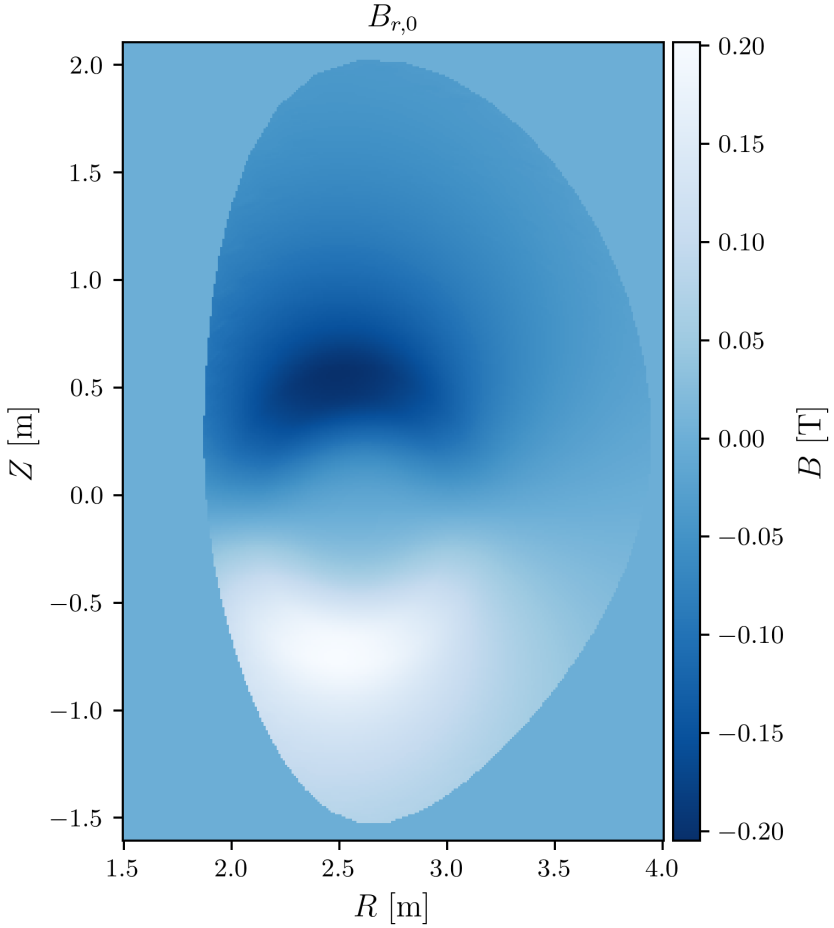

Figure 4.5: Radial component of the equilibrium magnetic field $B_{r,0}$ from JOREK simulation.

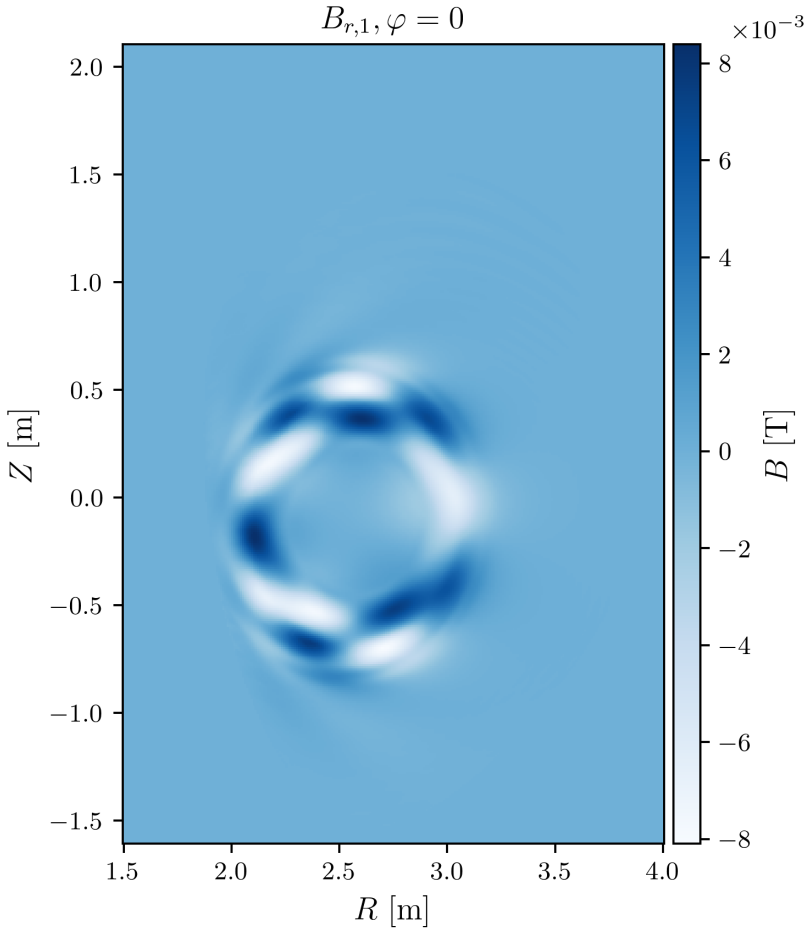

Figure 4.6: Radial component of the perturbative magnetic field $B_{r,1}$ for the zero toroidal angle from JOREK simulation.

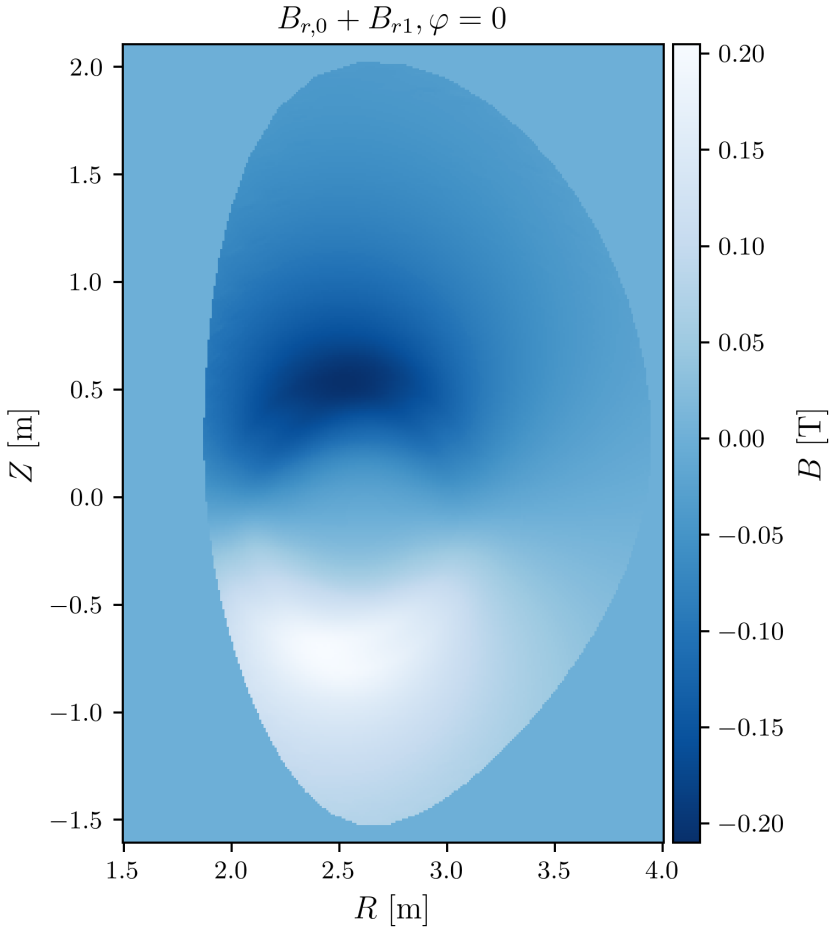

Figure 4.7: Superposition of the radial component of the equilibrium magnetic field $B_{r,0}$ and the perturbative magnetic field $B_{r,1}$ for the zero toroidal angle from JOREK simulation. The perturbative field's effect is almost invisible due to its smaller magnitude.

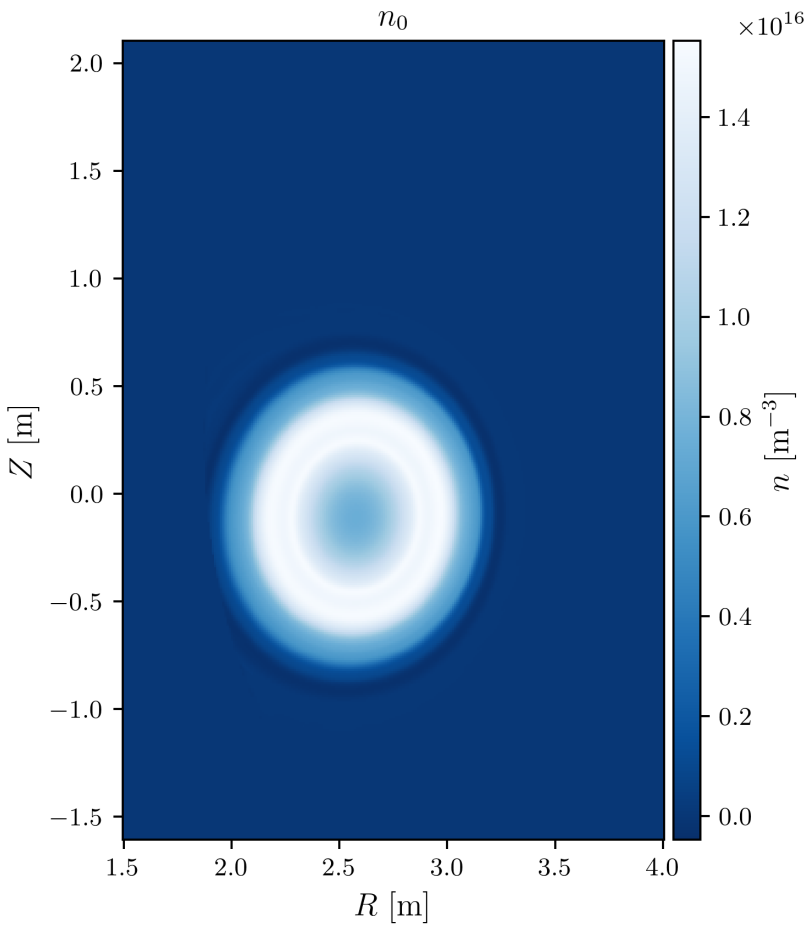

Figure 4.8: Toroidally symmetric component of runaway electron density n_0 from JOREK simulation.

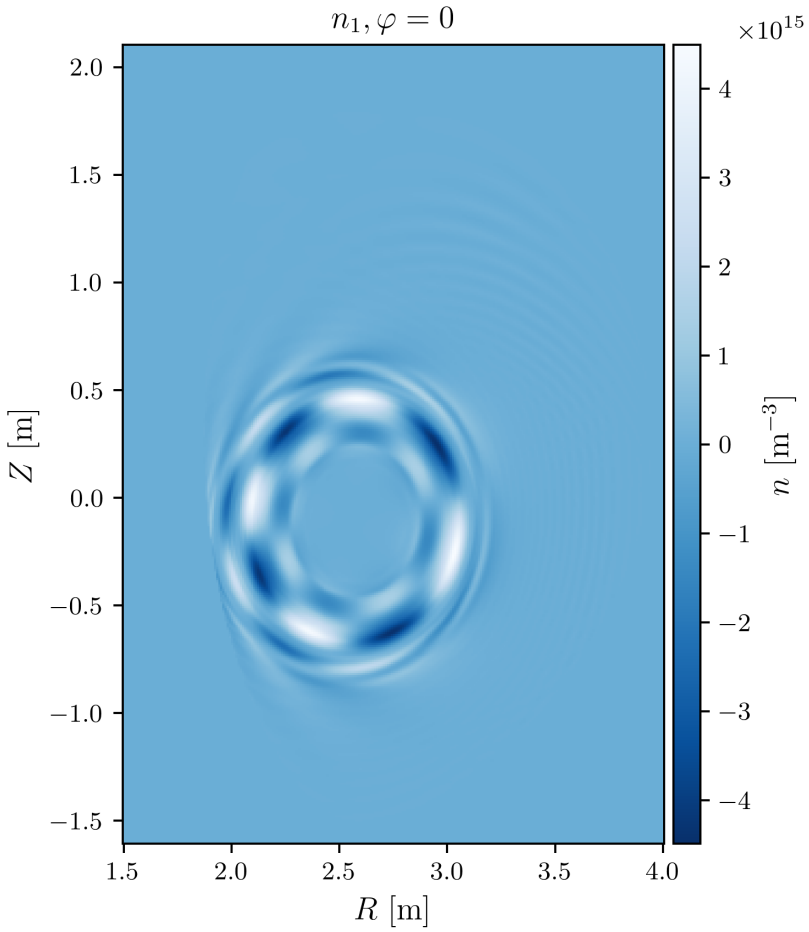

Figure 4.9: Toroidally asymmetric component of runaway electron density n_1 for the zero toroidal angle from JOREK simulation.

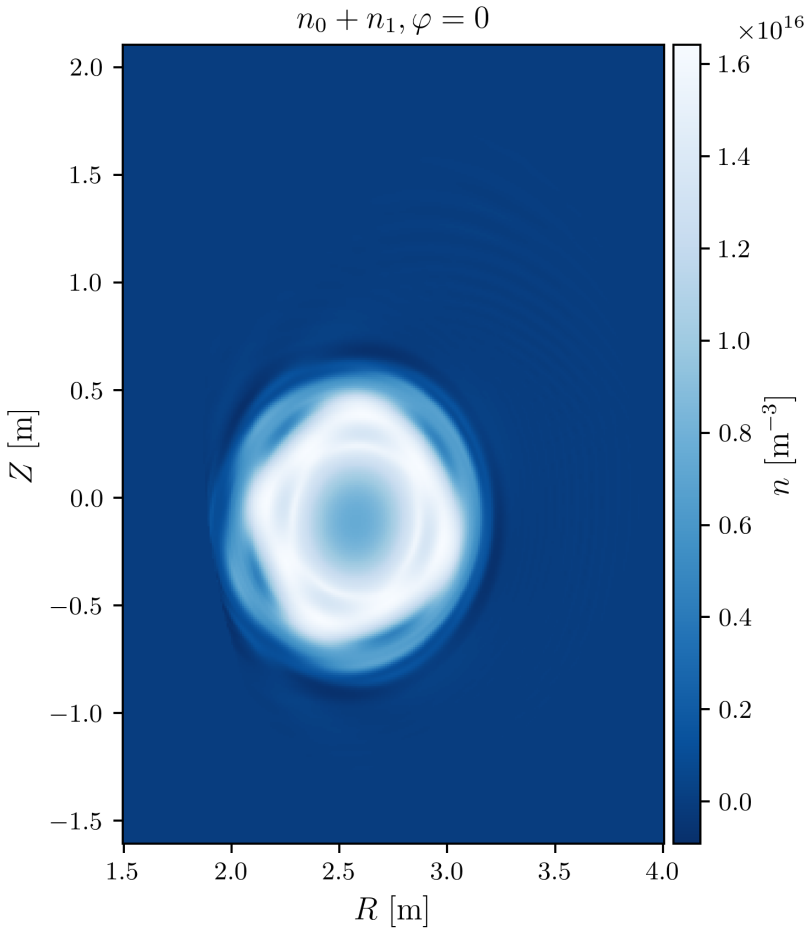

Figure 4.10: Superposition of the toroidally symmetric and asymmetric components of runaway electron density $n_0 + n_1$ for the zero toroidal angle from JOREK simulation. The perturbative component is clearly visible.

To demonstrate the capabilities of the newly integrated synchrotron radiation model in Cherab, a series of simulations were conducted, ranging from simple to more complex scenarios. It is important to note that the primary objective of this study was to verify the model's ability to replicate features observed in infrared camera images, rather than to perform interpretative modeling or achieve an exact match with experimental data. Future applications are intended for these more detailed analyses. The camera model in Cherab, closely approximating the experimental FOV of the KLDT-E5WC camera, was created using a Calcam [95] calibration file provided by S. Silburn, facilitating the creation of Raysect's *VectorCamera*.

The initial simulations were simplified, excluding reflections from the first wall and employing only the toroidally symmetric components of the magnetic field ($\boldsymbol{B} = \mathbf{B}_0$) and runaway electron density ($n = n_0$). The camera was set to observe wavelengths in the range $(3.1, 3.5)\,\mu$m and ten spectral bins. The toroidal magnetic field magnitude was 3.5T. The simulation results are presented in Fig. 4.11 and Fig. 4.12. Each simulation required approximately 9×10^3 s per single thread on an AMD EPYC 7542 processor.

In Fig. 4.11, a decaying tail in the velocity distribution was employed. The resulting image shows a distinct ring of SR radiation, aligning with the spatial

distribution of RE density from Fig. 4.8. However, the intensity of the forward-modelled SR ring decays more slowly towards the HFS, suggesting that a faster decaying velocity distribution might be more appropriate to reduce the density of higher-energy electrons that radiate more strongly on the LFS.

Fig. 4.12 presents a scan of RE energy. To simulate a bump on tail of the electron distribution function, the mean values were set to $\mu = 12.5\,\mathrm{MeV}$ in Fig. 4.12a, $\mu = 15\,\mathrm{MeV}$ in Fig. 4.12b, and $\mu = 17.5\,\mathrm{MeV}$ in Fig. 4.12c. The scale of the distribution was set to $\sigma = 3$ MeV. These simulations revealed a clear shift in the intensity distribution from the HFS to the LFS, demonstrating the impact of increased RE energy. The distribution in Fig. 4.12a appears to most closely match the experimental image in terms of radiation localization.

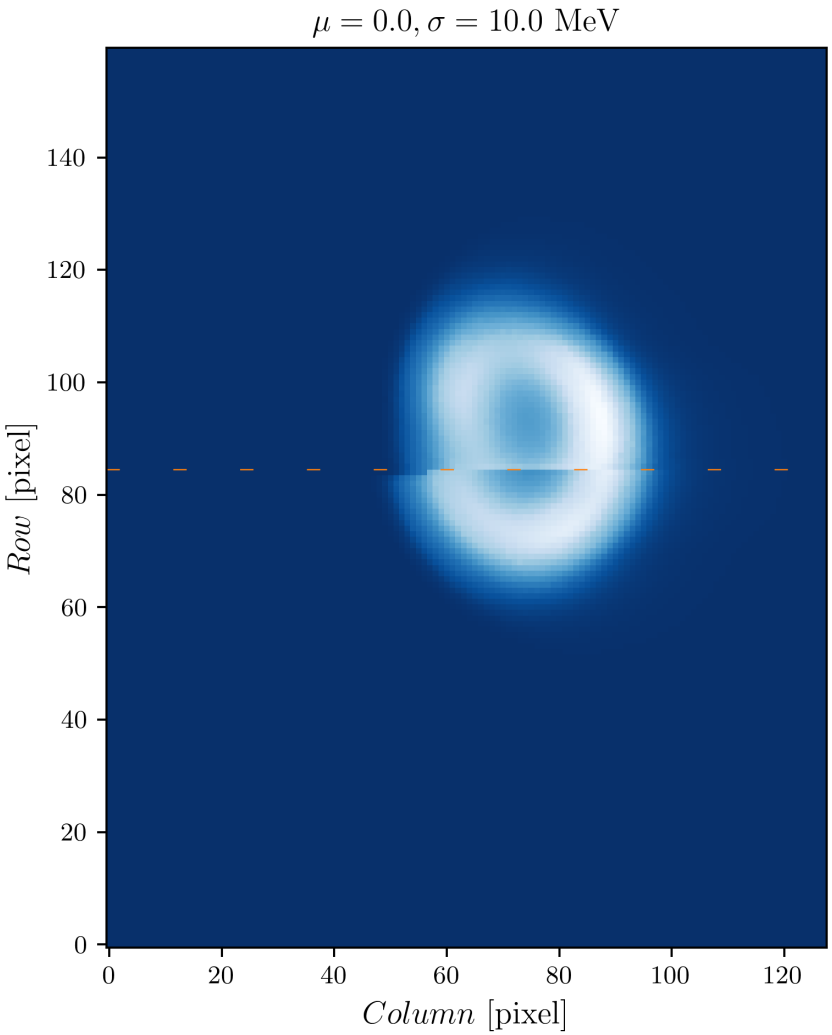

Figure 4.11: The figure illustrates a forward model of the KLDT-E5WC camera, capturing a SR spot. In this model, the distribution function parameters were established as $n = n_0$ and $\boldsymbol{B} = \boldsymbol{B}_0$, with the exclusion of reflective effects. The velocity distribution is characterised by a mean (μ) of 0 and a standard deviation (σ) of 10 MeV.

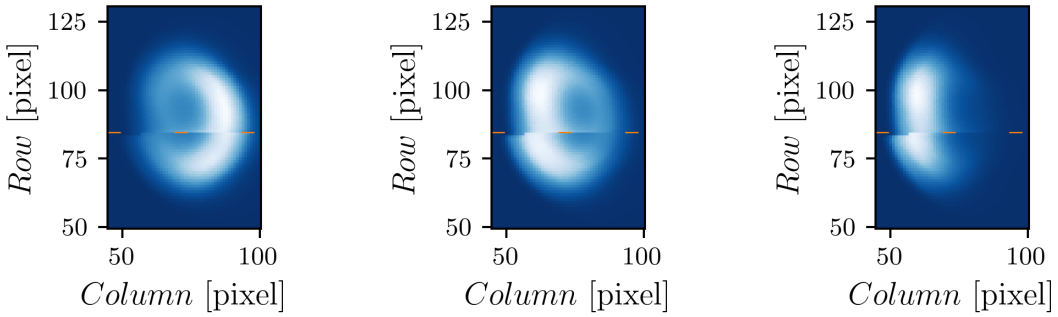

(a) $\mu = 12.5\,\mathrm{MeV}$ (b) $\mu = 15\,\mathrm{MeV}$ (c) $\mu = 17.5\,\mathrm{MeV}$

Figure 4.12: The trio of plots depicts forward models of the KLDT-E5WC camera, featuring SR. For these models, the distribution function was configured with $n = n_0$ and $\boldsymbol{B} = \boldsymbol{B}_0$, and reflections were deliberately omitted. The velocity distribution aimed to mimic a 'bump-on-tail' scenario. It was characterised by a constant $\sigma = 3\,\mathrm{MeV}$. The mean values (μ) were varied as follows: $\mu = 12.5\,\mathrm{MeV}$ in Fig. 4.12a, $\mu = 15\,\mathrm{MeV}$ in Fig. 4.12b, and $\mu = 17.5\,\mathrm{MeV}$ in Fig. 4.12c.

To illustrate the evolution of the spectral properties of the radiation observed in relation to the energy of RE and the observed radial position, simulations were conducted for the camera pixels in the row 63. These simulations were characterized by an extended spectral range $(0.5, 7.5)\,\mu\mathrm{m}$, high spectral resolution of 7 nm (1000 spectral bins), and the same velocity distribution functions as used in Fig. 4.12. The spectra simulated for pixels in columns 60, 70, and 80 of row 63 are exhibited in Fig. 4.13. The column number correlates with the magnitude of the toroidal magnetic field, explaining why the peak of the synchrotron radiation spectra shifts towards higher values for lower column numbers. This shift explains the effect of increased RE energy observed in Fig. 4.12.

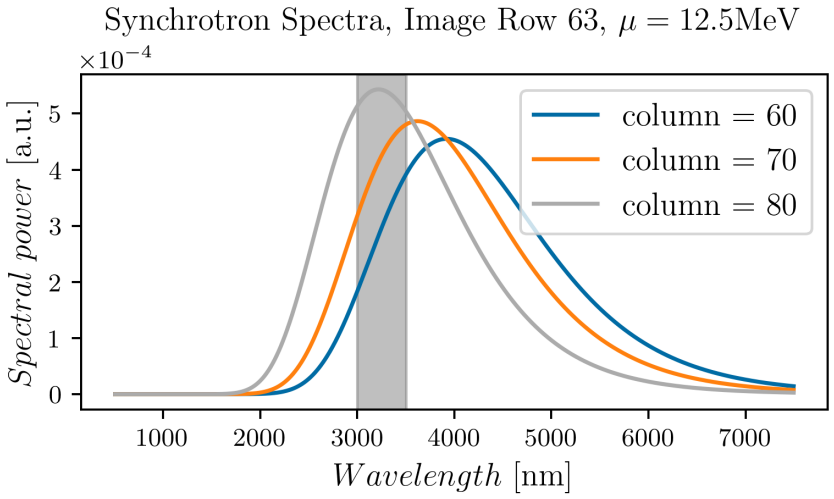

(a)

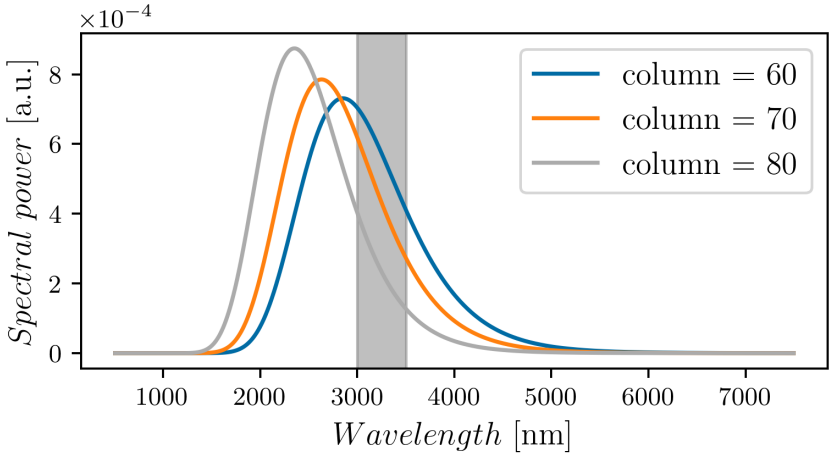

(b)

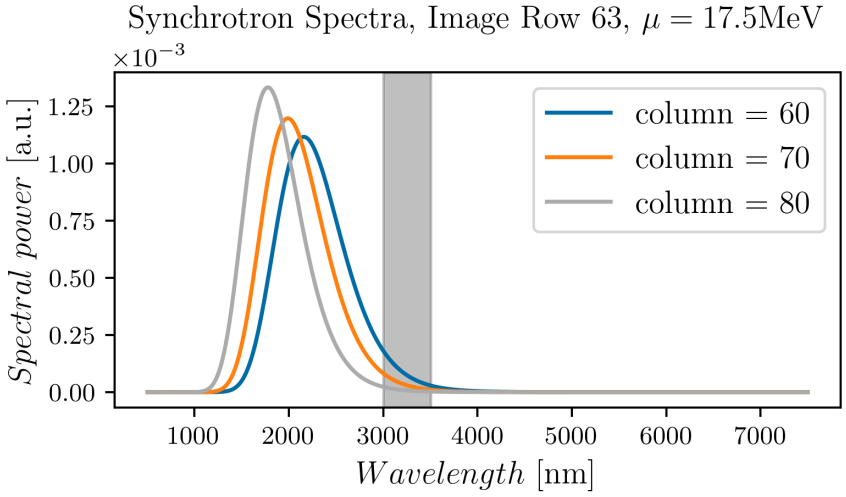

(c)

Figure 4.13: Synchrotron radiation spectra for three pixels in the image columns 60, 70 and 80 and row 63 are displayed. The grey stripe marks the sensitivity region of the KLDT-E5WC camera. As the column number decreases, the pixels observe the vessel more towards the LFS, experiencing lower toroidal magnetic field magnitudes which causes the peaks to shift to longer wavelengths, mirroring the effect from Fig. 4.12.

In the subsequent phase, the model was enhanced by incorporating toroidally asymmetric components of the magnetic field and runaway electron density. The simulation outcomes, integrating the spatial distribution of RE and $\mathbf{B}$ described by $n_0 + n_1, \boldsymbol{B} = \boldsymbol{B}_0 + \boldsymbol{B}_1$, are presented in Fig. 4.14. A decaying velocity distribution tail was modeled using parameters $\mu = 0.0$ and $\sigma = 10\,\mathrm{MeV}$. The inclusion of additional components for $\boldsymbol{B}$ and n resulted in a marginal increase in computational demands, with the simulation taking approximately $1.6 \times 10^4\,\mathrm{s}$ per single thread on an AMD EPYC 7542 processor.

Comparing the results of simulations without (Fig. 4.11) and with (Fig. 4.14) toroidal asymmetries reveals a significant difference. The predominantly poloidally symmetric ring pattern of SR in Fig. 4.11 is noticeably disrupted by magnetic islands in Fig. 4.14. To better illustrate this impact, Fig. 4.15 displays next to each other the two variants, with the first two images from the left representing the toroidally symmetric and asymmetric cases, respectively. The image on the right highlights the differences between them, revealing a visible poloidal mode structure.

Further investigation into the influence of n_1 and $\boldsymbol{B}_1$ components was conducted through additional simulations. The first case, depicted in Fig. 4.16, utilized the toroidally asymmetric component $n = n_0 + n_1$ of the spatial distribution of RE for toroidally symetric magnetic field $\mathbf{B}_0$. The images, arranged from left to right, show the toroidally symmetric case $n = n_0, \boldsymbol{B} = \mathbf{B}_0$, the toroidally asymmetric case $n = n_0 + n_1, \boldsymbol{B} = \mathbf{B}_0$, and the difference between the two. In Fig. 4.16c, a clear modal structure similar to Fig. 4.15c is evident. The second scenario, shown in Fig. 4.17, exclusively employed the toroidally asymmetric component of the magnetic field $n = n_0, \boldsymbol{B} = \mathbf{B}_0 + \boldsymbol{B}_1$. The panels are organized similarly to previous cases, but the rightmost panel lacks a clear structure. The noise in the image section where SR would typically appear results from Monte-Carlo sampling in Raysect's ray tracing procedure. This indicates that the periodic structures observed in Fig. 4.3 are indeed attributable to magnetic islands. The separate perturbation simulations for n_1 and $\boldsymbol{B}_1$ also suggest the reconfiguration of the RE density's spatial distribution plays a crucial role, whereas the predicted level of magnetic field's perturbation seems to have negligible visible impact in the simulations.

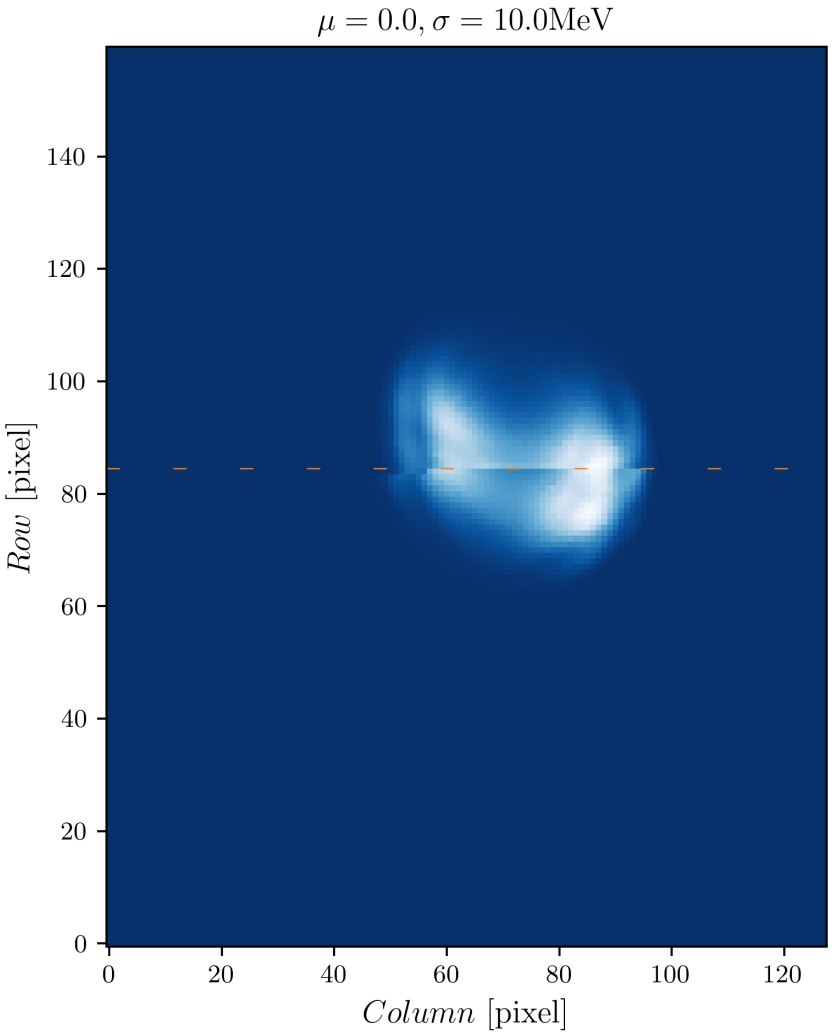

Figure 4.14: The figure illustrates a forward model of the KLDT-E5WC camera, highlighting a SR spot. In this model, the distribution function's properties were configured as $n = n_0 + n_1$ and $\boldsymbol{B} = \boldsymbol{B}_0 + \boldsymbol{B}_1$, with the exclusion of reflections. The velocity distribution is characterized by a mean (μ) of 0 and a standard deviation (σ) of 10 MeV

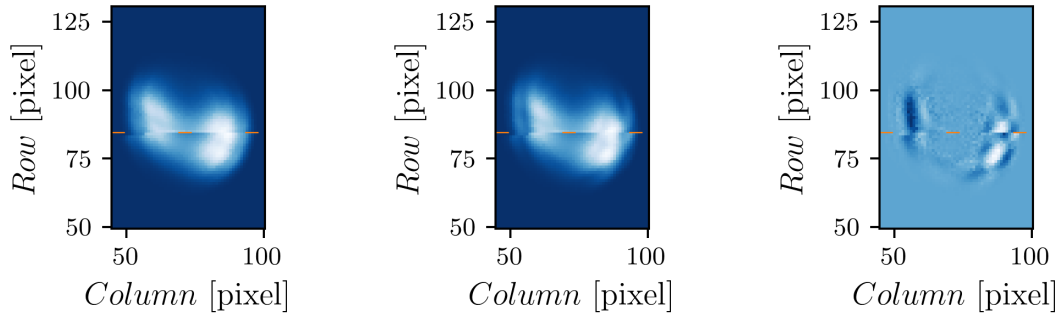

(a) $n_0, \boldsymbol{B}_0$ (b) $n_0 + n_1, \boldsymbol{B}_0 + \boldsymbol{B}_1$ (c) difference

Figure 4.15: The plots show the impact of integrating the toroidal asymmetric componens $\boldsymbol{B}_1$ and n_1 on the synchrotron image. The left panel presents the image generated using the forward model with parameters set as $n = n_0$ and $\boldsymbol{B} = \boldsymbol{B}_0$. The central panel depicts the image from the forward model with modified parameters: $n = n_0 + n_1$ and $\boldsymbol{B} = \boldsymbol{B}_0 + \boldsymbol{B}_1$. The right panel highlights the differences between these two images.

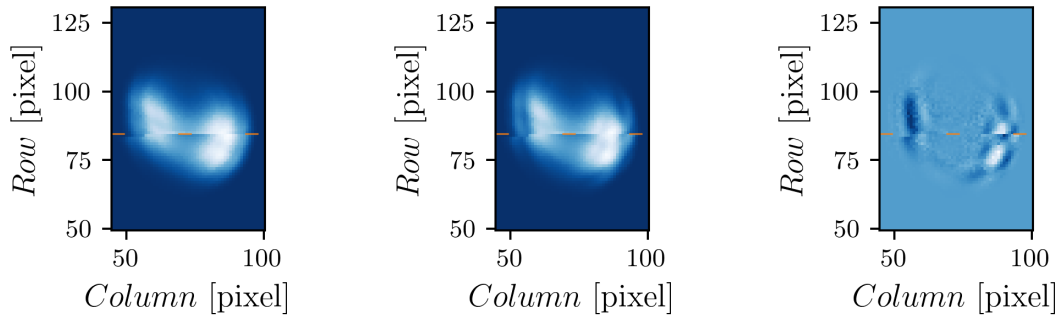

(a) $n_0, \boldsymbol{B}_0$ (b) $n_0 + n_1, \boldsymbol{B}_0$ (c) difference

Figure 4.16: The plots demonstrate the effect of incorporating solely the n_1 toroidal asymmetric component of the RE spatial distribution on the synchrotron image. The left panel depicts the image derived from the forward model with parameters set to $n = n_0$ and $\boldsymbol{B} = \boldsymbol{B}_0$. The middle panel illustrates the image resulting from the forward model including the asymmetric component, specified as $n = n_0 + n_1$ and $\boldsymbol{B} = \boldsymbol{B}_0$. The right panel contrasts the two images, showcasing the difference attributable to the n_1 component.

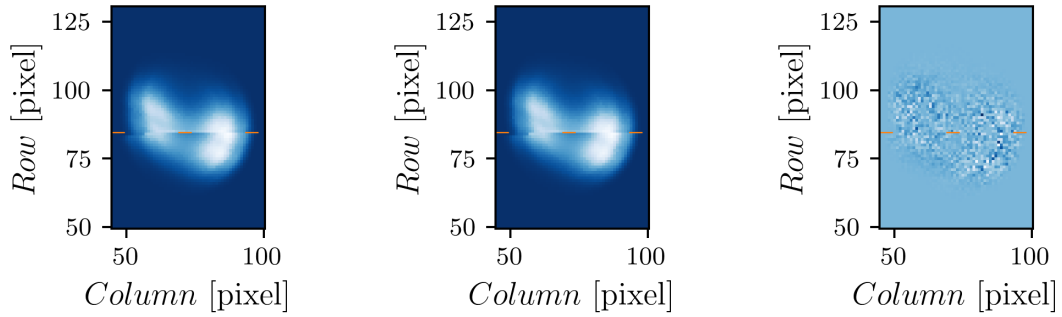

(a) $n_0, \boldsymbol{B}_0$ (b) $n_0, \boldsymbol{B}_0 + \boldsymbol{B}_1$ (c) difference

Figure 4.17: The plots highlight the effect of exclusively incorporating the $\boldsymbol{B}_1$ toroidal asymmetric component of magnetic field into the synchrotron image. The left panel displays the image generated by the forward model with parameters set to $n = n_0$ and $\boldsymbol{B} = \boldsymbol{B}_0$. The middle panel depicts the image obtained from the forward model modified to include the asymmetric component of magnetic field, defined as $n = n_0$ and $\boldsymbol{B} = \boldsymbol{B}_0 + \boldsymbol{B}_1$. The right panel contrasts these two images, illustrating the differential impact attributable to the $\boldsymbol{B}_1$ component.

In the final stage, the forward simulation of KLDT-E5WC SR radiation intensity was conducted, incorporating both toroidally perturbing components and a reflective first wall. To our knowledge, no existing code supports such a comprehensive simulation, rendering the addition of the SR model to Cherab a unique development. The surface properties of the plasma-facing tiles, integral to the simulation, were adopted from the Cherab-JET package as originally detailed in [96].

Simulations that include reflections are significantly more computationally intensive due to the substantially higher number of rays required to achieve an acceptable noise level. This simulation demanded approximately 1.6×10^6 s per single core on an AMD EPYC 7542 processor. The resultant image is showcased in Fig. 4.18. To accentuate the reflections, the same image was reproduced in Fig. 4.19 with exponentially rescaled intensity. The reflections vividly delineate structures such as outboard and inboard limiters, the divertor, and the upper part of the vessel.

To illustrate the contribution of reflections to the overall image, a triptych is presented in Fig. 4.20. The leftmost panel displays the image simulated without reflections, the middle panel includes reflections, and the rightmost panel, obtained by subtracting the non-reflective image from the reflective one, highlights the impact of reflections. The intensities in these images were exponentially rescaled to emphasize the reflections. The differential effect of reflections is further elaborated in Fig. 4.21 at an enlarged scale. Besides the clearly visible reflections, a distinct rectangular structure emerges in the central part of the image, occupied by direct SR radiation. This structure corresponds to the lower hybrid and ion cyclotron antennas, as detailed in Figure 5 of [91]. This observation suggests that reflections could significantly influence the inversion of RE distribution from infrared camera images. The influence is also clearly visible in the experimental image in Fig. 4.2 where the reflection from the antenna is also visible. However, it must be noted that accounting for reflections in fusion devices is challenging due to the plasma's alteration of first wall surface properties. Nonetheless, such

simulations can provide valuable estimates of the impact of reflections. The noisy appearance of the image in Fig. 4.21 can be attributed to insufficient ray tracing and aliasing effects, with the antenna structures likely being too small for the camera's resolution.

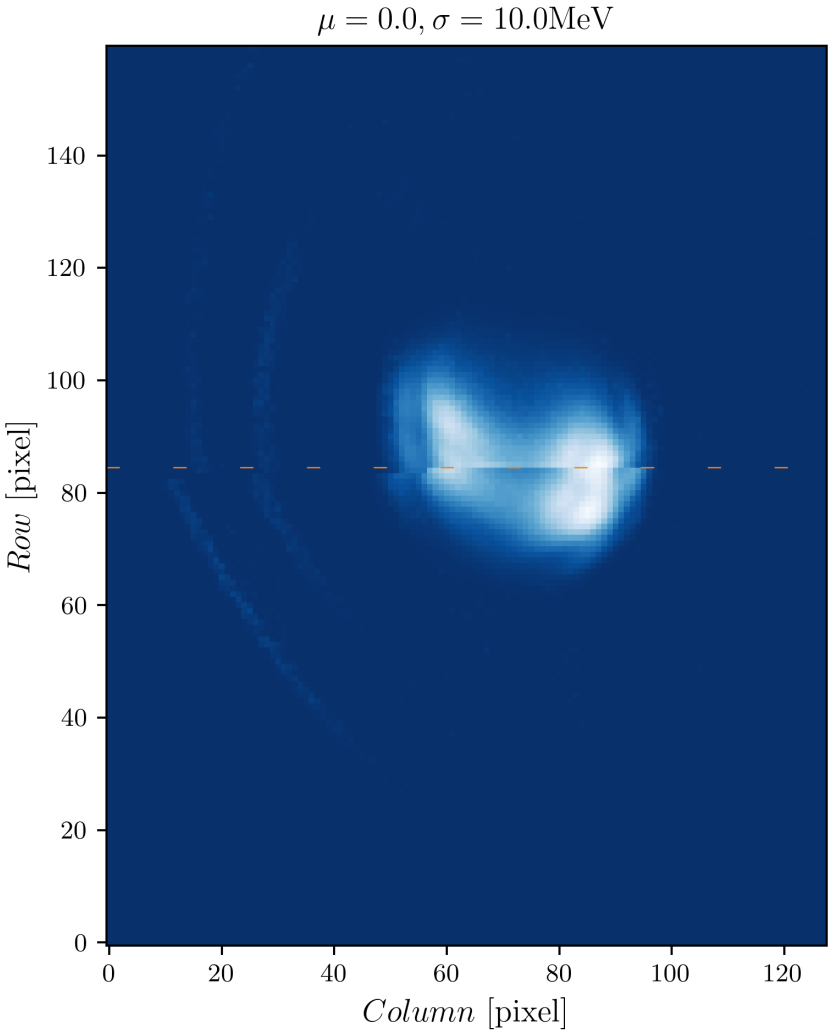

Figure 4.18: The figure illustrates a forward model of the KLDT-E5WC camera, showcasing a SR spot. In this model, the distribution function's properties were configured as $n = n_0 + n_1$ and $\boldsymbol{B} = \boldsymbol{B}_0 + \boldsymbol{B}_1$, inclusive of reflections. The velocity distribution is characterized by a mean (μ) of 0 and a standard deviation (σ) of 10 MeV.

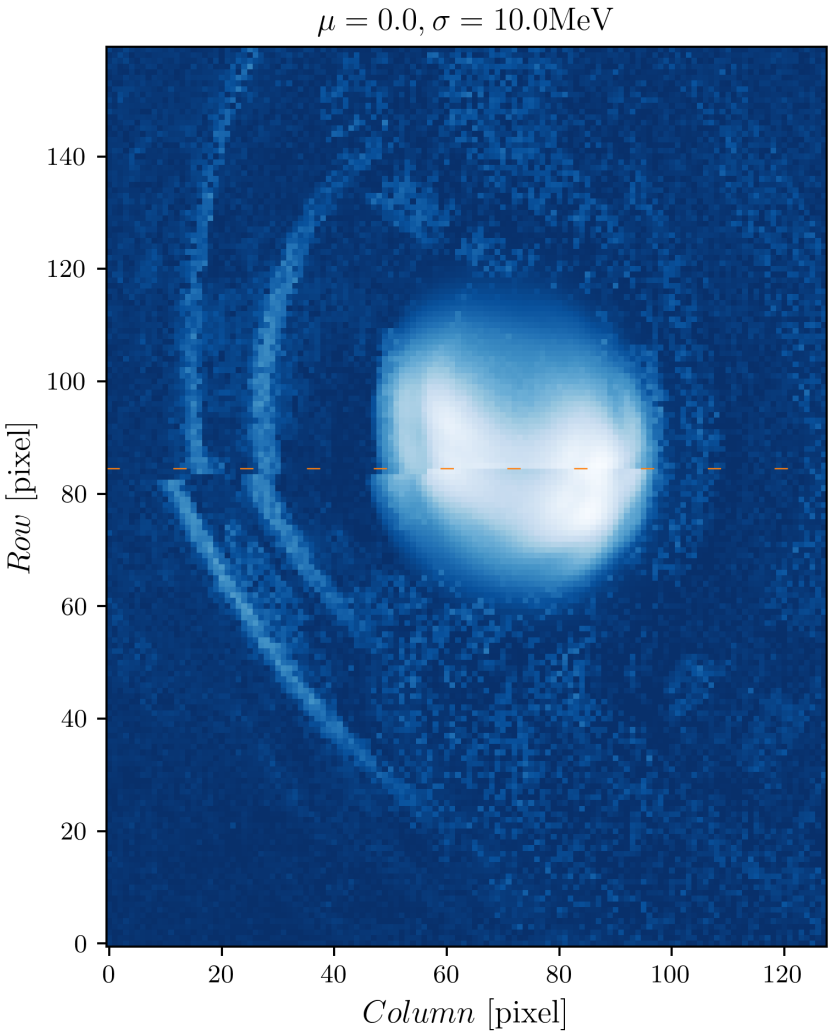

Figure 4.19: The figure displays the same results as those in Fig. 4.18. However, in this image, the intensity has been exponentially rescaled to amplify the subtler contributions arising from reflections, thereby providing a clearer visual representation of their impact.

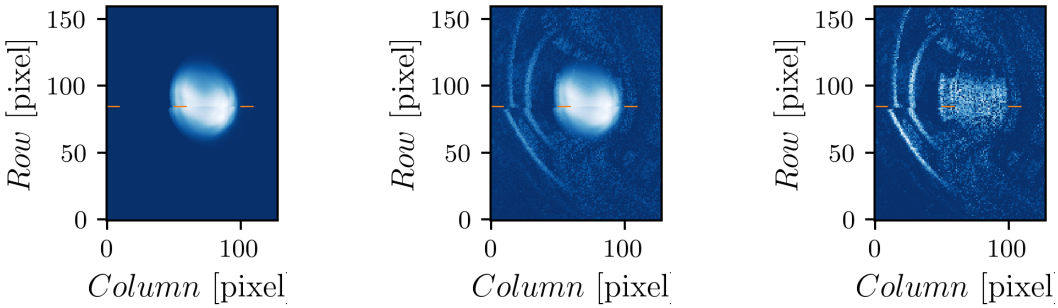

(a) $n_0, \boldsymbol{B}_0$ (b) $n_0 + n_1, \boldsymbol{B}_0 + \boldsymbol{B}_1$ (c) difference

Figure 4.20: The plots demonstrate the influence of incorporating reflections into the simulations. The intensity of the image was exponentially rescaled to enhance visually the reflections. The leftmost panel displays the image simulated without reflections, providing a baseline. The middle panel includes reflections, showcasing the altered image with this additional factor. The rightmost panel isolates and highlights the specific contribution of reflections to the image.

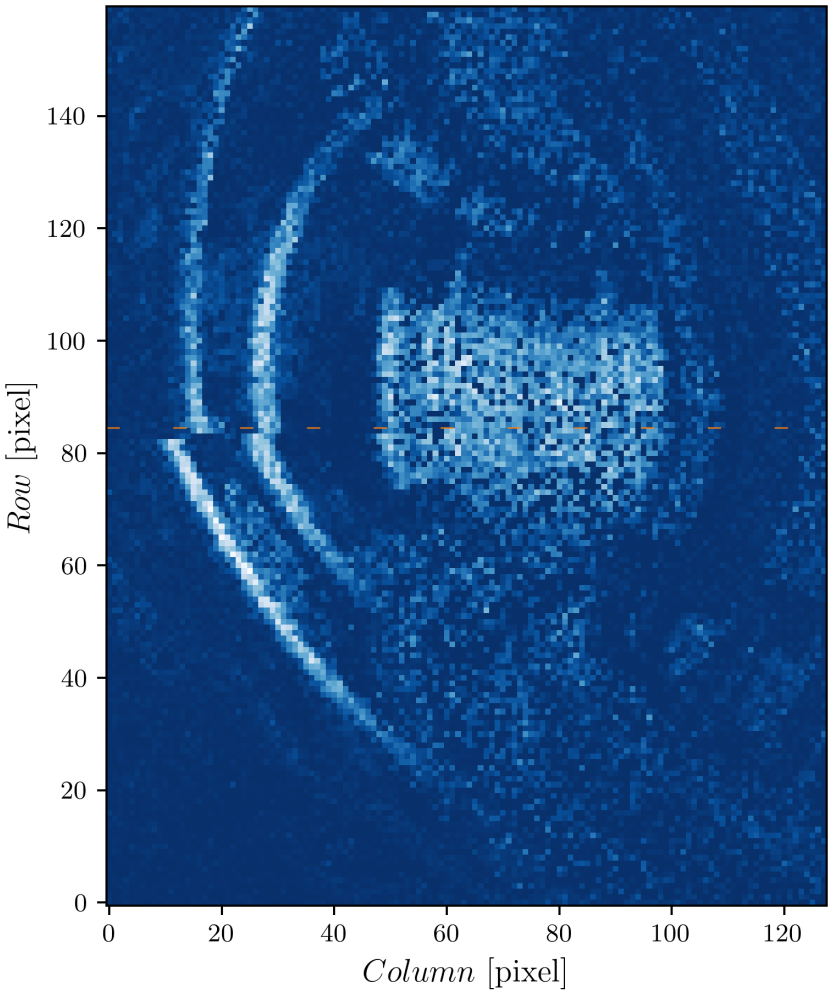

Figure 4.21: This image illustrates the contributions from reflections to the synchrotron radiation image. It was generated by subtracting the image simulated without reflections from the one including reflections. This is an enlarged version of the rightmost panel in Fig. 4.20, provided for greater clarity and detailed examination.

A final application of the newly developed model, as proposed by O. Ficker, involved simulating images for JET's KL7-E8WB wide-angle mid-infrared camera. This camera, observing the vessel counter-clockwise, is not positioned to directly observe SR. However, experimental data indicate that it captures reflected radiation during the RE beam phase, ostensibly originating from synchrotron radiation. To explore this hypothesis, a Calcam calibration of KL7-E8WB, provided by S. Silburn, was employed. The forward model was calculated using the distribution of RE and the $\boldsymbol{B}$ field, based on the JOREK simulation data. The velocity distribution function was set with $\mu = 0\,\mathrm{MeV}$ and $\sigma = 10\,\mathrm{MeV}$.

An experimental image captured by KL7-E8WB during the RE phase, when no other significant light sources for a mid-infrared camera except SR radiation were present, is presented in Fig. 4.22. Although the camera's observation direction aligns with the particle velocity, precluding direct SR observation, the image reveals pronounced reflections from the edges of inboard and outboard limiters and other LFS structures. This phenomenon was theorized to be reflected synchrotron radiation. The forward-modelled image for the KL7-E8WB camera is

shown in Fig. 4.23. A comparison of the two images highlights similar reflection patterns from limiter edges and LFS structures, supporting the notion that these reflections might originate from SR radiation. To the author's knowledge, this is the first simulation which was done to confirm the hypothesis. Notably, the discrepancies in reflection patterns also imply that forward modelling could be instrumental in refining the RE distribution function and beam profile, potentially offering deeper insights into RE dynamics during the discharge. This is especially intriguing considering the longer operational duration of the KL7-E8WB camera compared to the KLDT-E5WC, and its recording of numerous RE events.

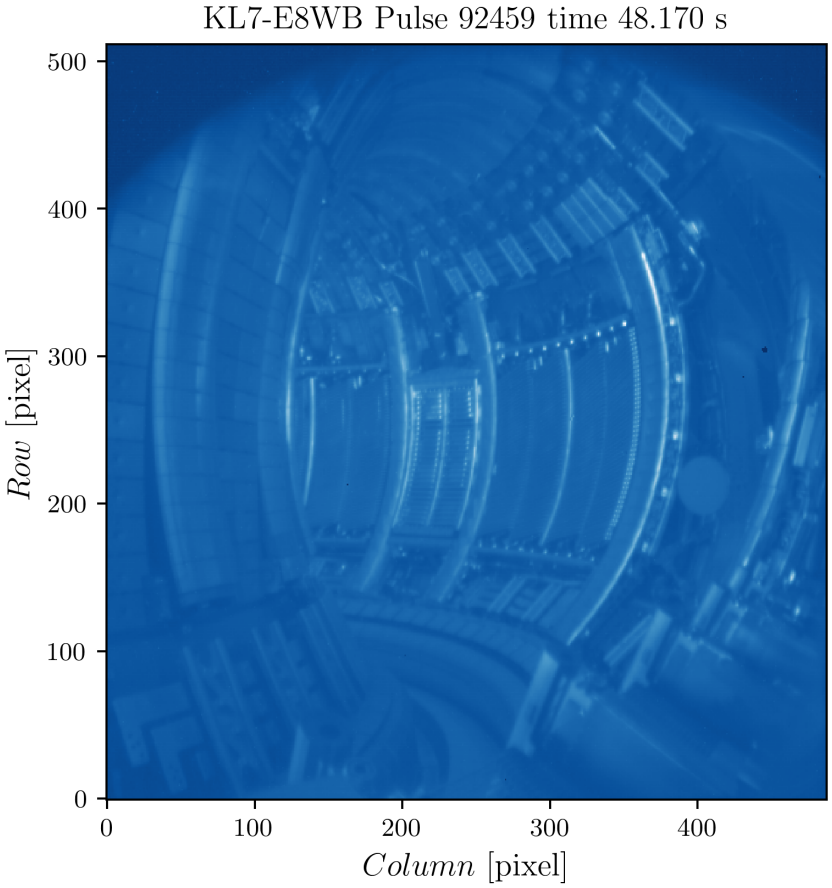

Figure 4.22: Image captured by the KL7-E8WB camera during pulse 92459 at a time of 48.17 s, corresponding to the RE beam phase.

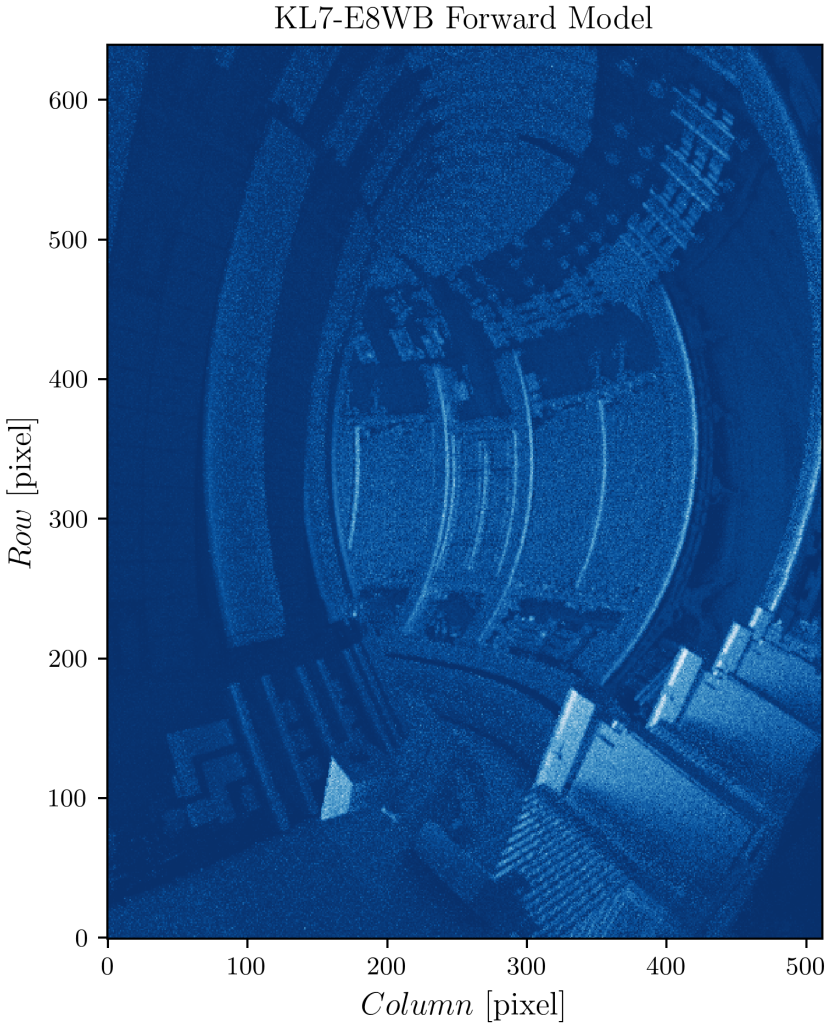

Figure 4.23: The image presents a forward model of JET's KL7-E8WB camera, capturing reflected synchrotron radiation. The velocity distribution function for this model was defined with $\mu = 0\,\mathrm{MeV}$ and $\sigma = 10\,\mathrm{MeV}$. Due to the camera's orientation, which aligns with the particle velocity direction, it is unable to directly observe any SR radiation.

4.4 Conclusions and Outlook

The newly developed model for forward modeling of synchrotron radiation in Cherab is a significant advancement, primarily influenced by two key ideas from the author. The first idea is the separation of the calculation of runaway electron trajectories from the radiation modeling and raytracing. This approach allows users to apply the model to a wide range of inputs, including analytical distribution functions, numerically simulated distributions, or a combination of both. The author advocates for this separation, believing that developing codes to solve all aspects simultaneously leads to architectural and design complexities, often resulting in suboptimal outcomes.

The second innovative aspect of this model is the use of a 6D distribution function for calculating radiation, instead of tracking individual particle trajectories as done in KORC and SOFT. This approach requires the distribution function to

include all the effects of the physics phenomena relevant for a synchrotron radiation simulation, such as spatial perturbation of the RE density caused by presence of magnetic islands. This approach efficiently mitigates noise from particle tracing and is particularly advantageous in complex topologies and distributions.

The model is designed to be user-friendly, versatile, and computationally efficient. It is capable of handling toroidally asymmetric RE distributions and 3D magnetic fields, and uniquely includes the capability to model reflections, thanks to Raysect's reverse raytracing algorithms. The capability of the model to accept various definitions of a distribution function makes its application broad. For example, analytically defined distribution functions can be used easily for predictive simulations as parameter scans or for interpretative simulations in which properties of distribution functions are inverted from experimental measurements. Another applicability is loading results of numerical simulations of RE dynamics, such as those from JOREK, and using the developed model as a mean of RE simulation validation. The last but not least is its relatively low computational cost. As was shown in this work, a computer with a single CPU and 32 cores can be effectively used to produce relatively extensive results in a reasonable time.

This model was applied in forward modeling images for JET's KLDT-E5WC mid-infrared camera. The initial examples demonstrated the model's effectiveness in simulating toroidally symmetric scenarios of $\boldsymbol{B}$ and RE distribution functions. Subsequently, the model's ability to simulate the effects of toroidal asymmetries was showcased, revealing poloidal structures that align with observations from the KLDT-E5WC camera. Separate simulations were conducted to distinguish the impacts of magnetic field perturbations from the perturbations of spatial distribution of RE. The reuslts indicate that spatial distribution of RE density predominantly influences the image features. The model was also used to scan the influence of changes of energy distribution of RE on the image. The results show that such simulations could be used to invert properties of the distribution function, such as the energy of runaway electrons by inversion of the image. This is a promising direction for future work which can also include variation of distribution in pitch angle, for example.

Reflections were also incorporated into the simulations, revealing their significant role in image intensity. Isolating the reflection component exposed features, such as from heating antennas, which were obscured in direct synchrotron radiation. This insight highlights the potential challenges in automatic inversions of runaway electron properties based on synchrotron radiation images, as reflections might lead to inaccuracies. Despite the demanding nature of simulating reflections, due to uncertainties in the properties of plasma-facing components, a preliminary understanding of reflection behavior could enhance optimization efforts and improve precision of delivered results.

Additionally, the model was applied to simulate images for JET's KL7-E8WB wide-angle mid-infrared camera. Although this camera does not directly observe synchrotron radiation, experimental data suggest it captures reflected SR during the RE beam phase. The simulated images showed similar reflection patterns to those in the experimental data, reinforcing the hypothesis that the camera observes reflected synchrotron radiation. To the author's knowledge, this is the first time such a simulation has been conducted. In future, the developed SR model could be used in combination with the KL7-E8WB images to enrich the list

of diagnostics useful for RE studies. This is especially intriguing considering the longer operational duration of the KL7-E8WB camera compared to the KLDT-E5WC, and its recording of numerous RE events.

The SR model was presented to the RE community during the Runaway Electrom Meeting in 2023. The feedback didn't include any reasons why the model shouldn't be developed further and collaboration with M. Hoppe, who is the author of SOFT code, was foreseen. Future enhancements to the SR model will thus involve integrating the full radiation pattern of particles and allowing velocity integration during ray tracing. This will not only calibrate the model but also enable comparisons with other plasma radiation sources. One of the unique applications will then be to study the influence of thermal radiation from heated plasma facing components on the aspects of SR images. The model's application to physics studies in JET and other tokamaks is anticipated, particularly in developing methods for inverting RE distribution function and magnetic field parameters. This direction was initiated at the EMTRAIC 2022 school at IPP Prague, where a group of students under the guidance of the SR team (J. Seidl, O. Ficker, E. Tomešová, M. Tomeš) developed a simple Bayesian optimization inverting parameters of runaway electron distribution function from a forward modelled image. Applying this method to experimental data is more challenging, thus integrating the model with data science techniques like machine learning and statistical analysis is planned for more effective results.

Conclusion

The thesis summarises the work done in forward and backward modelling of fusion spectroscopic diagnostics. The first chapter presents the developed module for Cherab which allows addition of diagnostics based on laser-plasma radiative interaction. The primary focus of adding the module was to introduce the capability to simulate Thomson scattering with Cherab. The module consists of a set of classes for description of the spatial and spectral properties of lasers. The radiation effects resulting from laser plasma interaction are handled by laser emission classes. An emission class implementing the Selden formula for Thomson scattering [27, 28] is added to the module to facilitate the modelling of Thomson scattering.

The module's practical application is exemplified through the creation of a model for the Thomson scattering diagnostic used at COMPASS. This model incorporates detailed representations of both core and edge collection optics, as well as optical fibre bundles. To validate the model, it is benchmarked against ray tracing simulations conducted using Zemax software. The comparison reveals good agreement between the two models.

Subsequently, the diagnostic model is employed to replicate spatial calibration measurements. During this process, a minor discrepancy is noted between the scattering angles and spot positions predicted by the model and those obtained from experimental results. This deviation could potentially be attributed to differences between the expected and actual positions of the optics.

The forward model of Thomson scattering is subsequently utilized with plasma electron profiles derived from experimental data. By inverting the forward-modeled diagnostic data back into electron temperature profiles, the model's accuracy is evaluated. The comparison between the input profiles and the inverted ones demonstrates the model's ability to yield precise data. Moreover, the model highlights potential areas for enhancing the backward model, especially in regions characterized by larger temperature gradients.

In the latter half of the chapter, the focus shifts to the newly developed backward model for inferring electron temperatures using a Bayesian approach. The advantages of this statistical method are underscored by contrasting the Bayesian model's results with those obtained from the traditional least squares error optimization approach. One of the key outcomes is the elimination of fluctuations in the edge temperature profiles, which are often caused by low signal intensity. This improvement will have significant improvement in the performance of automatic fitting of electron temperature profiles, used for example for pedestal studies. Additionally, the model brings to light the potentially negative impact of polychromator electronics on the results, proposing possible solutions to address this issue.

Plans are in place to expand the Thomson scattering emission model by including the depolarization effect. This initiative is motivated by the objective to utilize the module for forward modelling of ITER's Thomson scattering diagnostics, with development work on the core system already in progress.

The second chapter of the thesis focuses on inferring neon concentration in the divertor of JET during neon-seeded discharges. It details a statistical

model developed to invert intensities of neon spectral lines, as captured by divertor spectroscopy. This model operates under the assumption that there is negligible transport in the plasma. Additionally, it employs regularization based on the assumption of the most efficient condition, which constrains the possible combinations of electron temperature and density.

Before applying the developed model to experimental data, its performance is rigorously assessed using forward modelling. For this purpose, a forward model of the divertor spectroscopy diagnostic KT3 is constructed in Cherab. This forward model is combined with results from SOLPS simulations to generate synthetic data, which are then subjected to statistical inversion.

To evaluate the model's performance, a novel approach to model validation through forward modelling is implemented. This method considers the spatial distributions of plasma properties and radiation in the input plasma state, as well as the properties of the diagnostic as determined by the forward model. This approach enables a statistical-like assessment, resulting in a weighted distribution of plasma quantities observed by a diagnostic channel.

The distributions obtained from both the inversion process and the validation method are then compared. The comparison reveals that under the assumptions of zero transport and maximum radiation efficiency, there is an approximately 50% discrepancy between the inverted neon concentration values and the concentrations present in the input plasma profiles.

The model, despite the noted discrepancies, is subsequently applied to experimental data to derive inversions of neon concentration profiles from KT3 measurements at JET. The resulting profiles exhibit steep gradients, suggesting a significant influence of reflections from the first wall components. In these regions, the model predicts neon concentrations exceeding 20%. For channels less affected by reflections, the predicted concentrations are in the range of a few percent.

A comparison with neon concentrations estimated at the pedestal top reveals that the concentrations in the divertor are higher, which contrasts with theoretical predictions based on SOLPS simulations. This inconsistency underscores the need for further investigation into the impact of reflections on the inversion results. Additionally, ongoing efforts are being made to develop a model that incorporates transport effects in the plasma, aiming to enhance the accuracy and reliability of the inversion results in future applications.

The final chapter introduces a new forward model of synchrotron radiation for Cherab, setting itself apart from existing models. Its unique approach involves simulating radiation through direct integration with a runaway electron distribution function. This model operates on the principle that the distribution function encompasses all critical physical phenomena for synchrotron radiation, thereby eliminating the need for particle tracing and enhancing computational efficiency.

The model's exceptional versatility stems from its inputs: implementations of a fully six-dimensional distribution function and a fully 3D vector magnetic field. These implementations can either be derived from numerical simulations of runaway electron dynamics or error fields or be constructed from analytical descriptions based on theoretical and empirical research.

An additional benefit of this model is its capability to account for reflections from first wall components. This is made possible by the reverse ray tracing approach of Raysect, further broadening the model's applicability and accuracy

in simulating synchrotron radiation scenarios in fusion research environments.

The model's effectiveness is demonstrated through forward modelling of the synchrotron radiation images captured by JET's KLDT-E5WC and KL7-E8WB infrared cameras. The simulations integrate spatial distributions of runaway electron density and toroidally asymmetric magnetic fields, derived from JOREK simulations. To complete the electron distribution function definition, analytical formulae are used to describe the velocity space distribution.

For the KLDT-E5WC camera, the forward model generates images that qualitatively align with the experimental observations. These images notably replicate features attributed to magnetic islands and reflections. The model is further utilized to dissect the influences of toroidally asymmetric spatial redistribution of runaway electron density and the magnetic field on the synchrotron radiation images. This analysis indicates that the density redistribution primarily contributes to the observed visual features.

In the case of the KL7-E8WB camera, which observes the runaway electron beam in the co-current direction, direct observation of synchrotron radiation is not possible. However, strong reflections from first wall components are noted during discharge phases dominated by runaway electrons, presumed to originate from synchrotron radiation. The forward models of KL7-E8WB images display reflection patterns that bear resemblance to these observations, lending credibility to the hypothesis that these reflections are indeed a result of synchrotron radiation.

Future developments for the model include enhancing the radiation model by incorporating the correct radiation pattern. This improvement will enable absolute calibration of the model, facilitating direct comparisons between synchrotron radiation and other sources of radiation emanating from the plasma, as well as from heated surfaces. Such advancements will broaden the model's applicability and precision in analyzing and interpreting various radiation sources in fusion research contexts.

In conclusion, the surge in computational power has paved the way for more intricate forward and backward models in fusion research. The examples highlighted throughout the thesis demonstrate that linking forward and backward models can substantially enhance the information extracted from experimental data. This interconnection not only contributes to refining individual diagnostic systems and the backward models employed but also has the potential to optimize entire diagnostic sets. Such optimization is focused on improving the quality of plasma state reconstruction, thereby maximizing the informational yield from experimental endeavors in the field of fusion research.

Bibliography

[1] Jeffrey P Freidberg. *Plasma Physics and Fusion Energy*. Cambridge, England: Cambridge University Press, July 2008.

[2] A. Meakins et al. *Cherab-core*. Version 1.4.0. Cherab. 2024. URL: https://github.com/cherab/core (visited on 01/02/2024).

[3] S. Wiesen et al. "The new SOLPS-ITER code package". In: *Journal of Nuclear Materials* 463 (Aug. 2015), pp. 480–484. ISSN: 00223115. DOI: 10.1016/j.jnucmat.2014.10.012.

[4] A. Meakins and Carr M. *Raysect*. Version 0.8.1. Rayect Project. 2024. URL: https://github.com/raysect/source (visited on 01/02/2024).

[5] Meakins A. and Carr M. *Raysect*. Rayect Project. 2014. URL: https://www.raysect.org/ (visited on 01/02/2024).

[6] A. Meakins et al. *Cherab*. Cherab Team. 2022. URL: https://www.cherab.info/ (visited on 01/02/2024).

[7] Matt Pharr, Wenzel Jakob, and Greg Humphreys. *Physically based rendering: From theory to implementation*. MIT Press, 2023.

[8] M. Carr and A. et al. Meakins. *Image from Raysect Project Online Documentation*. http://www.raysect.org/_images/ray-tracing_directions.png. Accessed: [2024-01-01]. 2017.

[9] M. Carr and A. et al. Meakins. *Image from Raysect Project Online Documentation*. http://www.raysect.org/_images/calculate_emission.png. Accessed: [2024-01-01]. 2017.

[10] ADAS Project. *Open-ADAS*. Accessed: 2023-10-18. Atomic Data and Analysis Structure. 2020. URL: https://open.adas.ac.uk/.

[11] M Tomes et al. "Thomson scattering synthetic diagnostic module for the Cherab framework". In: *Review of Scientific Instruments* 92.5 (2021).

[12] M Carr et al. "Towards integrated data analysis of divertor diagnostics with ray-tracing". In: *44th EPS Conference on Plasma Physics*. European Physical Society. 2017.

[13] Dr Alex Meakins and Matthew Carr. *raysect/source: v0.5.2 Release*. 2018. DOI: 10.5281/ZENODO.1341376. URL: https://zenodo.org/record/1341376.

[14] P. Bilkova et al. "High resolution Thomson scattering on the COMPASS tokamak—extending edge plasma view and increasing repetition rate". In: *Journal of Instrumentation* 13 (01 Jan. 2018), pp. C01024–C01024. ISSN: 1748-0221. DOI: 10.1088/1748-0221/13/01/C01024.

[15] P Vondracek et al. "Preliminary design of the COMPASS upgrade tokamak". In: *Fusion Engineering and Design* 169 (2021), p. 112490.

[16] M Bassan et al. "Thomson scattering diagnostic systems in ITER". In: *Journal of Instrumentation* 11.01 (2016), p. C01052.

[17] P. Bohm et al. “Conceptual design of Thomson scattering diagnostics for the COMPASS-U tokamak”. In: *Review of Scientific Instruments* 92.8 (Aug. 2021). ISSN: 1089-7623. DOI: 10.1063/5.0043661. URL: http://dx.doi.org/10.1063/5.0043661.

[18] J. G. Clark et al. “First divertor Thomson scattering measurements on MAST-U”. In: *Review of Scientific Instruments* 93.10 (Oct. 2022). ISSN: 1089-7623. DOI: 10.1063/5.0101635. URL: http://dx.doi.org/10.1063/5.0101635.

[19] I Yamada et al. “Current status of the LHD Thomson scattering system”. In: *Journal of Instrumentation* 7.05 (May 2012), pp. C05007–C05007. ISSN: 1748-0221. DOI: 10.1088/1748-0221/7/05/c05007. URL: http://dx.doi.org/10.1088/1748-0221/7/05/C05007.

[20] A.W. DeSilva. “The Evolution of Light Scattering as a Plasma Diagnostic”. In: *Contributions to Plasma Physics* 40 (1-2 Apr. 2000). History of Thomson scattering¡br/¿, pp. 23–35. ISSN: 0863-1042. DOI: 10.1002/(SICI)1521-3986(200004)40:1/2<23::AID-CTPP23>3.0.CO;2-7.

[21] G. Fiocco and E. Thompson. “Thomson Scattering of Optical Radiation from an Electron Beam”. In: *Physical Review Letters* 10 (3 Feb. 1963), pp. 89–91. ISSN: 0031-9007. DOI: 10.1103/PhysRevLett.10.89.

[22] N. J. PEACOCK et al. “Measurement of the Electron Temperature by Thomson Scattering in Tokamak T3”. In: *Nature* 224 (5218 Nov. 1969), pp. 488–490. ISSN: 0028-0836. DOI: 10.1038/224488a0.

[23] S L Prunty. “A primer on the theory of Thomson scattering for high-temperature fusion plasmas”. In: *Physica Scripta* 89 (12 Dec. 2014), p. 128001. ISSN: 0031-8949. DOI: 10.1088/0031-8949/89/12/128001.

[24] John David Jackson. *Classical Electrodynamics*. 3rd ed. John Wiley & Sons, 1999. ISBN: 978-0-471-30932-1.

[25] O. Naito, H. Yoshida, and T. Matoba. “Analytic formula for fully relativistic Thomson scattering spectrum”. In: *Physics of Fluids B: Plasma Physics* 5 (11 Nov. 1993), pp. 4256–4258. ISSN: 0899-8221. DOI: 10.1063/1.860593.

[26] O. Naito, H. Yoshida, and T. Matoba. “Erratum: “Analytic formula for fully relativistic Thomson scattering spectrum” [Phys. Fluids B 5 , 4256 (1993)]”. In: *Physics of Plasmas* 1 (3 Mar. 1994), pp. 806–806. ISSN: 1070-664X. DOI: 10.1063/1.870779.

[27] AC Selden. “Simple analytic form of the relativistic Thomson scattering spectrum”. In: *Physics Letters A* 79.5-6 (1980), pp. 405–406.

[28] A.C. Selden. *Simple Analytic Form Of The Relativistic Thomson Scattering Spectrum*. 1982.

[29] Ian H Hutchinson. “Principles of plasma diagnostics”. In: *Plasma Physics and Controlled Fusion* 44.12 (2002), pp. 2603–2603.

[30] S.A. Bozhenkov et al. “The Thomson scattering diagnostic at Wendelstein 7-X and its performance in the first operation phase”. In: *Journal of Instrumentation* 12 (10 Oct. 2017), P10004–P10004. ISSN: 1748-0221. DOI: 10.1088/1748-0221/12/10/P10004.

[31] M N A Beurskens et al. “Pedestal width and ELM size identity studies in JET and DIII-D; implications for ITER”. In: *Plasma Physics and Controlled Fusion* 51 (12 Dec. 2009), p. 124051. ISSN: 0741-3335. DOI: 10.1088/0741-3335/51/12/124051.

[32] M. Komm et al. “Contribution to the multi-machine pedestal scaling from the COMPASS tokamak”. In: *Nuclear Fusion* 57 (5 May 2017), p. 056041. ISSN: 0029-5515. DOI: 10.1088/1741-4326/aa6659.

[33] A.F. Kornev et al. “Nd:YAG lasers for ITER divertor Thomson scattering”. In: *Fusion Engineering and Design* 146 (Sept. 2019), pp. 1019–1022. ISSN: 09203796. DOI: 10.1016/j.fusengdes.2019.01.147.

[34] Matthias Hoelzl et al. “The JOREK non-linear extended MHD code and applications to large-scale instabilities and their control in magnetically confined fusion plasmas”. In: *Nuclear Fusion* 61.6 (2021), p. 065001.

[35] R Scannell et al. “Design of a new Nd: YAG Thomson scattering system for MAST”. In: *Review of Scientific Instruments* 79.10 (2008).

[36] R Pasqualotto et al. “High resolution Thomson scattering for joint European torus (JET)”. In: *Review of Scientific Instruments* 75.10 (2004), pp. 3891–3893.

[37] Petra Bılková et al. “Design of new Thomson scattering diagnostic system on COMPASS tokamak”. In: *Nuclear Instruments and Methods in Physics Research Section A: Accelerators, Spectrometers, Detectors and Associated Equipment* 623.2 (2010), pp. 656–659.

[38] Estera Stefanikova et al. “Fitting of the Thomson scattering density and temperature profiles on the COMPASS tokamak”. In: *Review of Scientific Instruments* 87.11 (2016).

[39] L.L. Lao et al. “Reconstruction of current profile parameters and plasma shapes in tokamaks”. In: *Nuclear Fusion* 25.11 (Nov. 1985), p. 1611. DOI: 10.1088/0029-5515/25/11/007. URL: https://dx.doi.org/10.1088/0029-5515/25/11/007.

[40] Matt Newville et al. *lmfit/lmfit-py: 1.2.2*. Version 1.2.2. July 2023. DOI: 10.5281/zenodo.8145703. URL: https://doi.org/10.5281/zenodo.8145703.

[41] Du Phan, Neeraj Pradhan, and Martin Jankowiak. “Composable Effects for Flexible and Accelerated Probabilistic Programming in NumPyro”. In: *arXiv preprint arXiv:1912.11554* (2019).

[42] Eli Bingham et al. “Pyro: Deep Universal Probabilistic Programming”. In: *J. Mach. Learn. Res.* 20 (2019), 28:1–28:6. URL: http://jmlr.org/papers/v20/18-403.html.

[43] Richard McElreath. *Statistical Rethinking: A Bayesian Course with Examples in R and Stan, 2nd Edition*. 2nd ed. CRC Press, 2020. URL: http://xcelab.net/rm/statistical-rethinking/.

[44] Cameron Davidson-Pilon. *Bayesian methods for hackers: probabilistic programming and Bayesian inference*. Addison-Wesley Professional, 2015.

[45] P Bilkova et al. “Progress of development of Thomson scattering diagnostic system on COMPASS”. In: *Review of Scientific Instruments* 81.10 (2010).

[46] C. M. Penney, R. L. St. Peters, and M. Lapp. “Absolute rotational Raman cross sections for N2, O2, and CO2”. In: *J. Opt. Soc. Am.* 64.5 (May 1974), pp. 712–716. DOI: 10.1364/JOSA.64.000712. URL: https://opg.optica.org/abstract.cfm?URI=josa-64-5-712.

[47] R.A. Pitts et al. “Physics basis for the first ITER tungsten divertor”. In: *Nuclear Materials and Energy* 20 (Aug. 2019), p. 100696. ISSN: 2352-1791. DOI: 10.1016/j.nme.2019.100696. URL: http://dx.doi.org/10.1016/j.nme.2019.100696.

[48] A Loarte et al. “Chapter 4: Power and particle control”. In: *Nuclear Fusion* 47.6 (June 2007), S203–S263. ISSN: 1741-4326. DOI: 10.1088/0029-5515/47/6/s04. URL: http://dx.doi.org/10.1088/0029-5515/47/6/S04.

[49] R.P. Wenninger et al. “DEMO divertor limitations during and in between ELMs”. In: *Nuclear Fusion* 54.11 (Nov. 2014), p. 114003. ISSN: 1741-4326.

[50] J.H. You et al. “European DEMO divertor target: Operational requirements and material-design interface”. In: *Nuclear Materials and Energy* 9 (Dec. 2016), pp. 171–176. ISSN: 2352-1791. DOI: 10.1016/j.nme.2016.02.005. URL: http://dx.doi.org/10.1016/j.nme.2016.02.005.

[51] M. Siccinio et al. “Figure of merit for divertor protection in the preliminary design of the EU-DEMO reactor”. In: *Nuclear Fusion* 59.10 (Aug. 2019), p. 106026. ISSN: 1741-4326. DOI: 10.1088/1741-4326/ab3153. URL: http://dx.doi.org/10.1088/1741-4326/ab3153.

[52] SA Silburn et al. “Mitigation of divertor heat loads by strike point sweeping in high power JET discharges”. In: *Physica Scripta* 2017.T170 (2017), p. 014040.

[53] C. Giroud et al. “Impact of nitrogen seeding on confinement and power load control of a high-triangularity JET ELMy H-mode plasma with a metal wall”. In: *Nuclear Fusion* 53.11 (Sept. 2013), p. 113025. ISSN: 1741-4326. DOI: 10.1088/0029-5515/53/11/113025. URL: http://dx.doi.org/10.1088/0029-5515/53/11/113025.

[54] D. Eldon et al. “An analysis of controlled detachment by seeding various impurity species in high performance scenarios on DIII-D and EAST”. In: *Nuclear Materials and Energy* 27 (2021), p. 100963. ISSN: 2352-1791. DOI: https://doi.org/10.1016/j.nme.2021.100963. URL: https://www.sciencedirect.com/science/article/pii/S235217912100048X.

[55] SS Henderson et al. “Divertor detachment and reattachment with mixed impurity seeding on ASDEX Upgrade”. In: *Nuclear Fusion* 63.8 (2023), p. 086024.

[56] Carine Giroud et al. “High performance ITER-baseline discharges in deuterium with nitrogen and neon-seeding in the JET-ILW”. In: *2020 IAEA Fusion Energy Conf.* 2021, p–EX.

[57] H. P. Summers. *Atomic Data and Analysis Structure User manual*. Accessed: 2023-10-18. Atomic Data and Analysis Structure. 2004. URL: https://www.adas.ac.uk/manual.php.

[58] David Salzmann. *Atomic physics in hot plasmas*. 97. Oxford University Press, USA, 1998.

[59] H. P. Summers and M. G. O'Mullane. "Atomic Data and Modelling for Fusion: the ADAS Project". In: *AIP Conference Proceedings*. AIP, 2011. DOI: 10.1063/1.3585817. URL: http://dx.doi.org/10.1063/1.3585817.

[60] B.A. Lomanowski et al. "Inferring divertor plasma properties from hydrogen Balmer and Paschen series spectroscopy in JET-ILW". In: *Nuclear Fusion* 55 (12 Nov. 2015), p. 123028. ISSN: 0029-5515. DOI: 10.1088/0029-5515/55/12/123028.

[61] Elizaveta Kaveeva et al. "SOLPS-ITER drift modelling of JET Ne and N-seeded H-modes". In: *Nuclear Materials and Energy* 28 (2021), p. 101030.

[62] H W Morsi et al. "A visible and UV charge exchange spectroscopy system for the tritium phase of JET". In: *Plasma Physics and Controlled Fusion* 37 (12 Dec. 1995), pp. 1407–1431. ISSN: 0741-3335. DOI: 10.1088/0741-3335/37/12/005. URL: https://iopscience.iop.org/article/10.1088/0741-3335/37/12/005.

[63] A. Meigs et al. "Enhancement of JET's mirror-link near-ultraviolet to near-infrared divertor spectroscopy system". In: *Review of Scientific Instruments* 81 (10 Oct. 2010), 10E532. ISSN: 0034-6748. DOI: 10.1063/1.3502322.

[64] S.S. Henderson et al. "Determination of volumetric plasma parameters from spectroscopic N II and N III line ratio measurements in the ASDEX Upgrade divertor". In: *Nuclear Fusion* 58 (1 Jan. 2018), p. 016047. ISSN: 0029-5515. DOI: 10.1088/1741-4326/aa96be.

[65] Timo Ravensbergen et al. "Real-time feedback control of the impurity emission front in tokamak divertor plasmas". In: *Nature communications* 12.1 (2021), p. 1105.

[66] W. Sakaguchi et al. "In situ reflectivity of tungsten mirrors under helium plasma exposure". In: *Journal of Nuclear Materials* 390-391 (2009). Proceedings of the 18th International Conference on Plasma-Surface Interactions in Controlled Fusion Device, pp. 1149–1152. ISSN: 0022-3115. DOI: https://doi.org/10.1016/j.jnucmat.2009.01.276. URL: https://www.sciencedirect.com/science/article/pii/S0022311509003201.

[67] Julian Schwinger. "On the classical radiation of accelerated electrons". In: *Physical review* 75.12 (1949), p. 1912.

[68] IM Pankratov. "Analysis of the synchrotron radiation spectra of runaway electrons". In: *Plasma Physics Reports* 25 (1999).

[69] Hz Dreicer. "Electron and ion runaway in a fully ionized gas. I". In: *Physical Review* 115.2 (1959), p. 238.

[70] Boris N Breizman et al. "Physics of runaway electrons in tokamaks". In: *Nuclear Fusion* 59.8 (2019), p. 083001.

[71] FC Schuller. "Disruptions in tokamaks". In: *Plasma Physics and Controlled Fusion* 37.11A (1995), A135.

[72] Allen H Boozer. “Theory of tokamak disruptions”. In: *Physics of plasmas* 19.5 (2012).

[73] PC De Vries et al. “Survey of disruption causes at JET”. In: *Nuclear fusion* 51.5 (2011), p. 053018.

[74] TC Hender et al. “MHD stability, operational limits and disruptions”. In: *Nuclear fusion* 47.6 (2007), S128.

[75] R Sweeney et al. “Statistical analysis of m/n= 2/1 locked and quasi-stationary modes with rotating precursors at DIII-D”. In: *Nuclear Fusion* 57.1 (2016), p. 016019.

[76] Joan Decker et al. “Full conversion from ohmic to runaway electron driven current via massive gas injection in the TCV tokamak”. In: *Nuclear Fusion* 62.7 (2022), p. 076038.

[77] J Mlynar et al. “Runaway electron experiments at COMPASS in support of the EUROfusion ITER physics research”. In: *Plasma Physics and Controlled Fusion* 61.1 (2018), p. 014010.

[78] O Ficker et al. “Runaway electron beam stability and decay in COMPASS”. In: *Nuclear Fusion* 59.9 (2019), p. 096036.

[79] VV Plyusnin et al. “Study of runaway electron generation during major disruptions in JET”. In: *Nuclear Fusion* 46.2 (2006), p. 277.

[80] GF Matthews et al. “Melt damage to the JET ITER-like Wall and divertor”. In: *Physica Scripta* 2016.T167 (2016), p. 014070.

[81] O Ficker et al. “New Diagnostics Developments and Results in Support of Runaway Electron Studies at European Devices”. In: *29th IAEA Fusion Energy Conference (FEC 2023)*. 2023.

[82] A Dal Molin et al. “A new hard x-ray spectrometer for runaway electron measurements in tokamaks”. In: *Measurement Science and Technology* 34.8 (2023), p. 085501.

[83] J Cerovsky et al. “Progress in HXR diagnostics at GOLEM and COMPASS tokamaks”. In: *Journal of Instrumentation* 17.01 (2022), p. C01033.

[84] M Nocente et al. “MeV range particle physics studies in tokamak plasmas using gamma-ray spectroscopy”. In: *Plasma Physics and Controlled Fusion* 62.1 (2019), p. 014015.

[85] ON Jarvis. “Neutron measurement techniques for tokamak plasmas”. In: *Plasma physics and controlled fusion* 36.2 (1994), p. 209.

[86] Mathias Hoppe et al. “SOFT: a synthetic synchrotron diagnostic for runaway electrons”. In: *Nuclear Fusion* 58.2 (2018), p. 026032.

[87] L Carbajal et al. “Space dependent, full orbit effects on runaway electron dynamics in tokamak plasmas”. In: *Physics of Plasmas* 24.4 (2017).

[88] L Carbajal and D del-Castillo-Negrete. “On the synchrotron emission in kinetic simulations of runaway electrons in magnetic confinement fusion plasmas”. In: *Plasma Physics and Controlled Fusion* 59.12 (2017), p. 124001.

[89] Malcolm S. Longair. *High Energy Astrophysics*. 3rd ed. Cambridge University Press, 2011. DOI: 10.1017/CBO9780511778346.

[90] Cédric Reux et al. "Demonstration of Safe Termination of Megaampere Relativistic Electron Beams in Tokamaks". In: *Phys. Rev. Lett.* 126 (17 Apr. 2021), p. 175001. DOI: 10.1103/PhysRevLett.126.175001. URL: https://link.aps.org/doi/10.1103/PhysRevLett.126.175001.

[91] I Balboa et al. "Remote wide angle view broad wavelength viewing system compatible with DT operations in JET". In: *Plasma Physics and Controlled Fusion* 65.6 (2023), p. 064005.

[92] GTA Huysmans and Olivier Czarny. "MHD stability in X-point geometry: simulation of ELMs". In: *Nuclear fusion* 47.7 (2007), p. 659.

[93] Matthias Hoelzl et al. "The JOREK non-linear extended MHD code and applications to large-scale instabilities and their control in magnetically confined fusion plasmas". In: *Nuclear Fusion* 61.6 (2021), p. 065001.

[94] V Bandaru et al. "Magnetohydrodynamic simulations of runaway electron beam termination in JET". In: *Plasma Physics and Controlled Fusion* 63.3 (2021), p. 035024.

[95] Scott Silburn et al. *Calcam*. Version 2.12.0. Nov. 2023. DOI: 10.5281/zenodo.10116099. URL: https://doi.org/10.5281/zenodo.10116099.

[96] M Carr et al. "Physically principled reflection models applied to filtered camera imaging inversions in metal walled fusion machines". In: *Review of Scientific Instruments* 90.4 (2019).

List of Figures

List of Tables

List of Symbols

A_{t5}	offset of JET's divertor tile5 in cylindrical coordinates
B	magnitude of magnetic field
$\mathbf{B}_0$	equilibrium magnetic field
$\mathbf{B}_N$	Nth perturbation harmonic of the equilibrium magnetic field $\mathbf{B}_0$
$\mathbf{B}_N^{\cos}$	cosine component of the Nth perturbation harmonic of the equilibrium magnetic field $\mathbf{B}_0$
$\mathbf{B}_N^{\sin}$	sine component of the Nth perturbation harmonic of the equilibrium magnetic field $\mathbf{B}_0$
c	the speed of light in vacuuum
D_ε	Deuterium Balmer series spectral line, transition 7 – 2, wavelength 369.9
D_ζ	Deuterium Balmer series spectral line, transition 8 – 2, wavelength 388.8
D_η	Deuterium Balmer series spectral line, transition 9 – 2, wavelength 383.4
e	electron charge
$\boldsymbol{E}$	vector of electric field
m_{e}	electron mass
Ne_{369}	Neon-II spectral line multiplet, transition 2s2 2p4 3p1 4p5.5 – 2s2 2p4 3s1 4p5.5, wavelengths in nm: 366.41, 369.42, 370.96, 373.49, 375.12, 376.63, 377.71
Ne_{371}	Neon-II spectral line multiplet, transition 2s2 2p4 3p1 2d4.5 – 2s2 2p4 3s1 2p2.5, wavelengths in nm: 364.39, 371.31, 372.71
n_{e}	electron density
r_{e}	classical electrom radius
σ_{T}	Thomson cross section
T_{e}	electron temperature
$\boldsymbol{k}$	wave vector
n_0	equilibrium particle density
n_N	equilibrium particle density
$n_N^{\cos}$	cosine component of the Nth perturbation harmonic of the equilibrium particle density n_0
$n_N^{\sin}$	sine component of the Nth perturbation harmonic of the equilibrium particle density n_0
$\boldsymbol{r}$	position vector of a point in a frame of reference
$\mathbf{r}_{\mathrm{ch}}$	offset of JET's divertor tile5 in cylindrical coordinates
$\boldsymbol{S}$	Poynting vector of an electromagnetic wave
$\boldsymbol{v}$	vector of velocity
Δ_{t5}	slope of JET's divertor tile5 in cylindrical coordinates

γ	relativistic factor
λ	wavelength
μ_0	permeability of vacuum
ν_g	electron cylcotron frequency (gyro-frequency)
ω	angular frequency

List of Abbreviations

ADAS	Atomic Data and Analysis Structure
ADC	Analog-Digital Converter
APD	Avalanche Photo-Diode
CX	Charge Exchange collision
CXRS	Charge Exchange Recombination Spectroscopy
D-alpha	Deuterium alpha spectral line of the Balmer series
ELM	Edge Localised Mode
FOV	Field of View
HFS	Hiw Field Side
H-mode	high confinement mode
ITER	International Thermonuclear Experimental Reactor
JET	Joint European Torus
JPF	Jet Pulse File
JPN	Jet Pulse Number
KDE	Kernel Density Estimation
KT3	mirror-link divertor spectroscopy
KT3A	spectrometer A, mirror-link divertor spectroscopy
KT3B	spectrometer A, mirror-link divertor spectroscopy
LFS	Low Field Side
MAD	Mean Absolute Deviation around the mean
MIR	Mid Infra Red wavelength region
Nd:YAG	solid state laser, neodymium-doped yttrium aluminum garnet; $Nd:Y_3Al_5O_{12}$
NIR	Near Infra-Red wavelength region
Oct8-uvimp-b	Upper vertical port b in octant 8 of the JET vacuum vessel
OPEN-ADAS	Free version of ADAS. Includes higher level atomic data.
PEC	Photon Emissivity Coefficients provided by ADAS ADF15 files.
PFR	Private Flux Region
PPF	Post-Processed File
PPL	Probabilistic Programming Language
RE	Runaway Electrons
SOL	Scrape-Off Layer
SOLPS	Scrape-Off Layer Plasma Simulation, Edge plasma fluid-kinetic simulation code [3]
SR	Synchrotron Radiation
TOKAMAK	TOroidal'naya KAmera s MAgnitnymi Katushkami, Russian for toroidal chamber with magnetic coils
TS	Thomson Scattering
VIS	VISible wavelength region
WPTE	Work Package Tokamak Exploitation

Terminology

AbsorbingSurface	Absolutely absorbing surface in Raysect not generating any reflections or tramsissions
cylindrical	Right-handed cylindrical coordinate system (R, ϕ, Z) as defined in [**Sauter2013**]
FibreOptic	Raysect observer modelling an optical fibre.
InhomogeneousVolumeEmitter	Raysect's material for modelling of materials with no surface interaction and inhomogeneous volume emission.
LoggingRay	A single ray in Raysect's raytracing framework which after tracing stores information about its path and interactions with the scene
Node	Raysect's scenegraph Node class
Observer	Objects in Raysect's scenegraph measuring incident radiation. This is achieved by launching rays from the observer with given are and angular dependency and accumulaing their samples of the scene.
Plasma	Cherab's Plasma class storing information about plasma properties such as population profiles and force fields
primitive	Raysect's scenegraph node with an assigned geometry
Primitive	Raysect's scenegraph Node class
ScalarFunction3D	three dimensional scalar function defined by Raysect's function framework
Spectrum	Raysect's Spectrum class
*tile*5	One of the Plasma facing component tiles in the divertor of JET
ToroidalVoxelGrid	Cherab's class for implementing toroidally symmetric voxels which have a polygonal (single ear) cross-section in the poloidal plane
UniformEnergyDensity	Laser Profile with uniform distribution of volumetric energy density
VectorCamera	Raysect's observer imitating 2D camera chip with position of the pixels specified by 3D points and direction of observations by 3D vectors. The field of view of each pixel is then defined as a solid angle between the vectors of surrounding pixels.
VectorFunction3D	three dimensional vector function defined by Raysect's function framework

List of Publications

Impacted Publications

1. **Tomes, M.** et al. "Thomson scattering synthetic diagnostic module for the Cherab framework". In: *Review of Scientific Instruments* 92.5 (2021), p. 053532. DOI: 10.1063/5.0043786

2. **Tomes, M.** et al. "Feasibility study and CXRS synthetic diagnostic model for COMPASS upgrade based on Cherab and Raysect framework". In: *Fusion Engineering and Design* 170 (2021), p. 112498. DOI: https://doi.org/10.1016/j.fusengdes.2021.112498

3. **Tomes, M.** et al. "Calculation of edge ion temperature and poloidal rotation velocity from carbon III triplet measurements on the COMPASS tokamak". In: *Nukleonika* 61.4 (2016), pp. 443–451. DOI: DOI:https://doi.org/10.1515/nuka-2016-0073

4. J. Hecko et al. "Experimental evidence of very short power decay lengths in H-mode discharges in the COMPASS tokamak". In: *Plasma Physics and Controlled Fusion* 66.1 (2023), p. 015013. DOI: 10.1088/1361-6587/ad08f0

5. M. Hron et al. "Overview of the COMPASS results". In: *Nuclear Fusion* 62.4 (2022), p. 042021. DOI: 10.1088/1741-4326/ac301f

6. J. Horacek et al. "Predictive modelling of liquid metal divertor: from COMPASS tokamak towards Upgrade". In: *Physica Scripta* 96.12 (2021), p. 124013. DOI: 10.1088/1402-4896/ac1dc9

7. P. Bohm et al. "Conceptual design of Thomson scattering diagnostics for the COMPASS-U tokamak". In: *Review of Scientific Instruments* 92.8 (2021). DOI: 10.1063/5.0043661

8. I. Khodunov et al. "Real-time feedback system for divertor heat flux control at COMPASS tokamak". In: *Plasma Physics and Controlled Fusion* 63.6 (2021), p. 065012. DOI: 10.1088/1361-6587/abf03e

9. P. Vondracek et al. "Preliminary design of the COMPASS upgrade tokamak". In: *Fusion Engineering and Design* 169 (2021), p. 112490. DOI: https://doi.org/10.1016/j.fusengdes.2021.112490

10. R. Dejarnac et al. "Overview of power exhaust experiments in the COMPASS divertor with liquid metals". In: *Nuclear Materials and Energy* 25 (2020), p. 100801. DOI: https://doi.org/10.1016/j.nme.2020.100801

11. J. Horacek et al. "Modeling of COMPASS tokamak divertor liquid metal experiments". In: *Nuclear Materials and Energy* 25 (2020), p. 100860. DOI: https://doi.org/10.1016/j.nme.2020.100860

12. V. Weinzettl et al. “Constraints on conceptual design of diagnostics for the high magnetic field COMPASS-U tokamak with hot walls”. In: *Fusion Engineering and Design* 146 (2019), pp. 1703–1707. ISSN: 0920-3796. DOI: https://doi.org/10.1016/j.fusengdes.2019.03.020

13. O. Ficker et al. “Runaway electron beam stability and decay in COMPASS”. in: *Nuclear Fusion* 59.9 (2019), p. 096036

14. M. Komm et al. “Divertor impurity seeding experiments at the COMPASS tokamak”. In: *Nuclear Fusion* 59.10 (2019), p. 106035. DOI: 10.1088/1741-4326/ab34d2

15. O. Grover et al. “Limit cycle oscillations measurements with Langmuir and ball-pen probes on COMPASS”. in: *Nuclear Fusion* 58.11 (2018), p. 112010. DOI: 10.1088/1741-4326/aabb19

16. J. Seidl et al. “Electromagnetic characteristics of geodesic acoustic mode in the COMPASS tokamak”. In: *Nuclear Fusion* 57.12 (2017), p. 126048. DOI: 10.1088/1741-4326/aa897e

17. V. Weinzettl et al. “Progress in diagnostics of the COMPASS tokamak”. In: *Journal of Instrumentation* 12.12 (2017), p. C12015. DOI: 10.1088/1748-0221/12/12/C12015

18. V. Weinzettl et al. “Dust remobilization experiments on the COMPASS tokamak”. In: *Fusion Engineering and Design* 124 (2017), pp. 446–449. DOI: https://doi.org/10.1016/j.fusengdes.2017.01.044

19. R. Panek et al. “Conceptual design of the COMPASS upgrade tokamak”. In: *Fusion Engineering and Design* 123 (2017), pp. 11–16. DOI: https://doi.org/10.1016/j.fusengdes.2017.03.002

20. M. Imrisek et al. “Optimization of soft X-ray tomography on the COMPASS tokamak”. In: *Nukleonika* 61.4 (2016), pp. 403–408. DOI: https://doi.org/10.1515/nuka-2016-0066

21. V. Weinzettl et al. “High-resolution spectroscopy diagnostics for measuring impurity ion temperature and velocity on the COMPASS tokamak”. In: *Fusion Engineering and Design* 96 (2015), pp. 1006–1011. DOI: https://doi.org/10.1016/j.fusengdes.2015.04.006

22. R. Panek et al. “Status of the COMPASS tokamak and characterization of the first H-mode”. In: *Plasma Physics and Controlled Fusion* 58.1 (2015), p. 014015. DOI: 10.1088/0741-3335/58/1/014015

23. J. Mlynar et al. “Soft X-ray tomographic reconstruction of JET ILW plasmas with tungsten impurity and different spectral response of detectors”. In: *Fusion Engineering and Design* 96 (2015), pp. 869–872. DOI: https://doi.org/10.1016/j.fusengdes.2015.04.055

Conference Publications

24. **Tomes, M.** and V Weinzettl. "Calibration of High-resolution Spectrometer for C III Triplet Measurements". In: *Proceedings of the 24th Annual Conference of Doctoral Students – WDS 2015*. MATFYZPRESS, Prague. 2015. ISBN: 978-80-7378-311-2

25. G.I. Pokol et al. "Neutral Beam Penetration and Photoemission Benchmark". In: *47th EPS Conference on Plasma Physics*. Vol. 45A. European Physical Society. 2021. ISBN: 979-10-96389-13-1. URL: http://ocs.ciemat.es/EPS2021PAP/pdf/P1.1007.pdf

26. Carine Giroud et al. "High performance ITER-baseline discharges in deuterium with nitrogen and neon-seeding in the JET-ILW". in: *2020 IAEA Fusion Energy Conf.* 2021, p–EX

27. M. Dimitrova et al. "Effect of the gas puff location on the divertor plasma properties in COMPASS tokamak". In: *Journal of Physics: Conference Series*. Vol. 1492. 1. IOP Publishing. 2020, p. 012003

28. L. Kripner et al. "Towards the integrated analysis of tokamak plasma equilibria: PLEQUE". in: *46th EPS Conf. on Plasma Physics*. European Physical Society. 2019. URL: http://ocs.ciemat.es/EPS2019PAP/pdf/P4.1033.pdf

29. L. Kripner et al. "Towards the Integrated Analysis of Tokamak Plasma Equilibria: PLEQUE". in: *Proceedings of the 28th Annual Conference of Doctoral Students – WDS 2019*. MATFYZPRESS, Prague. 2019. ISBN: 978-80-7378-409-6

30. K. Mitosinkova et al. "DOUBLE code simulations of emissivities of fast neutrals for different plasma observation view-lines of neutral particle analyzers on the COMPASS tokamak". In: *Journal of Physics: Conference Series*. Vol. 992. 1. IOP Publishing. 2018, p. 012009

31. M. Dimitrova et al. "Effect of the resonant magnetic perturbation on the plasma parameters in COMPASS tokamak's divertor region". In: *Journal of Physics: Conference Series*. Vol. 982. 1. IOP Publishing. 2018, p. 012001

32. O. Ficker et al. "RE beam generation in MGI disruptions on COMPASS". in: *44th EPS Conference on Plasma Physics*. Vol. Vol. 41F. European Physical Society. 2017. ISBN: 979-10-96389-07. URL: http://ocs.ciemat.es/EPS2017PAP/pdf/P5.126.pdf

33. M. Komm et al. "First detachment studies on COMPASS tokamak using nitrogen seeding". In: *44th EPS Conference on Plasma Physics*. Vol. Vol. 41F. European Physical Society. 2017. ISBN: 979-10-96389-07. URL: http://ocs.ciemat.es/EPS2017PAP/pdf/P1.118.pdf

34. O. Grover et al. "Reynolds stress and fluctuation measurements with Langmuir and ball-pen probes in the vicinity of the L-H transition on COMPASS". in: *44th EPS Conference on Plasma Physics*. Vol. Vol. 41F.

European Physical Society. 2017. ISBN: 979-10-96389-07. URL: http://ocs.ciemat.es/EPS2017PAP/pdf/P2.181.pdf

35. J. Mlynar et al. "Soft X-ray tomography in support of impurity control in tokamaks". In: *Journal of Physics: Conference Series*. Vol. 768. 1. IOP Publishing. 2016, p. 012001

36. J. Mlynar et al. "Effects of plasma control on runaway electrons in the COMPASS Tokamak". In: *42nd EPS Conference on Plasma Physics*. Vol. 39E. European Physical Society. 2015. ISBN: 2-914771-98-3. URL: http://ocs.ciemat.es/EPS2015PAP/pdf/P4.102.pdf